Interactions magma-roche, déformation à haute température et anisotropie sismique dans le manteau de la transition continent-océan et dans la lithosphère océanique

Takako Satsukawa

UNIVERSITÉ MONTPELLIER II
SCIENCES ET TECHNIQUES DU LANGUEDOC

THÈSE

Pour obtenir le grade de

DOCTEUR DE L'UNIVERSITÉ MONTPELLIER II

Discipline : Structure et évolution de la Terre et des autres planètes

Ecole Doctorale : SIBAGHE

Présentée et soutenue publiquement

Par

Takako SATSUKAWA

le 8 février 2012

Interactions magma-roche, déformation à haute température et anisotropie sismique dans le manteau de la transition continent-océan et dans la lithosphère océanique

JURY

Benoît ILDEFONSE	Directeur de recherche (Université Montpellier 2 - GM)	Directeur de thèse
Katsuyoshi MICHIBAYASHI	Professeur associé (Shizuoka University)	Directeur de thèse
Mitsuhiro TORIUMI	Professeur (JAMSTEC/IFREE)	Rapporteur
Shoji ARAI	Professeur (Kanazawa University)	Rapporteur
Aiming LIN	Professeur (Shizuoka University)	Examinateur
Toshiaki MASUDA	Professeur (Shizuoka University)	Examinateur
Hideki WADA	Professeur (Shizuoka University)	Examinateur
David MAINPRICE	Directeur de recherche (Université Montpellier 2 - GM)	Examinateur

Résumé

Cette thèse regroupe deux études distinctes, qui documentent le contrôle des microstructures sur les propriétés sismiques des roches. La première partie traite du développement des orientations préférentielles cristallographiques (OPC) dans le manteau supérieur, associé aux interactions liquide/magma-roche, enregistré dans des xénolites de péridotites du bassin d'arrière-arc de la mer du Japon. Les caractéristiques microstucturales et géochimiques des échantillons étudiés montrent que l'ouverture arrière-arc active est associée à une déformation du manteau supérieure similaire à celle observée dans l'ophiolite d'Oman. L'initiation de l'extension d'arrière-arc n'est pas associée à de fortes interactions entre percolation magmatique et déformation, en comparaison avec les zones de rifting continentales, probablement en raison des taille et durée relativement petites de l'épisode d'ouverture. La seconde partie présente une base de données unique d'OPC de plagioclase de roches mafiques plus ou moins déformées. Les OPC sont classées en 3 types principaux; leurs caractéristiques en fonction du régime de déformation (magmatique ou plastique) sont présentées et discutées. Les propriétés sismiques calculées des roches gabbroiques montrent que l'anisotropie tend à croitre avec l'intensité des fabriques, bien qu'elle soit généralement faible, en raison des effets opposés des olivines/clinopyroxènes et du plagioclase.

Mot-clés : propriétés sismiques, déformation du manteau supérieur, croûte océanique, xénolites de péridotite, olivine, orthopyroxène, clinopyroxène, plagioclase, orientation préférentielle cristallographique, EBSD, interaction magma/fluide-roche, extension arrière-arc, rifting

Abstract

This thesis compiles two distinct studies that both document the control of microstructures on rock seismic properties. The first part deals with the development of crystallographic preferred orientations (CPO) in the uppermost mantle associated with melt/fluid-rock interactions, recorded in peridotites xenoliths from the Japan sea back-arc basin. The microstructural and geochemical characteristics of the studied samples reveal that active spreading is associated to uppermost mantle deformation similar to that observed in the Oman ophiolite. At the onset of back-arc spreading, there are no strong interactions between melt percolation and deformation in comparison to continental rift zones, probably due to the relatively small size and short duration of the spreading event. The second part presents a unique database of plagioclase CPO from variously deformed mafic rocks. CPO are grouped in three main types; their characteristics as a function of deformation regime (magmatic or crystal-plastic) are outlined and discussed. Calculated seismic properties of gabbroic rocks show that anisotropy tends to increase as a function of fabric strength, although it is generally weak, due to the competing effect of olivine/clinopyroxene and plagioclase.

Keywords : seismic properties, upper mantle flow, oceanic crust, peridotite xenoliths, gabbroic rocks, olivine, orthopyroxene, clinopyroxene, plagioclase, crystallographic preferred orientation, EBSD, melt/fluid-rock interaction, back-arc spreading, rifting

Résumé étendu

Cette thèse regroupe deux études distinctes, qui documentent et discutent le contrôle des microstructures sur les propriétés sismiques des roches. La première partie (chapitres 1 à 6) traite du développement des orientations préférentielles cristallographiques (OPC) dans le manteau supérieur, associé aux interactions liquide/magma-roche, enregistré dans des xénolites de péridotites du bassin d'arrière-arc de la mer du Japon. Ces chapitres s'appuient sur 3 articles publiés et 2 articles en préparation.

La seconde partie (Chapitre 7) présente une base de données unique d'OPC de plagioclase de près de 200 échantillons de roches mafiques plus ou moins déformées, et discute des propriétés sismiques des roches gabbroiques, calculées à partir de ces données cristallographiques. Ce chapitre constitue la première version d'un article en préparation. L'objectif final de ce travail sera de constituer une base de données en ligne de fabriques cristallographiques de plagioclase.

1. Caractéristiques microstructurales et pétrologiques de xénolites mantelliques de zones d'arrière-arc et de rifting continental; implications pour l'évolution et l'anisotropie sismique du manteau supérieur

Cette étude présente le développement des microstructures dans des péridotites mantelliques, en relation avec les processus d'interactions magma/fluide-roche, dans le contexte de l'ouverture arrière-arc de la Mer du Japon. Pour ce faire, deux séries de xénolites mantelliques ont été étudiées (Fig. 1) : (1) les péridotites d'Ichinomegata (Oga Peninsula, NE Japon) ont enregistré le stade d'ouverture mature du bassin

d'arrière-arc, et (2) les péridotites d'Oki-Dogo (SO Japon) ont enregistré les stades précoces d'extension et d'amincissement de la croûte continentale. Le volcan Ichinomegata est célèbre pour l'abondance de xénolites de péridotites, qui ont déjà fait l'objet de nombreuses études. La direction rapide de polarisation des ondes S télésismiques est orientée Est-Ouest côté arrière-arc, et approximativement Nord-Sud dans l'avant-arc. L'île d'Oki-Dogo est le site à xénolites mantelliques le plus proche du continent dans l'arc sud-ouest japonais, approximativement 60 km au large de l'île de Honshu. Une large zone à faibles vitesses sismiques observées dans les modèles tomographiques suggère la présence d'interactions entre magma et roche dans le manteau supérieur.

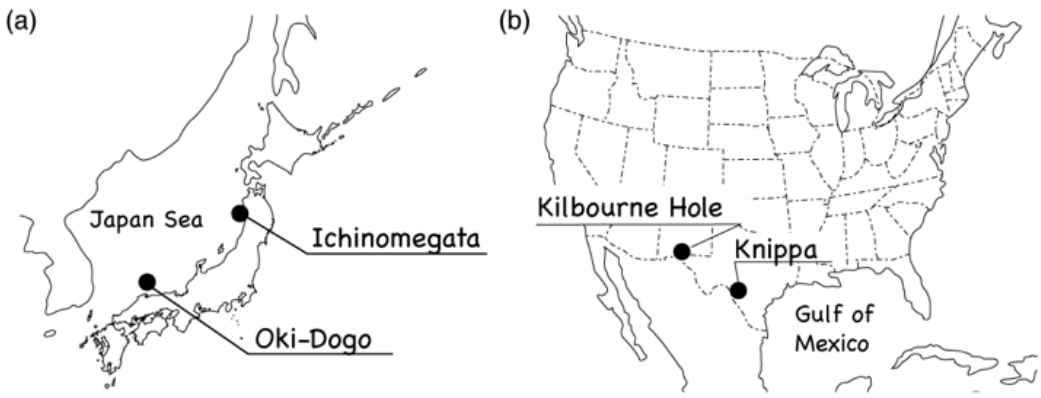

Figure 1. Cartes de localisation des xénolites mantelliques étudiées. (a) Ichinomegata (northeast Japan) et Oki-Dogo (southwest Japan). (b) Kilbourne Hole (New Mexico, USA) and Knippa (Texas, USA).

Les échantillons d'Ichinomegata et d'Oki-Dogo sont comparés à deux suites de xénolites en contexte continental (Fig. 1), dans le rift du Rio Grande (Kilbourne Hole, New Mexico, USA) et sur la marge Nord du Golfe du Mexique (Knippa, Texas, USA). Ces péridotites ont enregistré l'amincissement crustal (Knippa) et les stades précoces

de rifting actif (Kilbourne Hole) dans la croûte continentale. Kilbourne Hole fait partie de la province volcanique de Potrillo, l'un des plus grands champs volcaniques sous-saturés en silice dans le rift du Rio Grande. La direction moyenne des directions rapides d'ondes S est N22°, sub-parallèle à l'alignement des structures tectoniques régionales; le déphasage des ondes S est de ~1.2 s, ce qui est similaire à la moyenne globale dans les régions continentales. Une carrière à proximité de Knippa constitue le seul affleurement connu de péridotites mantelliques au Texas. Ces xénolites ont été remontés par les néphélinites relativement primitives de la province ignée de Balcones (~87 Ma), qui sont situées à la limite entre le craton Laurentien et la lithosphère transitionnelle Jurassique le long de la marge du Golfe du Mexique. Cette lithosphère transitionnelle comprend aussi les roches déformées de la chaîne tardi-Paléozoïque de Ouachita. Les données télésismiques montrent une augmentation rapide du déphasage, mais peu de changement dans la direction de polarisation en allant vers le Sud-Est depuis Junction (Texas).

La géochimie des minéraux des péridotites d'Ichinomegata est typique des péridotites résiduelles, appauvrie en terres rares légères (LREE). Cependant, leur forte anomalie positive en Th-U témoigne d'une possible origine métasomatique associée à la subduction de la plaque Pacifique. La composition chimique des péridotites d'Oki-Dogo montre qu'elles ont été affectées par des degrés variables de métasomatisme magmatique, qui peut-être associé à l'initiation de l'ouverture arrière-arc.

Les OPC d'olivine des péridotites d'Ichinomegata sont compatibles avec les systèmes de glissement (010)[100] and {0kl}[100]. L'angle entre le maximum de concentration [100] et la foliation décroit avec une intensité de fabrique croissante. En utilisant ces angles, le cisaillement (shear strain) est estimé entre 0.31 et 4.26. Les

estimations de température suggèrent que l'intensité des OPC (et donc la déformation) croit avec la profondeur. Ces observations indiquent que les microstructures de ces xénolites correspondent possiblement à un gradient de déformation lié à l'ouverture du bassin arrière-arc. Trois directions structurales distinctes sont présentes en lames mince dans ces péridotites : la trace de la foliation marquée par des lits riches en pyroxène, la direction moyenne de [100], et l'orientation préférentielle de forme des olivines. Le plan de cisaillement, qui porte [100], est oblique à la foliation. Ces caractéristiques microstructurales sont similaires à celles observées dans les péridotites de l'ophiolite d'Oman.

Les OPC d'olivine des péridotites d'Oki-Dogo sont compatibles avec le système de glissement classique (010)[100]. Elles montrent des concentrations de [010] relativement fortes, ainsi que des basses valeurs de Mg#. Néanmoins, l'absence de corrélation entre la chimie et l'intensité de la fabrique montre que, bien qu'elles aient pu être déformées en présence de liquide, la structure des péridotites d'Oki-Dogo n'est pas contrôlée par l'interaction entre déformation et percolation de magma.

Les OPC d'olivine des péridotites de Kilbourne Hole montrent des fabriques de type "b-axis fiber", avec de relativement fortes concentrations de [010] et une répartition en guirlandes de [100] et [001]. Les OPC d'olivine des péridotites de Knippa sont des fabriques de type "a-axis fiber", avec une concentration forte de [100] et une répartition en guirlandes de [010] et [001].

En résumé (Fig. 2), l'évolution du manteau supérieur enregistrée dans les xénolites d'Ichinomegata montre la préservation du gradient de déformation lors du dernier événement géologique, i.e., l'ouverture du bassin d'arrière-arc. A l'inverse, les péridotites d'oki-Dogo ne montrent pas de changement microstructural marqué associé au métasomatisme lié à l'initiation de cette ouverture arrière-arc; elles n'ont pas

enregistré d'interaction entre les processus de percolation magmatique et la déformation. Pour comparaison, la forte concentration de [010] dans les fabriques de Kilbourne Hole est liée à la déformation en présence de liquide magmatique en contexte de rifting continental. Les péridotites d'Oki-Dogo ont été affectées géochimiquement par des liquides magmatiques seulement en fin d'ouverture arrière-arc. Il n'existe pas d'échantillon, en contexte d'arrière-arc, comportant des fabriques cristallographiques très fortes comme celles de Knippa.

Cette étude apporte de nouvelles contraintes sur le comportement du manteau supérieur en contexte d'arrière-arc. Les caractéristiques microstructurales et géochimiques des échantillons étudiés montrent que l'ouverture arrière-arc active est associée à une déformation du manteau supérieur similaire à celle observée dans l'ophiolite d'Oman. L'initiation de l'extension d'arrière-arc n'est pas associée à de fortes interactions entre percolation magmatique et déformation, en comparaison avec les zones de rifting continentales, probablement en raison des taille et durée relativement petites de l'épisode d'ouverture.

La contribution du manteau supérieur dans la polarisation des ondes S télésismiques est, dans les quatre régions étudiées, évaluée et discutée en calculant les propriétés sismiques des péridotites échantillonnées à partir de leurs fabriques cristallographiques. Les péridotites d'Ichinomegata montrent une anisotropie compatible avec la présence d'une couche anisotrope dans le manteau llithosphérique supérieur. A Oki-Dogo, les anisotropies d'ondes P et S ne varient pas de manière significative malgré la variabilité chimique de ces péridotites (teneur en forsterite comprise entre 86 et 90). Après calcul des propriétés sismiques calculées, il est proposé que les xénolites de Kilbourne Hole proviennent d'une zone de cisaillement décrochante (foliation verticale et linéation horizontale).

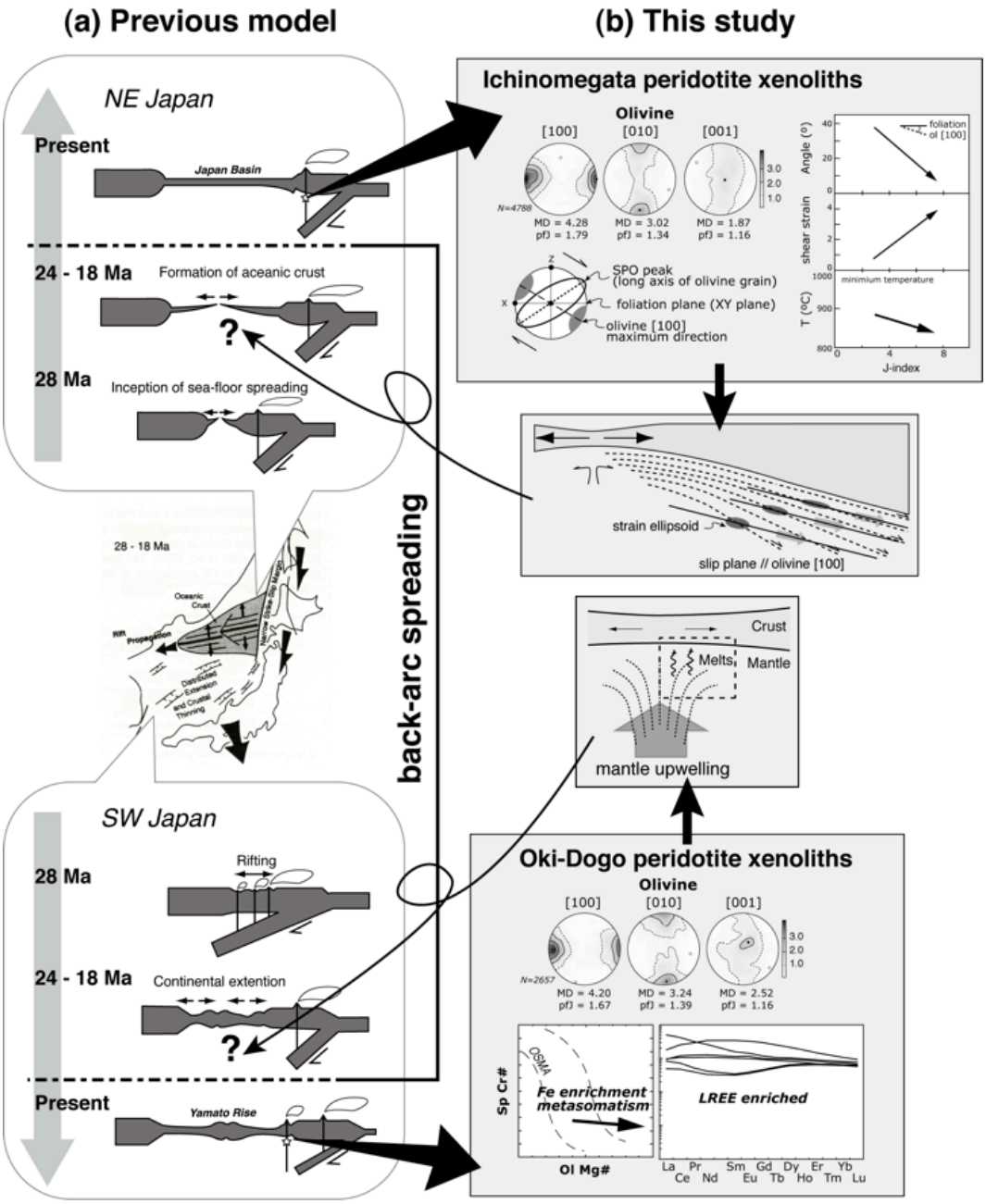

Figure 2. (a) Modèle schématique de l'ouverture de la mer du Japon (d'après Tamaki, 1995). (b) Résumé des caractéristiques microstructurales et pétrologiques des xénolites mantelliques d'Ichinomegata et Oki-Dogo et modèle schématique de l'évolution du manteau supérieur lors de l'ouverture du bassin d'arrière-arc.

La polarisation des ondes S observée dans le Rift du Rio Grande traduit cette fabrique

lithosphérique, mais la présence de liquide magmatique dans des fractures ou dikes parallèles à la foliation est requise car l'anisotropie cristallographique des xénolites est trop faible pour rendre compte du déphasage observé. Pour les péridotites de Knippa, en supposant une déformation mantellique horizontale, avec une direction d'écoulement parallèle aux directions rapides de polarisation des ondes S, les variations de déphasage peuvent être expliquées par la variabilité des fabriques qui ont préservé dans la lithosphère transitionnelle le gradient de déformation lié à l'orogène tardi-Paléozoique d'Ouachita. Les péridotites de Knippa sont globalement cohérentes avec une couche anisotrope dans le manteau lithosphérique qui intègre une histoire de déformation longue alternant des épisodes d'extension et de compression depuis la collision Gondwana-Laurentia.

2. Une base de données de fabriques de plagioclase: caractérisation des OPC et propriétés sismiques dans la croûte inférieure

La seconde partie de cette thèse présente une compilation exceptionnelle de près de 200 OPC de roches mafiques plus ou moins déformées. Les caractéristiques de ces fabriques en fonction du régime de déformation (magmatique ou plastique) sont présentées et discutées. Les échantillons proviennent de contextes géodynamiques variés, avec une majorité d'échantillons de la croûte océanique actuelle ou ophiolitique. Les échantillons océaniques ont été prélevés par forage ou par submersible, et proviennent de croûtes accrétées aux dorsales rapide (Hess Deep, plaque Cocos) et lente (Dorsale Sud-Ouest Indienne, Dorsale médio-Atlantique). Le plagioclase est la phase minérale dominante dans l'ensemble de ces échantillons. Les OPC sont classées en 3 types principaux : B) Un fort alignement de la normale au plan b (010) avec une

distribution en guirlande de [100], A) une forte concentration ponctuelle de l'axe a [100] avec des distributions en guirlandes parallèles de (010) et (001), et P) des maximum ponctuels de [100], (010] et (001). La majorité des CPO mesurées sont de types B et P, quelque soit le régime de déformation. Les CPO de type A sont moins communes; elles représentent 24% des échantillons déformées plastiquement (déformation par fluage-dislocation).

Les fabriques présentées dans cette compilation sont utilisées, avec celles des autres phases principales (olivine, pyroxène, amphibole) pour calculer et discuter les propriétés sismiques des roches gabbroiques de la lithosphère océanique. Les résultats de ces calculs montrent que l'anisotropie (jusqu'à 11% pour les ondes P et 15% pour les ondes S) tend à croitre avec l'intensité des fabriques (Fig. 3).

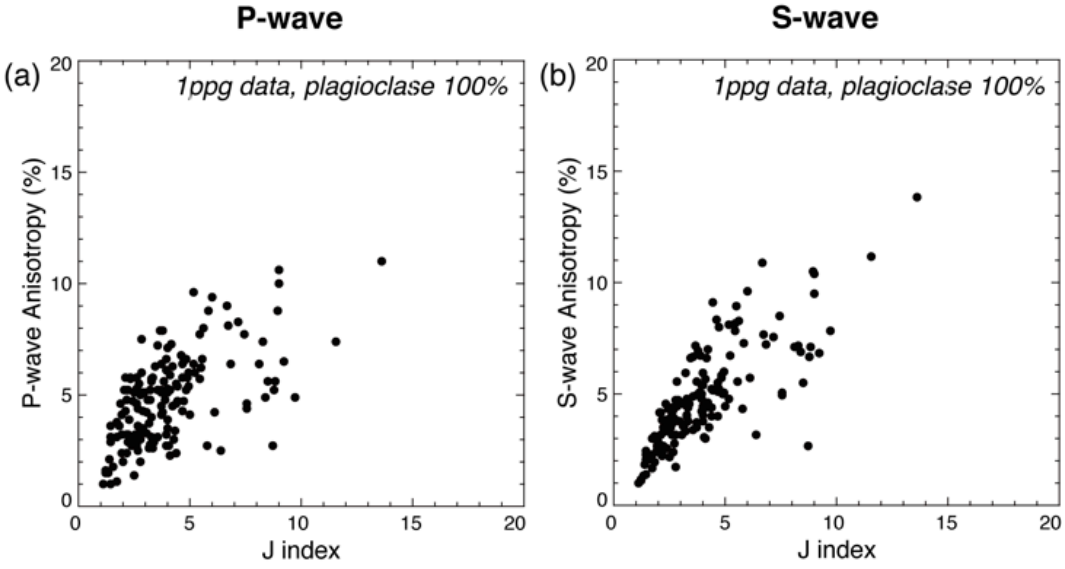

Figure 3. Anisotropie sismique calculée pour des aggrégats de plagioclase en fonction de l'intensité de fabrique J, pour les ondes P (a) et S (b).

Elle reste cependant généralement faible, en raison des effets opposés des olivines/clinopyroxènes et du plagioclase. L'anisotropie ne semble pas varier de façon

significative en fonction du régime de déformation et/ou de la provenance des échantillons. L'intensité des fabriques (caractérisée ici pour la première fois pour un minéral de basse symétrie par l'indice J) ne varie pas de façon systématique en fonction du type de CPO. Néanmoins, la concentration de [100] (type A) a une influence plus marquée sur l'anisotropie sismique dans les échantillons déformés plastiquement. A l'inverse, l'effet sur l'anisotropie sismique de l'alignement des plans (010) est plus marqué dans les échantillons déformés à l'état magmatique.

La signification statistique de cette base de données est probablement partiellement biaisée par l'abondance de certains types d'échantillons, en particulier ceux provenant de l'ophiolite d'Oman et du puits ODP 735B sur la dorsale Sud-Ouest Indienne. Cette compilation représente néanmoins la première vue d'ensemble des fabriques de plagioclases dans une séries d'échantillons présentant une grande variabilité de texture et provenant de divers contextes géodynamiques. Pour une compréhension complète des fabriques de plagioclase, il conviendra d'étendre cette base de données à un plus grand nombre d'échantillons, représentant une gamme exhaustive d'environnements géodynamiques; nous espérons publier cette base de donnée en ligne dans un futur proche, de telle sorte qu'elle puisse être progressivement complétée par la communauté internationale.

Acknowledgements

I first wish to express my gratitude to **Dr. Katsuyoshi Michibayashi** of Shizuoka University for his kind guidance, and critical discussions and suggestions for this thesis. I am grateful to **Dr. Benoit Ildefonse**, **Dr. David Mainprice**, **Dr. Marguerite Godard** and **Dr. Sylvie Demouchy** of Université Montpellier II, France, for their helpful recommendations and advice on my work, during my stays in Montpellier.

I would like to thank **Prof. Elizabeth Y. Anthony**, **Prof. Robert J. Stern**, **Prof. Jay Pulliam**, **Prof. Stephen S. Gao**, **Prof. Kelly H. Liu** and **Dr. Raye Urmidola** for their support and cooperation. **Prof. Toshiaki Masuda**, **Dr. Satish M. Kumar**, **Prof. Mitsuhiro Toriumi**, **Prof. Aimin Lin**, **Prof. Hideki Wada**, **Prof. Adolphe Nicolas**, **Prof. Françoise Boudier**, **Dr. Andréa Tommasi**, **Prof. Alain Vauchez**, **Dr. Jean-Louis Bodinier** and **Dr. Olivier Alard** are thanked for the encouragements, valuable suggestions, and discussions that helped to improve an early draft of the manuscript. I thank **Prof. Shoji Arai** of Kanazawa University, **Dr. Natsue Abe** of JAMSTEC and **Junji Yamamoto** of Kyoto University for their helpful recommendations regarding the sampling of Oki-Dogo peridotite xenoliths. I am specially thankful to **Dr. Tomoyuki Mizukami**, **Dr. Ikuo Katayama**, **Dr. Yoshio Kono**, **Dr. Keshav Shantanu**, **Dr. Vincent Soustelle**, **Dr. Luiz F. G. Morales**, **Dr. Claudio Marchesi** and **Dr. Ken-ichi Hirauchi** for their technical and helpful advice and support. I wish to thank to **Dr. Tatsu Kuwatani**, **Dr. Yumiko Harigane**, **Ms. Miki Tasaka**, **Mr. Masashi Muramoto**, **Mr. Yuya Kusafuka**, Michibayashi laboratory's members (**Ms. Yuri Shinkai**, **Mr. Naoaki Komori**, **Mr. Masashi Kino**, **Mr. Tatsunori Ikeya**, **Mr. Toshiya Umegaki**, **Mr. Yosuke Kondo**, **Ms. Ayaka**

Onoue, **Mr. Tomoki Shibata** and **Mr. Keisuke Furuhata**), graduated students and post-doctoral researchers of Université Montpellier II (**Dr. Mickaël Bonnin**, **Dr. Amélie Vergne**, **Ms. Kate Higgie**, **Mr. Roberto Agrusta**, **Mr. Steve Peuble**, **Mr. Théo Berthet**, **Mr. Camille Clerc**, **Mr. Grégory Fanjat**, **Ms. Fatna Kourim**, **Ms. Kamar Chetouani**, **Ms. Amel Barich**, **Mr. Zoltan Konc** and **Mr. Erwin Frets**) and my friends for their helpful advice.

CPO figures were produced using the interactive programs developed by **Dr. David Mainprice** of Université Montpellier II, France (ftp://www.gm.univ-montp2.fr/mainprice//CareWare_Unicef_Programs/). **Prof. Mitsuhiro Toriumi** and **Dr. Tatsu Kuwatani** are thanked for their assistance in operating the JEOL JXA-8200 electron microprobe at the University of Tokyo. **Dr. Satish M. Kumar** is thanked for his assistance in operating the JEOL JXA- 733 electron microprobe at of analytical instruments housed at the Center for Instrumental Analysis, Shizuoka University. I am grateful to **Prof. Hiroyuki Kagi** of University of Tokyo, Japan, for his assistance during Raman spectra analyses. **Dr. Fabrice Barou** is thanked for his assistance in operating SEM-EBSD facility (JEOL JSM- 5600 and CamScan X500FE Crystal Probe) at Géosciences Montpellier of Université Montpellier II. **Dr. Olivier Bruguier** is thanked for his assistance in operating the LA-ICPMS of Université Montpellier II. I thank **Dr. Aaron Stallard**, University of Canterbury, New Zealand, for improving the English of the manuscript and **Mr. Hideki Mori** for technical assistance with the preparation of thin sections. I thank the **IRIS DMS** for providing the seismic waveform data used in the study.

This work was supported by Grant-in-Aid for Scientific Research (223708) as part of a JSPS Research Fellowship for Young Scientists (to TS), research grant (16340151, 19340148, 22244062) from the Japan Society for the Promotion of

Science (to KM), a scholarship from the Mitsui Scholarship Foundation for Career Development awarded to TS, Texas Advanced Research Program (to EYA and RJS), and EAR-0750711 by the U.S. National Science Foundation (to JP, EYA, and RJS), the Norman Hackerman Advanced Research Program 003661-0003-2006 (to EYA and RJS) and the US National Science Foundation awards EAR-0739015 and EAR-0952064 (to KHL and SSG).

Finally, I deeply thank my family, **Mr. Hiroaki Satsukawa**, **Mrs. Teruyo Satsukawa** and **Ms. Hanako Satsukawa** for their attentive support.

Thesis Summary

This thesis compiles two independent studies on the uppermost mantle and oceanic lower crust, which share a discussion the microstructural constraints. This thesis is composed of seven chapters containing three individual papers published to earth science journals. Part I (Chapters 1-6) presents the development of microstructures in the uppermost mantle associated with melt/fluid-rock interactions, as studied and analyzed from peridotite xenoliths. Part II presents a unique database of about 200 plagioclase Crystallographic Preferred Orientations (CPO) from variously deformed gabbroic rocks, and discuss the seismic properties of these rocks as a function of fabric strength.

Chapter 1: "**Introduction**". This chapter introduces the geodynamics of back-arc spreading, an overview of the uppermost mantle structure in this context, and geological and seismological background of analyzed samples in this thesis.

Chapter 2: "**Microstructures and melt/fluid rock interactions of the uppermost mantle beneath the back-arc region of Japan Sea: Peridotite xenoliths from Ichinomegata, Oki-Dogo**". It presents an article entitled "Determination of slip system in olivine based on crystallographic preferred orientation and subgrain rotation axis: examples from Ichinomegata peridotite xenoliths, Oga peninsula, Akita prefecture" published in *The Journal of the Geological Society of Japan (Satsukawa and Michibayashi, 2009)*. This chapter describes the geochemical characteristics and microstructural evolution of peridotite xenoliths from the uppermost mantle lithosphere entrained by Ichinomegata and Oki-Dogo Island volcanoes.

Chapter 3: "**Seismic anisotropy of the uppermost mantle beneath the back-arc region of Japan Sea: Evidence from Ichinomegata and Oki-Dogo**

peridotite xenoliths". This chapter shows that the crystallographic anisotropy of Ichinomegata and Oki-Dogo described in Chapter 2 could be the dominant source of seismic anisotropy (i.e., observed delay times of shear-wave velocity) in the Japan Sea region.

Chapter 4: "**Seismic anisotropy of the uppermost mantle beneath the Rio Grande rift: Evidence from Kilbourne Hole peridotite xenoliths**". This chapter contains an article published in *Earth and Planetary Science Letters (Satsukawa et al., 2011)*. This article describes the shear-wave splitting observed in the Rio Grande rift, and proposes that it is a reflection of the lithospheric fabric and the presence of melt as thin cracks or dikes in the uppermost mantle.

Chapter 5: "**Uppermost mantle anisotropy beneath the southern Laurentian margin: Evidence from Knippa peridotite xenoliths**". This Chapter contains an article published in *Geophysical Research Letters (Satsukawa et al., 2010).* The mantle lithospheric fabrics revealed by the Knippa xenoliths mostly explain the magnitude of shear-wave splitting observed along the southern margin of the Laurentian craton, which could be related to 'frozen' deformation associated with the alternate processes of extension and compression beneath the southern Laurentian margin.

Chapter 6: "**Microstructure and seismic properties at the spreading/rifting zone**". This chapter provides a brief summary of the previous chapters, outlining the main microstructural and petrological characteristics of the four suites of peridotite xenoliths (Ichinomegata, Oki-Dogo, Kilbourne Hole and Knippa) analyzed in this thesis, and discussing the evolution of the uppermost mantle during back-arc spreading.

Chapter 7: "**A plagioclase fabric database: Characterization of CPO and**

seismic properties in the lower crust". This chapter presents a unique database of almost 200 plagioclase CPOs, and the calculated seismic properties of variously deformed gabbroic rocks from the oceanic lithosphere. CPO are grouped in three main types; their characteristics as a function of deformation regime (magmatic or crystal-plastic) are outlined and discussed. Calculated seismic properties of gabbroic rocks show that anisotropy tends to increase as a function of fabric strength, although it is generally weak, due to the competing effect of olivine/clinopyroxene and plagioclase.

Contents

PART I

Microstructural/petrological characteristics of peridotite xenoliths in the back-arc spreading/rifting zones and implication for the evolution and seismic anisotropy in the uppermost mantle

Chapter 1

Introduction

1-1. Geodynamics of spreading/rifting zones

In the 1960's, the establishment of the plate tectonics theory made possible the explanation of fundamental geological processes at the global scale, by providing a unified scheme for relating deep earth (mantle) dynamics and surface, crustal geodynamics. There are three types of plate boundaries: divergent boundaries (mid-ocean ridges or rifting zones), convergent boundaries (subduction zones or continental collision) and strike-slip or transform boundaries. Back-arc basins form at convergent plate boundaries and are due to extensional processes that represent local divergence in an overall convergent context. Divergent boundaries are recognized as spreading and rifting zone, and they are particularly important for producing crust, deformation of the lithosphere, asthenospheric flow, partial melting, and melt/fluid rock interaction. Evolution of ocean basins and the rifting of continents are fundamental components of plate tectonics, and the process of continental break-up remains debated (e.g., Kendall et al., 2005). All the aforementioned processes can result in anisotropic structures at all scales; decrypting these anisotropic structures, which control the geophysical signature and the rheological properties of the rocks, is essential to further constrain and understand the dynamics and evolution of the Earth.

1-2. Back-arc spreading

Back-arc spreading is a process that is intemately coupled with subduction, and is one of the various spreading tectonic contexts, resulting in the formation of back-arc basin. The Western Pacific region display many arc-trench systems, which include more than 70 % of all back-arc basins on the Earth (Fig. 1). There are two types of back-arc basins: oceanic type and continental types (Tamaki, 1995). The oceanic type is formed at the back-arc side of oceanic island arcs (e.g., Mariana trough,

Lau basin), whereas continental type occurs at the back-arc side of continental arcs (e.g., Japan sea, Kuril basin).

Two models are proposed to explain back-arc spreading (Fig. 2). Extensional stresses generated from trench rollback (and retrograde migration of their associated slabs) were identified as the likely origin of back-arc basins (Dvorkin et al., 1993; Faccenna et al., 1996; Jolivet et al., 1994). However, the exact mechanism as to how subduction dynamics controlled the process was not apparent. There are other processes besides trench motion that are important in producing back-arc basins. Extensional forces may arise from gravitational collapse of regions with thickened crust (Martinod et al., 2000), or from far-field stresses due to changes in plate direction and continent–continent collisions (Silver et al., 1998). These effects have been shown to be important for back-arc basin development in the Aegean and Japan Seas as their contribution likely modulated the more dominant extensional forces from roll-back subduction (Jolivet et al., 1994).

Based on observations of back-arc basin ages, histories of spreading, quiescence and compression in the overriding plate, Clark et al. (2008) modeled the time-development of subduction zones and back-arc basins. They found that quasi-episodicity is the dominant form of back-arc development in present times, in which the back-arc shifts between phases of rifting, spreading and quiescence (Clark et al., 2008). Those subduction zones for which the subducting plates are moving slowly, such as in the Mediterranean or the Scotia Sea, experience only pseudo-episodicity, where spreading moves linearly towards the trench but often does so in discrete ridge-jump events.

The Japan Sea is the one of the back-arc basins that has a complicated geological structure (Tamaki et al., 1992), dominated by the splitting of the eastern

margin of the Eurasian continent (e.g., Otofuji and Matsuda, 1984; Otofuji et al., 1985). Its floor is composed of oceanic crust, rifted continental crust and stretched continental crust (Tamaki et al., 1992). Tamaki (1995) proposed a tectonic model based on several topography, paleomagnetism, and ocean drilling studies (Fig. 3a). The proto-Japanese island arc initiated on the continental margin of the Eurasian plate (30 Ma), then back-arc spreading developed from the northeast Japan to the southwest Japan (Fig. 3b). In the initial stage, crustal thinning and extension was induced, and seafloor spreading was triggered by the breakup of the lithosphere along the strike-slip margin in the northeast Japan Sea. The spreading center propagated southwestward to increase the area of newly produced oceanic crust in the northeast Japan Sea (associated to normal seafloor spreading). The crust of the southwest Japan Sea was then extended and thinned from the arc crust, and formed basins and rises (Fig. 3c). However, the evolution of the japanese back-arc spreading is not fully understood; for example, the cause of formation, processes of evolution, similarity and differences to the mid ocean ridge are yet to be fully described (Tamaki, 1995). The petrography, geochemistry and microstructure of mantle peridotites are expected to be complicated in, such an active tectonic environment. Most of the basic geological structure of the present Japanese Islands was formed during this time. The surface dynamics are related to the deeper part. The objective of this study is to estimate the mantle flow evolution from the peridotite xenoliths carried up to the surface by japanese arc volcanoes. A few localities in Japan give access to mantle-derived xenoliths, which provide us with the geochemical, microstructural, and petrophysical information on deep processes and materials beneath the Japan Sea.

1-3. The uppermost mantle structure

1-3-1. Seismic anisotropy in the uppermost mantle

Seismic tomography, obtained by inversion of seismic velocity data with respect to a reference Earth model (e.g., Aki and Lee 1976), is a powerful tool to reveal the whole mantle structure and dynamics. Tomographic images depend on the initial reference models and hypocentral locations (e.g., Michael, 1988). Over the last decades, multiple networks of seismic stations have been deployed worldwide to investigate mantle wedge structures. Recent investigations of shear-wave splitting and petrophysical studies have shown the relationships between petrofabric and seismic anisotropies (e.g., Ben Ismaïl and Mainprice, 1998). Seismic anisotropy is present near the surface due to aligned cracks (e.g., Crampin, 1984), in the lower crust, upper and lower mantle due to the mineral preferred orientation (e.g., Karato, 1998; Mainprice et al., 2000). The seismic anisotropy resulting from olivine CPO tends to produce a maximum seismic wave velocity parallel to the direction of plastic flow within the upper mantle (Nicolas and Christensen, 1987). In some cases, other physical factors may contribute to the measured anisotropy, for example mineral shape preferred orientation and alignment of melt inclusions (e.g., Mainprice, 1997). The variation of seismic properties of the uppermost mantle is also controlled by the modal composition and the orientation of the structural frame (e.g., Nicolas and Christensen, 1987). The role of seismic anisotropy estimated from mantle rocks has become increasingly important to understand the evolution of the uppermost mantle. Seismic anisotropy is directly related to the elastic anisotropy of the volumetrically dominant phases of olivine, orthopyroxene and clinopyroxene, and to the statistical alignment of their crystallographic axes. Since the pioneering work of Nicolas and Christensen (1987), various peridotite samples have been examined around the world for this purpose.

There are several methods for calculating seismic properties, as reviewed in Mainprice (2007). We use the simplest and best known averaging techniques for obtaining estimates of the effective elastic constants of polycrystals, the Voigt (1928) and Reuss (1929) averages. In this calculation, one only uses the volume fraction of each phase, the orientation and the elastic constants of the single crystals or grains. In terms of statistical probability functions, these are first order bounds as only the first order correlation function is used, which is the volume fraction. Note that no information about the shape or position of neighboring grains is used. The Voigt average is found by simply assuming that the strain field is everywhere constant. The strain at every position is set equal to the macroscopic strain of the sample. M_{voigt} is then estimated by a volume average of local stiffnesses M_i with orientation x_i, and volume fraction x_i,

$$M_{voigt}=\sum x_i M_i$$

Reuss average is found by assuming that the stress field is everywhere constant. The stress at every position is set equal to the macroscopic stress of the sample. M_{Reuss} is then estimated by the volume average of local compliances M_i,

$$1/M_{Reuss}=\sum x_i/M_i$$

These two estimates are not equal for anisotropic solids, with the Voigt average being an upper bound and the Reuss average a lower bound. A realistic physical estimate of the moduli should lie between the Voigt and Reuss average bounds as the stress and strain distributions are expected to be somewhere between uniform strain (Voigt bound) and uniform stress (Reuss bound). Hill (1952) proposed using arithmetic mean of the Voigt and Reuss bounds, sometimes called the Hill or Voigt-Reuss-Hill (VRH) average,

$$M_{VRH}=1/2(M_{voigt}+M_{Reuss})$$

The VRH average is often close to experimental values, but it has no theoretical justification. As it is simple and easy to calculate the arithmetic mean of the Voigt and Reuss elastic tensors, most authors tend to apply the VRH average. In earth sciences the Voigt, Reuss and VRH averages have been widely used for averages of oriented polyphase rocks (e.g., Crosson and Lin, 1971). Although the Voigt and Reuss bounds are often far apart for anisotropic materials, they still provide the limits within which the experimental data should be found (e.g., Watanabe et al., 2011).

1-3-2. Peridotite in the upper mantle

The major cause of seismic anisotropy in the upper mantle is the crystallographic preferred orientations (CPOs) of olivine. Numerous studies tried to constrain anisotropy from naturally deformed samples, experimentally deformed samples and numerical simulation. The CPOs do not only cause seismic anisotropy, but also record some aspects of the deformation history. Direct analysis of the uppermost mantle samples allows one to jointly discuss mantle geodynamic evolution and the effect of deformation on seismic properties. Peridotite xenoliths are usually brought up by alkaline basalts or by kimberlites, and sample the uppermost mantle beneath oceanic hotspots, continental rifts and continental cratons (e.g., Nixon, 1987). Such magmas can transport various deep-seated rocks, including peridotite xenoliths, which give us direct evidence of petrological and fabric characteristics (e.g., Arai et al., 2000).

Olivine is the major constituent mineral of peridotites, and is one of the most studied minerals in Earth Sciences. Experimental and natural sample studies are the basis for the olivine CPO classification, illustrating the role of stress and water content as the controlling factors for the development of five CPO types (A, B, C, D and E;

Fig. 4). These five CPO types are assumed to represent the dominant slip system activity, such that A ≡ [100](010), B ≡ [001](010), C ≡ [001](100), D ≡ [100]{0kl}, and E ≡ [100](001). Mainprice (2007) added an additional class AG-type CPO, which is quite common in naturally deformed samples.

The evolution of the uppermost mantle is strongly linked to partial melting and refertilization processes. Recent studies have shown that percolating melts may react with the mantle lithosphere, leading to enrichment in fusible components; i.e., refertilization via the crystallization of pyroxenes and spinel (e.g., Le Roux et al., 2007, 2008). Experimental deformation of partially molten assemblages reveals that the presence of melt, even in low fractions, results in a large reduction in viscosity (Hirth and Kohlstedt, 1995; Rosenberg and Handy, 2005; Takei, 2005). In addition, deformation may result in a higher transient permeability and facilitate melt segregation (e.g., Rosenberg and Handy, 2000; Holtzman et al., 2003). This feedback between melt percolation and deformation, as observed experimentally, has also been proposed, based on observations of geological structures, to be responsible for the development of shear zones in the middle and lower crust (e.g., Vauchez and Tommasi, 2003) and in the shallow mantle (Kelemen and Dick, 1995). At the plate scale, it has also been suggested (based on geodynamical models and seismic anisotropy data) that magmas play an essential role in the initiation of rifting (e.g., Buck, 2006; Kendall et al., 2006) and in the erosion of the lithosphere above mantle plumes (Thoraval et al., 2006). Therefore, interactions between melt percolation and deformation in the mantle are important in the evolution of the lithosphere, controlling its composition and mechanical behavior.

1-4. Geological and seismological background of analyzed samples

Direct analysis of natural samples allows one to constrain their deformation history, and the effect of this deformation on seismic properties. In order to understand the development of microstructures in the uppermost mantle associated with melt/fluid rock interactions in peridotites in back-arc spreading settings, as well as the implication for the seismic properties of the uppermost mantle, we used peridotite xenoliths from four localities in the Japan back-arc region and other extensional tectonic setting for comparison. In the Japan Sea back-arc basin, Ichinomegata peridotites xenoliths preserved a mature stage of normal seafloor spreading, whereas Oki-Dogo peridotites preserved the extension and the thinning of continental crust at the onset of bac-arc opening. For comparison, we have studied spinel peridotite xenoliths from Kilbourne Hole (New Mexico, USA) and peridotite xenoliths from Knippa (Texas, USA), two different extensional tectonic settings. Peridotite xenoliths from Kilbourne Hole represented the early stages of spreading in an active rift zone, whereas Knippa peridotites xenoliths were derived from the mantle lithosphere that could have recorded deformations in relation to the thinning of continental crust on the plate margin.

1-4-1. Ichinomegata, NE Japan

Ichinomegata volcano is located on the Oga Peninsula, in the northeast Japan arc (Fig. 5a). It is very famous for the abundant deep-seated xenoliths, and there are many previous petrological and geochemical studies (e.g., Kuno, 1967; Abe et al., 1995). The host magma is calc-alkali andesite to dacite, ca. 10,000 yr in age (Horie, 1964). Peridotites are most frequently lherzolite, sometimes veined by hornblendite with pargasite and rarely phlogopite (Abe et al., 1998). Those amphiboles, spinel-pyroxene symplectite and exsolution lamella of clinopyroxene in orthopyroxene

are mantle metasomatic minerals, due to addition of hydrous melt/fluid to dry peridotite (e.g., Abe and Arai, 1993).

1-4-2. Oki-Dogo, SW Japan

The Oki-Dogo Island is an important site for studying mantle xenoliths because it marks the most continent-ward occurrence of mantle peridotite xenoliths in the SW Japan arc, approximately 60 km offshore from Honshu Island (Fig. 5a). The metamorphic age of the basement complex is ca. 200 Ma, as determined by the Sm–Nd isochron method (Tanaka and Hoshino, 1987) and Pb–Pb analyses of zircon (Yamashita & Yanagi, 1994). The alkaline basalts that contain the xenoliths were erupted during the Pliocene–Pleistocene (from 4.38±0.23 to 0.55±0.09 Ma) (Uto et al., 1994), after the opening of the Japan Sea, which is thought to have occurred during the Oligocene–Miocene (28–18 Ma) as a consequence of back-arc spreading (e.g., Tamaki et al., 1992). Numerous mafic and ultramafic xenoliths, including residual mantle peridotite, have been reported from the island (Takahashi, 1975, 1978a, 1978b).

1-4-3. Kilbourne Hole (New Mexico, USA)

Continental rifting is a complex process involving deformation of the lithosphere, asthenospheric flow, and partial melting; each of these processes can result in seismically anisotropic structures. As such, the significance of shear-wave splitting, in particular whether it represents lithospheric fabric or asthenospheric flow, remains controversial (Gao et al., 2008). Measurements of shear-wave splitting using P-to-S converted phase (SKS, SKKS, and PKS) play a crucial role in imaging the orientation and degree of polarization of mantle fabrics, and in constraining models for the formation of these fabrics (Silver, 1996; Savage, 1999; Liu, 2009).

The Kilbourne Hole maar (Fig. 5b) exposes Quaternary basanites containing both crustal and mantle xenoliths (Hamblock et al., 2007). It is roughly elliptical in shape, almost 3 km in length, and from 100 to 125 m deep. Using ^{3}He surface exposure methods, the age of eruption has been constrained to 10–20 ka (Anthony and Poths, 1992; Williams, 1992); thus, the xenoliths represent essentially ambient conditions for the Rio Grande rift. Kilbourne Hole is a part of the Potrillo volcanic field (Anthony et al., 1992; Thompson et al., 2005), which consists of cinder cones, maars, and fissure flows of basanitic and alkalic basalt composition. The Potrillo volcanic field is one of the largest silica-undersaturated volcanic fields in the Rio Grande rift, and has been interpreted as representing the products of small-degree partial melting of a volatile-charged asthenosphere. Based on their observation of olivine CPO in Kilbourne Hole peridotite xenoliths from the Rio Grande rift, Bussod and Irving (1981) proposed that deformation was accompanied by syntectonic recrystallization in the presence of intercrystalline fluid. However, these samples were analyzed using a universal stage, and the seismic properties of the mantle beneath the Rio Grande rift were not considered.

1-4-4. Knippa (Texas, USA)

The nature of ocean-continent transitional lithosphere is complicated. Measuring shear-wave splitting (SKS) images the orientation and degree of polarization of mantle fabrics, and constrain models for the formation of these fabrics, including the mantle beneath south central North America (Gao et al., 2008). In spite of the robustness of SKS measurements, it is often not clear if anisotropy inferred from these measurements resides in the mantle lithosphere or asthenosphere (Fouch and Rondenay, 2006). Here we are interested in understanding fabrics for mantle

xenoliths from southern Texas, and use this information to understand shear-wave splitting for upper mantle beneath the northern margin of the Gulf of Mexico (GoM). A previous study documented significant shear wave splitting beneath this region, with fast directions parallel to the Texas GoM continental margin (Gao et al., 2008). They noted that SKS splitting reached an apparent maximum where the crust was thinnest and discussed the parallelism of the observed mantle anisotropy and the SE edge of the Laurentian cratonic keel.

A quarry near Knippa, Texas exposes Late Cretaceous basanites containing upper mantle xenoliths (Fig. 5b). This is the only known mantle peridotite locality in Texas (Young and Lee, 2009). Mantle xenoliths were carried up by Late Cretaceous (~87 Ma) quite primitive nephelinites of the Balcones Igneous Province (BIP) (Griffin et al., 2010). BIP volcanoes approximate the boundary between the ~1.1-1.4 Ga southernmost Laurentian (Texas) craton and Jurassic age transitional lithosphere along the GoM margin. The transitional lithosphere also involves the deformed rocks of the Ouachita fold belt (Keller et al. 1989).

The lithosphere that formed or was reworked during these tectonics events is preserved across a region that extends from the Grenville province of the craton (Anthony, 2005) to Jurassic oceanic crust in the GoM. Therefore, it is likely that the Knippa peridotite xenoliths are derived from the uppermost mantle lithosphere. The region is dominated by alternate episodes of extension and compression. The associated mantle microstructure could preserve some of this deformation, suggesting an important potential for tectonic inheritance and overprinting.

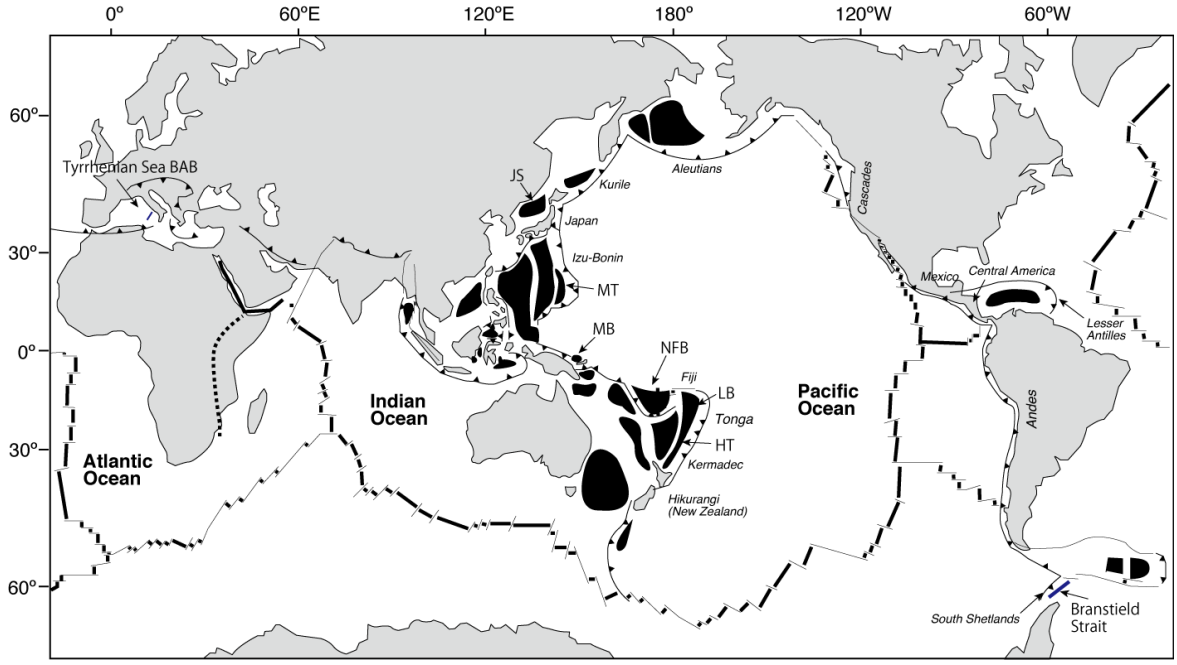

Figure 1. Locality map of back-arc basins (black areas) in the world. Modified from Tamaki and Honza (1991). More than 70 % of back-arc basins are located in the Western Pacific region. JS: Japan Sea; MT: Mariana trough; MB: Manus Basin; NFB: North Fiji Basin; LB: Lau Basin; HT: Havre trough.

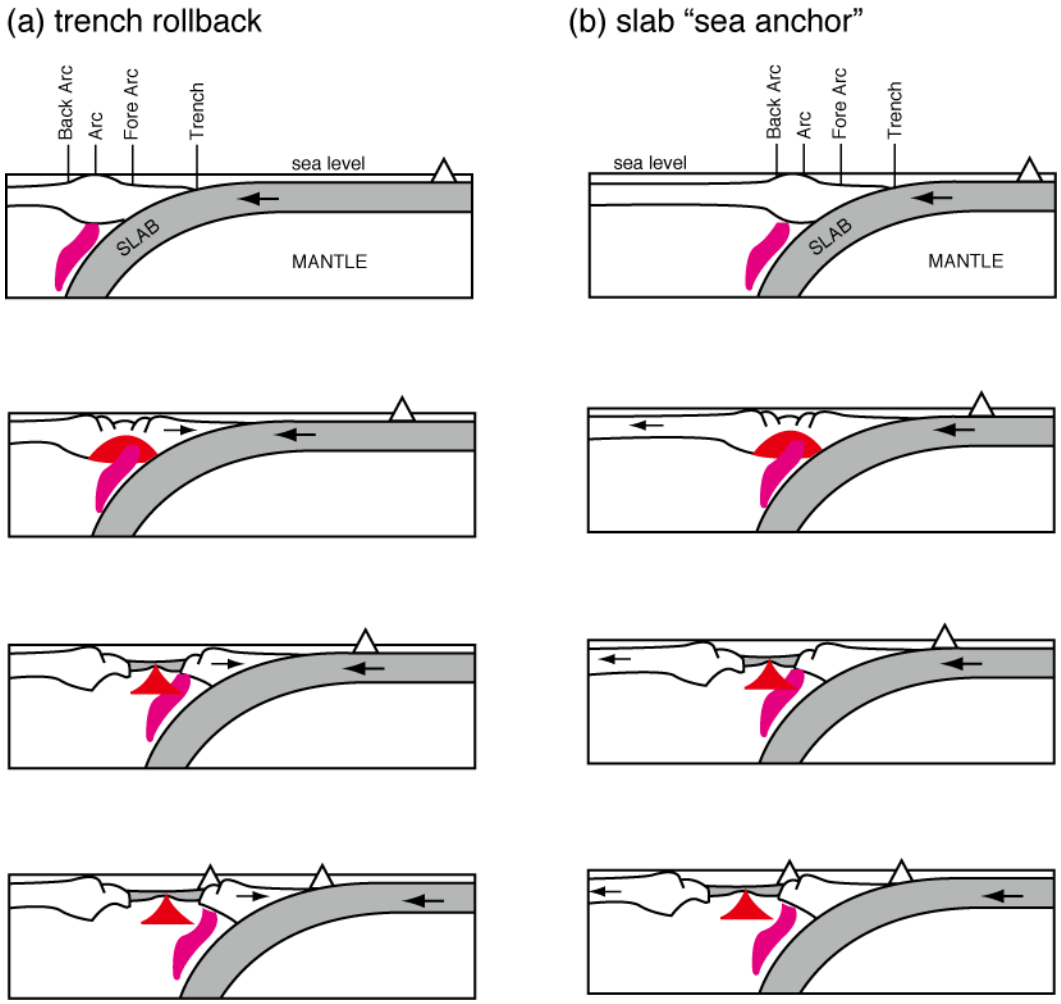

Figure 2. Schematic models of back-arc spreading mechanism. (a) trench rollback model, (b) slab “sea anchor” model. Modified from Martinez et al. (2007).

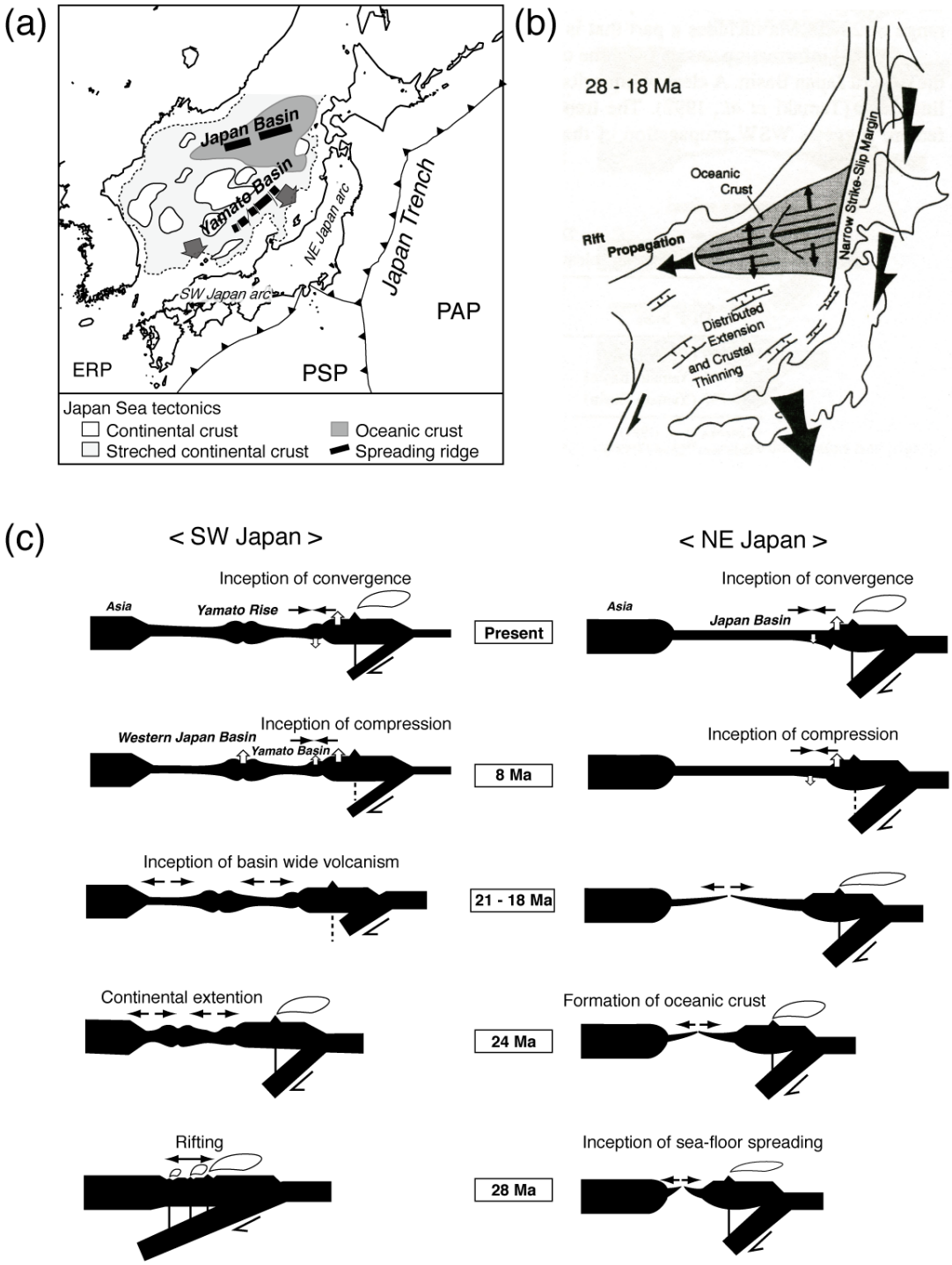

Figure 3. (a) Crustal component of the Japan Sea. The NE domain consist in oceanic crust, whereas the SW domain consist of continental and stretched continental crust. PSP: Philippine Sea Plate; PAP: Pacific Plate; ERP: Eurasia. Modified from Kimura et al. (2003). (b, c) Schematic model the Japan Sea opening (modified from Tamaki, 1995). The NE domain was formed by normal seafloor spreading, whereas the SW domain was formed by the extension and thinning of the continental crust.

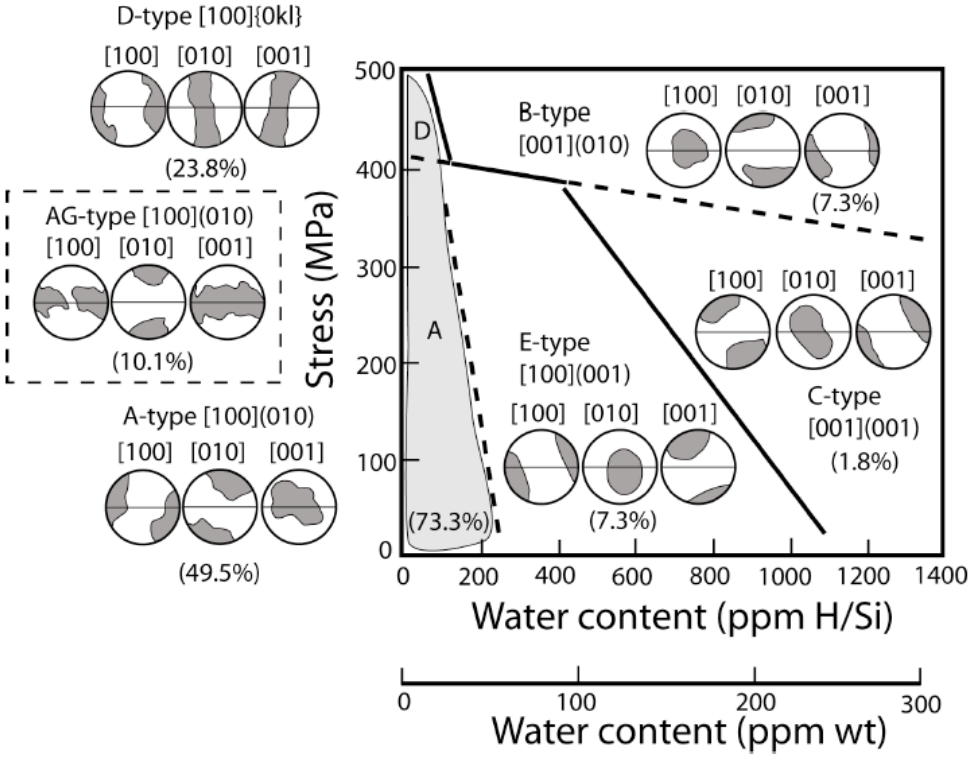

Figure 4. Classification of olivine CPOs as a function of stress and water content (Mainprice, 2007). The water content scale in ppm H/Si is that originally used by Jung and Karato (2001). The numbers in brackets are the percentage of samples with the fabric types found in the database of Ben Ismaïl and Mainprice (1998).

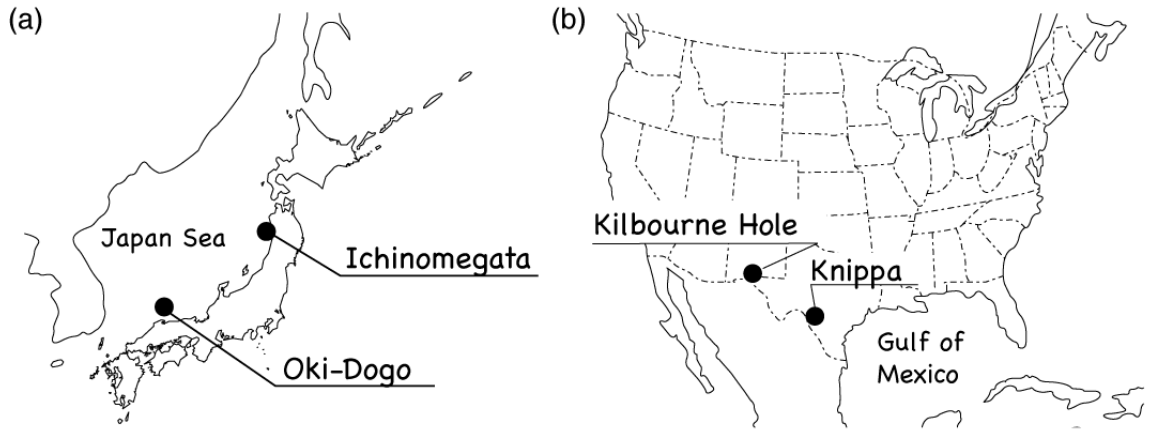

Figure 5. Locality map of mantle xenoliths studied in this PhD. (a) Ichinomegata (northeast Japan) and Oki-Dogo (southwest Japan). (b) Kilbourne Hole (New Mexico, USA) and Knippa (Texas, USA).

Chapter 2

Microstructures and melt/fluid rock interactions of the uppermost mantle beneath the back-arc region of Japan Sea: Peridotite xenoliths from Ichinomegata and Oki-Dogo

Originally Published in modified form as "Determination of Slip System in Olivine Based on Crystallographic Preferred Orientation and Subgrain-Rotation Axis: Examples from Ichinomegata Peridotite Xenoliths (Oga Peninsula, Akita Prefecture)" by T. Satsukawa and K. Michibayashi, *The Journal of the Geological Society of Japan*, **115**(6), 288-291. (In Japanese with English abstract), 2009,

Abstract

The uppermost mantle in the back arc region of subduction zones is a site of complex interactions between deformation, partial melting, fluid migration, and melts percolation. To constrain these interactions and their effects on olivine fabric, we analyze microstructures, geochemical analysis, crystallographic preferred orientations, and water contents of spinel peridotite xenoliths from the back arc region of the Japan arc. The three sample locations correspond to slightly different geological settings from northeast Japan (Ichinomegata) to southwest Japan (Oki-Dogo and Shingu). The mineral chemistry of Ichinomegata peridotites shows a typical residual peridotite trend, depleted in LREE (light rare earth element). However, their strong Th-U positive anomaly indicates a possible metasomatic origin associated with the subduction of the Pacific plate. The chemical composition of Oki-Dogo peridotites shows that they were affected by various degree of melt metasomatism, which might be related to back-arc spreading. Olivine CPO of Ichinomegata peridotites are consistent with slip on (010)[100] and {0kl}[100]. The angle between the [100] maximum concentration and the foliation decreases with increasing fabric strength, indicating that these samples record a strain gradient related to back-arc spreading. Olivine CPO of Oki-Dogo peridotites are consistent with the (010)[100] slip system. Samples have low Mg# and show relatively high concentration in [010], however there were no strong relationships among them. Although peridotite xenoliths from Oki-Dogo Island could be deformed in the presence of melt, there was no strong interaction between deformation and melt percolation.

Key words: peridotite xenoliths, the uppermost mantle flow, back arc region, Japan

Sea opening.

2-1. Introduction

The Japan Sea is one of the back-arc basins with a complicated geological structure (Tamaki et al., 1992); it was initiated by splitting the eastern margin of the Eurasian continent (e.g., Otofuji and Matsuda, 1984; Otofuji et al., 1985). Its floor is composed of oceanic crust, rifted continental crust and stretched continental crust (Tamaki et al., 1992). There are only a few known localities that produce mantle-derived xenoliths, which provide us with information on deep processes and materials beneath the Japan Sea.

The Ichinomegata volcanic crater is one of just a few localities where deep-level inclusions can be found in an island arc setting in all over the world (Fig. 1a). Peridotite xenoliths record the possible occurrence of an anisotropic layer in the uppermost mantle lithosphere that might be related to 'frozen' deformation during back-arc spreading along the northeast Japan arc. Ichinomegata is very famous for the abundant deep-seated xenoliths, and there are many previous petrological and geochemical studies (e.g., Kuno, 1967; Abe et al., 1995). The host magma is calc-alkali andesite to dacite, ca. 10,000 yr in age (Horie, 1964). Peridotites are most frequently lherzolite, which are sometimes veined by hornblendite with pargasite and rarely phlogopite (Abe et al., 1998). Amphiboles, spinel-pyroxene symplectite and exsolution lamella of clinopyroxene in orthopyroxene are mantle metasomatic minerals, due to the addition of hydrous melt/fluid to dry peridotite (e.g., Abe and Arai, 1993).

Peridotite xenoliths from the uppermost mantle lithosphere entrained by the Ichinomegata volcano preserve strong asymmetric fabrics. This anisotropic structure

in the uppermost mantle lithosphere could have preserved the deformation during back-arc spreading along the northeast Japan arc, related to normal seafloor spreading system during the Japan Sea opening.

The evolution of the uppermost mantle is strongly linked to partial melting and refertilization processes. Recent studies have shown that percolating melts may react with the mantle lithosphere, leading to enrichment in fusible components; i.e., refertilization via the crystallization of pyroxenes and spinel (e.g., Le Roux et al., 2007, 2008). Experimental deformation of partially molten assemblages reveals that the presence of melt, even in low fractions, results in a large reduction in viscosity (Hirth & Kohlstedt, 1995; Rosenberg & Handy, 2005; Takei, 2005). In addition, deformation may result in a higher transient permeability and facilitate melt segregation (e.g., Rosenberg and Handy, 2000; Holtzman et al., 2003). This feedback between melt percolation and deformation, as observed experimentally, has also been proposed, based on observations of geological structures, to be responsible for the development of shear zones in the shallow mantle (Kelemen & Dick, 1995). Therefore, interactions between melt percolation and deformation in the mantle are important in the evolution of the lithosphere, controlling its composition and mechanical behavior.

The uppermost mantle beneath the SW Japan arc is dry and has a steeper geothermal gradient than that beneath the NE Japan arc, as deduced from petrologic studies of mafic and ultramafic xenoliths from Oki-Dogo Island, SW Japan, and Megata volcano, NE Japan (Takahashi, 1978a; Abe, 1997; Arai et al., 1998, 2000). This conclusion is supported by the results of recent studies on mantle xenoliths from many other localities throughout the Japan arcs. For example, Arai et al. (1998, 2000) proposed that the type of mantle peridotite beneath the SW Japan arc depends on the degree of metasomatism by Fe-rich melts superimposed on the primary residual

characteristics.

Oki-Dogo Island is an important site for studying mantle xenoliths because it marks the most continent-ward occurrence of mantle peridotite xenoliths in the SW Japan arc, approximately 60 km offshore from Honshu Island (Fig. 1a). Numerous mafic and ultramafic xenoliths, including residual mantle peridotite, have been reported from the island (Takahashi, 1975, 1978a, 1978b). Kaneoka et al. (1978) and Nagao and Takahashi (1993) reported the Ar and Sr isotope geochemistry and noble gas geochemistry, respectively, of ultramafic xenoliths from Oki-Dogo Island. Many previous studies have investigated the petrology and geochemistry of residual peridotite xenoliths from the Japan arcs and Japan Sea (see Arai et al., 1998).

Abe et al. (2003) presented petrological and mineral composition data, including trace-element contents, for spinel lherzolite xenoliths from Oki-Dogo, following the publication of preliminary data by Abe et al. (1999). Abe et al. (2003) discussed upper mantle processes beneath the Japan arcs and the Japan Sea, based on petrological data obtained from residual peridotite xenoliths from other localities such as Oshima-Oshima, Megata, Aratoyama, Kurose, Onyama, Takashima, Shingu, and Fukuejima, and based on trace element data from clinopyroxene within peridotite xenoliths from Kurose, located on the Japan Sea coast, within the SW Japan arc (Fig. 1) (Abe et al., 1998; Arai et al., 2001). Abe et al. (2003) argued that mantle metasomatism was induced by the intrusion of evolved melts beneath the SW Japan arc and the degree of melting in the upper mantle during opening of the Japan Sea. Moreover, Yamamoto et al. (2007) estimated the equilibrium pressure of mafic and ultramafic xenoliths from Oki-Dogo Island based on the pressure of CO_2 fluid inclusions preserved in minerals, yielding a depth of 25–29 km for lherzolites.

With the exception of Takahashi (1978a, 1978b), no previous study has undertaken a systematic petrophysical analysis of spinel lherzolite xenoliths from the residual mantle underneath the Japan arcs. In the present paper, we describe the microstructure of peridotite xenoliths from Ichinomegata and Oki-Dogo Island with the aim of understanding the evolution of the uppermost mantle beneath the back-arc side of the Japan arc. For the comparison, we also show the fabric characteristic from Shingu (Fig. 1a), which is not in the back-arc region.

There are less previous study has undertaken a microstructural analysis of spinel lherzolite xenoliths from the residual mantle underneath the Japan arcs with the exception of some papers (e.g., Toriumi and Karato, 1978; Toriumi, 1980; Matsumoto and Toriumi, 1986). Peridotite xenoliths from the uppermost mantle lithosphere in Oki-Dogo preserve fabrics and petrological characteristics, which could have been induced by back-arc spreading along the northeast Japan arc, and be related to extension and thinning of the continental crust during the Japan Sea opening. Changes in composition and texture of the uppermost mantle rocks affect the seismic properties.

2-2. Geological setting and petrography of peridotite xenoliths

Here are briefly described the petrographical characteristics, and geological context of peridotite xenoliths from Ichinomegata, Oki-Dogo, and Shingu in the Japan arcs.

2-2-1. Ichinomegata peridotite xenoliths

The Ichinomegata Volcano, located on Oga Peninsula, northeast Japan (Fig. 1a, b), is one of the few places on Earth where deep-level xenoliths occur in the

back-arc region of an island arc. The host magma is calc-alkali andesite to dacite in composition and is ca. 10,000 yr in age. The Ichinomegata xenoliths suite is composed of peridotites, websterites, clinopyroxenites, gabbros, amphibolites, and other shallow-level rocks such as granitic and metavolcanic rocks and sediments (e.g., Abe et al., 1998). The peridotite xenoliths are up to 30 cm in diameter, but usually less than 10 cm (Fig. 2a). The xenoliths are generally lherzolite with some harzburgite that have secondary pargasite and rare phlogopite of mantle metasomatic origin due to the addition of hydrous melt/fluid to dry peridotite (e.g., Abe et al., 1998).

In this study, we selected thirteen spinel peridotite xenoliths for detailed petrophysical analyses. Most of the peridotite xenoliths have a pervasive main foliation composed of compositional banding defined by pyroxene-rich and pyroxene-poor layers, and a lineation defined by elongate pyroxene grains (Fig. 2a). We analyzed microstructures from XZ thin sections cut perpendicular to the foliation (XY plane) and parallel to the lineation (X). The lherzolites contain olivine, orthopyroxene, clinopyroxene, and spinel, and show equigranular texture (Fig. 2b). Large olivine grains commonly contain subgrain boundaries (Fig. 2c) and show undulose extinction. Triple-junction grain boundaries are observed (Fig. 2a), mainly among olivine grains. Orthopyroxene porphyroclasts contain exsolution lamellae of clinopyroxene (Fig. 2d). The pyroxenite xenoliths contain orthopyroxene, clinopyroxene, and minor olivine (Fig. 2e).

2-2-2. Oki-Dogo peridotite xenoliths

The Oki-Dogo Island is located in the Japan Sea (Fig. 1a), on a shelf that extends from Shimane Peninsula to Oki Bank. Basement on the island consists of a gneissic metamorphic complex (Fig. 1c). The metamorphic age of the basement

complex is ca. 200 Ma, as determined by the Sm–Nd isochron method (Tanaka and Hoshino, 1987) and Pb–Pb analyses of zircon (Yamashita & Yanagi, 1994). The alkaline basalts that contain the xenoliths were erupted during the Pliocene–Pleistocene (from 4.38±0.23 to 0.55±0.09 Ma) (Uto et al., 1994), after the opening of the Japan Sea, which is thought to have occurred during the Oligocene–Miocene (28–18 Ma) as a consequence of back-arc spreading (e.g., Tamaki et al., 1992).

According to Takahashi (1978a, 1978b), five basalt lava flows on Oki-Dogo Island contain abundant ultramafic and mafic xenoliths, including mantle-derived spinel lherzolite. These basalts contain 2–15% normative nepheline, 45.0–49.1 wt% SiO_2, and yield FeO/MgO values of 0.60–1.15 (Uto et al., 1994). Takahashi (1978a) described approximately 70 ultramafic and mafic xenoliths in detail, and divided them into five groups based on mineral assemblage and microstructure. Takahashi (1975) reported that in Oku village, large amounts of angular ultramafic and mafic xenoliths are densely packed in a dyke (Fig. 3a) that represents a volcanic neck. The five groups of xenoliths identified by Takahashi (1978b) are as follows: (1) spinel lherzolite, (2) banded spinel peridotite, (3) banded plagioclase peridotite, (4) gabbro, and (5) granulite.

Xenoliths on the island are up to 10 cm in diameter (generally 1–3 cm). Spinel lherzolite xenoliths are the dominant xenolith type in the Kuroshima Basalt lava, whereas it is less abundant or absent in the other alkali basalt lavas. We collected 78 samples of spinel lherzolite from Kuroshima (KRB; a small island (<200 m across) near Oki-Dogo Island) and Oki-Dogo Island (OKD), along with several pyroxenites (e.g., OKD7-3) and gabbros (e.g., OKD08). Within samples greater than 3 cm in size, it is possible to recognize a foliation (XY plane) and lineation (X direction) defined by

compositional banding and aligned spinel grains.

Thin sections were cut perpendicular to the foliation (Z) and parallel to the lineation (X; i.e., XZ-sections). For samples less than 3 cm in size, for which structures could not be identified, thin sections were cut at random orientations. For detailed analyses, we selected the 17 samples of lherzolite (of 78 in total) that contained the best-preserved peridotite microstructures, and selected one sample each of pyroxenite and gabbro.

The lherzolites contain olivine, orthopyroxene, clinopyroxene, and spinel, and show equigranular texture (Fig. 3b). Large olivine grains commonly contain subgrain boundaries (Fig. 3c), and show undulose extinction. Triple-junction grain boundaries are observed, mainly among olivine grains. Orthopyroxene porphyroclasts contain exsolution lamellae of clinopyroxene (Fig. 3d). The pyroxenite xenoliths contain orthopyroxene, clinopyroxene, and minor olivine (Fig. 3e), whereas the gabbro xenoliths contain plagioclase, orthopyroxene, clinopyroxene, and minor olivine (Fig. 3f).

2-2-3. Shingu peridotite xenoliths

Shingu, in Shikoku Island, is a very special locality of mantle xenoliths on the Japan Island arcs (Takamura, 1978). There are two sheets of dikes of alkali basaltic composition that contain abundant crustal and mantle xenoliths, which are expected to carry unique information that we cannot obtain from xenoliths elsewhere on the Japan arcs (Arai et al., 2007). They cut crystalline schists of the Sambagawa metamorphic belt of high-pressure intermediate type (Miyashiro, 1973). Goto (1986) found several other dikes of similar chemical characteristics within the Sambagawa belt in Shikoku Island. The host alkali basalt is characterized by the abundance of

carbonate minerals and hydrous minerals (biotite and amphibole), and the term "lamprophyre" is preferable, also taking the occurrence as dike into account. The age of host rock is 18 Ma, being older than the host rocks of other mantle-derived xenoliths from the Southwest Japan arc (Uto et al., 1987; Uto, 1990). We found a variety of ultramafic xenoliths (harzburgite, lherzolite, dunite, wehrlite, pyroxenite and kaersutitite), and most of the pyroxenites and kaersutitite (hornblendite) belong to Group II (Goto and Arai, 1987).

The peridotite xenoliths are mostly small (<5 cm across) and angular. They are rather fine-grained and show protogranular to porphyroclastic textures (Goto and Arai, 1987; Arai et al., 2000). Group I rocks are frequently penetrated by Group II rocks in individual xenoliths (=composite xenoliths; Irving, 1980). We can thus expect serious chemical effect on peridotite by the magma involved in the formation of Group II rocks (Goto and Arai, 1987; Arai et al., 2000).

2-3. Mineral composition

2-3-1. Major elements

The chemical compositions of olivine, orthopyroxene, clinopyroxene, and spinel were analyzed using a JEOL electron microprobe (JXA733) housed at the Center for Instrumental Analysis, Shizuoka University, Japan. Analytical conditions were 15 kV accelerating voltage and 12 nA probe current. Ferrous and ferric iron contents of spinel were calculated assuming spinel stoichiometry. Data are shown in Table 1 – 4. Cr# was calculated as the Cr/(Cr+Al) atomic ratio of spinel. Mg# was calculated as the Mg/(Mg+total Fe) atomic ratio for silicates and the Mg/(Mg+Fe^{2+}) atomic ratio for spinel.

The relationship between the Mg# (Fo content) of olivine and the Cr# of

spinel are plotted in Fig. 4 with previous studies. On an OSMA (olivine spinel mantle array) diagram, the samples plot in the field of residual peridotite of mantle origin (Arai, 1994). The Fo content of olivine grains of Ichinomegata peridotites ranges from 88 to 90 (Fig. 4a). The Cr# (= Cr/(Cr+Al)) of spinel is low (0.13–0.36; Fig. 4a). The spinel lherzolite from Ichinomegata volcano is quite normal in Mg relative to typical mantle peridotite xenoliths found in alkaline basalts (Abe et al., 2003).

The Fo content of olivine grains of Oki-Dogo peridotites ranges from 86 to 90 (Fig. 4b). The NiO content of olivine is relatively constant among grains, being ~0.30 wt% (range, 0.30–0.41 wt%), and shows a weak positive correlation with Fo content (Table 3). The Cr# (= Cr/(Cr+Al)) of spinel is low (0.17–0.45; Fig. 4b), and $Fe^{3+}/(Cr+Al+Fe^{3+})$ is < 0.1 (Table 3). Spinel in lherzolite from Oki-Dogo Island has the characteristics of mantle spinel, as defined by Dick and Bullen (1984). Orthopyroxene is enstatite (En 86.8–90.3), and contains moderate concentrations of CaO (1.01–1.29 wt%) and Al_2O_3 (2.81–4.94 wt%) (Table 4). Clinopyroxene is Cr-diopside to augite in composition, or Mg-rich augite containing 0.05–1.24 wt% Cr_2O_3. Clinopyroxene contains 3.61–6.18 wt% Al_2O_3 and 19.78–21.55 wt% CaO (Table 4).

The Fo content of olivine grains of Shingu peridotites ranges from 87 to 90 (Fig. 4c). The Cr# (= Cr/(Cr+Al)) of spinel is low (0.35–0.44; Fig. 4c). Some peridotites in Oki-Dogo and Shingu are plotted off the OSMA, which indicates that these are possibly metasomatized by melts (Arai et al., 2000).

Equilibrium temperatures of Ichinomegata peridotites were calculated using the Ca-Orthopyroxene thermometer of Brey and Köhler (1990), and were estimated in the range 850 to 1000ºC (Table 5). This estimate is in good agreement with previous studies, and could represent a cooling event in the mantle lithosphere (Takahashi,

1986). It appears that the peridotite xenoliths are derived from relatively shallow levels in mantle, at 30 to 40 km depth (Takahashi, 1986), where the depth of the Moho is estimated to be approximately 28 km (Zhao et al., 1990).

Equilibrium temperatures of Oki-Dogo peridotites were calculated using the clinopyroxene thermometer of Nimis and Taylor (2000), the two-pyroxene and the Ca-Orthopyroxene thermometer of Brey and Köhler (1990), yielding temperatures of 1044–1134, 1040–1127, and 1021–1092 °C, respectively (Table 6).

2-3-2. Trace elements

In situ trace-element analyses of clinopyroxenes were performed by laser ablation induced coupled plasma mass spectroscopy (LA-ICP-MS) on thick (150mm) sections at the AETE facility, Geosciences Montpellier, using a single-collector double-focusing sector field Element XR (eXtended Range) high-resolution (HR-) ICP-MS system, coupled with a Geolas (Microlas) automated platform housing a ArF 193 nm Compex 102 laser from LambdaPhysik. Measurements were conducted in an ablation cell of 30 cm^3 in a He atmosphere, which enhances the sensitivity and reduces inter-element fractionation (Günther & Heinrich, 1999). The helium gas stream and particles from the sample were mixed with Ar before entering the plasma. Data were acquired in the fast E-scanmode at low resolution (M/DM1/4300). Signals were measured in Time Resolved Acquisition (TRA) mode, devoting 2 min for the blank, and 1min for cpx analysis. The laser was fired using an energy density of 15 J/cm^2 at a frequency of 5Hz and using a spot size of 77 mm. Oxide level, measured using the ThO/Th ratio, was below 0.7%. ^{43}Ca was used as an internal standard and the concentrations were calibrated against the NIST 612 rhyolitic glass using the values given by Pearce et al. (1997). Data were subsequently reduced using the GLITTER

software (Van Achterbergh et al., 2001) by carefully inspecting the time-resolved analysis to check for absence of heterogeneities (inclusions or fractures) in the analysed volume. Representative mineral analyses are reported in Table 7 and 8.

For Ichinomegata peridotites, although fairly constant within a given samples, rare earth elements (REE) in clinopyroxene, orthopyroxene and olivine show extreme variations between the different samples, in the range 0.001 - 10 times chondritic abundances (Fig. 5b). All three minerals show depleted LREE (light rare earth elements) patterns. Figure 5(a) shows the trace element contents of the three minerals. In clinopyroxene, there are high positive anomalies in Th-U.

REE in clinopyroxene, orthopyroxene and olivine of Oki-Dogo peridotites show extreme variations between the different samples, in the range 0.0001 - 100 times chondritic abundances (Fig. 6b). Clinopyroxene are slightly enriched in LREE, whereas orthopyroxene and olivine show depleted LREE patterns. Figure 6(a) shows the trace elements contents of the three minerals. There are high positive anomalies in Ce and Th in clinopyroxene, and Zr and Hf in orthopyroxene.

2-4. FTIR analyses of water contents in olivine and pyroxenes

2-4-1. Analytical procedures

Water contents in our samples were obtained using unpolarized mid-infrared radiation collected with a FTIR Bruker IFS66V/S spectrometer coupled with a Bruker Hyperion microscope at the Laboratoire des Colloïdes, Verres et Nanomatériaux (LCVN) at Université Montpellier 2, France. The technical setup of the IR microscope and the MCT detector are identical to those described by Demouchy et al. (2011), with a square aperture of 100 microns; 200 scans were accumulated for each spectrum at a resolution of 4 cm^{-1}. The thickness of doubly polished sections of the samples for

FTIR analyses ranges from 477 μm to 548 m. Despite their infrequent occurrences, cracks and inclusions were strictly avoided. However, due to the small grain size of two xenoliths (OKD04 and OKD69), pyroxenes could not be analyzed, and several grain boundaries were unfortunately included in some olivine analyses. To avoid thickness interferences in some case (i.e., sinusoidal fringes), the crystals were put on a CaF_2 plate with a thin layer of fluorolube^{TM} at the interface between the sample and the CaF_2 plate.

After background-baseline correction and thickness normalization to 1 cm, the hydroxyl content was determined for each spectrum using the empirical calibration from Paterson (1982):

$$C_{OH} = \frac{\varphi_i}{150\zeta}\int \frac{k\,(\nu)}{3780-\nu}\,d\nu \qquad (1)$$

where C_{OH} is the concentration of hydroxyl, ξ is an orientation factor that equals 1/3 for unpolarized measurements, $k(\nu)$ is the absorption coefficient for a given wavenumber ν, and ψ_i is the density factor, which is chemistry and density dependent (the values for olivine and orthopyroxene are 2695 and 2769 wt ppm H_2O, respectively; see calculation method in Bolfan-Casanova et al., 2000). Spectrum integration was performed between 2800 cm^{-1} and 4000 cm^{-1}. The calibration from Paterson (1982) may underestimate the water content in some nominally anhydrous minerals (Libowitzky and Rossman 1997; Bell et al. 2003), Nevertheless the same calibration was used here for both sets of sample and for all the mineral phases to insure consistency during comparison of the water contents.

2-4-2. Results

Figure 7 shows typical unpolarized FTIR spectra for olivines and orthopyroxenes in Ichinomegata peridotites (TSI03, I892, I906, I702, TSI06) and

Oki-Dogo peridotites (KRB15, OKD04, OKD45-2, OKD64 and OKD69). The olivine spectra are rather homogeneous. Water contents in the studied samples range from 2 to 7 ppm H_2O by weight for Ichinomegata, and from 2 to 6 ppm H_2O by weight for Oki-Dogo (Table 9). These values are in the same range as the water contents in olivine from spinel-peridotite xenoliths sampling the continental lithosphere above the western North America, Patagonia and Carpathian subduction zones (Demouchy, 2004; Peslier & Luhr, 2006; Falus et al., 2008).

For Ichinomegata samples, orthopyroxene spectra are characterized by major O-H absorption bands at 3598 cm^{-1} and by broader minor peaks around 3424 cm^{-1} (Fig. 8). This pattern is typical for orthopyroxene from mantle xenoliths (Peslier et al., 2002; Grant et al., 2007). Water contents are very heterogeneous, varying from 75 to 271 ppm (Table 9). There is abundant water in clinopyroxene. Clinopyroxene spectra are characterized by major O-H absorption bands at 3637 and 3472 cm^{-1} (Fig. 8). Water contents are also very heterogeneous, varying from 292 to 347 ppm (Table 9). Water contents in bulk rock are estimated using modal compositions, ranging from 46 to 134 ppm (Table 9).

For Oki-Dogo samples, orthopyroxene spectra are characterized by major O-H absorption bands at 3571 and 3520 cm^{-1} and by broader minor peaks around 3523 cm^{-1} (Fig. 8). This pattern is typical for orthopyroxene from mantle xenoliths (Peslier et al., 2002; Grant et al., 2007). Water contents are very heterogeneous, varying from 6 to 35 ppm (Table 9). There is abundant water in clinopyroxene. Clinopyroxene spectra is characterized by major O-H absorption bands at 3598 cm^{-1} (Fig. 8). Water contents are also very heterogeneous, varying from 8 to 98 ppm (Table 9). Water contents in bulk rock are estimated using modal compositions, ranging from 4 to 10 ppm (Table 9).

2-5. Microstructures of peridotite xenoliths

2-5-1. Methods of fabric analysis

To examine the conditions of deformation in detail, we have measured the crystallographic preferred orientations (CPOs) of the three main constituent minerals: olivine, orthopyroxene, and clinopyroxene. These data were obtained by electron backscatter diffraction (EBSD) using the SEM-EBSD facility at Géosciences Montpellier, France. The EBSD patterns are generated by the interaction of a vertical incident electron beam with a polished thin section, tilted at 70°, in a scanning electron microscope (JEOL JSM 5600). The diffraction pattern is projected onto a phosphor screen and recorded using a digital CCD camera. The resulting image is then processed and indexed in terms of crystal orientation using the CHANNEL5 software distributed by Oxford Instruments HKL.

For each sample, we obtained CPO maps covering almost the entire thin section (usually 35 mm long and 20 mm wide), with sampling steps from 25 to 40 μm, depending on the grain size (Fig. 9); rates of indexation in the raw maps range from 50% to 80%. Post-acquisition data treatment allowed us to filter the data and increase map quality by (1) filling the non-indexed pixels that have up to eight identical neighbors with the same orientation, (2) identifying the grains (i.e. continuous domains characterized by an internal misorientation < 12º), and (3) within each olivine crystal, searching and correcting for systematic indexation errors caused by the olivine hexagonal pseudo-symmetry, which results in similar diffraction patterns for orientations differing by a rotation of 60º around [100]. The resulting orientation maps were verified by the operator to avoid over-extrapolation of the data at each step. To

avoid over-representation of large crystals, CPOs are plotted as one measurement per grain (average orientation of the crystal).

2-5-2. Crystallographic preferred orientations (CPOs) of peridotite xenoliths

The measured CPOs are presented on equal-area, lower-hemisphere projections (Figs. 9 to 12).

For Ichinomegata peridotite xenoliths, Fig. 9 shows the EBSD maps and olivine CPOs. Olivine CPOs display a well-developed axial [100] pattern (Figs. 9, 10a) characterized by a strong point concentration of [100] axes sub-parallel to the lineation, which is systematically the dominant slip direction for olivine. This interpretation is corroborated by the predominance of (100) subgrain boundaries in the crystallographic orientation maps (Fig. 9d). Other axes, [010] and [001] show weak girdle normal to [100] (Fig. 10a). To infer a dominant slip system for the olivine, inverse pole figures were generated by plotting the direction of interest into the sample space. The inverse pole figures for the olivine in the direction of X (lineation), Y and Z (foliation normal) are shown in Fig. 10b. The inverse pole figures show that olivine [100] is preferentially aligned sub-parallel to the lineation and the [010] is aligned subnormal to the foliation, indicating that the [100] axis was a dominant slip direction on the dominant (010) slip plane. In sample I708, [100] is sub-parallel to the lineation; however, a weak concentration of [010] and [001] is observed in the direction normal to the foliation, indicating that the slip is not well defined ({0kl}[100] slip system). For orthopyroxene, although most of CPOs are weak; a (010)[001] pattern (shear direction is [001] and shear plane is (010)) occurs in two oriented samples (I667, I909 and I708) (Fig. 11a). Clinopyroxene CPOs are generally nearly random, although some samples show a weak (010)[001] slip (I909, I906 and I708) (Fig. 11b).

The CPOs of olivine, orthopyroxene, and clinopyroxene measured for Oki-Dogo peridotites and Shingu peridotites are shown in Figs. 12 and 13. Because the foliation and lineation could not be determined macroscopically in samples, thin-sections were cut in random orientations, rather than parallel to the lineation and normal to the foliation. To allow a straightforward comparison between the CPO of the different localities, data were rotated to display the maximum concentrations of olivine [100] and [010] axes parallel to the east - west and north - south directions, respectively. The olivine CPOs show a distinct preferred alignment of [100] and [010]. The CPOs of orthopyroxene shows weak concentrations, with [001] axes slightly sub-parallel to the olivine [100]. The CPOs of diopside shows random fabrics, although some samples show [001] axes slightly sub-parallel to the olivine [100].

2-5-3. Analysis of subgrain rotation axes

To fully describe the CPO of a mineral, the orientations of the crystallographic axes of each crystal should be known with respect to an external reference frame (XYZ), which is usually defined in terms of the rock structure (e.g., X parallel to the lineation, Y normal to lineation within the foliation plane, and Z normal to the foliation). However, the external reference frame could not be determined for some samples because of their small size (< 3 cm) and the lack of macroscopic structure. The orientations of many of the thin sections are therefore random or independent of the orientation of the foliation and lineation. Accordingly, to determine the slip system(s), we analyzed the characteristics of subgrain rotation with the aim of identifying the slip system that operated in olivine during deformation (e.g., Satsukawa and Michibayashi, 2009).

Subgrains are formed by either edge dislocations (representing the edge of a

half-plane in a distorted crystal lattice) or screw dislocations (representing a twisted lattice) (e.g., Passchier and Trouw, 2005). A subgrain boundary can be thought of as a plane that separates two parts of an originally continuous crystal that have rotated slightly with respect to each other (Fig. 14). Such boundaries can therefore be classified according to the orientation of the rotation axis relative to the subgrain boundary. Subgrain boundaries that form with rotation axes oriented parallel to the boundary are known as tilt walls; those with axes oriented normal to the boundary are known as twist walls (Passchier and Trouw, 2005). A tilt wall (Fig. 14) consists of an array of edge dislocations with the same Burgers vector (slip direction). The slip direction is indicated by the axis oriented normal to the subgrain boundary. The rotation axis was calculated based on the orientations of the lattices of the paired subgrains (using the software HKL channel5, Oxford Instruments). The other axis of olivine was interpreted to be oriented normal to the slip direction, on the slip plane.

We compare the two methods for identifying the slip system (from CPO data and from the rotation axis analysis described above) on Ichinomegata samples, for which the structural reference frame (X, Y, Z) is known. Three olivine CPOs are shown in Fig. 15. They display a well-developed axial [100] pattern characterized by a strong point concentration of [100] axes sub-parallel to the lineation, which is systematically the dominant slip direction for olivine. [010] is normal to [100] (Fig. 15a), indicating that the slip system is (010)[100] (Fig. 16a). For other samples, [010] and [001] show weak girdle normal to [100] (Fig. 15b, c), indicating that the [100] axis was a dominant slip direction and the (010) and (001) plane was a dominant slip plane: the {0kl} [100] slip system (Fig. 16b).

Figure 17(a) shows photomicrograph of an olivine subgrain boundary of Ichinomegata peridotites. Foliation is horizontal and lineation is E-W. A and B in Fig.

17a are points where crystallographic orientations were measured. Fig. 17b shows a great circle that indicates the orientation of the subgrain boundary, as measured on a universal stage, and circles that correspond to the orientation of olivine [100] (after Fig. 17c, which shows CPO data at the point of A and B), representing the slip direction. When [100] is oriented subnormal to the subgrain boundary, with a rotation axis sub-parallel to the boundary, the boundary is identified as a tilt wall boundary. The axis of the misorientation between the subgrains is estimated to be [001], as plotted on an inverse pole figure in figure 4d. Thus, the slip direction is [100] and the axis of subgrain rotation is [001]; the remaining axis, [010], is oriented normal to the slip direction, on the slip plane. Thus, the slip system is (010)[100].

Using the above method, the subgrain rotation axis is determined for three samples. Figure 18 shows a great circle that indicates the orientation of the subgrain boundary, and circles that correspond to the orientation of olivine [100] (after Fig. 15 which shows CPO data), representing the slip direction. The axis of the misorientation between the subgrains is plotted on an inverse pole figure (Fig. 19). For sample I909, misorientation axis is estimated to be [001], thus the slip system is (010)[100]. For others, misorientation axis is distributed from [001] to [010], indicate that slip system is {0kl}[100]. The slip system defined by subgrain rotation axes is consistent with that determined from the CPO.

Oki-Dogo peridotites analyzed in this way, most of the subgrain-rotation axes are oriented parallel to [001] or [010] (Fig. 20a). All data regarding the axes of subgrain rotation are shown in Figure 20b. The rotation axes of peridotite xenoliths of Oki-Dogo Island are dominantly orientated parallel to [001], [010] being a less frequent case.

2-5-4. Fabric strength of olivine

To characterize CPOs, we determined the fabric strength (*J*-index), distribution density (*pfJ*-index) and misorientation index (*M*-index) of the principal crystallographic axes (for definitions of the *J*-index, *pfJ*-index, and *M*-index, see Mainprice et al., 2000; Michibayashi and Mainprice, 2004; Skemer et al., 2005). Table 10 lists the number of measured olivine grains, the *J*-index values calculated for each xenoliths, M-index and the maximum density and *pfJ*-index value for each pole figure. The *J*-index is the volume-averaged integral of the squared orientation densities; it has a value of unity for a random CPO and is infinite for a single crystal. Most natural peridotites yield values between 2 and 20, with a peak around 8 (Ben Ismaïl and Mainprice, 1998), and those of the present study range from 2.56 to 7.94 (Table 10). In Oki-Dogo, *J*-index values range from 5.30 to 24.76 (*M*-index: 0.068–0.319). *M*-index, which corresponds to the differences between the observed distribution of uncorrelated misorientation angles and that predicted for a fandom fabric. It has a value of zero for a random CPO and unity for a single crystal. Misorientation angle distribution and M-index are shown in Fig. 10(c).

J- and *M*- indices show a good linear correlation (R^2=0.97, Fig. 21), indicating that both indices correctly represent the CPO strength of the studied samples. As most published CPO data for natural peridotites and experimental aggregates have their strength expressed as *J*-indices, we choose to use this index in the following discussion.

2-5-5. Microstructural analysis

Ichinomegata peridotite xenoliths display a foliation defined by compositional banding of pyroxene-rich and pyroxene-poor layers, and a lineation

defined by elongated pyroxene grains. Most of the peridotite xenoliths have medium- (<5 mm) to fine-grained (<1 mm) granular texture, whereas only two of the peridotite xenoliths have porphyroclastic textures.

From the EBSD maps (Fig. 9), we can extract several parameters about olivine microstructure; grain size, aspect ratio and angle of grain long axis. Olivine grain size (diameter) histogram is shown in Figure 22. Grain sizes range from 34 μm to 4.67 mm (Fig. 22b). The mean grain size ranges from 350 to 652 μm, and the fine-grained population is high (Fig. 22a). The *J*-index is correlated with the olivine grain size distribution like in Avacha peridotite xenoliths (Soustelle et al., 2010). They show that the fine-grained population has a strong influence on the estimation of the sample *J*-index if it is calculated by using one measurement per grains, as fine grains are more numerous on a given analyzed surface. The population of fine grains is relatively high in our samples (Fig. 22a). Hence we must test for the variability of the CPO intensity as a function of grain size. The analysis of the *J*-indices for different grain size populations in sample shows that fine (< 0.5 mm) and intermediate grains (0.5 - 1 mm) have lower *J*-indices than coarse grains, whereas *J*-indices calculated by using gridded data have higher values (Fig. 23). EBSD data with one measurement per grain, which are used in the calculation of *J*-indices, are generated from the full orientation dataset from mapping data. Here, we prefer to use one measurement per grain for later discussion on the relation of CPOs to the microstructure.

The peridotite xenoliths with granular texture display shape-preferred orientations (SPOs) of olivine that are oriented oblique to the main foliation (Fig. 24a). Olivine grains with either large grain size or high aspect ratio are oriented closer to the foliation (Fig. 24b, c). However, there is no correlation between grain size and aspect ratio (Fig. 25a, b). Although the obliqueness of foliation tends to weaken as olivine

grain size decreases, the angle between the foliations and SPO is constantly around 20º, indicating that these are steady-state microstructures. So-called 'oblique foliation' is a typical microstructure resulting from shear deformation (e.g., Nicolas and Christensen, 1987). The similar nature of the oblique foliations within all the peridotite xenoliths indicates that their origins are related to a pervasive event in the uppermost mantle lithosphere beneath the northeast Japan arc.

2-6. Discussion

2-6-1. Evidence for fluid/melts rock interaction in peridotite xenoliths from Japan arc

The spinel lherzolites from Oki-Dogo and Shingu show variable trends in olivine Mg# and Spinel Cr#. On an OSMA (olivine spinel mantle array) diagram, the samples plot in the field of residual peridotite of mantle origin (Fig. 4) (Arai, 1994). The data provided by Abe et al. (2003) are plotted in Fig. 4. Combined with data from the present study, two trends of metasomatism are recognized, possibly reflecting the degree of melt extraction prior to metasomatism (Arai, 1994). Thus, the figure shows the degree of melt extraction using two different symbols. Samples with low Mg# show evidence of metasomatism. The spinel lherzolite from Oki-Dogo is rich in Fe relative to typical mantle peridotite xenoliths found in alkaline basalts (Abe et al., 2003), and it is also similar in peridotites from Shingu (Goto and Arai, 1987). Such Fe-rich (Fo < 88) Cr-diopside series peridotites occur in several sites throughout the world, including New South Wales, Australia (Wilkinson and Binns, 1977), British Columbia, Canada (Brearly et al., 1984), Oahu, Hawaii (Sen and Leman, 1991), and SW Japan (Aratoyama: Fujiwara and Arai, 1982).

Other Fe-rich lherzolite xenoliths, modally metasomatized and containing phlogopite, have been reported in association with typical Mg-rich xenoliths at Salt

Lake, Hawaii (Goto and Yokoyama, 1988). Some peridotite xenoliths from Megata volcano are also Fe-rich, as well as being strongly metasomatized and containing > 10 vol% sparsely distributed veinlets of amphibole and hornblendite (Abe et al., 1992). The evidence of Th-U positive anomaly in clinopyroxene indicates that there is fluid metasomatism in Ichinomegata peridotites. Water contents of these samples are intermediate (Fig. 7 and Table 9); it is also consistent with the evidence of fluids interaction.

In contrast, Fe-rich peridotite xenoliths from Aratoyama (Fujiwara and Arai, 1982) and Shingu (Goto and Arai, 1987), as well as those from Oki-Dogo (SW Japan), do not contain hydrous phases and show no evidence of modal mantle metasomatism (Arai et al., 2000). Arai et al. (2000) proposed that Fe-rich peridotites (Cr-diopside series) in the upper mantle were intruded by Fe-rich cumulates and/or Fe-rich ultramafic rocks (Al-augite series), because they are found exclusively in regions that contain abundant Al-augite series and/or Fe-rich ultramafic xenoliths. Water content in pyroxenes is low (Fig. 7 and Table 9), suggesting that water in peridotites was easily moved in melts if water was contained in rocks before the metasomatism. Pyroxenes coexisting with olivine appear to retain more initial OH contents than olivine even though the main minerals in the mantle (olivine, orthopyroxene and clinopyroxene) are nominally anhydrous (e.g., Peslier et al., 2002). Abe et al. (2003) explained the origin of Fe-rich cumulates in terms of REE-enrichment metasomatism after depletion by melt extraction, based on the LREE-enriched U-shaped trace element patterns obtained for clinopyroxene. Moreover, we found that Oki-Dogo peridotites are influenced by various degrees of melts based on REE patterns, which varies from U-shaped patterns to enriched patterns.

2-6-2. Dominant slip systems of minerals in peridotite xenoliths

CPOs of olivine are well developed, implying that peridotite xenoliths in this study deformed mainly by dislocation creep. The correlation between the shape and crystal preferred orientations is a reliable tool to constrain the dominant slip systems in olivine. This results in alignment of the dominant slip direction with the shear direction and of the normal to the slip plane with the normal to the shear plane (or foliation) in simple shear (or pure shear) deformation (Zhang and Karato, 1995; Tommasi et al., 2000; Bystricky et al., 2000). In samples of Oki-Dogo and Shingu, however, the foliation and lineation cannot be easily identified. Since the foliation and lineation could not be determined macroscopically in samples, thin-sections were cut in random orientations, rather than parallel to the lineation and normal to the foliation. Other observations are needed to constrain the dominant slip system. To constrain the active slip system, we used the analysis of subgrain rotation axes (see 2-5-3. Analysis of subgrain rotation axes). The rotation axes accommodate low angle (< 12º) misorientations within a crystal; variations in crystallographic orientation within a grain or across a low angle grain boundary (subgrain boundary), as well as the orientation of subgrain boundaries, are directly related to the dislocations forming the boundary (Frank and Read, 1950; Amelinckx and Dekeyser, 1959).

Olivines of Ichinomegata have been deformed essentially by slip on the {0kl}[100] systems, which occurred under high temperature conditions (~1200ºC), low water contents and relatively low shear stress (e.g., Mainprice, 2007). The slip system of samples from Oki-Dogo and Shingu were estimated from the analysis of subgrain rotation axes. The olivine slip direction of these samples is mainly [100], and (010) is normal to the [100], indicating that olivines deform by slip on (010)[100]. For the Shingu samples, some have strong concentration in [010] with girdle distribution

of olivine [100] and [001]. It suggests that slip direction is both [100] and [001], which are formed in the presence of melt (Holtzman et al., 2003). We do not find (001)[100], which system has been interpreted to dominate in olivine under low stress conditions in the presence of moderate water contents (Mehl et al., 2003; Katayama et al., 2004).

For orthopyroxene, most of the [001] axes are more concentrated than [100] or [010] sub-parallel to the lineation, indicating dominantly [001] slip (Fig. 11b). Combined with other axes, CPO data may indicate (100)[001] and/or (010)[100] slip. Considering the pressure and temperature in the uppermost mantle, the dominant slip system in orthopyroxene is expected to be (100)[001] (Doukhan et al., 1986); however, the (100)[010] slip system is the most readily activated, and hence the most common one (Naze et al., 1987). The obliquity between the olivine and orthopyroxene CPO is common in naturally deformed peridotites (e.g., Tommasi et al., 2004, 2006; Le Roux et al., 2008, Soustelle et al., 2010). It is usually interpreted as resulting from lower finite strains in stronger orthopyroxene crystals (Mackwell, 1991) for a given macroscopic strain.

Clinopyroxene CPO data suggest a nearly random fabric, with a weak concentration in (010) normal to the foliation and [001] parallel to the lineation. It is difficult to identify the slip system.

2-6-3. Implication for the dynamics of the back-arc region and the development of oceanic lithosphere

Although the original orientations of the Ichinomegata peridotite xenoliths were lost during their volcanic transport to the surface, we are able to derive quantitative constraints on the structure within the lithospheric mantle. In this case, it

is likely that regional-scale structures within the uppermost mantle lithosphere are sub-horizontal, as described below.

The opening of the Japan Sea is thought to have occurred over the period 25 to 13 Ma as a consequence of back-arc spreading within the northeast Japan arc; most of the basic geologic structure of the present Japanese Islands was generated during this time (Fig. 26) (e.g., Sato, 1994). The depth of the Moho beneath the Ichinomegata crater is approximately 28 km near the coast of the Japan Sea (Zhao et al., 1990), while the temperature of the Moho is thought to be about 850ºC (Kushiro, 1987). The depth of the Moho becomes deeper, up to 38 km, toward the northeast Japan arc (Zhao et al., 1990), where temperatures are 950 to 1000ºC (Kushiro, 1987). The peridotite xenoliths analyzed in the present study came from relatively shallow levels in the mantle, about 30 to 40 km in depth, and at equilibrium temperatures in the range 850 to 1000ºC (Takahashi, 1986). Therefore, it is likely that the Ichinomegata peridotite xenoliths are derived from the uppermost mantle lithosphere in the region dominated by horizontal extension during back-arc spreading (Fig. 26).

From the eight samples of Ichinomegata peridotite xenoliths, we found that the angle between olivine [100] maximum and foliation decreases with increasing *J*-index (Fig. 27a), and this relationship is independent of grain size (Fig. 27b). Figure 28 shows the variation of temperature estimated from the Ca-Orthopyroxene thermometer of Brey and Köhler (1990) at 1.0 GPa with *J*-index. Samples that have high J-index have lower temperature. Although temperature varies from approximately 830 to 1200 ºC, we assume that the lowest temperature preserve the closet to the surrounding environment. From this assumption, this temperature variation suggests that *J*-index increases with decreasing depth.

The correlation between shape and crystal preferred orientation is a reliable

tool to constrain the deformation systems. Figure 29 presents a simple summary from our microstructural (SPO and CPO) observations. The peridotite xenoliths have shape-preferred orientations (SPOs) of olivine that are oriented oblique to the main foliation and also display an obliquity with the olivine [100] maximum and main foliation. We have two models to define the shear plane, as follows.

1) The slip plane is defined by foliation. Zhang and Karato (1995) carried out simple shear experiments on olivine aggregates at 1200 ºC and 1300 ºC over a range of shear strains to investigate olivine fabric evolution. They found that the originally random fabric of the aggregates evolved to CPO with a [100] maximum parallel to the flow direction.

2) Slip direction is defined by olivine [100]. The principle idea comes from the field observation of Oman ophiolite (Ceuleneer et al., 1988) and experiments (Nicolas et al., 1973) which were performed in an axial geometry. Bubbles in olivine grains aligned with the flow direction at high strain.

According to the above two models, and assuming that Ichinomegata peridotite xenoliths preserved horizontal extension due to back-arc spreading, we show the possible angular relationships for the evolution of SPO and CPO (Fig. 29b). Only case 2 is consistent with our observations.

Olivine CPOs can then be used to infer shear strain. The relationships between shear strain and the orientation of a marker layer are shown in Figure 30a. Shear strain is calculated from the change in pyroxene layer orientation in the kinematic reference frame, shown on the stereo net in Fig. 30b. Following the method of Ramsay and Graham (1970) and Ramsay (1980), shear strain, γ, is given by:

$$\gamma = \cot(\alpha') - \cot(\alpha)$$

where α is the initial angle of the layering defined by the pyroxene rich compositional banding with respect to the shear plane, and α′ is the deflection angle, as shown in Figure 30a. In this study, since we assume that the shear direction is the maximum direction of olivine [100], α′ is the angle between the olivine [100] maximum and the foliation (layer). Since xenoliths usually lack well-defined finite strain markers, we have no evidence of pre-existing foliation. We calculated shear strain with changing initial direction of layering (α) from 45º to 90º, as shown in Figure 30b. As a result, shear strain varies from 0.31 to 4.26 (Fig. 30c). Shear strain increases with increasing *J*-index (Fig. 30d).

The change in the angle of the olivine [100] maximum relative to the shear plane with increasing strain is compared to naturally deformed sample, experimental results and models in Fig. 31(a). In comparison to experiments, the Ichinomegata peridotites are observed to require higher strain to align with the shear direction. Ichinomegata samples partly agree with predictions from VPSC (alpha 1)(Tommasi et al., 2000), however they mostly do not agree with either VPSC or DRex models (Kaminski and Ribe, 2001). These differences indicate that the models do not replicate all aspects of the natural environment or shear strain might be highly estimated.

The evolution of fabric strength with strain is also important for constraining models of CPO formation. The fabric strength of Ichinomegata peridotites is compared with naturally deformed sample, experimental results and models in Figure 31b. Although the Ichinomegata peridotites seem to record higher shear strain than experimental dataset and model predictions for a given value of J, they are relatively similar to the Josephine peridotites. Ichinomegata peridotites have similar CPO type to Josephine peridotites, which have more girdle distribution in [010] and [001] compared to experimental samples. The rapid increase in J-index with shear strain

observed in the experiments results from alignment of [010] and [001] axes. The [010] and [001] girdled patterns in the Josephine samples lead to lower *J*-indices. *J*-indices strengthens than predicted by the theoretical models for Ichinomegata peridotites.

Based on the above discussion, a schematic model of the mantle evolution beneath the Ichinomegata volcano is shown in Fig. 32. Peridotite xenoliths with higher *J*-index values tend to be more closely aligned with olivine [100] and foliation, suggesting that these composite planar structures resulted from shearing in the uppermost mantle. Also, peridotite with higher *J*-index tends to have lower minimum temperature, and a wide range of temperatures (Fig. 32b). These structures, with the documented variability of CPO strength and related inferred shear strain, possibly indicate a vertical strain gradient during back-arc spreading related to the opening of the Japan Sea (Fig. 32d). Although the original orientations of the Ichinomegata peridotite xenoliths were lost during their volcanic transport to the surface (Fig. 32e), our results provide an improved framework for estimation of CPO evolution models from mantle xenoliths.

2-6-4. Relationships between deformation and melt-rock interaction in the metasomatized peridotites

Oki-Dogo and Shingu peridotites represent that part of the mantle affected by melt–rock interactions, as revealed by their melt-metasomatism geochemical signature. To understand the effects of metasomatism on the development of CPOs, the relationship between the Mg# of olivine and fabric strength (*J*-index) is shown in Figure 33b. *J*-index slightly increases with decreasing olivine Mg# (Fig. 33b). Because the *J*-index is a function of shear strain, the peridotites show increasing shear strain with degree of metasomatism. Le Roux et al. (2008) proposed that strain is

localized by the presence of melt, whereas Tommasi et al. (2008) showed that the *J*-index decreases with decreasing olivine Mg# (Fo < 90). However, the three samples that have low Fo contents (< 87) are inconsistent with this trend and record low strain.

Considering the above results, the observed small-scale variations in *J*-index may be explained by strain gradients or by a higher contribution of melt-enhanced diffusion processes, compared to those samples that show a weaker CPO. The occurrence of high melts fractions favors diffusion-accommodated deformation and results in a decrease in CPO intensity (Hirth & Kohlstedt, 1995; Holtzman et al., 2003). In contrast, at very low melt fractions, melt is essentially confined to triple-junctions grain boundaries and does not exist as an interconnected phase that enables rapid diffusion. Nevertheless, such melt may reduce the contact area between grains, leading to a local increase in stress (Hirth & Kohlstedt, 1995). In turn, higher stress may enhance dislocation creep and CPO development. Therefore, the observed variation in *J*-index in peridotites may result from deformation in the presence of variable fractions of melt over time.

To further assess the measured CPO patterns, we report the maximum density of CPOs (Fig. 33b-d), LS-index (Fig. 33e), and pfJ-index (Fig. 33f-h). The LS-index is presented by Ulich and Mainprice (2005), and is used to quantify CPO characteristics This method is based on well-established technique of eigenvalue analysis of pole figures. For example, figure 12 shows a case (Sample KRB15) of the variation of the [100] and [010] from point maxima to girdles distributions. The LS-index is defined as $1/2[2-(P_{010}/(G_{010}+P_{010}))-(P_{100}/(G_{100}+P_{100}))]$, where P = fabric indices for point maximum distribution defined by eigenvalue and G = fabric indices for girdle distribution defined by eigenvalue. The maximum densities of [010] relatively strengthens with decreasing Mg# (Fig. 33c), however there are not strong

relationships among them. This finding indicates that the slip planes became stronger during Fe-enrichment metasomatism. The sample SNG0709, consisting of almost exclusively olivine, have the highest maximum density of [100] and [001].

These variations in CPO densities are also observed in the CPO patterns. The CPO patterns obtained for KRB15, OKD69 (Fig. 12), SNG0707 (Fig. 13) show a strong concentration of [010] axes compared to [100] and [001]. However, most of the olivine CPO has a strong concentration in [100], indicating the (010)[100] slip system. The [010] axes define a point maximum and the [100] axes form a girdle, together defining an AG-type pattern (Mainprice, 2007). AG-type olivine CPO patterns have been observed in peridotites worldwide, including in the Ronda massif (Vauchez & Garrido, 2001; Soustelle et al., 2009), the Lherz massif (Le Roux et al., 2008), the Oman Ophiolite (Boudier & Nicolas, 1995), subcontinental xenoliths from Siberia (Tommasi et al., 2008), cratonic xenoliths (Ben Ismaïl et al., 2001; Vauchez et al., 2005), and xenoliths from the Canary Islands and the Kerguelen Islands (Vonlanthen et al., 2006; Bascou et al., 2008).

The "AG-type" CPO patterns measured in the present study are similar to the pattern described by Holtzman et al. (2003), which reported that it may also result from strain partitioning associated with melt segregation, as produced in a deformation experiment involving olivine in the presence of 4% MORB. Thus, it suggests that peridotite xenoliths from Oki-Dogo Island might be deformed in the presence of melt. This hypothesis is consistent with the above geochemical evidences proposed for the peridotites xenoliths. However, the Oki-Dogo peridotites show no clear change in microstructure and CPO with metasomatism, and the slip system is mostly (010)[100] rather than AG-type. Thus, we do not observe pronounced changes in olivine CPO related to melt-metasomatism.

It is important to consider the context of deformation and metasomatism in the studied samples, as we cannot infer the timing of these events based on the above analysis. If peridotites are metasomatized after the deformation event during which olivine CPOs developed, variations in olivine CPO or the intensity of the CPO would show no correlation with chemical composition. This observation, together with our microstructural analysis, suggests that in the present case, reactive melt percolation postdated deformationp. Indeed, an analysis of subgrain rotation axes reveals that subgrain boundaries in these peridotites are dominantly (100) tilt boundaries, indicating the dominant activation of [100] glide. Many olivine crystals retain well-defined subgrains, suggesting limited annealing. Thus, the absence of annealing features in olivine is inconsistent with static recrystallization.

Partial melting, percolation, and interaction of melt with host mantle rocks are processes that affect the lithospheric mantle above a mantle plume. Abe et al. (2003) concluded that the Oki-Dogo peridotite xenoliths are slightly more Fe-rich than are other mantle peridotite xenoliths from around the world. Here, we consider the timing of deformation and metasomatism in the structural history of the uppermost mantle in the back-arc of the southwest Japan arc.

Kimura et al. (2005) provided an interpretation of the structure beneath SW Japan based on petrological analyses of volcanic rocks. The model proposed by Kimura et al. (2005), as shown in Fig. 34(b), involve four tectonic stages: 1) the Pacific Plate was subducted at 25–14 Ma; 2) the Philippine Sea Plate begun to subduct at 17–12 Ma, the Japan Sea began to open, and upwelling of mantle asthenosphere occurred; 3) the rate of subduction decreased between 12 and 4 Ma; and 4) xenoliths were erupted, and slab melting occurred at 4–0 Ma.

Given that the peridotite xenoliths from Oki-Dogo Island were affected by

melts, we must consider the timing of melt-induced metasomatism of the peridotite xenoliths; i.e., whether it was related to asthenospheric upwelling or slab melting. Kimura et al. (2005) argued that slab melting occurred below about 100 km depth. Yamamoto et al. (2007) proposed that lherzolite from Oki-Dogo Island originated at depths of 25–29 km. Abe et al. (2003) argued that mantle metasomatism was induced by the intrusion of evolved melts beneath the SW Japan arc and the degree of melting in the upper mantle during opening of the Japan Sea. Iwamori (1989) concluded that volcanism in SW Japan was caused by the upwelling of mantle material associated with the opening of the Japan Sea, as across-arc variations in basalt composition in the central Chugoku district show the opposite trend to those in the NE Japan arc, and cannot be explained by processes related to the subduction of oceanic lithosphere at the Nankai trough or Japan trench.

The opening of the Japan Sea is thought to have occurred during the period 20–15 Ma as a consequence of back-arc spreading along the Japan arc; most of the basic geological structure of the present Japanese Islands was formed during this time (e.g., Sato, 1993). During this period of back-arc spreading, SW Japan underwent clockwise rotation, whereas NE Japan underwent anticlockwise rotation (Tamaki et al., 1995) (Fig. 34a). As a result, the Japan Sea adjacent to NE Japan consists of oceanic crust, whereas the Japan Sea adjacent to SW Japan consists of continental crust (locally stretched). Thus, it is important to compare NE and SW Japan in order to reconstruct the evolution of the uppermost mantle in association with back-arc spreading in the Japan arc.

Back-arc spreading within the Japan arc propagated progressively from NE to SW Japan (e.g., Sato, 1993; Kimura et al., 2005). Based on the above discussion, we argue that peridotite xenoliths from Oki-Dogo Island in SW Japan record an initial

stage of back-arc spreading. In SW Japan, peridotites were influenced by melts generated in association with asthenospheric upwelling (Fig. 35).

Overall, peridotites from the uppermost mantle in SW Japan were deformed in the presence of inhomogeneously distributed melt produced by asthenospheric upwelling associated with back-arc spreading. The peridotites were subsequently transported to the surface, retaining the structures formed in association with back-arc spreading. Then we conclude that the Oki-Dogo peridotite xenoliths record a continuous history of back-arc spreading, especially the initiation of back-arc spreading.

2-7. Conclusion

Microstructures, geochemical analysis, crystallographic preferred orientations (CPO) measurements and analysis, and water contents of spinel peridotite xenoliths obtained from the back arc region of Japan arc (Ichinomegata and Oki-Dogo) were investigated.

The mineral chemistry of Ichinomegata peridotites show a typical residual peridotite trend, depleted in LREE (light rare earth element). Olivine CPO of Ichinomegata peridotites are consistent with slip on (010)[100] and {0kl}[100], and the angle between the [100] maximum concentration and the foliation decreases with increasing fabric strength. By using those angles, shear strain is estimated to vary between 0.31 and 4.26, and temperature variations possibly suggested that *J*-index increases with decreasing depth of the original xenolith location. These observations indicate a strain gradient that could be related to back-arc spreading.

Oki-Dogo peridotites are affected by various degree of metasomatism by melt derived from the upwelling asthenosphere. Water content in pyroxenes is low,

suggesting that water in peridotites was moved to melts if water was present in rocks before metasomatism. Pyroxenes coexisting with olivine appear to retain their initial OH contents better than olivine even though the main minerals in the mantle (olivine, orthopyroxene and clinopyroxene) are nominally anhydrous (e.g., Peslier et al., 2002). Olivine CPOs of Oki-Dogo peridotites are consistent with the (010)[100] slip system. Samples have low Mg# and show relatively high concentration in [010], however, this relationship is not significant. Although peridotite xenoliths from Oki-Dogo Island could be deformed in the presence of melt during back-arc spreading, there appears to be no strong interaction between deformation and melt percolation.

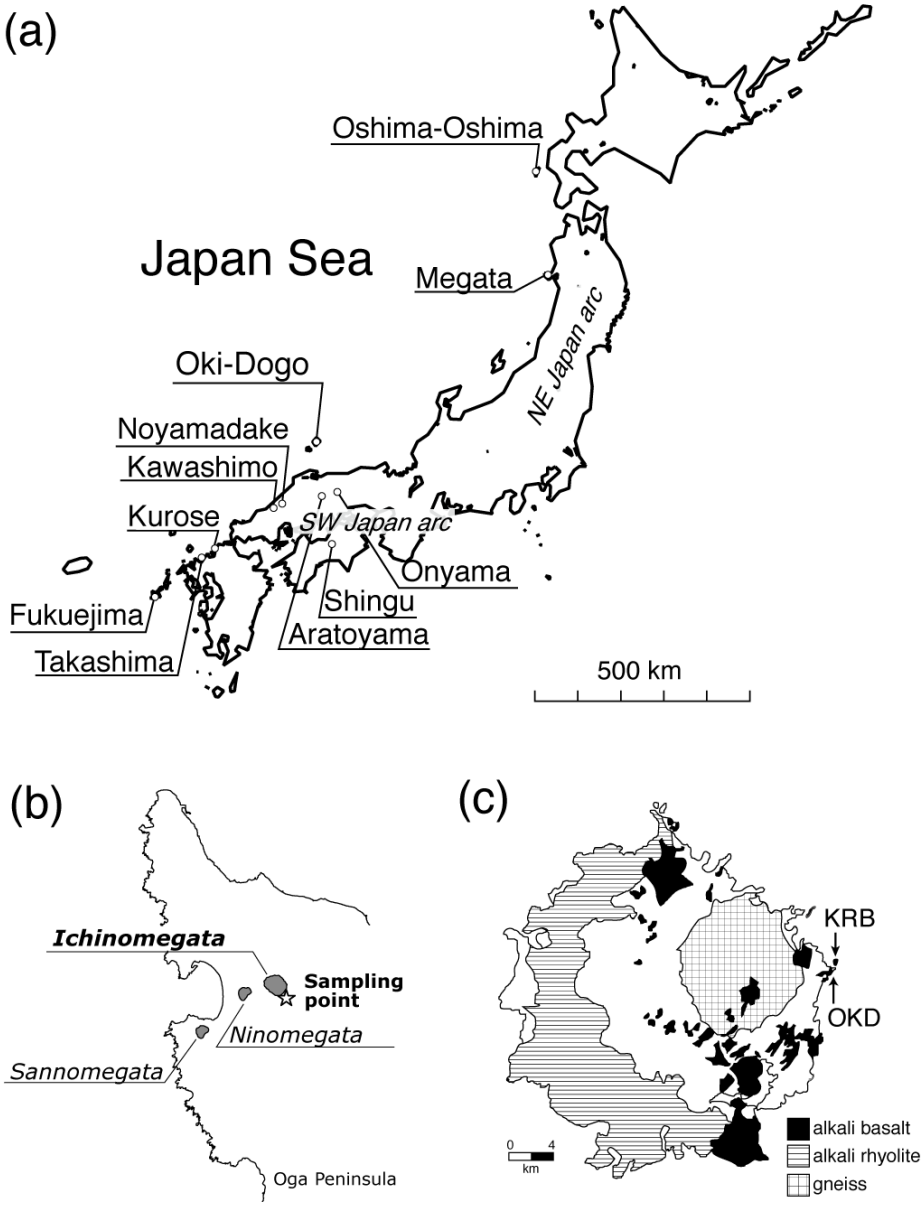

Figure 1. (a) Locality map of mantle xenoliths from the Japan arcs. Shown are selected localities of mantle xenoliths in the southwest (SW) and northeast (NE) Japan arcs. (b) Locality map of mantle xenoliths of the Ichinomegata volcano (Oga peninsula, Akita prefecture) in northeast Japan. The star indicates the sampling location. (c) Locality map of mantle xenoliths of the Oki-Dogo Island (Kuroshima basalt and OKD volcanic neck). The distributions of Plio-Pleistocene alkali basalt, and Miocene–Pliocene alkali rhyolite and basement gneiss complex are taken from Takahashi (1978a) and Uchimizu (1966). KRB: Kuroshima basalt; OKD: Oki-Dogo. Modified from Abe et al. (2003).

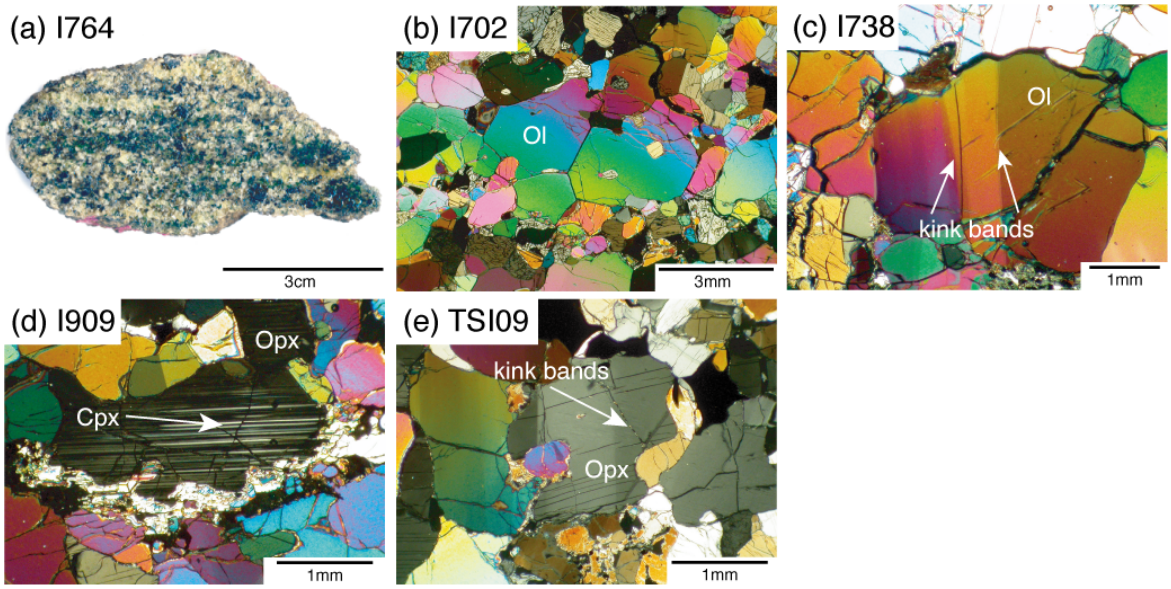

Figure 2. Ichinomegata peridotite xenoliths (b to c: photomicrographs; cross-polarized light). (a) Slabed sample shows a clear compositional banded structure (I764). (b) Olivine grains with 120° triple junction (I702). (c) Large olivine grains showing subgrain boundaries (kink bands) (I738). (d) Orthopyroxene porphyroclast with clinopyroxene exsolution lamellaes (I909). (e) Large orthopyroxene grains showing subgrain boundaries (TSI09).

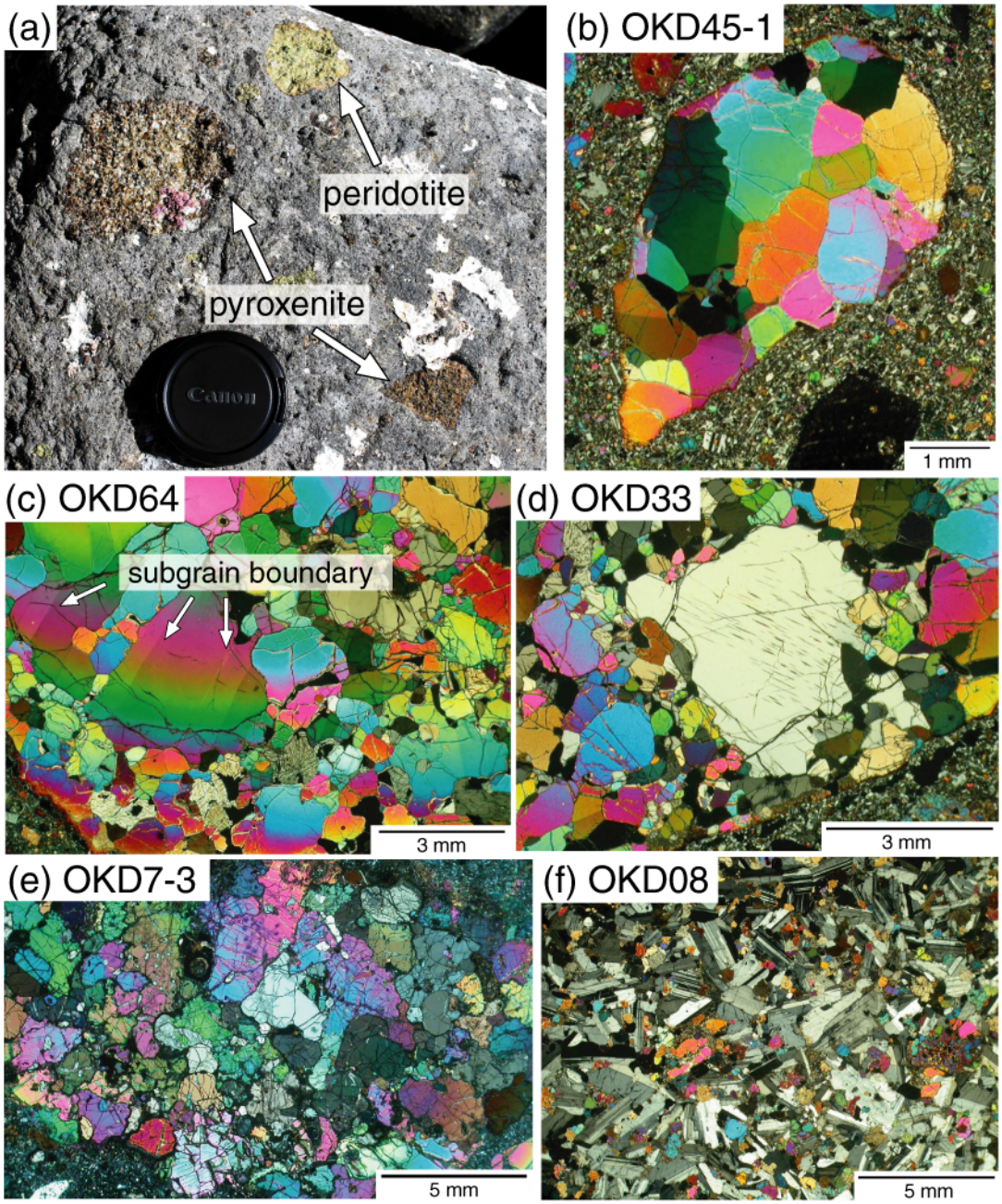

Figure 3. Oki-Dogo ultramafic and mafic xenoliths (b to f: photomicrographs; cross-polarized light). (a) Boulder including ultramafic and mafic xenoliths (indicated by white arrows) at an outcrop of Kuroshima alkali basalt. (b to d) Peridotite xenoliths (samples OKD45-1, OKD64, OKD33). (c) Large olivine grains show subgrain boundaries. (d) Orthopyroxene porphyroclast with clinopyroxene exsolution lamellaes. (e) Pyroxenite xenolith (OKD7-3). (f) Gabbro xenolith (OKD08).

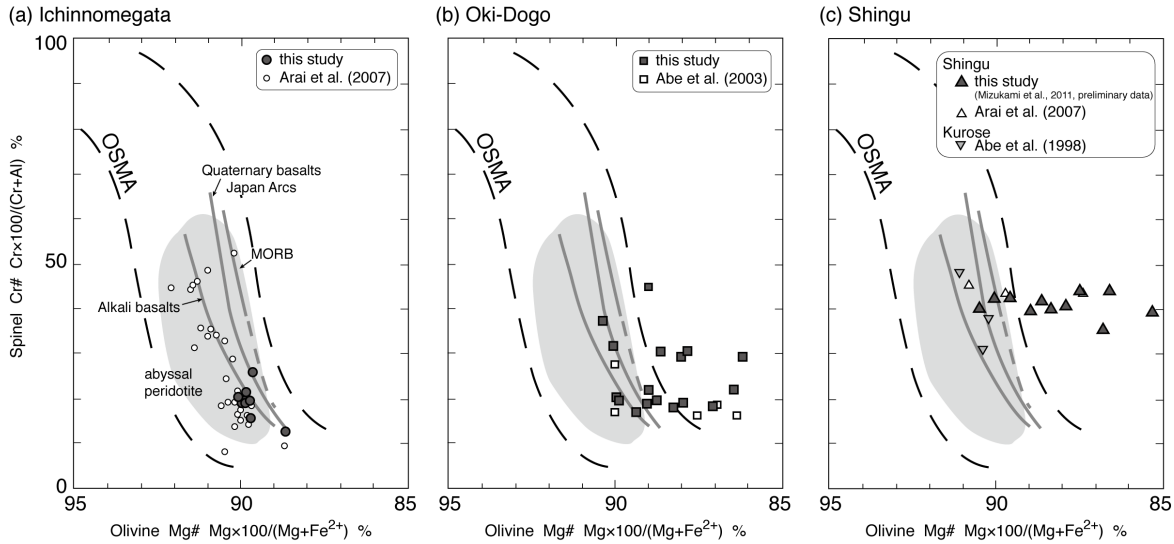

Figure 4. Relationship between the olivine Mg# and the spinel Cr# (Cr/(Cr+Al) atomic ratio) in analyzed samples of (a) Ichinomegata, (b) Oki-Dogo, and (c) Shingu. OSMA; olivine-spinel mantle array (Arai, 1994).

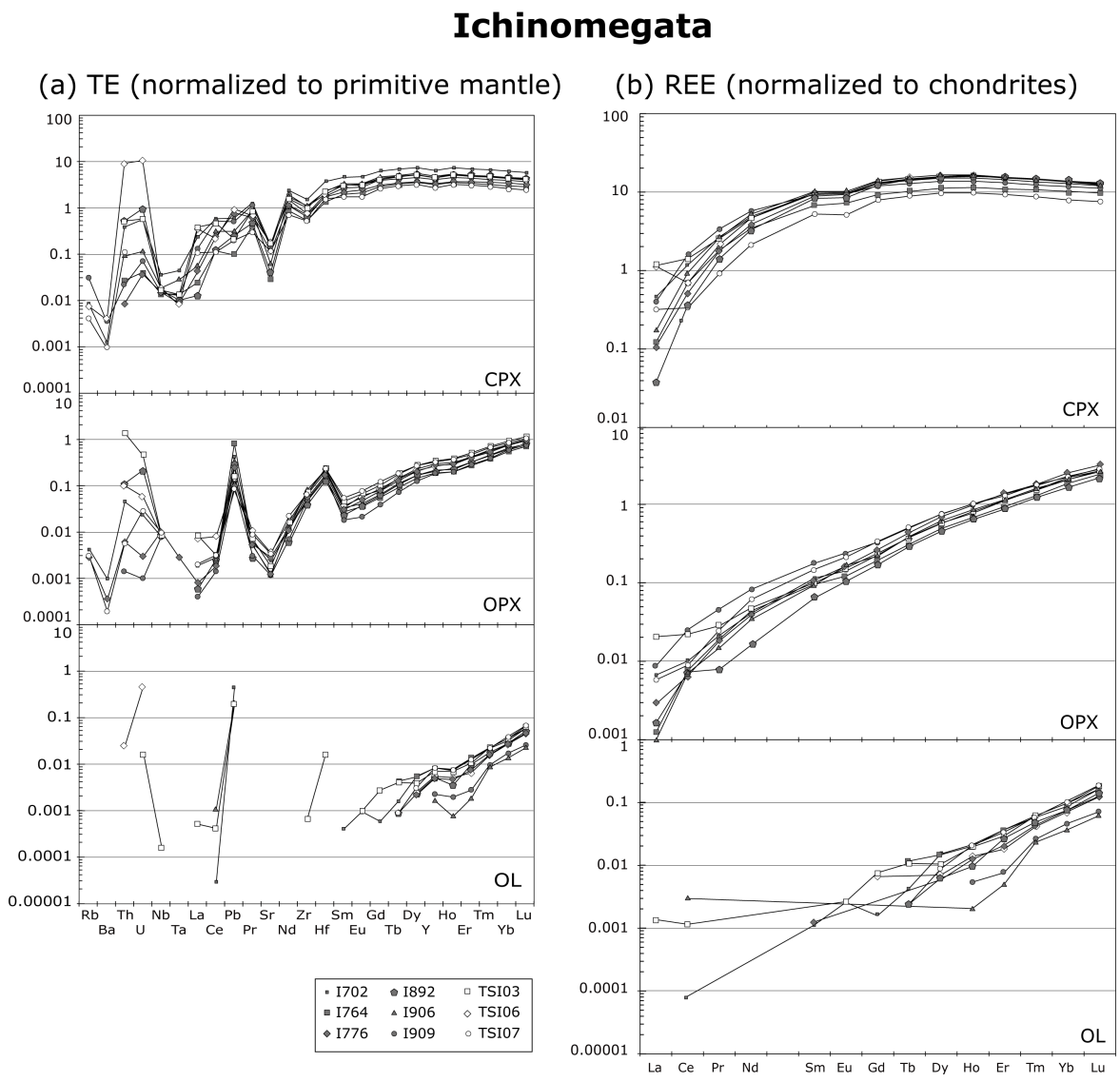

Figure 5. (a) Primitive mantle-normalized trace element compositions of clinopyroxene, orthopyroxene and olivine in nine Ichinomegata peridotite xenoliths. (b) Chondrite-normalized REE compositions of clinopyroxene, orthopyroxene and olivine in nine Ichinomegata peridotite xenoliths.

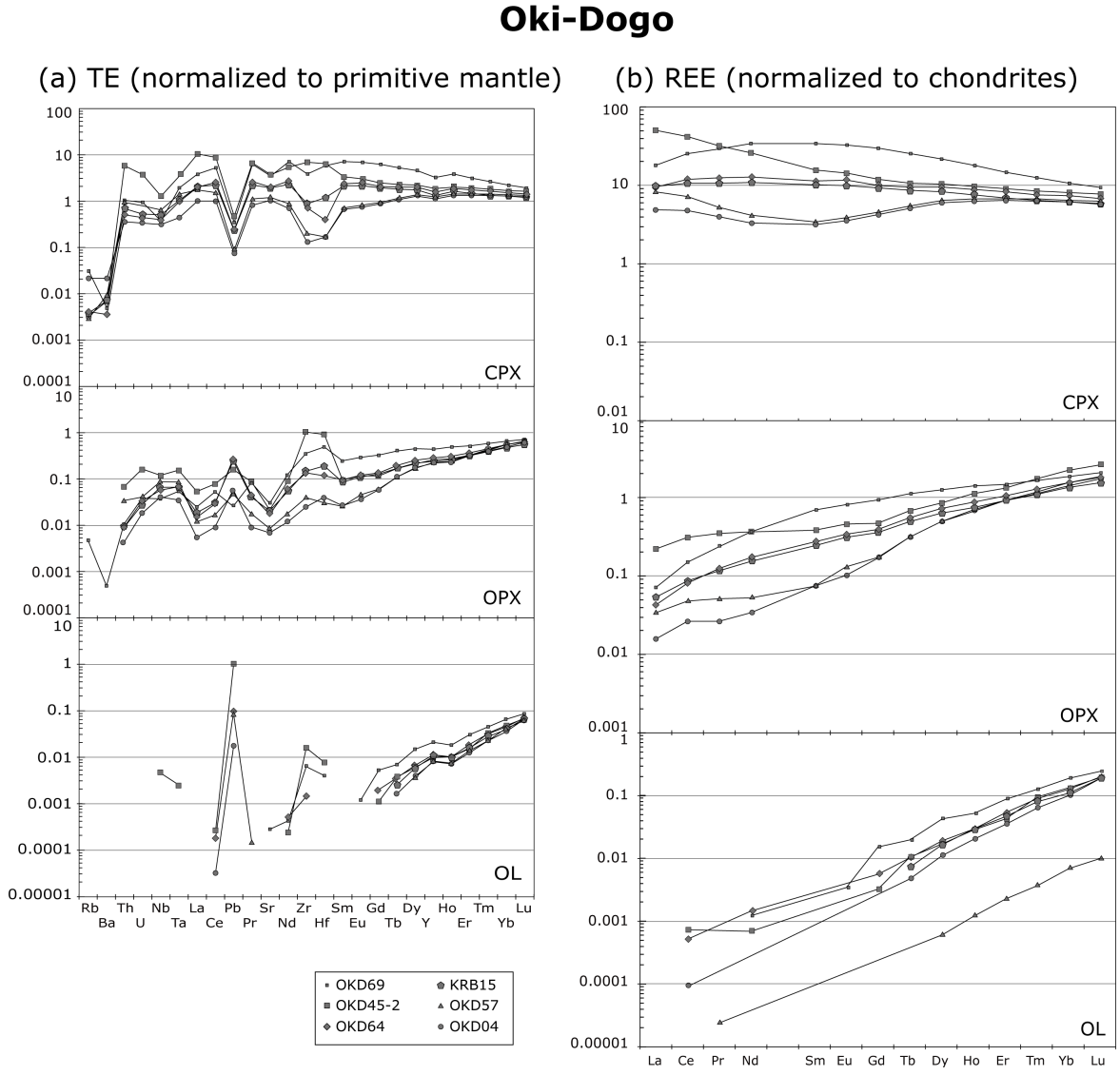

Figure 6. (a) Primitive mantle-normalized trace element compositions of clinopyroxene, orthopyroxene and olivine in six Oki-Dogo peridotite xenoliths. (b) Chondrite-normalized REE compositions of clinopyroxene, orthopyroxene and olivine in six Oki-Dogo peridotite xenoliths.

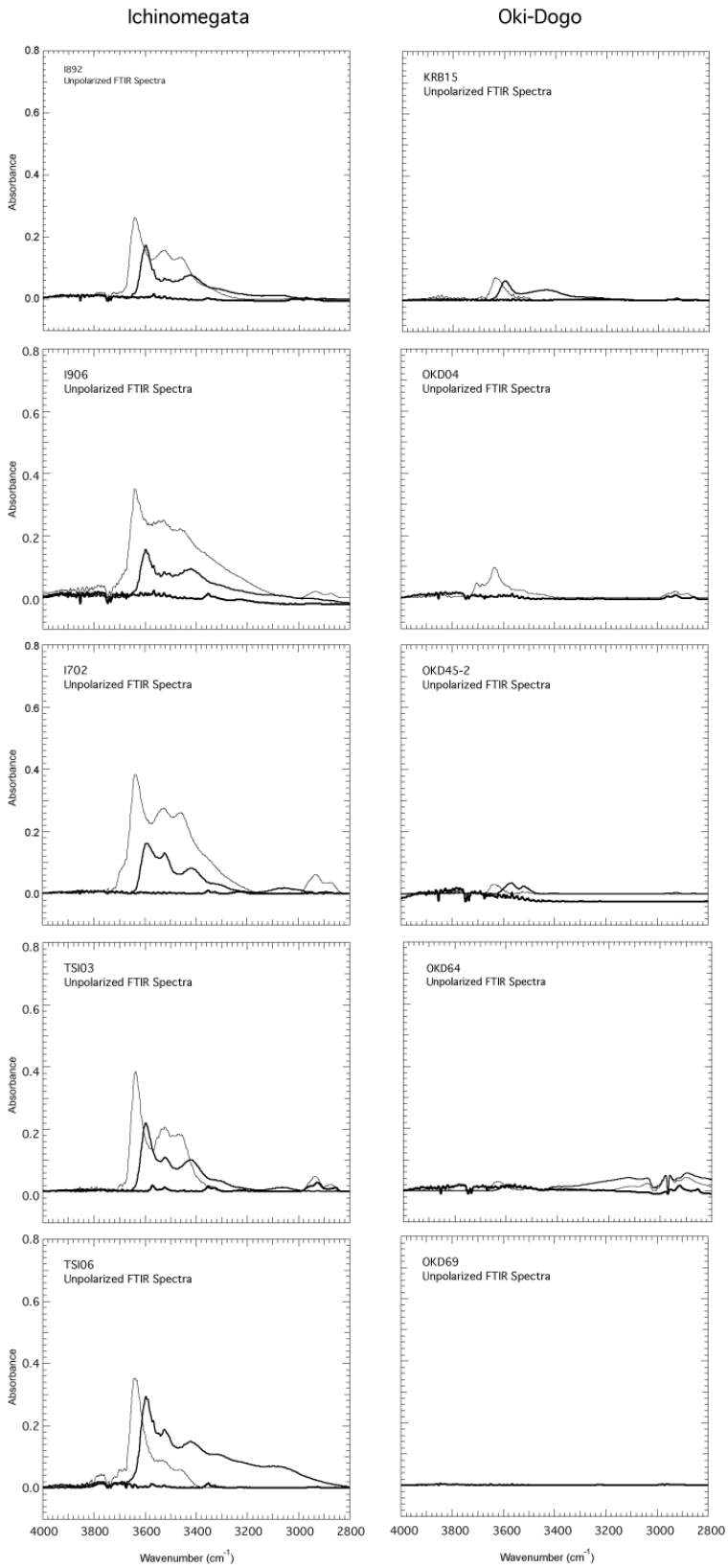

Figure 7. Representative unpolarized IR spectra for clinopyroxene, orthopyroxene and olivine in analyzed peridotite xenoliths. Spectra are normalized to 1 cm of thickness.

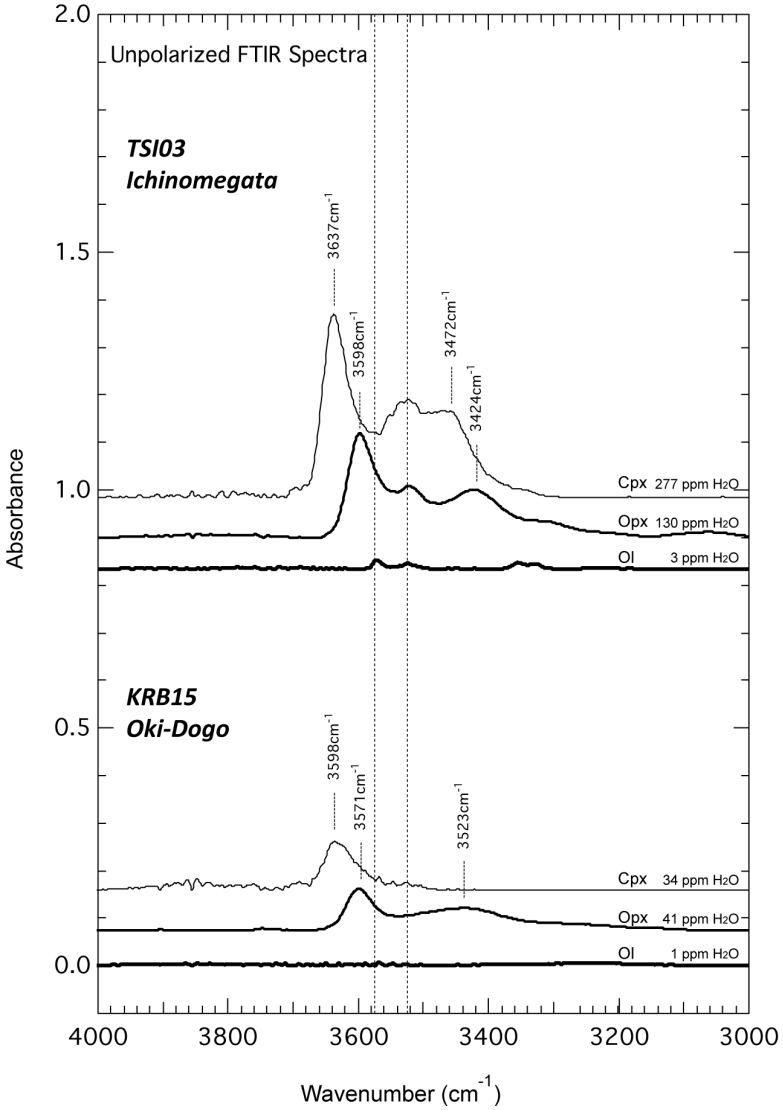

Figure 8. Representative unpolarized IR spectra for clinopyroxene, orthopyroxene and olivine in sample of TSI03 and KRB15. Spectra are normalized to 1 cm of thickness.

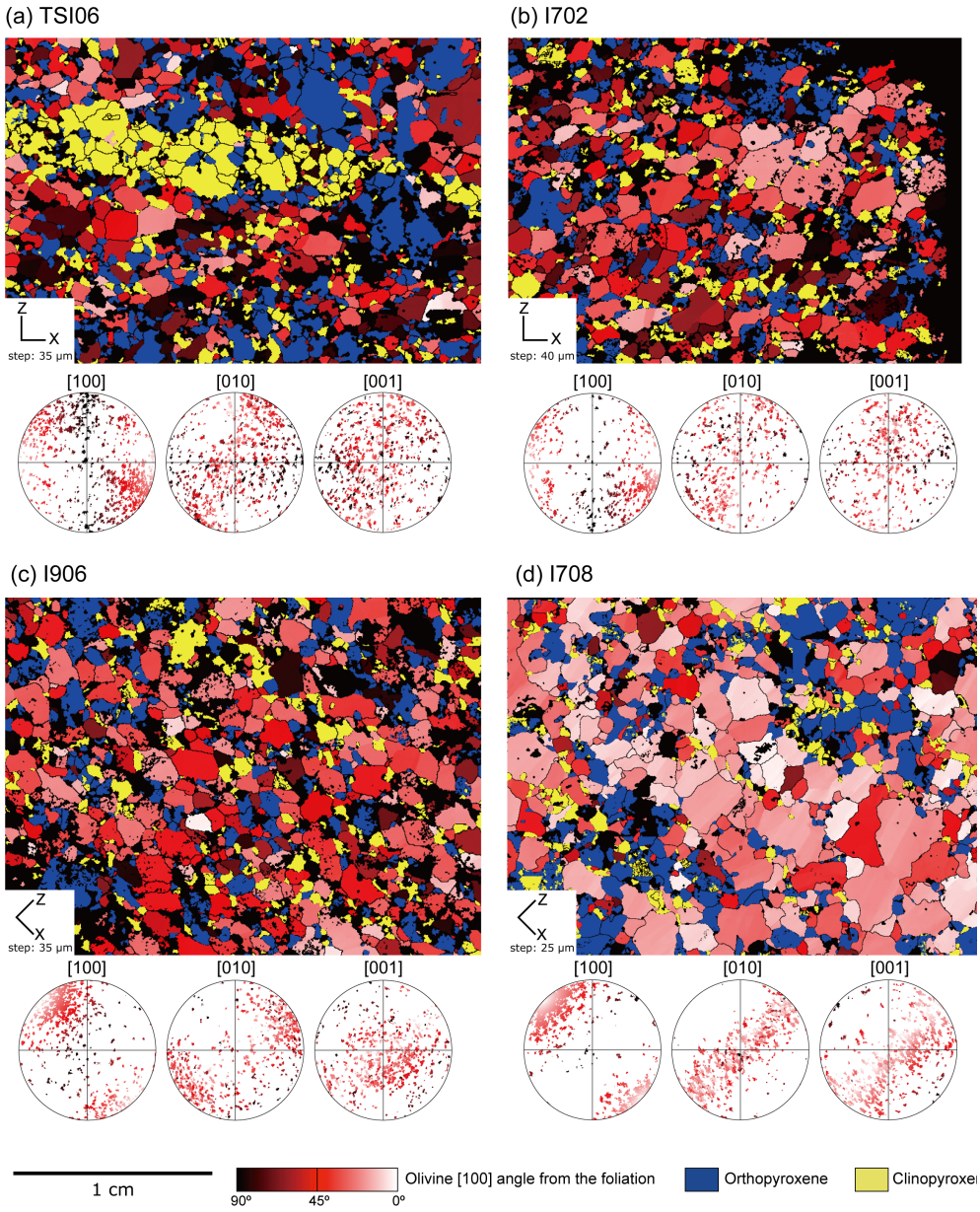

Figure 9. Examples of crystallographic orientation maps, and corresponding equal-area lower hemisphere stereographic projections in the thin-section reference frame of [100], [010] and [001] axes of olivine in Ichinomegata peridotite xenoliths. Red scale in the maps indicates the angle between the orientation of olivine [100] and the foliation plane (XY plane) indicated by the pyroxene-rich compositional banding.

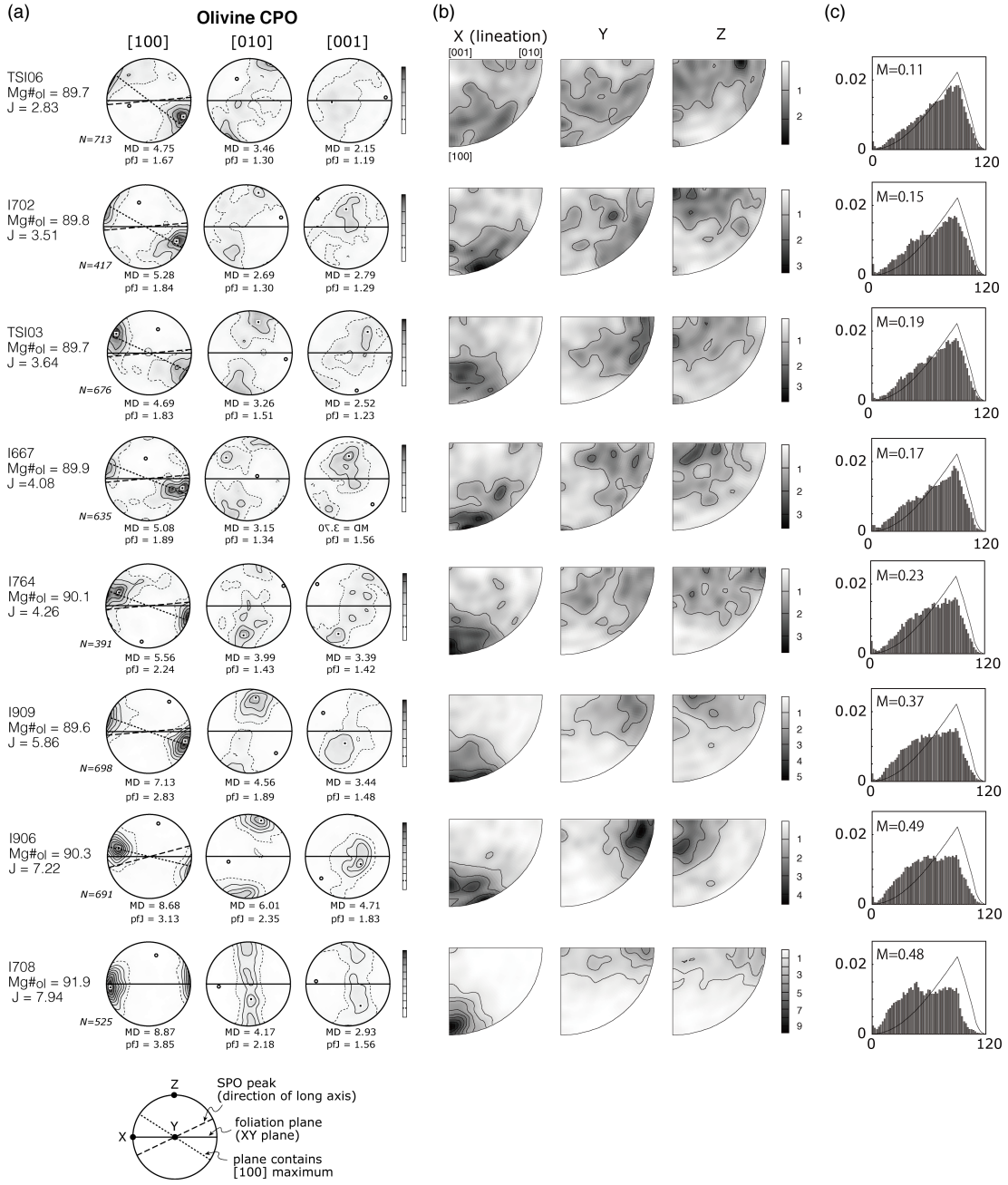

Figure 10. (a) Crystallographic preferred orientations (CPOs) of olivine in Ichinomegata peridotite xenoliths. Lower hemisphere, equal-area stereographic projections, contours at one multiple of uniform distribution. N is the number of measured grains. *J* and *pfJ* are indexes of fabric intensity, and MD is the maximum density (see Table 10) (b) Inverse pole figures of olivine. A half scatter width of 30º was used. The grey-scale coding refers to the density of the data points. (c) Misorientation distributions of uncorrelated misorientation angles for each samples, with *M* values indicated. The solid line is the theoretical orthorhombic random distribution (Grimmer, 1979).

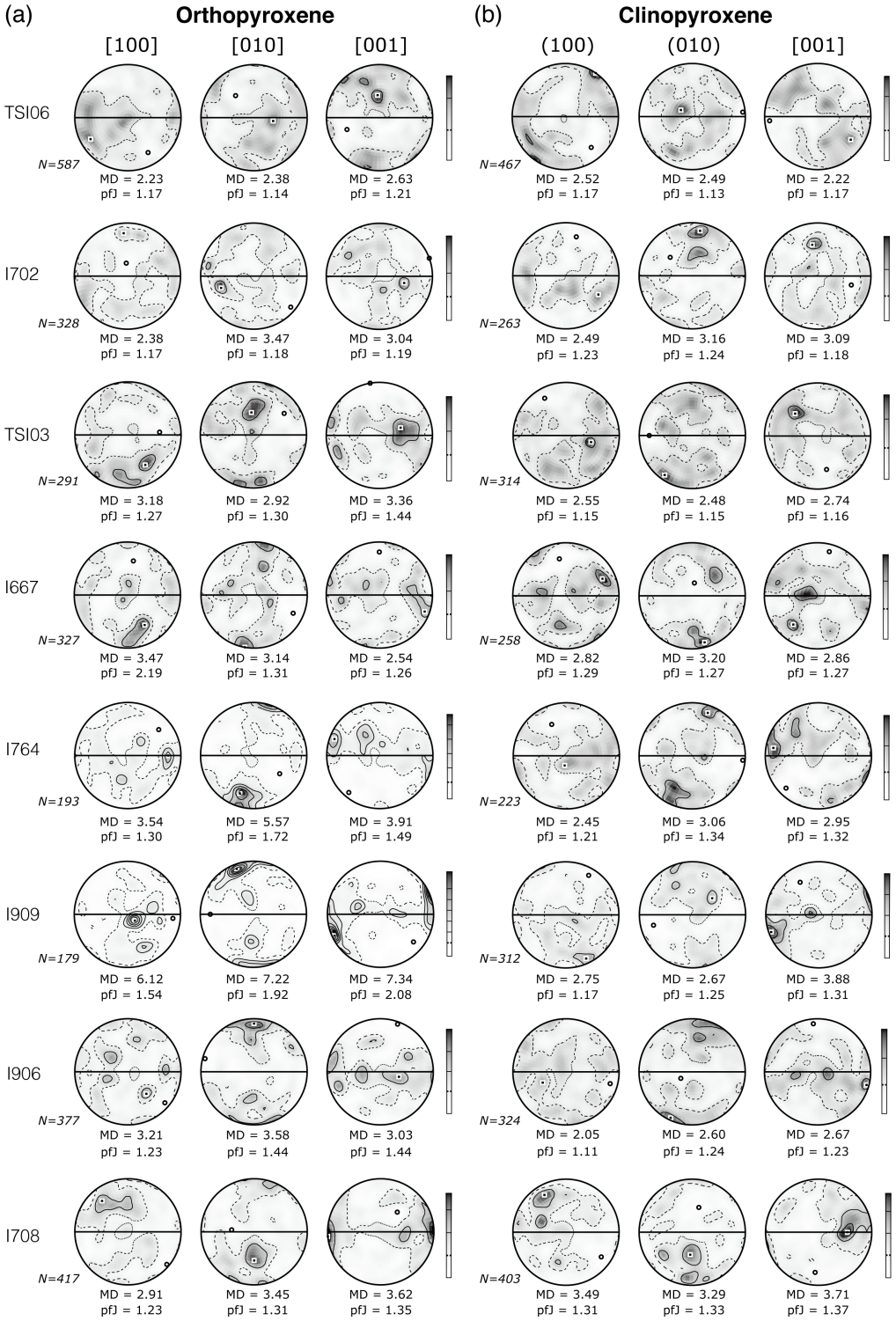

Figure 11. Crystallographic preferred orientations (CPOs) of orthopyroxene (a) and clinopyroxene (b) in Ichinomegata peridotite xenoliths. Lower hemisphere, equal-area stereographic projections, contours at one multiple of uniform distribution. N is the number of measured grains. *pfJ* are indexes of fabric intensity, and MD is the maximum density (see Table 10).

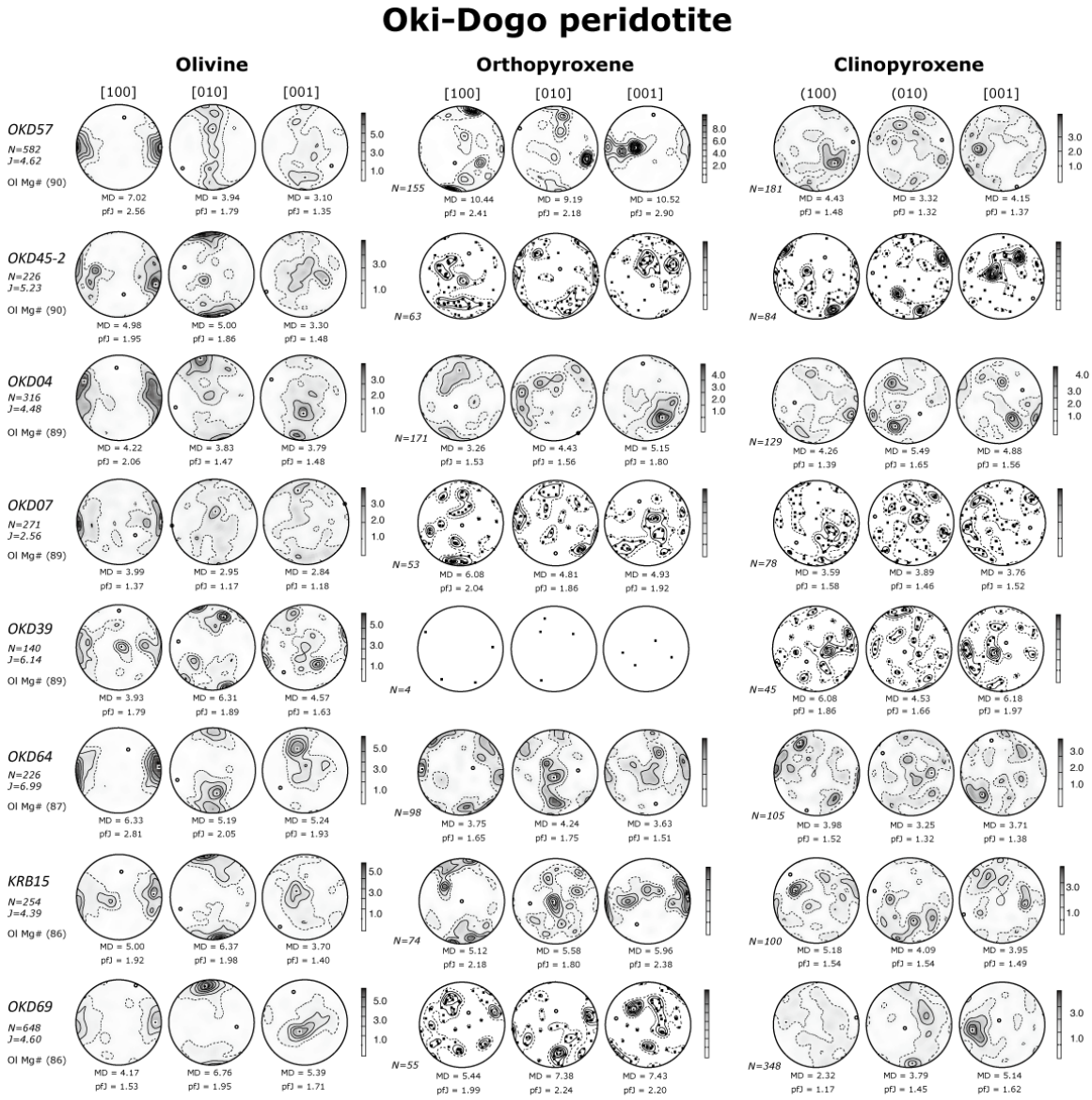

Figure 12. Crystallographic preferred orientations (CPOs) of olivine, orthopyroxene and clinopyroxene of Oki-Dogo peridotite xenoliths. Lower hemisphere, equal-area stereographic projections, contours at one multiple of uniform distribution. N is the number of measured grains. *J* and *pfJ* are indexes of fabric intensity, and MD is the maximum density (see Table 10).

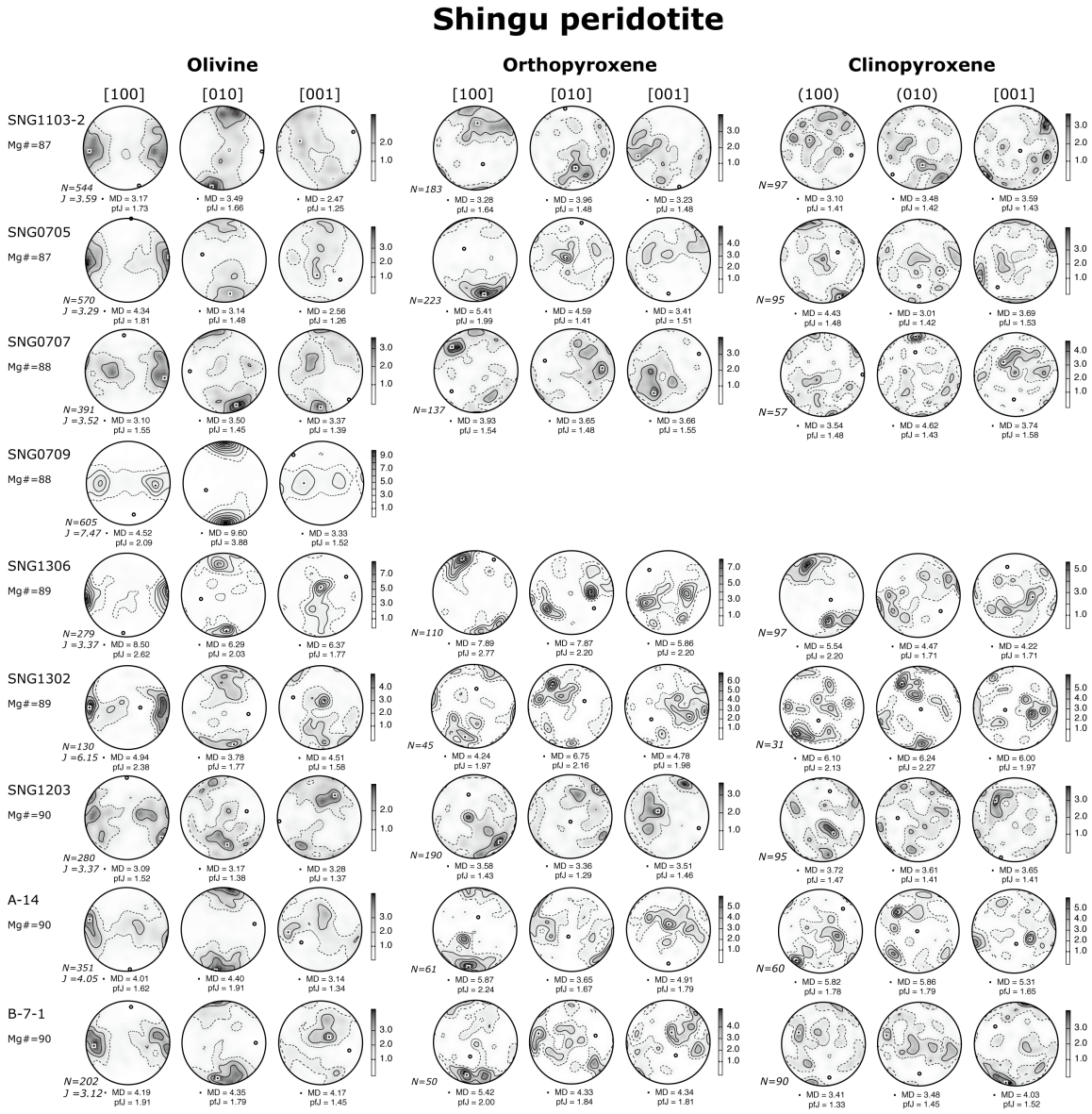

Figure 13. Crystallographic preferred orientations (CPOs) of olivine, orthopyroxene and clinopyroxene of Shingu peridotite xenoliths. Lower hemisphere, equal-area stereographic projections, contours at one multiple of uniform distribution. N is the number of measured grains. *J* and *pfJ* are indexes of fabric intensity, and MD is the maximum density (see Table 10).

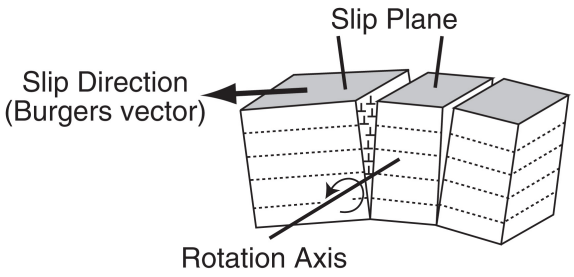

Figure 14. Crystal rotation and tiltwall orientations across an olivine single crystal. The slip direction (Burgers vector) is indicated by the axis normal to the subgrain boundary. The rotation axis is calculated by the two subgrain orientations. The axis excepted for slip direction and rotation axis is interpreted to be normal to the slip plane. Modified after Mehl et al. (2003).

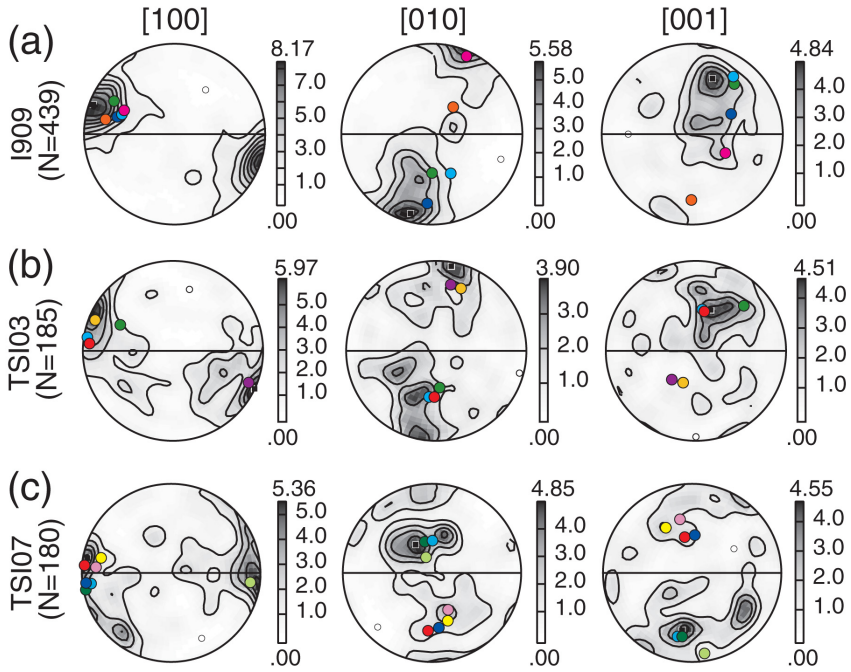

Figure 15. Olivine crystallographic preferred orientation (CPO) data obtained by the EBSD technique in Ichinomegata peridotite xenoliths. (a) I909, (b) TSI03 and (c) TSI 07. Equal-area, lower-hemisphere projections. Contours at multiples of uniform distribution. Foliation is horizontal and lineation is E-W. N is the number of measurements. Symbols (color circles) correspond to those in Fig. 18 and Fig. 19.

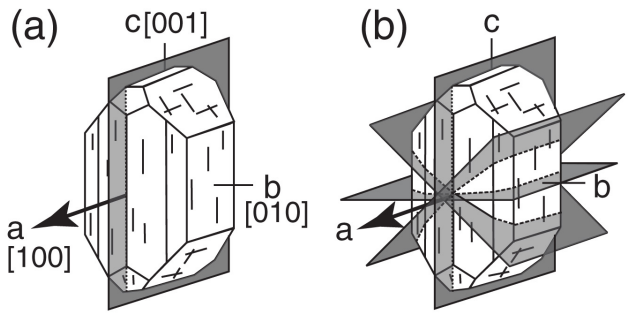

Figure 16. Slip systems in olivine single crystal. The bold arrows show slip direction, while the gray rectangles show slip planes. (a) (010)[100]. (b) {0kl}[100].

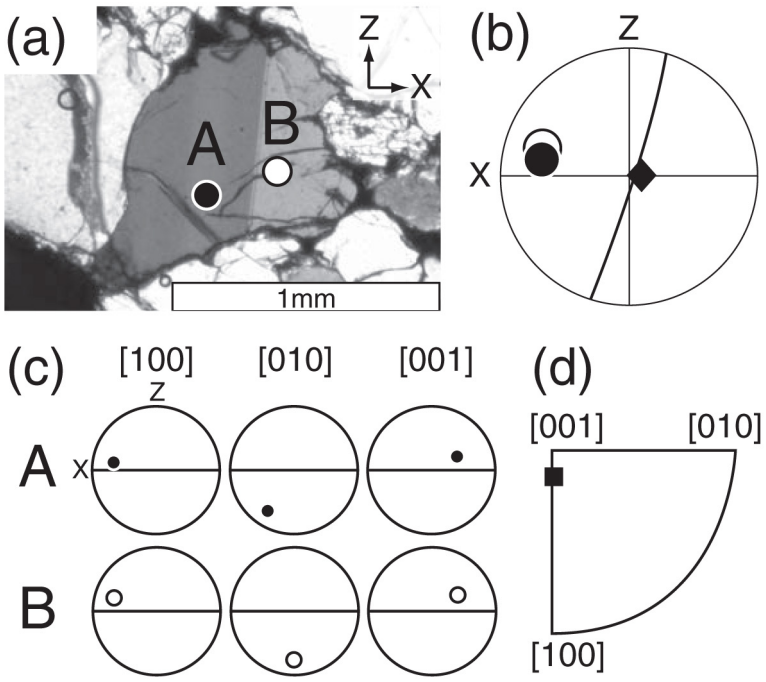

Figure 17. The subgrain-rotation axis method. (a) Photomicrograph of an olivine subgrain boundary in sample I909. Foliation is horizontal and lineation is E-W. Scale bar is 1mm. Crossed-polarized light. A and B are points where crystallographic orientations were measured. (b) A great circle indicates the subgrain-boundary orientation obtained by a universal stage. Circles correspond to the orientations of olivine. Diamond is the misorientation axis across the subgrain boundary. Assuming the slip direction is [100], this subgrain boundary is considered to be a tilt boundary with [100] edge dislocations, because the subgrain boundary is subnormal to [100] and subparallel to the misorientation axis. (c) Crystallographic orientation data at the points of A and B. Equal-area, lower-hemisphere projections. (d) The misorientation axis between subgrains A and B plotted on an inverse pole figure.

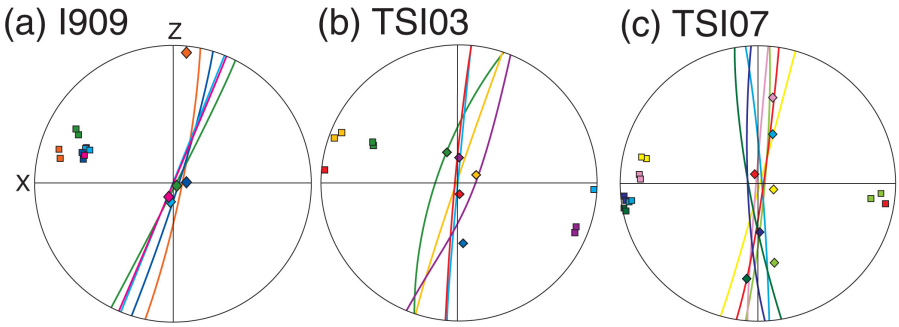

Figure 18. Great circles show subgrain-boundary orientations obtained by universal stage measurements. Squares correspond to the orientations of olivine [100], which is supposed to be the slip direction. Diamonds are the orientations of misorientation axes across subgrain boundaries. Symbols (color circles) correspond to those in Fig. 15 and Fig. 19.

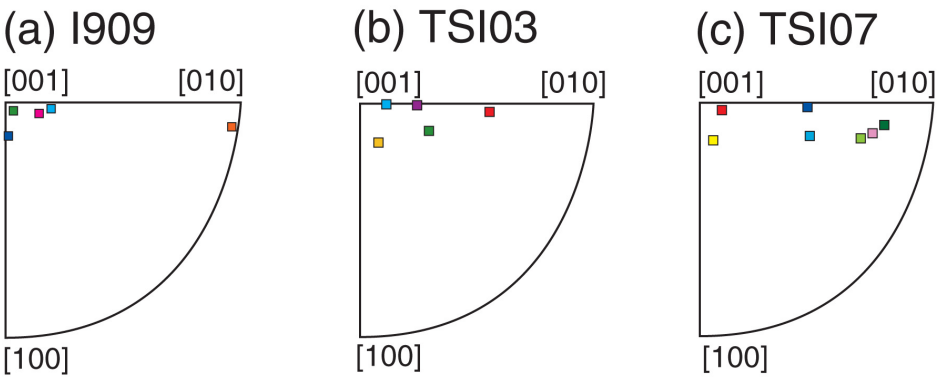

Figure 19. Misorientation axes across measured subgrain-boundaries plotted on inverse pole figures. (a) I909. (b)TSI03. (c)TSI07. Symbols (color circles) correspond to those in Fig. 15 and Fig. 18.

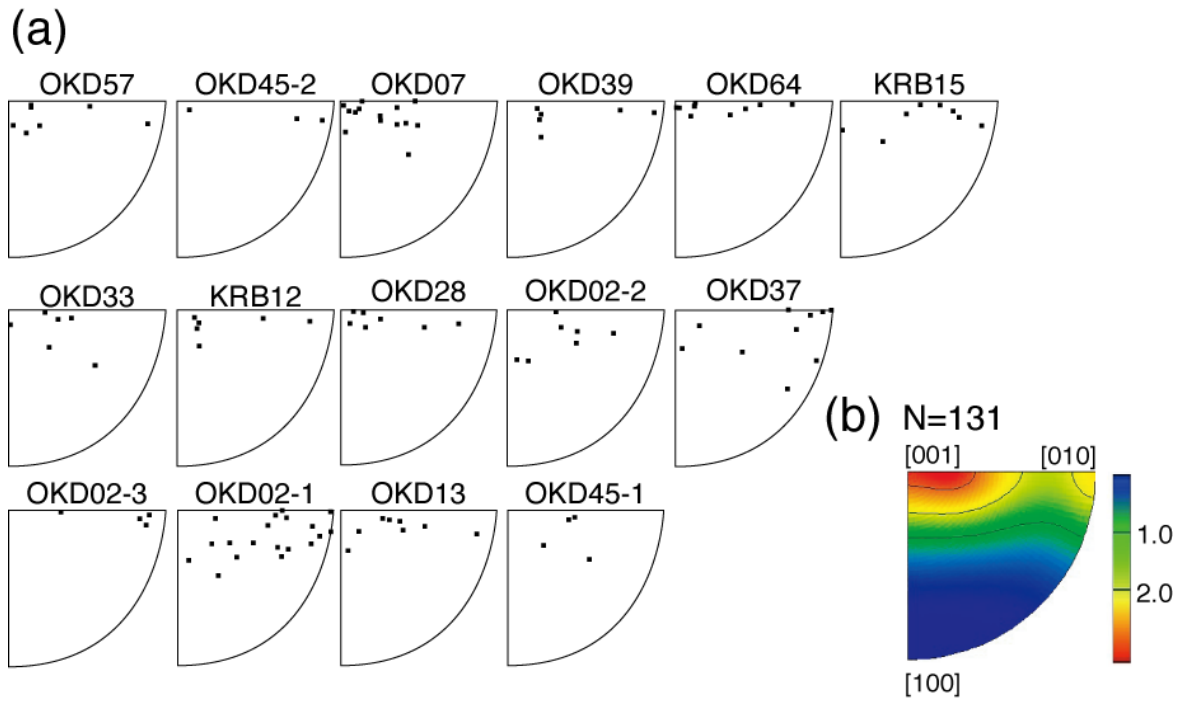

Figure 20. (a) Subgrain-rotation axes of measured subgrains plotted on inverse pole figures. (b) Subgrain-rotation axes of all measured subgrains of peridotite xenoliths from Oki-Dogo Island plotted on an inverse pole figure. Contours are multiples of uniform distribution.

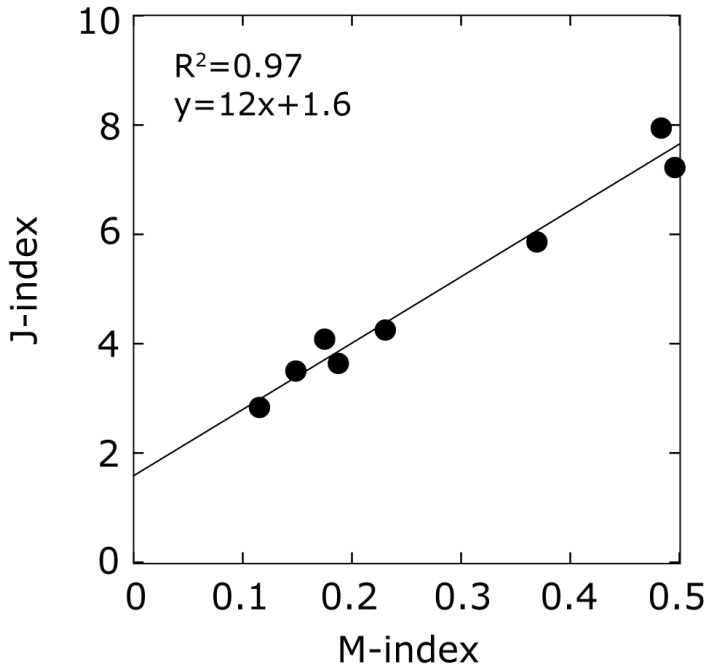

Figure 21. Strength of olivine crystallographic preferred orientation in the studied samples characterized by the J and the M indices. The high correlation coefficient (R^2) indicates that these two measures of the CPO strength are consistent.

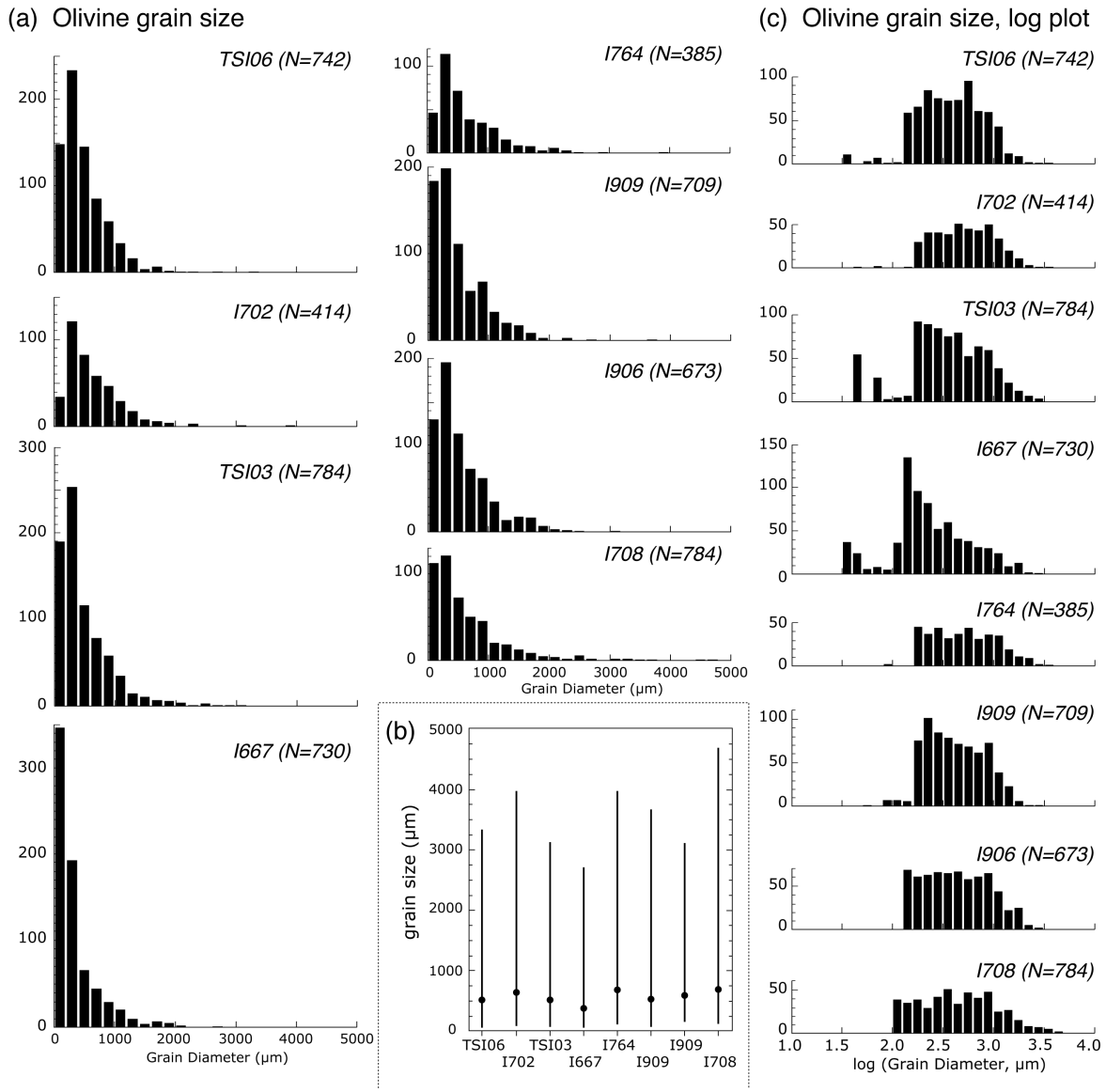

Figure 22. (a) Olivine grain size histogram for Ichinomegata peridotite xenoliths. Outlines of olivine grains were automatically traced by CHANNEL 5 software from crystallographic orientation map obtained by EBSD. We measured a total of 385 to 784 olivine grains per sample. (b) Range of grain size (diameter in μm) of olivine. Black circles show the average grain size. (c) Logarithmic grain-size distributions of olivine grains.

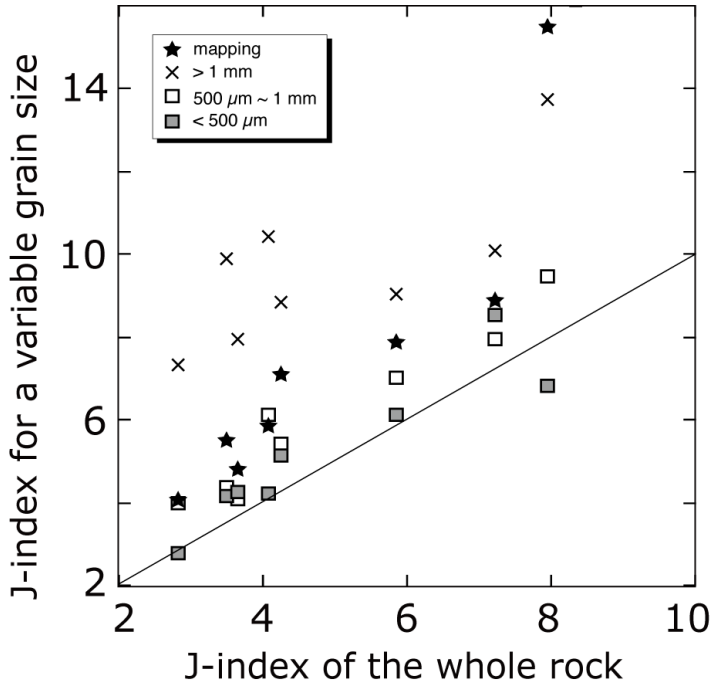

Figure 23. J-index for various olivine grain size populations versus J-index of the whole rock. Stars, J-index calculated from grid data; cross symbols, coarse grains (φ > 1 mm); open squares, intermediate grains (φ between 1 and 0.5 mm); gray squares, fine grains (φ < 0.5 mm).

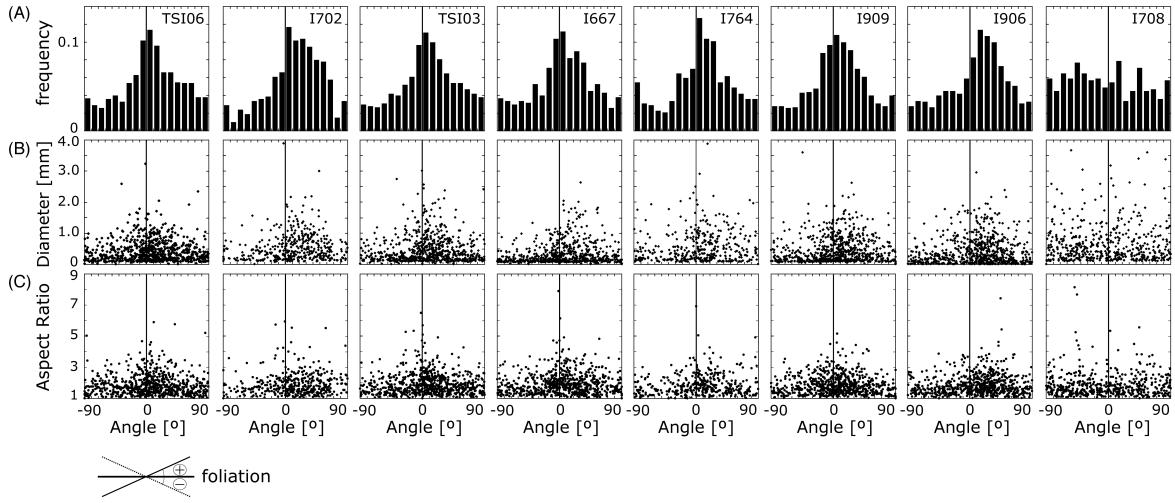

Figure 24. (a) Orientation distributions of olivine grains with respect to the trace of the foliation (X). The angles between the shape-preferred orientation (SPO) and the foliation are approximately 10 – 20º. (b) Relationship between orientation distribution of olivine grains with foliation and grain size. (b) Relationship between orientation distribution of olivine grains with foliation and grain aspect ratio.

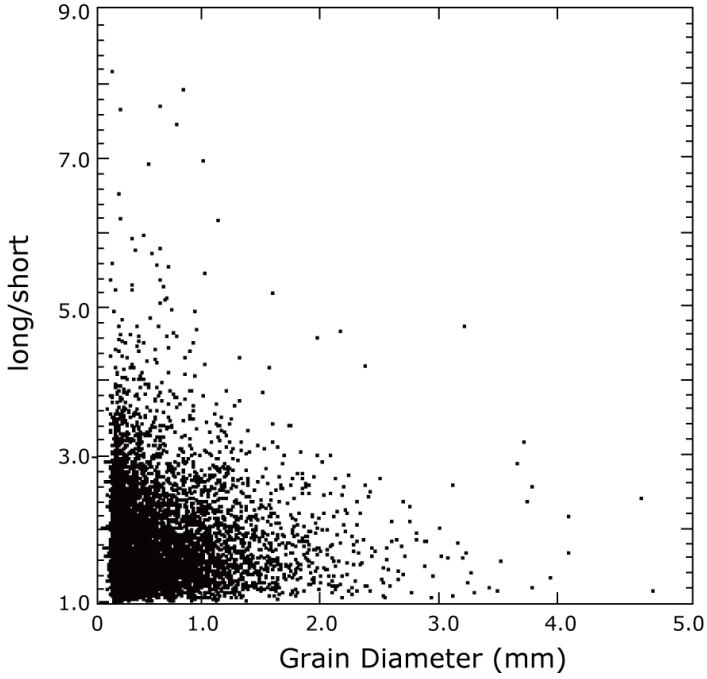

Figure 25. Relationship between olivine grain diameter and aspect ratio (long axis/short axis of the representative ellipsoid) in Ichinomegata peridotite xenoliths.

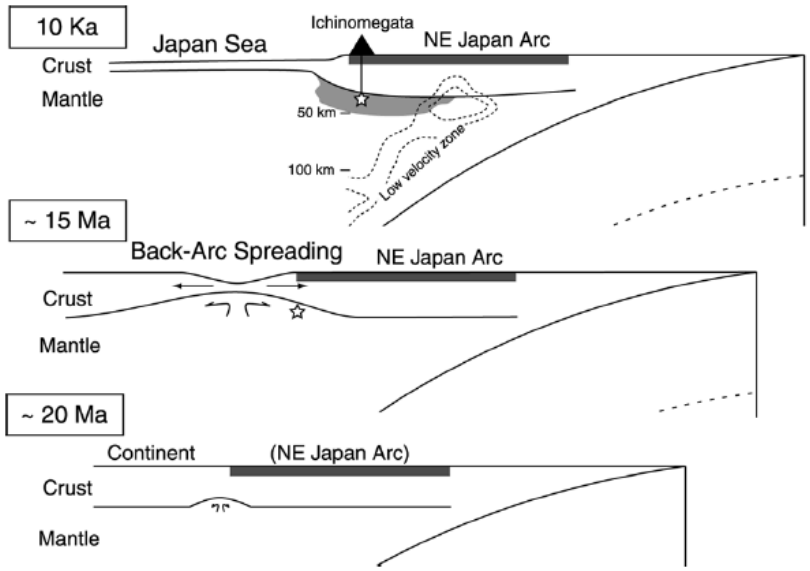

Figure 26. Schematic diagrams showing the tectonic evolution of the northeast Japan arc between ca 20 Ma and 10 Ka (after Michibayashi et al., 2006). Star symbols indicate inferred locations of the Ichinomegata peridotite xenoliths within the mantle. The shaded area in the vicinity of the star symbol at 10 Ka shows the possible thickness of the seismically anisotropic layer, from which the measured delay times of S-waves can be explained.

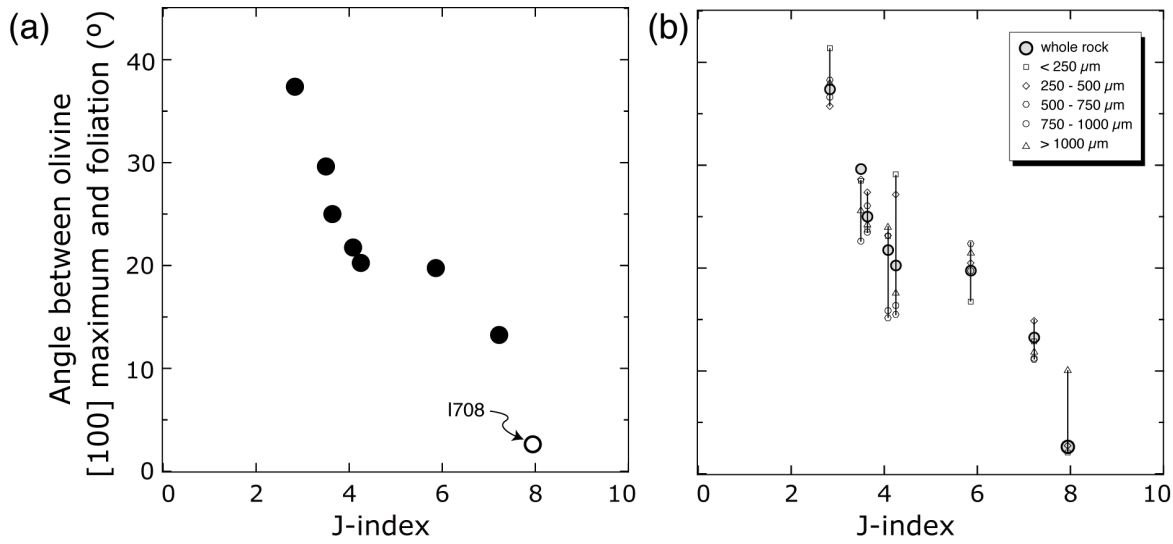

Figure 27. (a) Relationship between the J-index and the angle between olivine [100] maximum and foliation of Ichinomegata peridotite xenoliths. (b) Angle between olivine [100] maximum and foliation for various olivine grain size populations versus J-index of the whole rock. Gray circles: J-index calculated from whole rock data; triangles: coarse grains (φ > 1 mm); circles: relatively coarse grains (φ between 1 and 0.75 mm); polygons: intermediate grains (φ between 0.50 and 0.75 mm); diamond shapes: relatively fine grains (φ between 0.25 and 0.50 mm); squares: fine grains (φ < 0.25 mm).

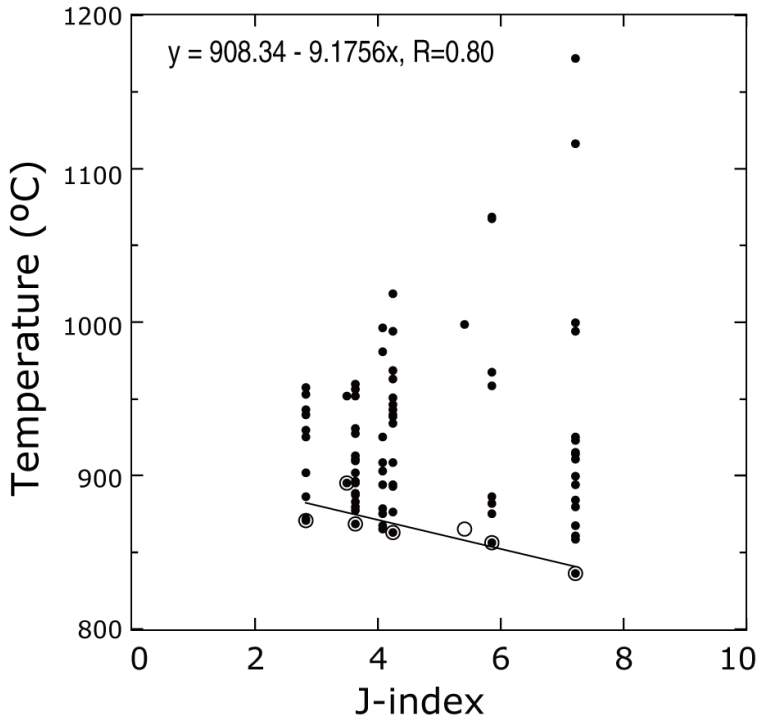

Figure 28. Relationships between the J-index and the equilibrium temperature of Ichinomegata peridotite xenoliths.

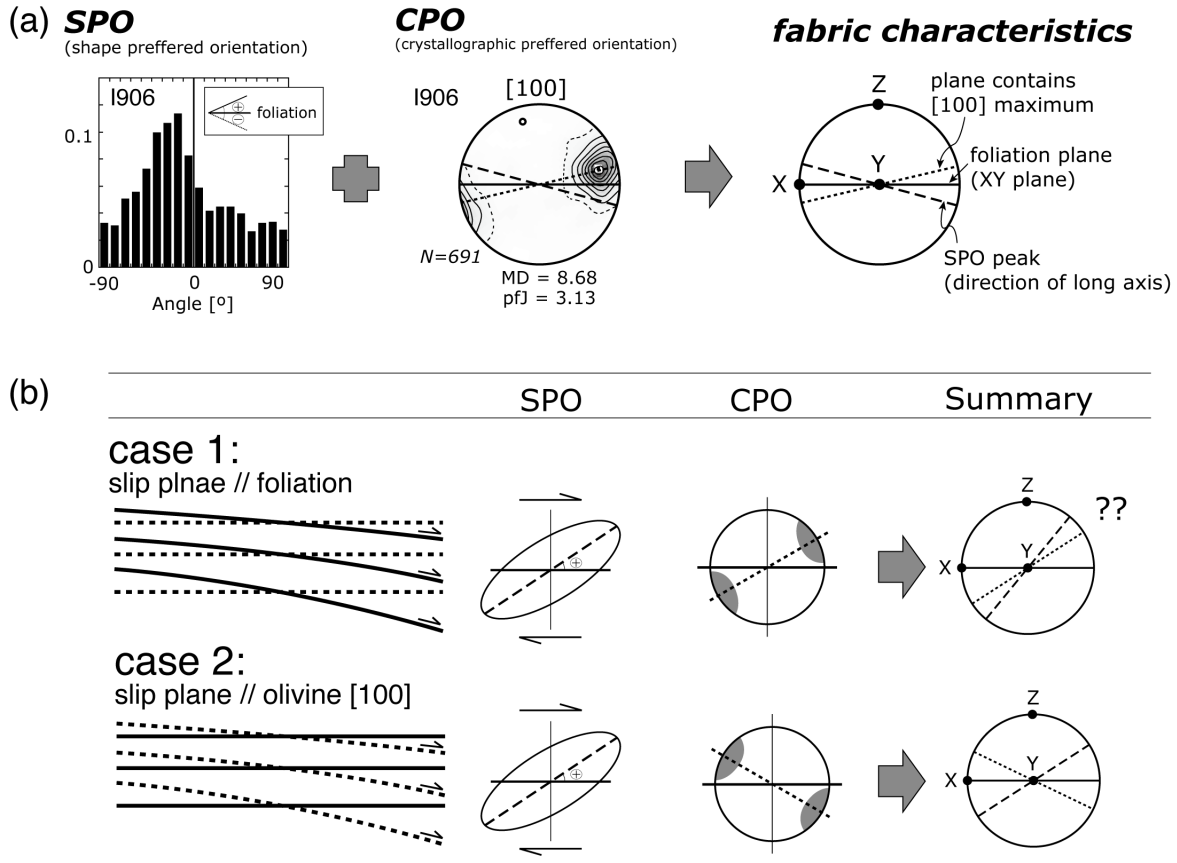

Figure 29. (a) Sketch showing how to define the fabric characteristics from SPO (shape preferred orientation) and CPO (crystallographic preferred orientation). (b) Schematic model for the estimation of shear sense in Ichinomegata peridotite xenoliths. Case 1: slip plane is defined by foliation; Case 2: slip plane is defined by olivine [100] axis.

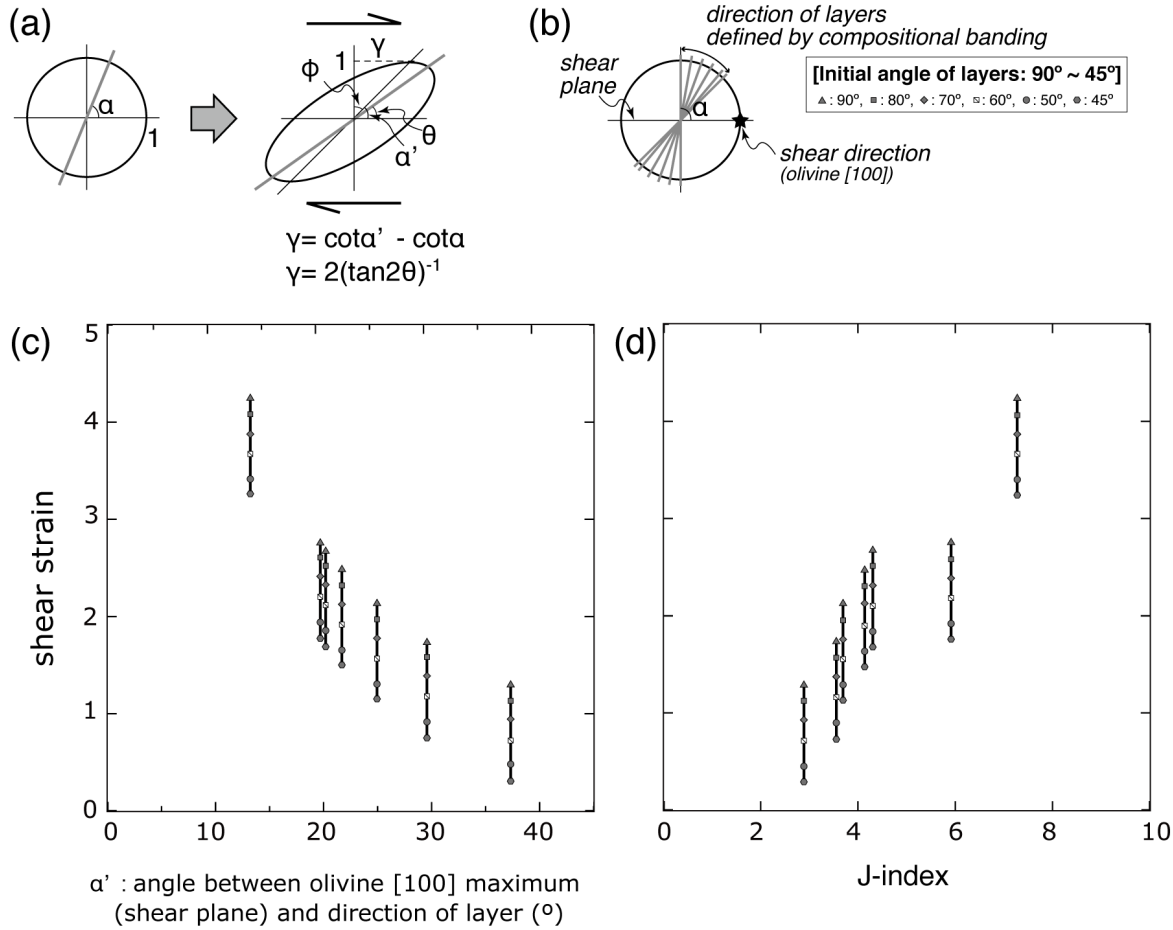

Figure 30. (a) The geometric relationship of shear strain, γ, with the orientation of a marker layer, which initially lies at an angle α to the shear plane and is deflected to a smaller angle, α'. The orientation of the finite strain ellipse long axis is represented by the angle θ and is not coincident with the marker layer. Diagram adapted from Ramsay and Graham (1970). (b) Stereo net of the variation of layer (compositional banding) orientations with respect to the shear plane. (c) Calculated shear strain from equation shown in (a) with angle (α') from 45º to 90º. (d) Relationships between J-index and shear strain based on (c) results.

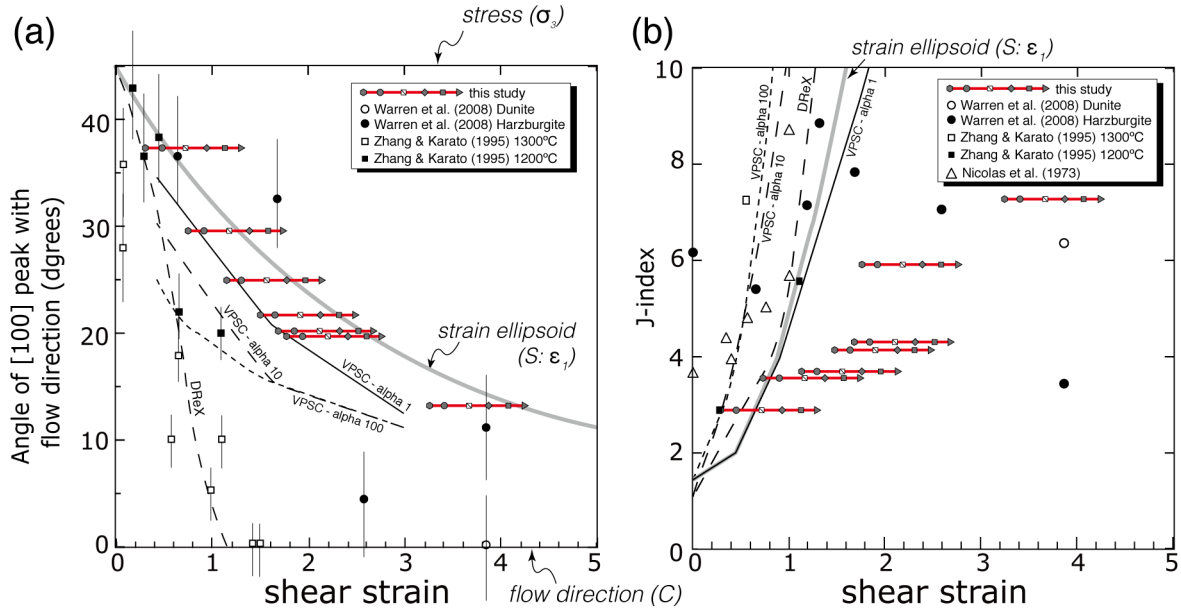

Figure 31. (a) Angle of the olivine [100] maximum to the shear plane as a function of shear strain in the Ichinomegata peridotite xenoliths (red bars), Josephine peridotites (Warren et al., 2008), experiments (Zhang and Karato, 1995), and models. The models and experiments initially have random fabrics, represented by an average angle of 45º to the shear direction. The simple model (solid gray line) is finite strain ellipsoid and shear. VPSC is the best fit (α = 1, 10, 100) of the viscoplastic self-consistent model (Tommasi et al., 2000) to the experiments. DRex is the best fit of the dynamic recrystallization model (Kaminski and Ribe, 2001) to the experiments. (b) Variation in the J-index as a function of shear strain. The results for the Ichinomegata peridotite xenoliths are shown as red bars. Also shown are Josephine peridotites (Warren et al., 2008), Nicolas et al. (1975) experiments, Zhang and Karato (1995) experiments (from the J-index calculation by Tommasi et al., 2000), the VPSC model and DRex model.

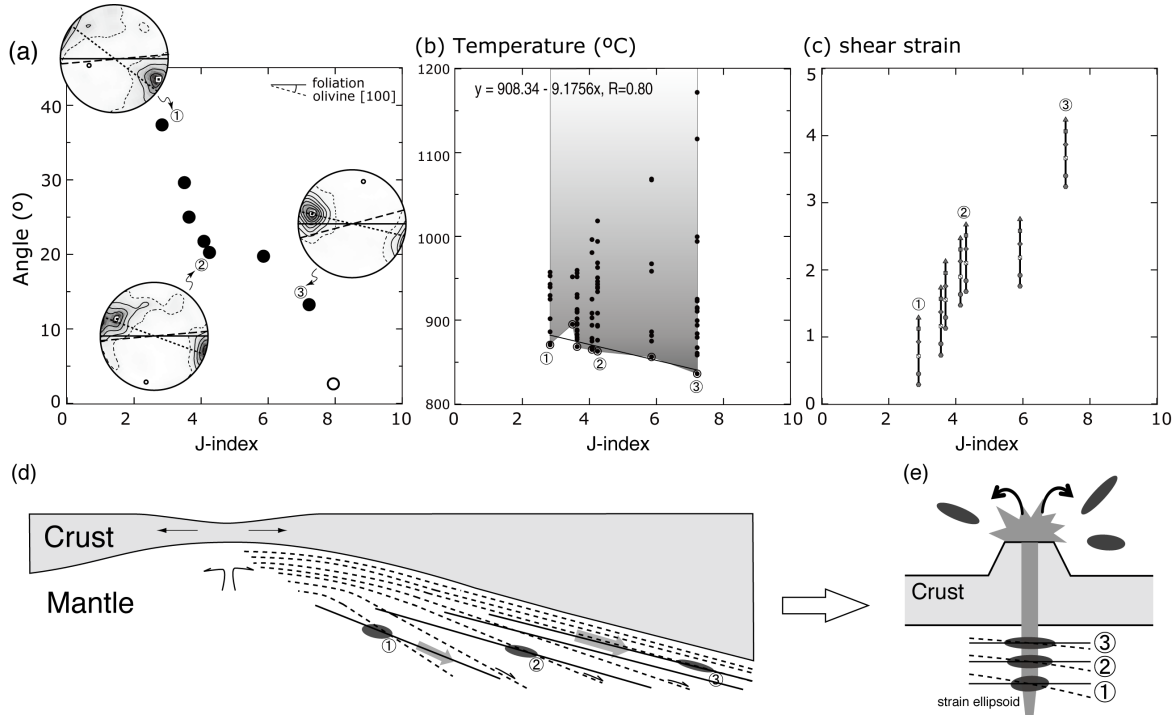

Figure 32. Schematic model of the mantle evolution beneath the Ichinomegata volcano. (a) ~ (c) show a summary of this study. (a) Angle between olivine [100] maximum and foliation decreases with increasing J-index. (b) Minimum temperature is lower in the samples that have higher J-index. (c) Shear strain increases with increasing J-index. (d) Mantle evolution during back-arc spreading based on our observations. Upper mantle peridotites in the shallower part, where a lower temperature is assumed, sheared higher than in the deeper part. At the present time, xenoliths which recorded frozen textures were erupted in the surface (e).

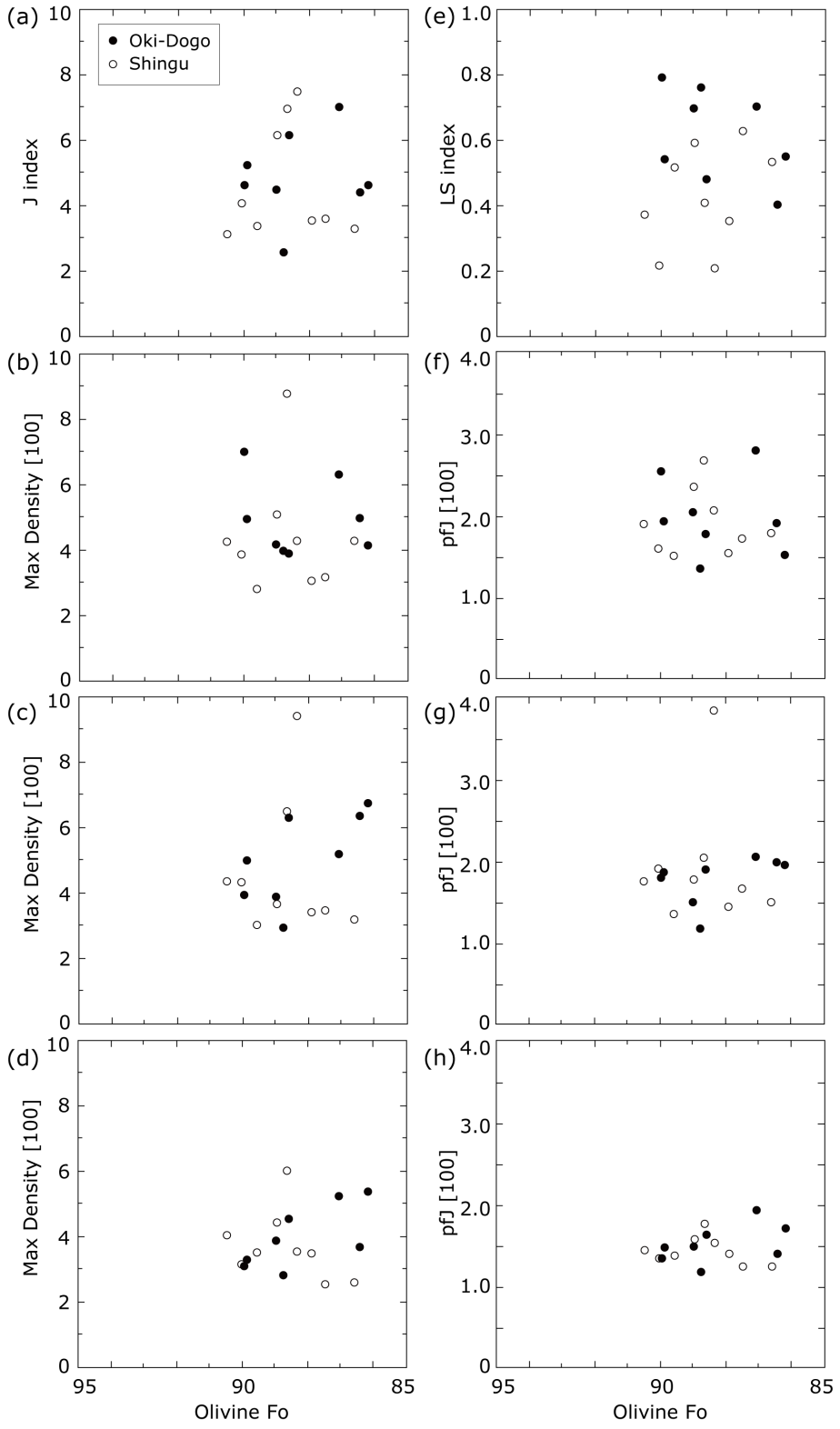

Figure 33. Evolution of olivine CPO as function of the olivine Fo (Mg#) in Oki-Dogo and Shingu peridotite xenoliths. (a) CPO strength (*J*-index). (b)–(d) Maximum density of the distribution of the [100], [010], and [001] axes of olivine. (e) Ls-index.(f)–(h) pfJ-index of the [100], [010], and [001] axes of olivine.

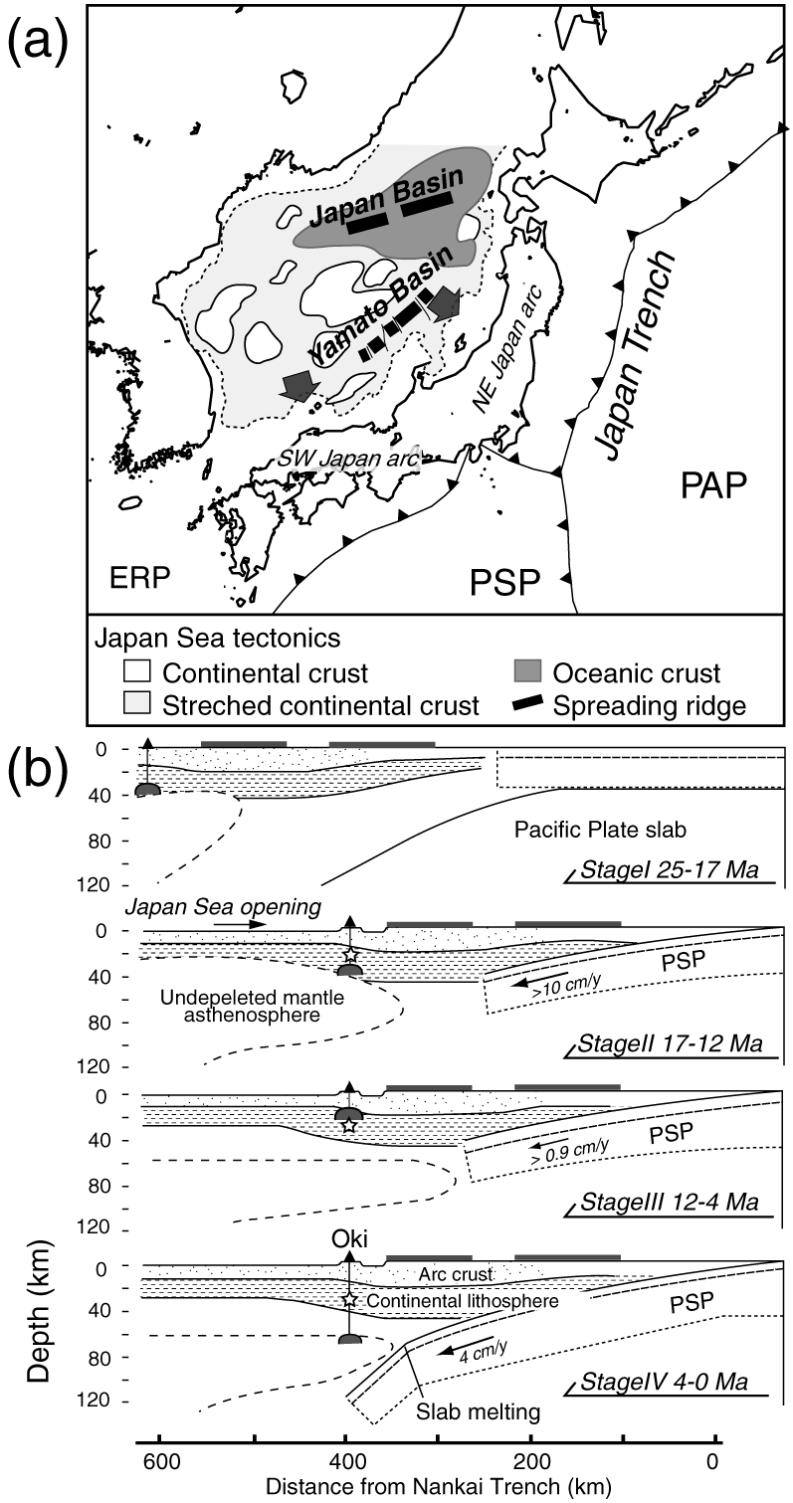

Figure 34. (a) Schematic model of the opening of the Japan Sea. (b) Evolution of the uppermost mantle beneath southwest (SW) Japan, based on petrological analyses of volcanic rocks. Star symbols indicate the inferred location of the Oki-Dogo peridotite xenoliths within the mantle. Modified after Kimura et al. (2005). PSP: Philippine Sea Plate; PAP: Pacific Plate; ERP: Eurasia Plate.

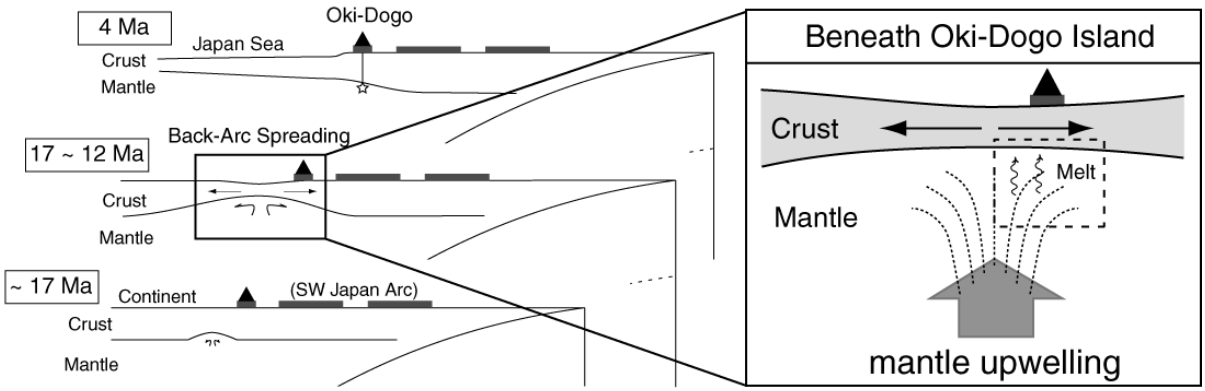

Figure 35. Schematic diagrams showing the tectonic evolution of the southwest Japan arc between ca. 17 and 4 Ma. The enlarged sketch to the right shows the evolution of the uppermost mantle during the period of back-arc spreading beneath the Japan Islands and Oki-Dogo Island. The dotted rectangle indicates the uppermost mantle domain sampled by peridotite xenoliths analysed in this study.

Table 1. Results of electron microprobe analyses of olivine and spinel within peridotite xenoliths from Ichinomegata.

	Sample number											
	I667	I702	I738	I764	I776	I777	I892	I906	I909	TSI03	TSI06	TSI07
Olivine												
SiO_2	40.08	39.93	40.03	39.98	39.71	39.92	39.31	40.24	39.59	40.16	39.96	39.75
TiO_2	0.00	0.00	0.04	0.00	0.00	0.00	0.00	0.01	0.06	0.00	0.01	0.04
Al_2O_3	0.04	0.02	0.00	0.05	0.03	0.00	0.03	0.01	0.00	0.00	0.02	0.04
FeO[a]	10.12	10.11	11.32	9.85	9.99	9.85	9.93	9.12	10.30	10.16	10.34	10.10
MnO	0.04	0.08	0.08	0.12	0.06	0.06	0.20	0.11	0.04	0.14	0.08	0.10
MgO	50.52	50.16	49.71	50.04	50.30	49.34	49.82	50.13	49.97	49.79	50.53	50.20
CaO	0.10	0.07	0.03	0.08	0.07	0.11	0.03	0.01	0.04	0.07	0.08	0.10
Na_2O	0.00	0.01	0.00	0.00	0.00	0.00	0.00	0.00	0.00	0.00	0.00	0.00
K_2O	0.00	0.00	0.00	0.01	0.00	0.00	0.01	0.00	0.01	0.00	0.00	0.02
Cr_2O_3	0.00	0.00	0.04	0.00	0.07	0.03	0.00	0.00	0.00	0.00	0.00	0.07
NiO	0.00	0.00	0.00	0.00	0.00	0.00	0.00	0.01	0.00	0.00	0.00	0.00
V_2O_3	0.00	0.00	0.00	0.00	0.00	0.00	0.00	0.42	0.00	0.00	0.00	0.00
Total	100.90	100.39	101.26	100.11	100.21	99.32	99.33	100.06	100.01	100.34	101.02	100.41
Mg#[b]	0.90	0.90	0.89	0.90	0.90	0.90	0.90	0.91	0.90	0.90	0.90	0.90
Spinel												
SiO_2	0.03	0.00	0.01	0.05	0.00	0.01	0.06	0.07	0.03	0.00	0.06	0.01
TiO_2	0.15	0.10	0.06	0.03	0.00	0.04	0.09	0.04	0.22	0.18	0.08	0.09
Al_2O_3	47.57	47.12	53.99	47.63	49.69	48.87	49.51	47.28	43.70	48.29	52.67	49.77
Fe_2O_3	5.39	3.52	4.81	3.66	2.18	3.91	3.50	3.21	4.27	4.70	2.95	2.44
FeO	10.30	9.56	10.98	9.88	9.60	10.41	9.95	10.21	11.92	10.32	8.87	9.45
FeO[a]	15.16	12.73	15.31	13.18	11.56	13.93	13.09	13.10	15.76	14.55	11.53	11.64
MnO	0.03	0.10	0.07	0.20	0.02	0.00	0.15	0.18	0.09	0.05	0.05	0.11
MgO	19.20	19.15	19.43	18.89	19.46	19.10	19.38	18.76	17.66	19.11	20.42	19.55
CaO	0.00	0.01	0.00	0.01	0.02	0.00	0.01	0.01	0.00	0.00	0.02	0.00
Na_2O	0.00	0.00	0.00	0.00	0.00	0.00	0.00	0.00	0.04	0.02	0.00	0.00
K_2O	0.02	0.00	0.00	0.02	0.00	0.00	0.01	0.00	0.00	0.00	0.00	0.01
Cr_2O_3	18.10	19.00	11.51	18.07	17.65	17.44	17.19	19.66	22.76	17.48	14.48	17.38
NiO	0.00	0.00	0.00	0.00	0.00	0.00	0.00	0.32	0.00	0.00	0.00	0.00
V_2O_3	0.00	0.00	0.00	0.00	0.00	0.00	0.00	0.08	0.00	0.00	0.00	0.00
Total	100.80	98.56	100.86	98.43	98.61	99.78	99.84	99.82	100.68	100.14	99.60	98.79
Mg#[b]	0.77	0.78	0.76	0.77	0.78	0.77	0.78	0.72	0.73	0.77	0.80	0.79
Cr#[c]	0.20	0.21	0.13	0.20	0.19	0.19	0.19	0.22	0.26	0.20	0.16	0.19

[a]total Fe; [b]$Mg/(Mg+Fe^{2+})$ atomic ratio for silicate; [c]Cr/(Cr+Al) atomic ratio; [d]total trivalent cation ($Al+Cr+Fe^{3+}$).

Table 2. Results of electron microprobe analyses of orthopyroxene and clinopyroxene within peridotite xenoliths from Ichinomegata.

	Sample number											
	I667	I702	I738	I764	I776	I777	I892	I906	I909	TSI03	TSI06	TSI07
Orthopyroxene												
SiO_2	53.88	54.43	54.78	53.77	53.24	53.76	53.69	54.68	54.46	54.06	54.40	53.83
TiO_2	0.15	0.12	0.01	0.12	0.12	0.16	0.08	0.12	0.17	0.22	0.14	0.07
Al_2O_3	3.99	3.82	3.64	3.40	3.68	4.19	3.64	3.61	3.84	3.93	3.99	3.87
FeO[a]	6.98	6.66	7.27	6.25	6.33	7.16	6.42	6.75	7.01	6.92	6.46	6.76
MnO	0.17	0.11	0.20	0.19	0.23	0.14	0.10	0.23	0.06	0.10	0.00	0.13
MgO	34.12	33.58	33.38	34.20	34.29	33.19	33.76	33.75	34.16	34.10	34.18	33.86
CaO	0.60	0.73	0.65	0.64	0.57	0.60	0.59	0.45	0.64	0.62	0.58	0.48
Na_2O	0.00	0.02	0.00	0.00	0.02	0.00	0.03	0.01	0.02	0.03	0.05	0.01
K_2O	0.03	0.00	0.00	0.00	0.02	0.01	0.00	0.00	0.01	0.02	0.01	0.02
Cr_2O_3	0.59	0.66	0.42	0.45	0.39	0.61	0.53	0.04	0.61	0.69	0.34	0.63
NiO	0.00	0.00	0.00	0.00	0.00	0.00	0.00	0.41	0.00	0.00	0.00	0.00
V_2O_3	0.00	0.00	0.00	0.00	0.00	0.00	0.00	0.08	0.00	0.00	0.00	0.00
Total	100.50	100.13	100.35	99.02	98.89	99.81	98.84	100.13	100.98	100.70	100.15	99.64
Mg#[b]	0.90	0.90	0.89	0.91	0.91	0.89	0.90	0.90	0.90	0.90	0.90	0.90
Clinoyroxene												
SiO_2	50.49	50.96	51.02	51.07	51.32	53.76	50.88	51.09	50.92	50.49	50.75	50.57
TiO_2	0.31	0.54	0.47	0.42	0.44	0.16	0.45	0.43	0.48	0.54	0.54	0.26
Al_2O_3	6.38	5.06	4.86	4.37	4.52	4.19	4.85	5.12	4.63	5.12	5.42	4.39
FeO[a]	3.71	2.51	3.05	2.64	2.37	7.16	2.24	2.34	2.74	3.08	2.71	2.79
MnO	0.14	0.00	0.06	0.09	0.05	0.14	0.04	0.13	0.09	0.05	0.05	0.00
MgO	17.40	16.83	16.24	16.80	16.44	33.19	16.13	15.44	16.36	16.31	16.58	16.71
CaO	21.09	22.56	23.13	22.83	23.65	0.60	23.07	22.82	23.41	23.14	22.37	23.36
Na_2O	0.49	0.63	0.38	0.35	0.57	0.00	0.59	0.72	0.30	0.42	0.84	0.25
K_2O	0.00	0.00	0.02	0.00	0.03	0.01	0.00	0.00	0.02	0.01	0.00	0.01
Cr_2O_3	0.77	1.09	0.95	0.81	0.99	0.61	0.95	0.07	1.07	1.17	1.21	0.68
NiO	0.00	0.00	0.00	0.00	0.00	0.00	0.00	1.07	0.00	0.00	0.00	0.00
V_2O_3	0.00	0.00	0.00	0.00	0.00	0.00	0.00	0.06	0.00	0.00	0.00	0.00
Total	100.78	100.19	100.17	99.38	100.39	99.81	99.19	99.28	100.02	100.33	100.48	99.01
Mg#[b]	0.89	0.92	0.90	0.92	0.93	0.89	0.93	0.92	0.91	0.90	0.92	0.91

[a]total Fe; [b]$Mg/(Mg+Fe^{2+})$ atomic ratio for silicate.

Table 3. Results of electron microprobe analyses of olivine and spinel within peridotite xenoliths from Olki-Dogo.

	Sample number																
	OKD 33	OKD 69	KRB 15	OKD 57	OKD 45-2	KRB 12	OKD 28	OKD 04	OKD 39	OKD0 2-2	OKD 02-1	OKD 37	OKD 07	OKD0 2-3	OKD 64	OKD 13	OKD 45-1
Olivine																	
SiO_2	40.19	39.64	39.26	39.85	39.95	40.15	40.06	39.63	39.30	39.68	39.71	39.25	40.70	39.98	39.45	40.18	40.16
TiO_2	0.00	0.01	0.03	0.00	0.00	0.00	0.01	0.00	0.00	0.00	0.03	0.03	0.01	0.00	0.00	0.00	0.01
Al_2O_3	0.02	0.03	0.04	0.03	0.04	0.01	0.03	0.03	0.05	0.04	0.02	0.03	0.03	0.03	0.04	0.02	0.03
FeO[a]	9.31	13.11	13.31	10.75	10.04	10.99	10.71	10.83	11.03	10.32	11.89	11.40	10.88	12.01	12.38	9.83	11.57
MnO	0.14	0.22	0.15	0.19	0.17	0.14	0.14	0.11	0.12	0.12	0.18	0.14	0.13	0.24	0.20	0.15	0.11
MgO	48.91	45.93	47.66	49.82	50.03	49.86	48.86	49.09	48.12	48.70	48.07	48.11	48.25	49.24	46.84	49.69	47.77
CaO	0.09	0.14	0.13	0.11	0.10	0.09	0.10	0.12	0.10	0.10	0.13	0.13	0.09	0.10	0.11	0.11	0.11
Na_2O	0.01	0.02	0.00	0.00	0.02	0.01	0.02	0.00	0.00	0.01	0.01	0.02	0.00	0.00	0.00	0.01	0.00
K_2O	0.00	0.00	0.01	0.00	0.00	0.00	0.00	0.00	0.01	0.01	0.00	0.01	0.00	0.00	0.00	0.00	0.01
Cr_2O_3	0.07	0.06	0.09	0.02	0.00	0.02	0.03	0.03	0.03	0.03	0.01	0.02	0.00	0.03	0.03	0.05	0.02
NiO	0.36	0.30	0.33	0.33	0.38	0.39	0.41	0.33	0.39	0.33	0.35	0.33	0.39	0.32	0.32	0.40	0.34
V_2O_3	0.01	0.00	0.00	0.00	0.00	0.00	0.00	0.00	0.00	0.03	0.01	0.00	0.01	0.02	0.01	0.01	0.00
Total	99.10	99.44	100.99	101.10	100.72	101.66	100.35	100.17	99.14	99.36	100.40	99.46	100.49	101.97	99.40	100.44	100.14
Mg#[b]	0.90	0.86	0.86	0.90	0.90	0.89	0.89	0.89	0.89	0.89	0.88	0.88	0.89	0.88	0.87	0.90	0.88
Spinel																	
SiO_2	0.07	0.26	0.13	0.11	0.08	0.08	0.19	0.10	0.40	0.12	0.17	0.07	0.35	0.09	0.09	0.12	0.10
TiO_2	0.02	1.37	0.29	0.13	0.26	0.35	0.12	0.13	0.61	0.10	0.19	0.73	0.09	0.26	0.37	0.22	0.43
Al_2O_3	34.84	38.16	45.17	48.41	49.58	30.42	49.49	46.30	39.57	50.64	39.96	49.03	49.11	49.01	48.99	45.47	41.24
FeO[a]	17.32	19.38	17.16	13.55	13.35	16.67	12.92	14.90	15.93	12.68	16.39	14.74	13.54	14.85	15.99	15.15	15.99
MnO	0.17	0.14	0.17	0.08	0.07	0.16	0.10	0.10	0.09	0.12	0.18	0.09	0.11	0.08	0.10	0.22	0.15
MgO	14.62	15.54	17.31	18.65	19.54	15.74	19.44	18.60	16.97	19.79	16.96	18.87	18.96	18.56	18.79	18.00	16.80
CaO	0.01	0.01	0.00	0.01	0.01	0.00	0.00	0.01	0.01	0.01	0.00	0.00	0.01	0.01	0.01	0.01	0.01
Na_2O	0.00	0.00	0.00	0.00	0.00	0.02	0.00	0.01	0.00	0.00	0.01	0.01	0.00	0.01	0.00	0.01	0.00
K_2O	0.01	0.00	0.00	0.00	0.00	0.00	0.01	0.00	0.00	0.00	0.00	0.01	0.00	0.00	0.01	0.00	0.00
Cr_2O_3	30.89	23.75	18.67	18.42	18.15	36.81	17.12	19.35	25.76	15.50	25.95	15.73	17.89	16.95	16.47	21.19	25.27
NiO	0.23	0.24	0.27	0.36	0.28	0.18	0.37	0.33	0.23	0.37	0.26	0.33	0.33	0.28	0.33	0.29	0.29
V_2O_3	0.11	0.10	0.08	0.12	0.10	0.13	0.10	0.12	0.14	0.10	0.13	0.13	0.10	0.09	0.09	0.10	0.13
Total	98.63	99.57	99.81	99.82	101.77	101.01	100.21	100.43	100.14	99.82	100.67	100.20	100.82	100.60	101.78	101.18	100.79
Mg#[b]	0.65	58.85	0.72	0.76	0.77	0.69	0.78	0.76	0.72	0.79	0.71	0.76	0.76	0.75	0.75	0.74	0.70
Cr#[c]	0.37	0.29	0.22	0.20	0.20	0.45	0.19	0.22	0.30	0.17	0.30	0.18	0.20	0.19	0.18	0.24	0.29
Fe^{3+}/Y[d]	0.04	0.07	0.06	0.03	0.04	0.05	0.04	0.05	0.05	0.04	0.05	0.05	0.03	0.04	0.05	0.04	0.04

[a]total Fe; [b]Mg/(Mg+Fe^{2+}) atomic ratio for silicate; [c]Cr/(Cr+Al) atomic ratio; [d]total trivalent cation (Al+Cr+Fe^{3+}).

Table 4. Results of electron microprobe analyses of orthopyroxene and clinopyroxene within peridotite xenoliths from Olki-Dogo.

	Sample number														
	OKD 33	KRB 15	OKD 57	OKD 45-2	KRB 12	OKD 28	OKD 04	OKD 02-2	OKD 02-1	OKD 37	OKD 07	OKD 02-3	OKD 64	OKD 13	OKD 45-1
Orthopyroxene															
SiO_2	55.85	53.44	54.05	54.33	55.63	54.29	54.29	54.44	53.35	52.74	54.54	53.87	53.17		
TiO_2	0.02	0.14	0.05	0.16	0.08	0.06	0.11	0.03	0.09	0.29	0.05	0.12	0.11		
Al_2O_3	3.18	4.52	4.44	4.62	2.81	4.56	4.39	4.49	4.18	4.94	4.52	4.72	4.55		
FeO[a]	6.17	8.30	6.51	6.42	6.58	6.62	7.06	6.73	7.87	9.31	6.93	7.47	7.90		
MnO	0.14	0.13	0.13	0.12	0.09	0.14	0.18	0.15	0.14	0.16	0.16	0.18	0.18		
MgO	32.77	30.72	32.07	32.70	33.70	32.50	32.02	32.61	31.42	30.97	31.71	31.97	31.76		
CaO	1.01	1.29	1.13	1.14	1.11	1.15	1.15	1.12	1.28	1.26	1.13	1.14	1.30		
Na_2O	0.07	0.08	0.05	0.08	0.05	0.05	0.08	0.06	0.07	0.11	0.06	0.05	0.09		
K_2O	0.00	0.00	0.01	0.01	0.01	0.00	0.00	0.01	0.00	0.00	0.01	0.00	0.00		
Cr_2O_3	0.75	0.59	0.65	0.59	0.75	0.55	0.57	0.51	0.68	0.44	0.62	0.53	0.56		
NiO	0.12	0.09	0.15	0.12	0.12	0.07	0.08	0.13	0.09	0.05	0.13	0.07	0.13		
V_2O_3	0.01	0.03	0.02	0.05	0.01	0.02	0.01	0.00	0.02	0.01	0.04	0.01	0.04		
Total	100.08	99.33	99.25	100.33	100.93	100.01	99.95	100.28	99.19	100.27	99.89	100.13	99.78		
Mg#[b]	0.90	0.87	0.90	0.90	0.90	0.90	0.89	0.90	0.88	0.86	0.89	0.88	0.88		
Clinopyroxene															
SiO_2	52.51	51.13	51.93	51.59	52.74	51.71	52.14	50.38	52.00	50.91	52.54	52.26	52.06	51.09	51.59
TiO_2	0.07	0.37	0.19	0.48	0.24	0.44	0.28	1.08	0.16	1.00	0.14	0.34	0.28	0.29	0.51
Al_2O_3	3.75	5.87	5.34	5.57	3.61	5.75	5.52	6.06	4.67	6.18	5.13	5.78	5.81	4.73	5.10
FeO[a]	2.94	4.31	3.35	3.43	2.93	3.39	3.69	3.48	3.81	3.67	3.47	4.05	4.10	3.21	3.72
MnO	0.08	0.10	0.11	0.12	0.09	0.13	0.12	0.09	0.13	0.09	0.12	0.10	0.06	0.15	0.12
MgO	17.04	16.24	16.85	16.45	17.65	16.63	16.56	16.84	16.72	16.06	16.41	16.65	16.31	17.07	16.53
CaO	21.55	19.78	21.03	20.96	20.77	20.55	20.74	20.83	20.85	19.79	20.96	20.16	20.52	21.27	19.90
Na_2O	0.69	1.04	0.56	0.81	0.78	0.77	0.90	0.43	0.71	1.09	0.57	0.79	0.95	0.56	1.02
K_2O	0.00	0.02	0.00	0.00	0.00	0.00	0.00	0.00	0.01	0.00	0.00	0.00	0.00	0.01	0.01
Cr_2O_3	1.13	0.07	0.84	0.87	1.16	0.84	0.88	0.81	0.05	1.19	0.80	0.88	0.86	1.06	1.24
NiO	0.08	0.02	0.07	0.05	0.09	0.07	0.07	0.11	0.04	0.00	0.06	0.08	0.04	0.07	0.06
V_2O_3	0.02	1.08	0.00	0.02	0.04	0.00	0.23	0.03	1.06	0.02	0.03	0.04	0.06	0.02	0.02
Total	99.87	100.01	100.28	100.36	100.11	100.28	100.92	100.13	100.20	100.01	100.25	101.12	101.06	99.51	99.82
Mg#[b]	0.91	0.87	0.90	0.90	0.91	0.90	0.89	0.90	0.89	0.89	0.89	0.88	0.88	0.90	0.89

[a]total Fe; [b]$Mg/(Mg+Fe^{2+})$ atomic ratio for silicate.

Table 5. Calculated equilibrium temperatures (°C) of peridotite xenoliths from Ichinomegata volcano.

Geothermometer	Brey&Köhler (1990) Ca in opx
Pressure (GPa)	1.0
Sample number	
I667	911
I702	954
I708	883
I738	927
I764	927
I777	913
I892	910
I906	942
I909	925
TSI03	918
TSI06	904
TSI07	867

Table 6. Calculated equilibrium temperatures (°C) of peridotite xenoliths from Oki-Dogo.

Geothermometer	N&T[a]	B&K[b]	B&K[b]
	cpx	2px[c]	opx
Pressure (GPa)	0.8	0.8	0.8
Sample number			
OKD33	1044	1040	1021
OKD69	-	-	-
KRB15	1117	1109	1091
OKD57	1096	1089	1054
KRB12	1101	1096	1051
OKD45-2	1070	1083	1043
OKD28	1105	1109	1056
OKD04	1095	1094	1057
OKD02-2	1080	1100	-
OKD37	1101	1096	1048
OKD39	-	-	1089
OKD07	1102	1088	1083
OKD64	1099	1094	1050
OKD02-3	1134	1127	1053
OKD02-1	1088	1072	1092
OKD13	1074	1070	1046
OKD45-1	1113	-	-

[a]Nims and Taylor (2000); [b] Brey and Köhler (1990).

Table 7. Trace element concentrations in olivine and orthopyroxene mineral separates in samples of Ichinomegata peridotite xenoliths.

Sample	I702	I764	I776	I892	I906	I909	TSI03	TSI06	TSI07
Clinopyroxene									
Ti	3011.135	2447.637	2749.193	2833.410	3288.353	3118.050	3104.857	3083.603	2365.198
Rb	0.004	0.005	0.007	0.011	0.006	0.019	0.006	0.005	0.003
Sr	2.183	2.423	0.836	0.812	1.354	2.861	3.261	3.876	2.462
Y	19.968	15.410	20.210	19.970	23.127	17.643	20.147	21.693	12.538
Zr	11.418	8.077	8.183	6.855	13.040	11.493	10.680	8.993	5.792
Nb	0.017	0.011	0.014	0.012	0.014	0.010	0.011	0.014	0.010
Ba						0.022		0.028	0.006
La	0.104	0.028	0.023	0.008	0.041	0.087	0.254	0.258	0.073
Ce	0.679	0.416	0.286	0.208	0.580	0.883	0.797	0.415	0.199
Pr	0.241	0.168	0.152	0.126	0.255	0.297	0.229	0.198	0.084
Nd	2.169	1.560	1.638	1.442	2.488	2.449	2.033	2.104	0.973
Sm	1.370	0.991	1.222	1.178	1.596	1.314	1.344	1.470	0.783
Eu	0.528	0.406	0.490	0.456	0.603	0.504	0.513	0.554	0.289
Gd	2.482	1.828	2.391	2.328	2.941	2.234	2.505	2.730	1.574
Tb	0.495	0.371	0.488	0.494	0.582	0.438	0.508	0.554	0.324
Dy	3.660	2.767	3.627	3.655	4.287	3.220	3.743	4.050	2.400
Ho	0.808	0.618	0.811	0.832	0.938	0.706	0.841	0.900	0.537
Er	2.247	1.759	2.280	2.351	2.599	1.971	2.326	2.472	1.489
Tm	0.328	0.261	0.329	0.346	0.372	0.287	0.342	0.368	0.215
Yb	2.063	1.678	2.061	2.149	2.305	1.830	2.124	2.264	1.320
Lu	0.288	0.241	0.290	0.311	0.321	0.258	0.303	0.322	0.185
Hf	0.776	0.529	0.572	0.539	0.740	0.578	0.715	0.632	0.494
Ta	0.001		0.001	0.000	0.001	0.000	0.001	0.000	
Pb	0.075	0.145	0.025	0.045	0.060	0.088	0.038	0.188	0.037
Th	0.022	0.001	0.003	0.044	0.008	0.002	0.042	0.829	0.010
U	0.008	0.001	0.001	0.020	0.003	0.001	0.012	0.239	
Orthopyroxene									
Ti	813.755	730.980	807.237	776.017	969.973	948.125	894.610	989.597	990.090
Rb	0.003		0.002					0.002	0.002
Sr	0.050	0.058	0.026	0.000	0.025	0.054	0.073	0.037	0.070
Y	0.968	0.821	1.188	0.910	1.302	1.211	1.186	1.515	1.429
Zr	0.713	0.510	0.589	0.423	0.888	0.839	0.775	0.777	0.744
Nb	0.006	0.006	0.007	0.006	0.006	0.006	0.006	0.006	0.007
Ba	0.007		0.002						0.001
La	0.001		0.001	0.000		0.002	0.005	0.006	0.001
Ce	0.005	0.004	0.003	0.005	0.004	0.013	0.014	0.006	0.006
Pr	0.002	0.001	0.001	0.001	0.001	0.004	0.003	0.002	0.002
Nd	0.016	0.017	0.015	0.008	0.016	0.031	0.023	0.020	0.029
Sm	0.014	0.012	0.013	0.010	0.015	0.022	0.016	0.020	0.023
Eu	0.007	0.006	0.008	0.006	0.010	0.011	0.009	0.011	0.013
Gd	0.038	0.033	0.045	0.036	0.047	0.056	0.050	0.060	0.072
Tb	0.012	0.010	0.013	0.011	0.015	0.015	0.015	0.019	0.020
Dy	0.121	0.103	0.145	0.119	0.162	0.158	0.150	0.194	0.197
Ho	0.036	0.032	0.046	0.037	0.050	0.047	0.047	0.061	0.060
Er	0.152	0.128	0.188	0.149	0.196	0.184	0.193	0.242	0.221
Tm	0.032	0.027	0.038	0.032	0.042	0.037	0.040	0.050	0.047
Yb	0.309	0.260	0.354	0.290	0.366	0.320	0.365	0.435	0.394
Lu	0.056	0.051	0.066	0.058	0.069	0.059	0.071	0.081	0.075
Hf	0.060	0.044	0.052	0.039	0.067	0.059	0.066	0.070	0.071
Ta			0.000						
Pb	0.075	0.148	0.044	0.054	0.024	0.032	0.025	0.029	0.014
Th	0.004	0.000	0.001	0.009	0.001		0.008	0.112	0.000
U	0.000		0.000	0.004		0.000	0.001	0.009	0.001

Table 7. *(Continued)*

Sample	I702	I764	I776	I892	I906	I909	TSI03	TSI06	TSI07
Olivine									
Ti	6.640	7.833	6.903	7.242	2.088	12.967	10.200	4.156	9.027
Rb	0.000								
Sr	0.000								
Y	0.036	0.036	0.022	0.022	0.007	0.010	0.030	0.023	0.036
Zr	0.005	0.022	0.002	0.012		0.004	0.007	0.033	0.003
Nb	0.000						0.000		
Ba	0.000								
La	0.000						0.000		
Ce	0.000				0.002		0.001		
Pr	0.000								
Nd	0.000								
Sm	0.000		0.000						
Eu	0.000						0.000		
Gd	0.000						0.002	0.001	
Tb	0.000	0.000		0.000			0.000		0.000
Dy	0.004	0.004	0.002	0.002			0.003	0.002	0.002
Ho	0.001	0.001	0.001	0.001	0.000	0.000	0.001	0.001	0.001
Er	0.006	0.006	0.003	0.004	0.001	0.001	0.005	0.003	0.006
Tm	0.002	0.002	0.001	0.001	0.001	0.001	0.002	0.001	0.002
Yb	0.017	0.015	0.013	0.013	0.006	0.008	0.017	0.012	0.018
Lu	0.004	0.004	0.003	0.004	0.002	0.002	0.005	0.003	0.005
Hf	0.000						0.005		
Ta	0.000								0.000
Pb	0.079	0.436	0.085	0.061	0.037	0.091	0.034	0.145	0.033
Th	0.000							0.002	
U	0.000			0.000			0.000	0.010	

Table 8. Trace element concentrations in olivine and orthopyroxene mineral separates in samples of Ichinomegata peridotite xenoliths.

Sample	KRB15	OKD04	OKD45-2	OKD57	OKD64	OKD69
Clinopyroxene						
Ti	2844.120	1005.617	3122.057	1157.693	2877.410	7460.133
Rb	0.004	0.023	0.004	0.003	0.004	0.033
Sr	67.310	37.330	133.207	42.617	71.420	124.845
Y	10.180	8.537	14.127	9.327	11.990	24.708
Zr	16.620	2.422	129.050	3.737	13.380	72.533
Nb	0.610	0.373	1.543	0.758	0.467	0.444
Ba	0.083	0.251	0.080	0.109	0.042	0.057
La	2.374	1.176	12.140	2.026	2.298	4.400
Ce	6.710	3.005	26.410	4.510	7.465	15.768
Pr	1.023	0.384	3.133	0.510	1.216	2.848
Nd	5.185	1.587	12.363	1.967	6.170	16.158
Sm	1.599	0.490	2.463	0.534	1.789	5.315
Eu	0.595	0.211	0.852	0.230	0.694	1.940
Gd	1.928	0.888	2.483	0.952	2.083	6.238
Tb	0.331	0.198	0.411	0.207	0.364	0.961
Dy	2.151	1.570	2.706	1.674	2.463	5.658
Ho	0.442	0.366	0.556	0.391	0.511	1.055
Er	1.163	1.078	1.533	1.139	1.384	2.497
Tm	0.167	0.166	0.222	0.174	0.199	0.325
Yb	1.061	1.063	1.406	1.127	1.271	1.836
Lu	0.149	0.152	0.201	0.165	0.176	0.243
Hf	0.611	0.088	3.330	0.087	0.198	3.055
Ta	0.070	0.030	0.238	0.098	0.067	0.135
Pb	0.072	0.022	0.147	0.027	0.075	0.107
Th	0.097	0.052	0.821	0.132	0.073	0.148
U	0.019	0.012	0.130	0.028	0.016	0.033
Orthopyroxene						
Ti	838.150	381.935	919.673	409.703	975.645	1596.440
Rb						0.003
Sr	0.432	0.145	0.513	0.181	0.364	0.627
Y	1.121	1.003	1.355	1.049	1.325	2.012
Zr	1.678	0.279	13.323	0.444	1.517	4.115
Nb	0.048	0.030	0.096	0.064	0.041	0.027
Ba						0.003
La	0.013	0.004	0.043	0.008	0.010	0.017
Ce	0.055	0.017	0.158	0.030	0.051	0.094
Pr	0.011	0.003	0.027	0.005	0.012	0.023
Nd	0.074	0.016	0.139	0.025	0.083	0.177
Sm	0.038	0.012	0.048	0.012	0.043	0.110
Eu	0.019	0.006	0.022	0.008	0.021	0.049
Gd	0.076	0.035	0.080	0.037	0.083	0.196
Tb	0.019	0.012	0.021	0.012	0.021	0.044
Dy	0.166	0.129	0.178	0.128	0.190	0.334
Ho	0.044	0.039	0.052	0.040	0.051	0.082
Er	0.155	0.155	0.181	0.158	0.181	0.256
Tm	0.029	0.030	0.036	0.031	0.034	0.044

Table 8. *(Continued)*

Sample	KRB15	OKD04	OKD45-2	OKD57	OKD64	OKD69
Yb	0.238	0.246	0.312	0.273	0.273	0.325
Lu	0.041	0.046	0.055	0.049	0.048	0.054
Hf	0.060	0.013	0.323	0.009	0.037	0.155
Ta	0.003	0.001	0.007	0.004	0.003	0.002
Pb	0.047	0.011	0.034	0.009	0.053	0.005
Th	0.001	0.000	0.007	0.003	0.001	0.001
U	0.001	0.000	0.004	0.001	0.001	0.001
Olivine						
Ti	36.250	15.097	36.445	17.160	31.097	92.520
Rb						0.049
Sr	0.016	0.019				0.919
Y	0.047	0.037	0.045	0.038	0.051	0.115
Zr	0.023	0.007	0.177	0.008	0.016	0.708
Nb	0.001	0.001	0.003	0.002	0.002	0.063
Ba						0.122
La						0.009
Ce		0.000	0.000		0.000	0.029
Pr				0.000		0.001
Nd			0.000		0.001	0.005
Sm						0.001
Eu						0.000
Gd			0.001		0.001	0.003
Tb	0.000	0.000	0.000		0.000	0.001
Dy	0.004	0.003	0.004	0.003	0.005	0.013
Ho	0.002	0.001	0.002	0.001	0.002	0.004
Er	0.008	0.006	0.007	0.007	0.009	0.016
Tm	0.002	0.002	0.002	0.002	0.002	0.003
Yb	0.019	0.017	0.023	0.021	0.022	0.031
Lu	0.005	0.005	0.005	0.004	0.005	0.008
Hf			0.002			0.015
Ta			0.000			0.004
Pb	0.058	0.003	0.187	0.015	0.018	0.048
Th						0.006
U						0.006

Table 9. Water contents of olivines and pyroxenes in samples of Ichinomegata and Oki-Dogo peridotite xenoliths.

	sample#	water content [ppm] (number of measurements)			
		olivine	orthopyroxene	clinopyroxene	bulk
Ichinomegata	I-892	4 (10)	175 (3)	298 (3)	68
	TSI06	7 (8)	271 (4)	292 (3)	134
	I-906	5 (7)	75 (4)	347 (6)	60
	I-702	4 (7)	155 (3)	304 (3)	70
	TSI03	2 (3)	137 (7)	208 (7)	46
Oki-Dogo	OKD64	6 (3)	6 (2)	8 (2)	6
	KRB15	2 (10)	35 (6)	30 (4)	10
	OKD45-2	2 (3)	17 (4)	10 (2)	5
	OKD04	4 (7)	-	98 (2)	7
	OKD69	4 (4)	-	-	4

Table 10. Characteristics of crystallographic preferred orientations in Ichinomegata peridotite xenoliths.

sample#	N	J	M	MD			pfJ		
				[100]	[010]	[001]	[100]	[010]	[001]
Ichinomegata									
I-667	635	4.08	0.17	5.08	3.15	3.70	1.89	1.34	1.56
I-702	417	3.51	0.15	5.28	2.69	2.79	1.84	1.30	1.29
I-708	525	7.94	0.48	8.87	4.17	3.01	3.89	2.18	1.58
I-738	527	5.88		6.62	4.20	3.65	2.73	1.91	1.51
I-764	391	4.26	0.23	5.58	3.99	3.39	2.24	1.43	1.42
I-777	117	4.43		3.79	3.86	3.74	1.50	1.52	1.36
I-892	330	5.78		6.90	4.09	4.35	2.45	1.64	1.66
I-906	691	7.22	0.49	8.68	6.01	4.71	3.13	2.35	1.83
I-909	698	5.86	0.37	7.13	4.56	3.44	2.83	1.89	1.48
TSI03	676	3.64	0.19	4.69	3.26	2.52	1.83	1.51	1.23
TSI06	713	2.83	0.11	4.75	3.46	2.15	1.67	1.30	1.19
TSI07	380	4.10		6.71	3.35	2.66	2.13	1.43	1.31
Oki-Dogo									
OKD04	316	4.48	0.22	4.20	3.88	3.90	2.06	1.49	1.49
OKD07	271	2.56	0.21	4.00	2.95	2.84	1.37	1.17	1.18
OKD39	140	6.14	0.10	3.93	6.31	4.57	1.79	1.89	1.63
OKD45-2	226	5.23	0.18	4.98	5.00	3.30	1.95	1.86	1.48
OKD57	582	4.62	0.19	7.02	3.94	3.10	2.56	1.79	1.35
OKD64	226	6.99	0.22	6.33	5.19	5.24	2.81	2.05	1.93
OKD69	648	4.60	0.08	4.17	6.76	5.39	1.53	1.95	1.71
KRB15	254	4.39	0.13	5.00	6.37	3.70	1.92	1.98	1.40

N: Number of measurements; J: *J*-index; M: M-index; MD: Max density; pfJ: pfJ-index

Chapter 3

Seismic anisotropy of the uppermost mantle beneath the back-arc region of Japan Sea: Evidence from Ichinomegata and Oki-Dogo peridotite xenoliths

Abstract

A dense network of seismic stations has been deployed across the northeast Japan arc to investigate mantle wedge structures. To obtain independent petrophysical constraints, we determined the seismic properties of peridotite xenoliths from Ichinomegata and Oki-Dogo in the back-arc region, which were brought to the surface from the mantle lithosphere by volcanic eruptions. We calculated the seismic properties of the xenoliths from olivine and pyroxene crystallographic preferred orientations (CPOs), and single crystal elastic constants. The small magnitude of measured S-wave splitting (delay time of 0.22 s in the area where the xenoliths were entrained) beneath Ichinomegata can be explained by the average seismic properties of mantle xenoliths for an approximately 20-km thick horizontal anisotropic layer, indicating that the mantle lithosphere could be the dominant source of seismic anisotropy. To constrain the effects of metasomatism on the seismic anisotropy, we calculated the seismic properties of Oki-Dogo peridotites, which have been affected by Fe enrichment with lower Mg# (=Mg/Mg+Fe) of olivine than that of typical residual peridotites of the upper mantle. CPO and seismic anisotropy are little affected by the percolation of melts, even though reactions change their composition. Our results revealed systematic across-arc variations in both fast directions and delay times, with implications for the different anisotropic structures between the northern and the southern parts of back-arc region of Japan Sea.

Key words: peridotite xenoliths; Ichinomegata; Oki-Dogo Island; Fe-enrichment metasomatism; seismic anisotropy

3-1. Introduction

Measurements of shear-wave splitting play a crucial role in imaging flow patterns within mantle wedges (e.g., Nakajima and Hasegawa, 2004; Audoine et al., 2004); however, observed shear-wave splitting from earthquakes of intermediate depth may be affected by anisotropy in the mantle wedge, the crust, and the slab. If shear-wave splitting occurs due to mineral CPOs, it is necessary to understand the amount of strain in the mantle wedge and the elastic coefficients of minerals to evaluate the delay time along ray paths.

Shear-wave polarization anisotropy has been systematically investigated in the mantle wedge of the northeast Japan arc; fast directions in the back-arc side are oriented nearly E-W, whereas fast directions in the fore-arc side are oriented approximately N-S (Nakajima and Hasegawa, 2004). Seismic anisotropy observations from the back-arc side of the northeast Japan arc are generally interpreted in terms of the CPO of mantle minerals related to present-day mantle process such as mantle wedge convection and plate motion (Nakajima and Hasegawa, 2004; Ishise and Oda, 2005). Here, we report on a study of peridotite xenoliths from the uppermost mantle lithosphere entrained by the Ichinomegata Volcano in the back-arc region of northeast Japan.

In southwest Japan, a large low velocity zone is observed from seismic tomography images (Nakajima and Hasegawa, 2007), which is suggested to be a zone of interaction between melts and rocks. Tommasi et al. (2004) investigated seismic anisotropy in peridotite xenoliths from French Polynesia, and shows that increasing interaction with plume-related melts results in significant Fe-enrichment of the peridotites, but does not modify seismic anisotropy. Lee (2003) proposed that thermal anomaly and Fe-enrichment of olivine would produce a negative seismic anomaly. In

this chapter, we calculated the seismic properties of Oki-Dogo peridotite xenoliths to constrain the relationships between seismic anisotropy and melt-rock interaction preserved in peridotite xenoliths in the back-arc region.

3-2. Geological setting and samples

The studied samples are eight peridotite xenoliths from the Ichinomegata volcano and eight peridotite xenoliths from the Oki-Dogo Island, located in the Japan Sea (Fig. 1). The detailed microstructural study of these peridotites is presented in Chapter 2.

The depth of the Moho beneath the Ichinomegata volcano is approximately 28 km near the coast of the Japan Sea (Zhao et al., 1990), while the temperature of the Moho is thought to be about 850ºC (Kushiro, 1987). The depth of the Moho becomes deeper, up to 38 km in depth, toward the northeast Japan arc (Zhao et al., 1990), where temperatures are 950 to 1000ºC (Kushiro, 1987). The peridotite xenoliths analyzed in the present study came from relatively shallow levels in the mantle, i.e., 30 to 40 km depth, at equilibrium temperatures in the range 850 to 1000ºC (Takahashi, 1986).

The origin of Oki-Dogo peridotites was estimated by Yamamoto et al. (2007). They show that the equilibrium pressure of mafic and ultramafic xenoliths from Oki-Dogo Island, based on the pressure of CO_2 fluid inclusions preserved in minerals, gives a depth of 25–29 km for lherzolites, just below the Moho. The chemical composition of Oki-Dogo peridotites shows that they were affected by various degree of metasomatism by melt, which might be related to back-arc spreading (Chapter 2).

Olivine CPO obtained with the SEM-EBSD facility at Géosciences Montpellier, France, are presented in Chapter 2. The details of results of CPOs are

shown in Figs. 2 and 3 in the present chapter. For calculating the average seismic anisotropy, the CPO data for each sample were adjusted to an external reference frame in which the maximum Vp is parallel to the reference direction X, and the minimum Vp is parallel to the Z-axis, following the procedure presented in Satsukawa et al. (2011).

3-3. Rock seismic properties

Seismic properties of each sample were computed by averaging individual grain elastic-constant tensors as a function of the CPO and modal composition. This method enables the calculation of the three-dimensional distribution of seismic velocities in an anisotropic polycrystalline aggregate (Mainprice and Humbert, 1994). In the present calculations, we used Voigt–Reuss–Hill averaging of single-crystal elastic constants at ambient conditions (Abramson et al., 1997; Chai et al., 1997; Collins and Brown, 1998).

Since the olivine Mg# varies from 86 to 90 in Oki-Dogo samples, we calculated the olivine density and its elastic constants to constrain the effect of the compositional changes induced by melt-rock interactions on the seismic properties. By using the method reported in Tommasi et al. (2004), i.e., by taking into account the dependence of olivine single crystal elastic constants and density of olivine on its composition (Bass, 1995), these factors are calculated as follows:

Density: -10.977 × Ol Mg# (0~100) + 4329.1

C_{11}: 0.0061 × Fo + 2.6589

C_{22}: 0.0032 × Fo + 1.6795

C_{33}: 0.0003 × Fo + 2.3193

C_{44}: 0.0035 × Fo + 0.3203

C_{55}: 0.0034 × Fo + 0.4643

C_{66}: 0.0024 × Fo + 0.5699

C_{12}: -0.0028 × Fo + 0.9374

C_{13}: -0.0023 × Fo + 0.9200

C_{23}: -0.0017 × Fo + 0.9219

Figure 4 shows the calculated density as a function of the forsterite content of olivine in each sample compared with the French Polynesia xenoliths (Tommasi et al., 2004).

Based on the geothermobarometric analysis, we calculated the seismic properties assuming conditions of 900°C and 1.0 GPa for Ichinomegata peridotites (Fig. 5 and Table 1), and 1000 °C and 0.8 GPa for Oki-Dogo peridotites (Fig. 6 and Table 1). This method has been described in detail in various previous papers (e.g., Pera et al., 2003; Tasaka et al., 2008).

Combining the CPO data from each of the eight xenoliths, the CPO of an average sample was obtained, with the same weighting applied to each measurement, regardless of the number of measurements acquired from each xenoliths (Fig. 7a, c).

The olivine CPO of Ichinomegata average sample shows a-axis fiber patterns characterized by a strong concentration in [100], with a weak girdle of [010] and [001]. For orthopyroxene, CPO data may indicate (100)[001] slip. In contrast, clinopyroxene CPO data suggest a nearly random fabric, with a weak concentration in [001] parallel to the foliation (Fig. 7a). Olivine CPO of Oki-Dogo average sample shows a-axis fiber patterns characterized by a strong concentration in [100], with a weak point maximum of [010] and weak girdle of [001]. For orthopyroxene, CPO data may indicate (100)[001] slip. In contrast, clinopyroxene CPO data suggest a nearly random fabric, with a weak concentration in [001] parallel the foliation (Fig. 7c).

On average, olivine aggregates show the fastest P-wave propagation parallel

to the highest density of [100], and the slowest parallel to the highest density of [010]; polarization anisotropies are highest in directions approximately normal to the highest density of [010]. The orientation of the polarization plane of the fastest S-wave (Vs_1) indicates the orientation of the great circle containing the [100] maximum.

For Ichinomegata samples, Vp of the olivine aggregate ranges from 7.59 to 8.49 km/s; Vp anisotropy is 11.2% and AVs_{max} is 7.85%. For orthopyroxene, the average anisotropies are small: Vp ranges between 7.60 and 7.72 km/s, Vp anisotropy is 1.5%, and AVs_{max} is 1.82%. Although clinopyroxene has weaker CPOs and smaller amount of measured values than orthopyroxene, its seismic anisotropy is larger: Vp ranges between 8.25 and 8.56 km/s, Vp anisotropy is 3.6%, and AVs_{max} is 1.64% (Fig. 7b).

Vp calculated for the olivine component of Oki-Dogo samples ranges from 7.56 to 8.35 km/s; Vp anisotropy is 9.7% and AVs_{max} is 6.96%. For orthopyroxene, the average anisotropies are small: Vp ranges between 7.52 and 7.74 km/s, Vp anisotropy is 2.9%, and AVs_{max} is 3.24%. Although clinopyroxene has weaker CPOs and smaller amount of measured values than orthopyroxene, its seismic anisotropy is larger: Vp range between 8.29 and 8.43 km/s, Vp anisotropy is 1.7%, and AVs_{max} is 2.26% (Fig. 7d).

Based on the modal composition of peridotites, we recalculated the seismic properties for the mean compositions of Ichinomegata lherzolites ($Ol_{70}Opx_{16}Cpx_{14}$; Fig. 8a), and Oki-Dogo lherzolites ($Ol_{84}Opx_9Cpx_8$; Fig. 8b). Using this approach, P-wave propagation is, as expected because olivine is the dominant phase, fastest parallel to the highest density of [100] and slowest parallel to the highest density of [010], and polarization anisotropies are highest at directions approximately normal to the highest density of [010]. Vp/Vs_1 and Vp/Vs_2 ratios are highest for propagation

directions that are normal and parallel, respectively, to the highest density of [100] of olivine. Although these anisotropy patterns do not change significantly as the olivine volume fraction decreases, P- and S-wave velocities and anisotropies decrease.

We have calculated variations in seismic properties as a function of modal composition for the structural planes XY for horizontal shear, XZ for lateral shear, and YZ for vertical shear (Fig. 9 and 10). In these Figures, gray shaded squares represent the ranges of modal compositions of the peridotite xenoliths studied herein. To estimate the effect of modal composition on seismic properties, we varied the mineral composition from 100% olivine to 50% olivine + 50% pyroxene, by stepwise additions of 10% orthopyroxene or clinopyroxene. We have extrapolated variations in Vp anisotropy, the maximum Vs anisotropy (Figs. 9a, 10a), Vp (Figs. 9b, 10b), the anisotropy of Vs (Figs. 9c, 10c), the average of Vp (Figs. 9d, 10d), the deviation of Vp (Figs. 9e, 10e), and Vp/Vs (Figs. 9f, 10f) with respect to the olivine volume fraction, assuming that the propagation direction of seismic wave is vertical. As a result, the effect of the second most abundant phase on seismic properties is highly dependent on structural orientation. Vp anisotropy decreases as the volume fraction of orthopyroxene increases (Figs. 9a, 10a), whereas average Vp, unlike other factors, increases with the addition of clinopyroxene (i.e., decreasing olivine abundance; Figs. 9b, d and 10b, d). Vp/Vs does not differ significantly as a function of modal olivine abundance.

3-4. Interpretation and discussion

Although the original orientations of the Ichinomegata peridotite xenoliths were lost during their volcanic transport to the surface, we are able to derive quantitative constraints on the intrinsic anisotropy within the lithospheric mantle.

If the structures within the uppermost mantle lithosphere beneath the Ichinomegata volcano were randomly oriented, the peridotite xenoliths analyzed in the current study would make no contribution to the observed shear-wave splitting. However, it is likely that regional-scale structures within the uppermost mantle lithosphere are oriented horizontally, as described in Chapter 2. The thickness (T) of an anisotropic layer is given by $T = (100dtVs_{mean})/AVs$, where dt is the delay time of S-waves, Vs_{mean} is the average velocity of the fast and slow velocities, and AVs is the anisotropy for a specific propagation direction expressed as a percentage (e.g., Pera et al., 2004). Accordingly, the observed delay times (e.g., 0.22 s at Oga Peninsula where the Ichinomegata Volcano is located) can be explained by the seismic properties of our average peridotite xenolith for an approximately 20-km thick anisotropic layer with a horizontal foliation. It is noted that the bulk anisotropy should be less than that in each individual sample due to destructive interferences (e.g., Ben Ismaïl and Mainprice, 2001), so that it might be necessary to have a thicker anisotropic layer.

S-wave seismograms of intermediate-depth earthquakes show small delay times but regionally coherent polarizations, where the E-W fast anisotropy occurs from the back-arc region to the volcanic front above the low velocity zones (Nakajima and Hasegawa, 2004). Although low velocity zones are commonly attributed to partially melted mantle (e.g., Kushiro, 1987), the propagation of a partial-melting front across the lithosphere would not erase the pre-existing CPO and related seismic anisotropy, even if it does modify the microstructure (Vauchez and Garrido, 2001). Consequently, mantle lithosphere in the back-arc region is possibly one of the dominant sources of seismic anisotropy, which is presently commonly attributed to corner flow.

Oki-Dogo peridotite xenoliths modified by melt percolation demonstrate the

possible occurrence of an anisotropic layer in the uppermost mantle lithosphere that might be related to 'frozen' deformation during back-arc spreading along the southwest Japan arc. To constrain the effect of the compositional changes induced by melt-rock interactions on the seismic properties, analysis of P- and S-waves velocities as a function of the olivine forsterite content in each sample shows that S-waves velocities decrease with Fe-enrichment in olivine (Fig. 11a). However, P-waves velocities are not sensitive to the olivine forsterite content (Fig. 11b). Figure 11(c, d) shows the P- and S-waves anisotropy as a function of the olivine forsterite content in each sample. Lherzolite which have low Mg# have relatively high anisotropy for S-wave, particularly (Fig. 11d). Since Oki-Dogo samples do not display any macroscopic structure (e.g., foliation defined by compositional layering), seismic anisotropy may only be related to flow in the uppermost mantle by assuming that olivine [100] and [010] axes alignment, respectively. Overall, CPO and seismic anisotropy are little affected by the percolation of melts, even though reactions change their composition. The Fe enrichment results in an increase in density and decrease in S-wave velocity, however, P-wave and S-wave anisotropies do not show significant changes. This anisotropy could be one of the dominant sources in explaining the observed delay times of shear-wave velocity in this region.

Our results reveal systematic across-arc variations in seismic anisotropy, with implications for the difference in anisotropic structures between the northern and the southern parts of back-arc region of Japan Sea.

Figure 1. Locality map of mantle xenoliths from the Japan arcs. Shown are selected localities of mantle xenoliths in the southwest (SW) and northeast (NE) Japan arcs. Ichinomegata volcano is located in the Oga Peninsula (Akita prefecture, NE Japan), and Oki-Dogo Islands is located in the Shimae prefecture (SW Japan).

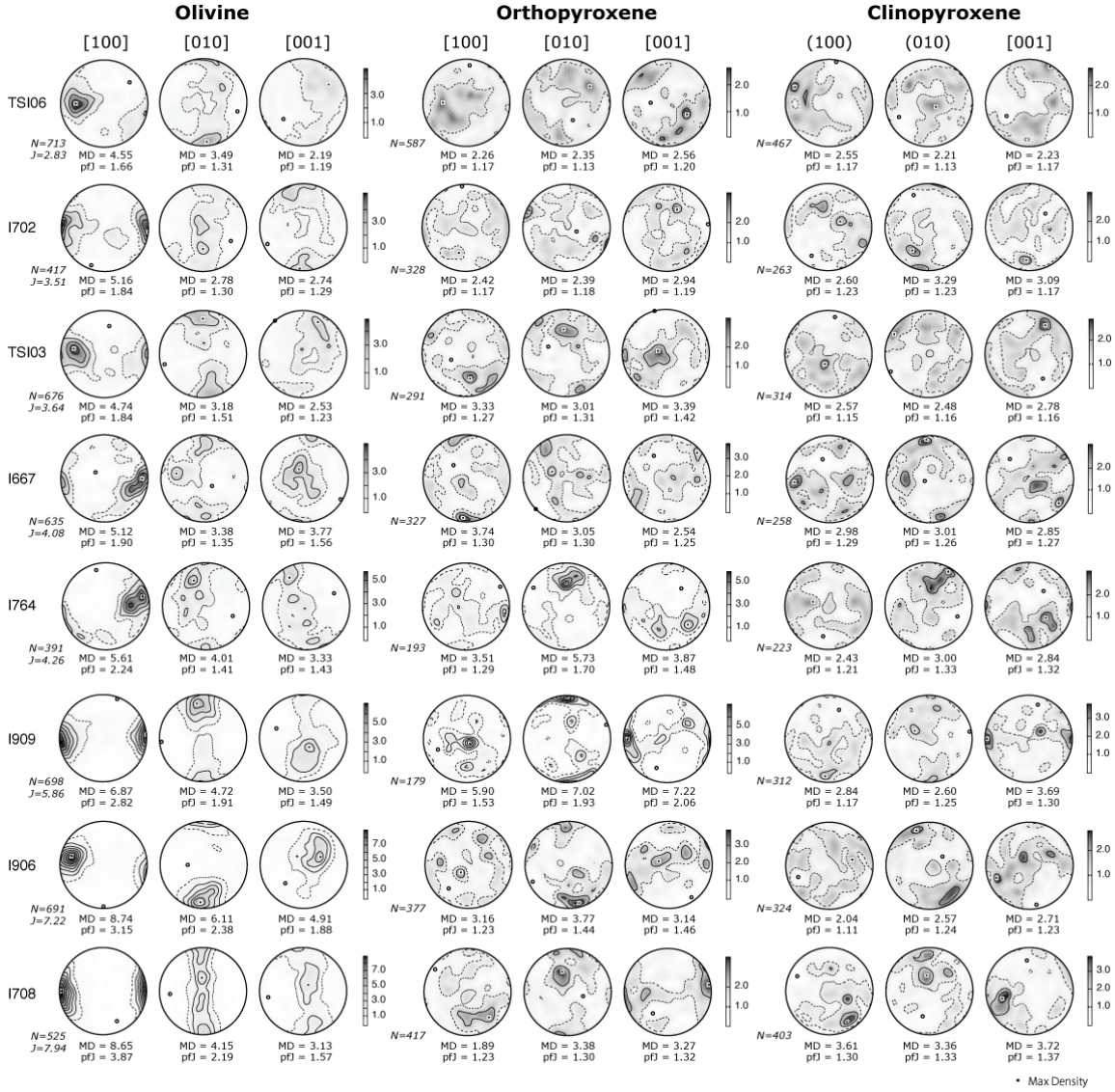

Figure 2. Olivine, orthopyroxene and clinopyroxene CPOs of Ichinomegata peridotite xenoliths. To maximize the average seismic anisotropy in Figure 5, the orientation data for each sample were rotated to align the maximum calculated Vp with the reference direction X (east or west in the pole figure) and the minimum calculated Vp with Z (north or south in the pole figure).

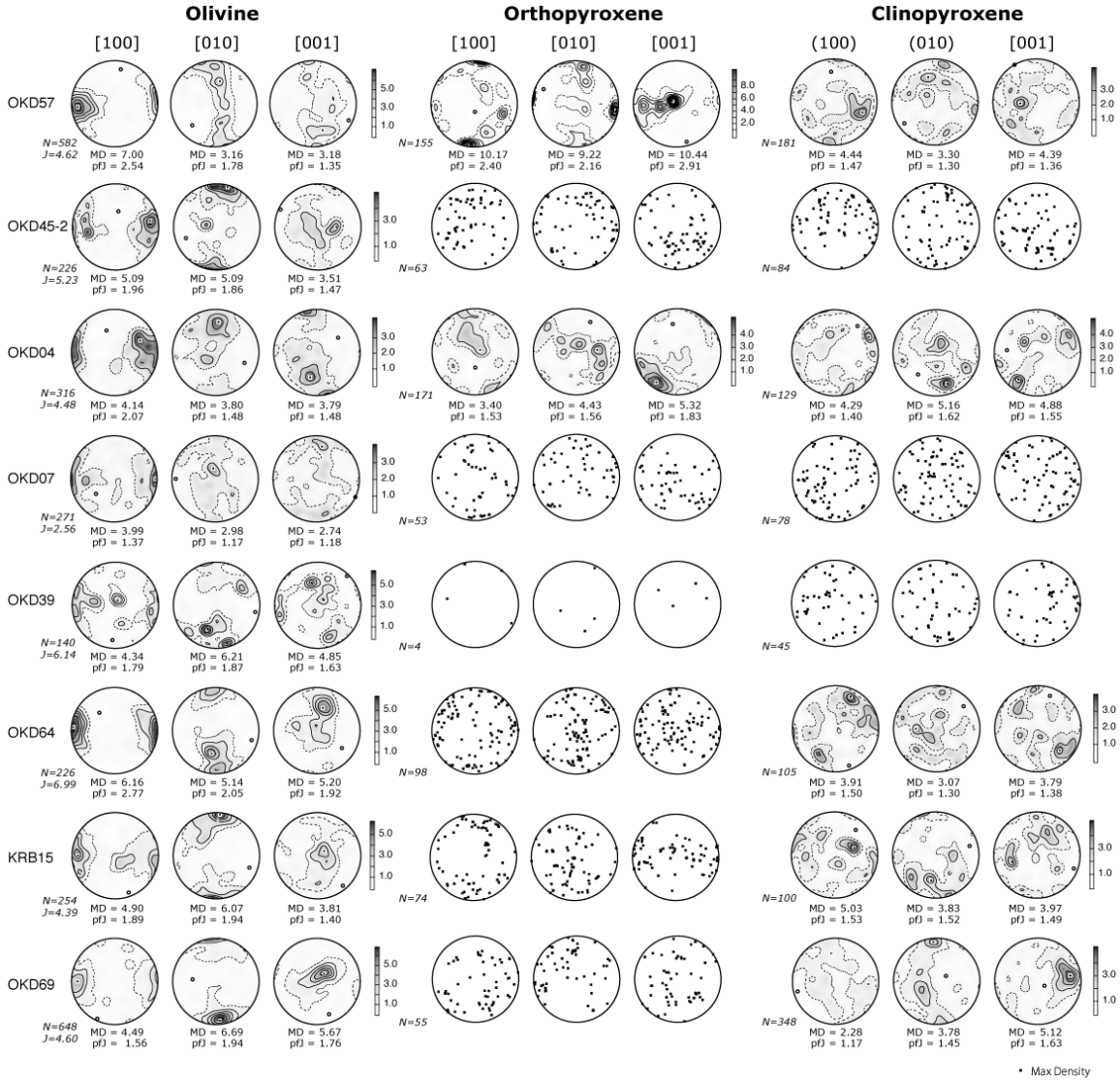

Figure 3. Olivine, orthopyroxene and clinopyroxene CPOs of Oki-Dogo peridotite xenoliths. To maximize the average seismic anisotropy in Figure 6, the orientation data for each sample were rotated with the result that the maximum Vp is parallel to the reference direction X (east or west in the pole figure) and the minimum Vp is parallel to Z (north or south in the pole figure).

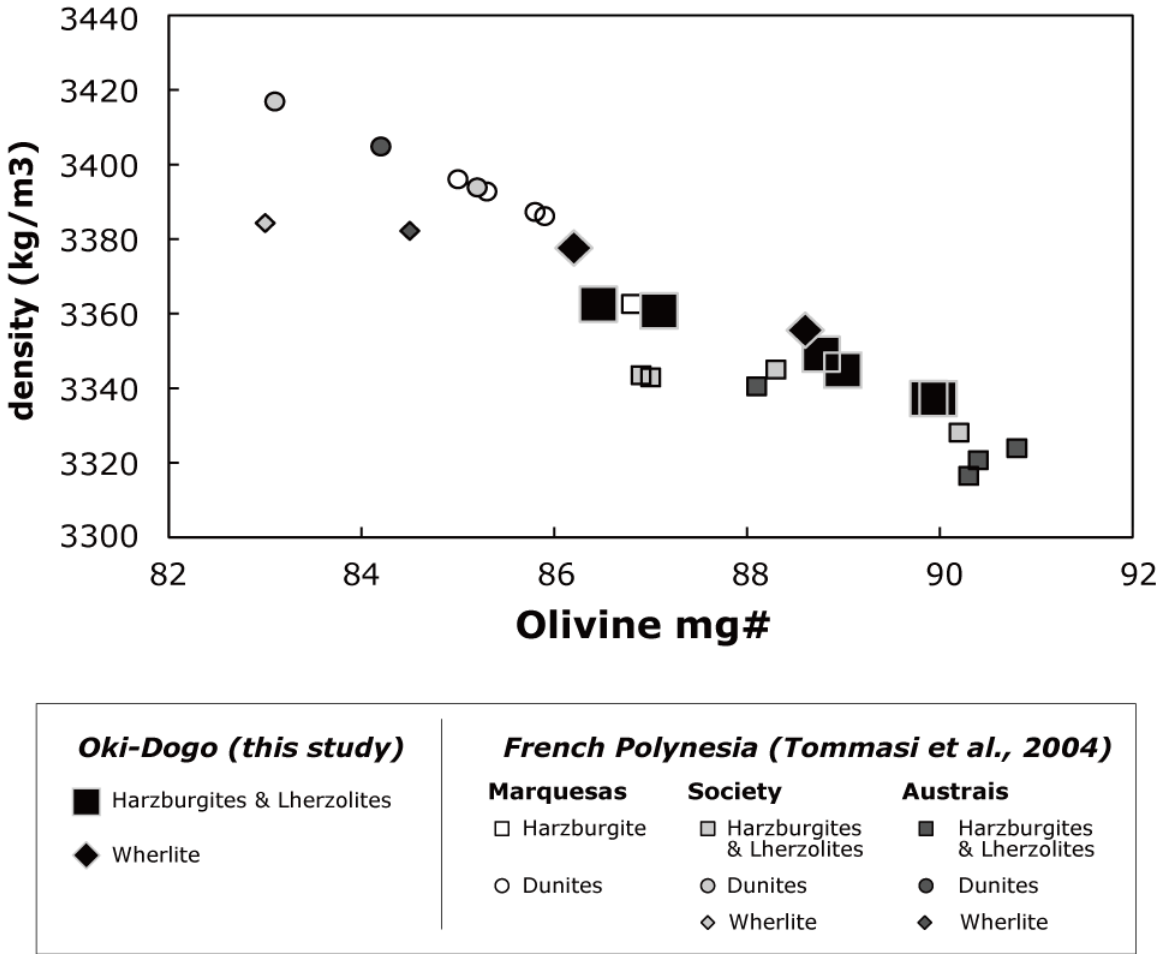

Figure 4. Density of Oki-Dogo samples as a function of the forsterite content of olivine, compared to samples from French Polynesia (Tommasi et al., 2004).

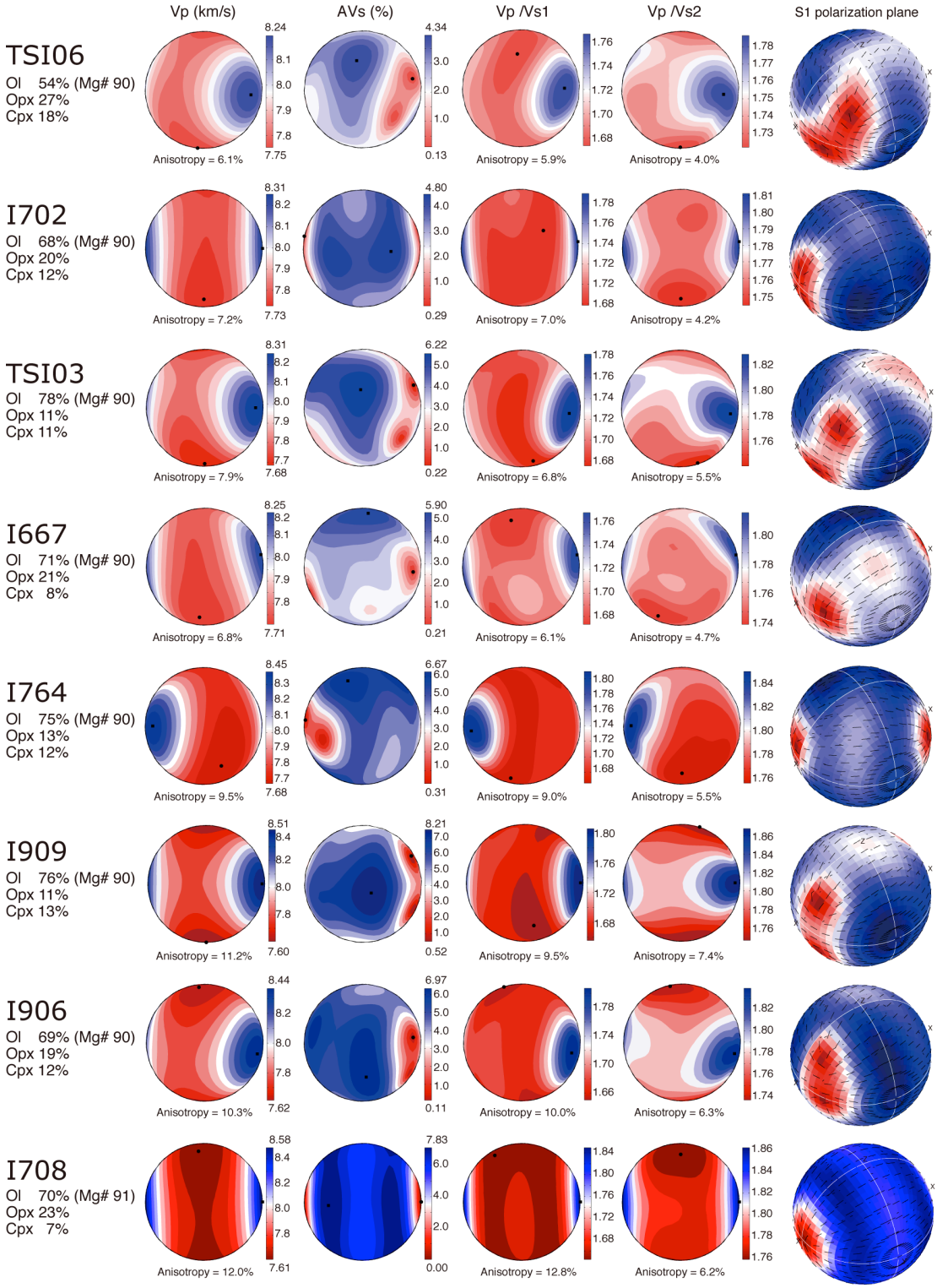

Figure 5. Seismic properties of Ichinomegata peridotite xenoliths. These data were calculated from the crystallographic preferred orientation data shown in Fig. 2. From left to right: P-wave velocity and anisotropy, S-wave anisotropy, Vp/Vs_1, Vp/Vs_2, and polarization of the fast shear wave S_1.

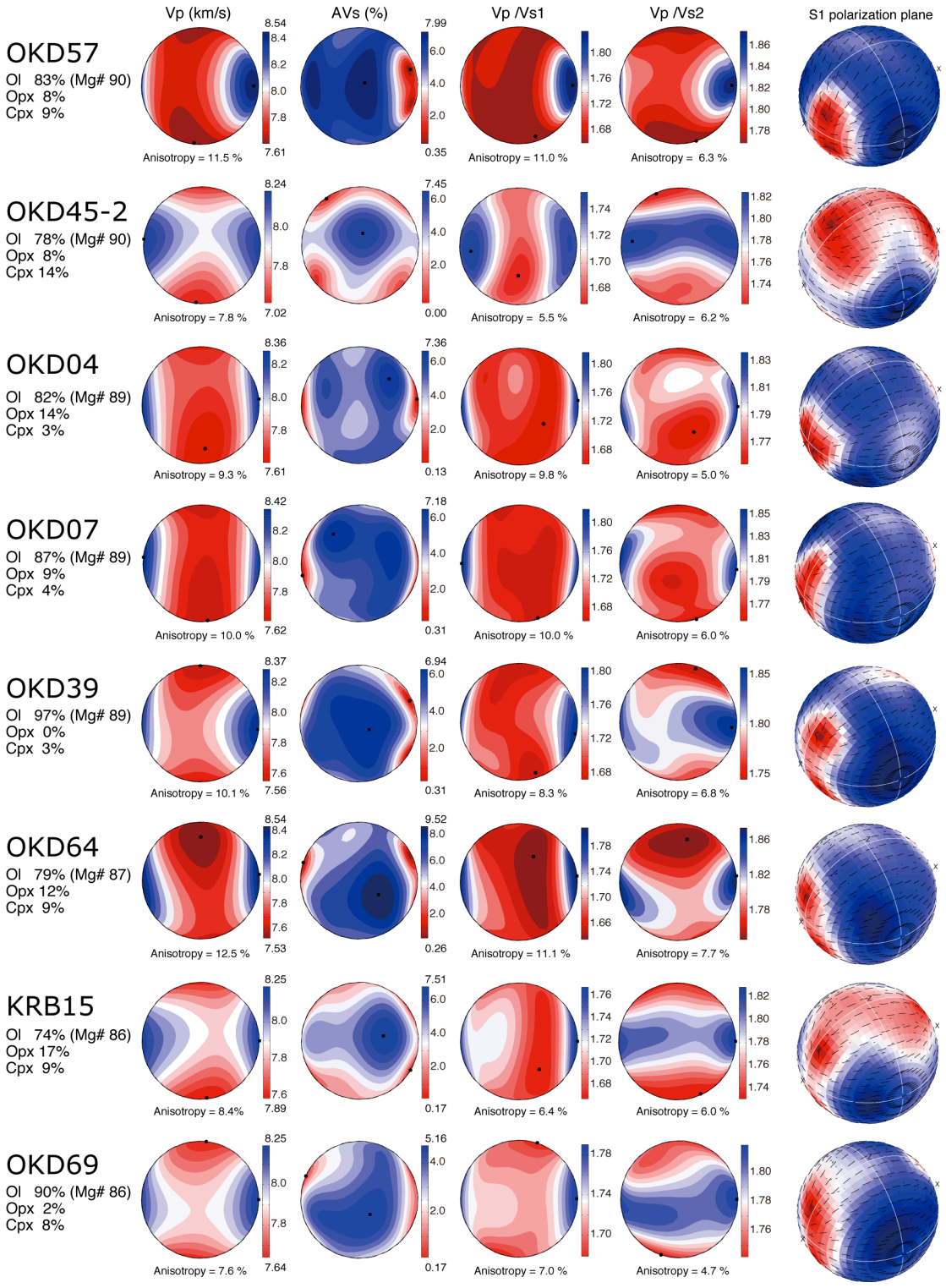

Figure 6. Seismic properties of Oki-Dogo peridotite xenoliths. These data were calculated based on crystallographic preferred orientation data in Fig. 3. From left to right: P-wave velocity, S-wave anisotropy, Vp/Vs_1, Vp/Vs_2, and the polarization of the fast shear wave S_1.

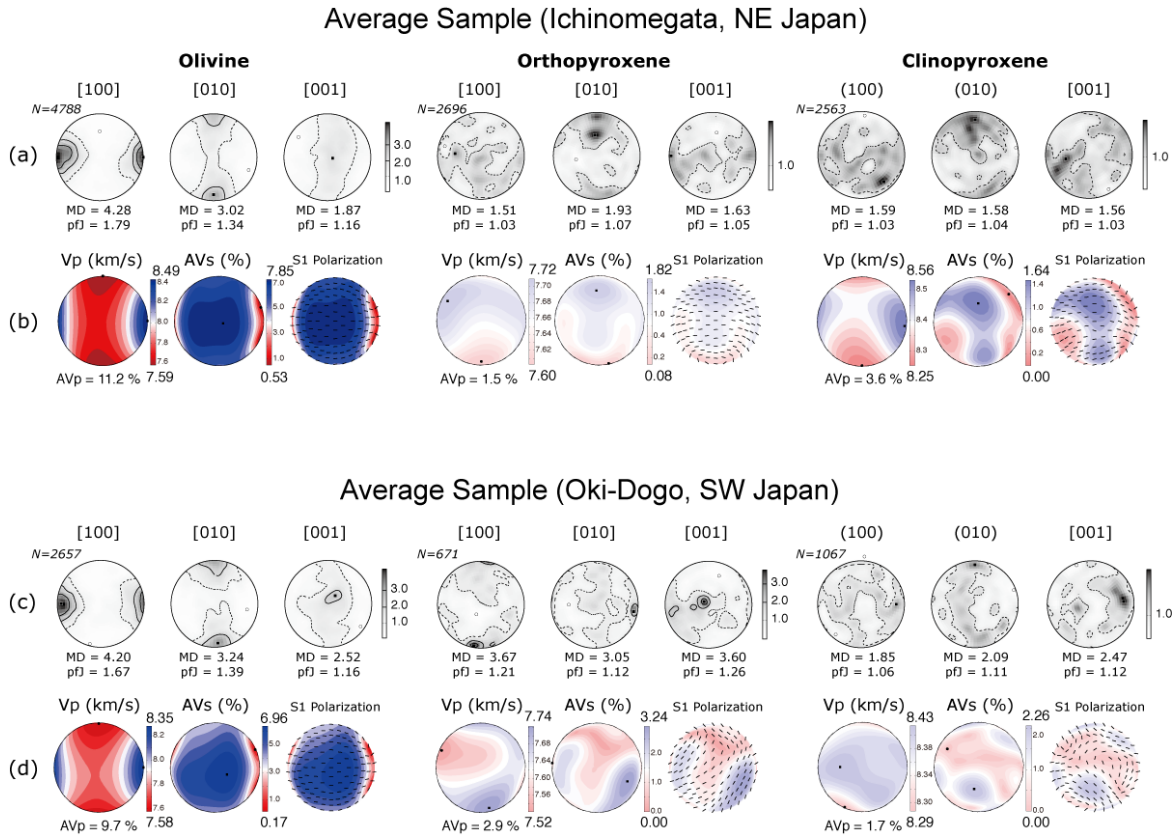

Figure 7. (a, c) Crystallographic preferred orientation (CPO) data for the average sample, obtained by summing the CPO of six peridotite xenoliths from each locality. CPOs are plotted on equal-area, lower hemisphere projections, contour are multiples of the uniform distribution, N is the number of measurements, *pfJ* is an index of fabric intensity, and MD is the maximum density. (b, d) Seismic properties of the average sample for each mineral (olivine, orthopyroxene and clinopyroxene) computed from the average CPOs based on grid data at a temperature of 1000ºC and pressure of 1.0 GPa (b) and a temperature of 1000ºC and pressure of 0.8 GPa (d). Contours are multiples of uniform density. The Vp plot shows the three-dimensional distribution of the P-wave velocity, anisotropy is (Vp_{max}-Vp_{min})/(Vp_{mean}); AVs is the three-dimensional distribution of the polarization plane of the fast split S-wave (S1), as a function of the orientation of the incoming wave relative to the structural frame of the sample. Each small segment represents the trace of the polarization plane at the point at which S1 penetrates the hemisphere.

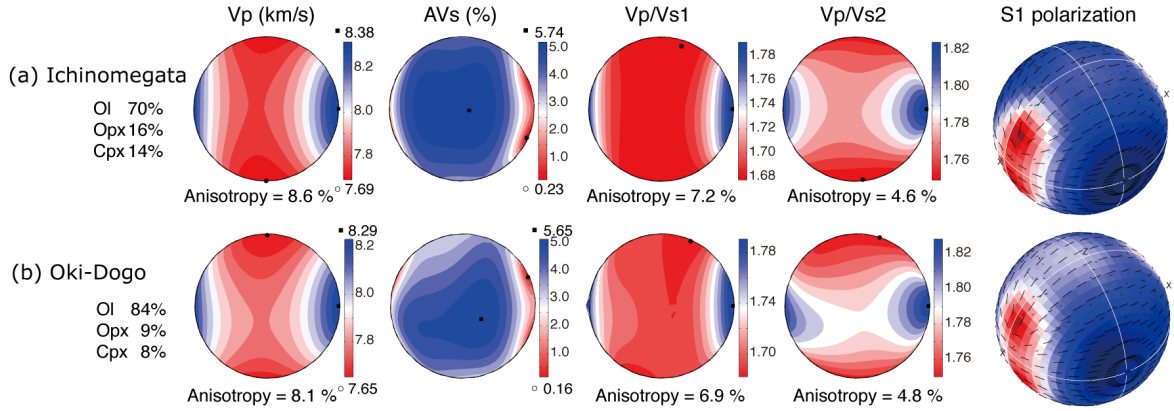

Figure 8. Seismic properties of average samples. From left to right: P-wave velocity and anisotropy, S-wave anisotropy, Vp/Vs_1, Vp/Vs_2, and polarization of the fast shear wave S_1. (a) Ichinomegata. (b) Oki-Dogo.

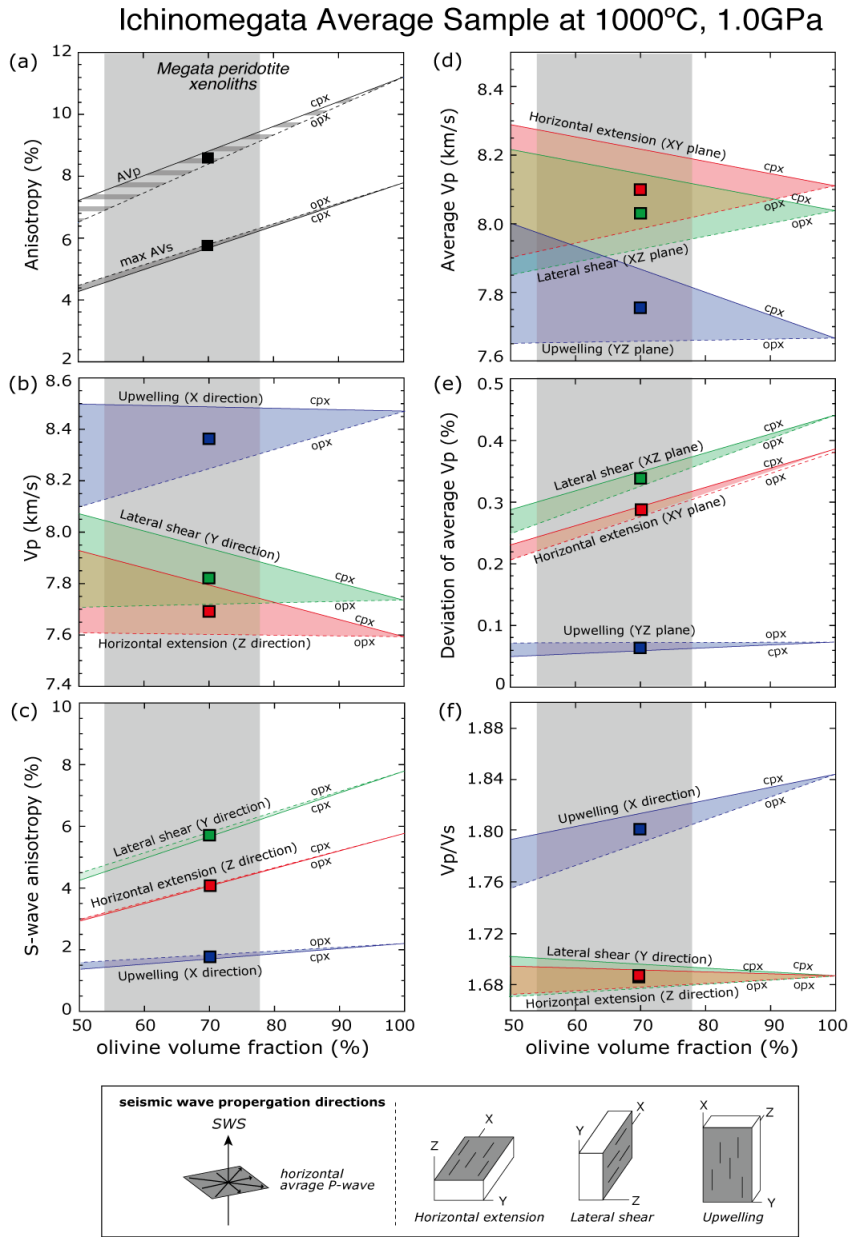

Figure 9. Variations of (a) Vp anisotropy and the maximum Vs anisotropy, (b) Vp, (c) S-wave anisotropy, (d) average Vp, (e) deviation of average Vp, and (f) Vp/Vs as a function of mantle composition at a temperature of 1000 ºC and pressure of 1.0 GPa. Solid lines represent compositions ranging from 50% olivine + 50 % clinopyroxene to 100% olivine; broken lines represent compositions ranging from 50% olivine + 50 % orthopyroxene to 100% olivine. Contours are shown for three geodynamic models: red for horizontal extension, green for lateral shear, and blue for upwelling. Within the box, the shaded area represents the plane of the foliation, and lines indicate lineation. Squared symbols indicate the mean composition of the Ichinomegata lherzolites. Gray shaded areas represent the range of modal composition of peridotites.

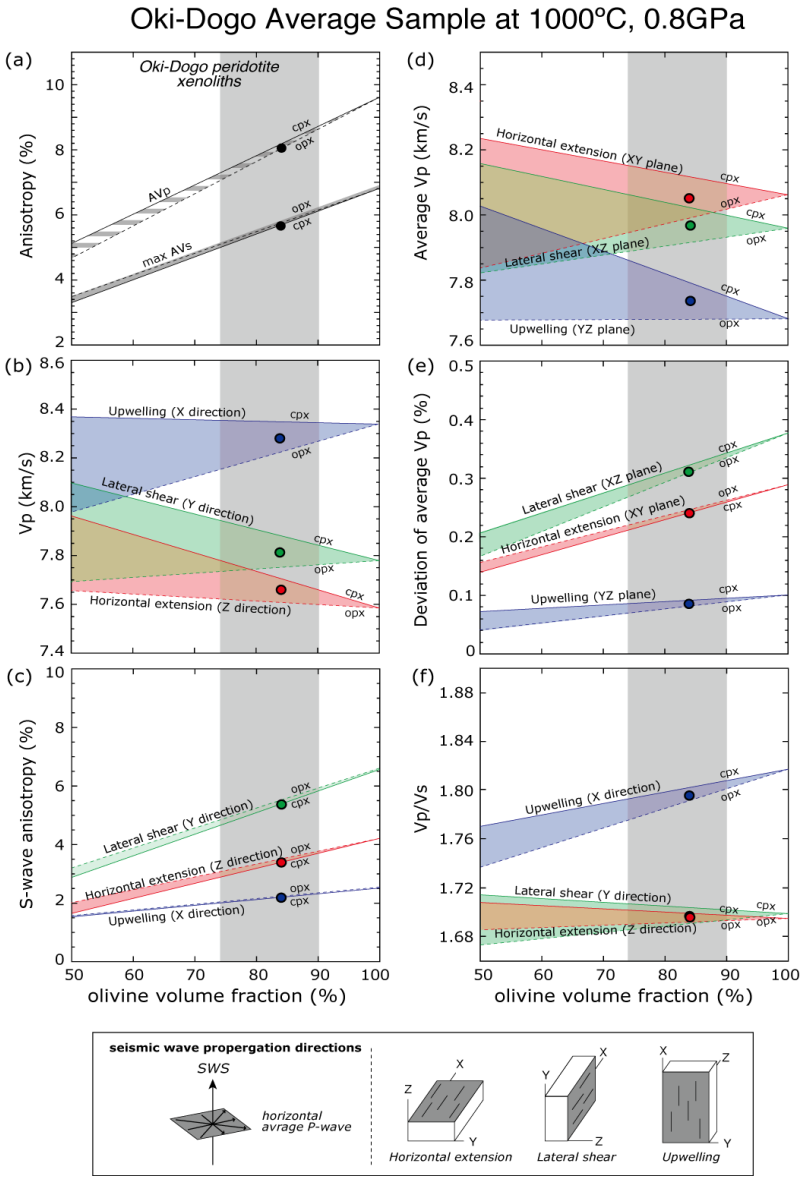

Figure 10. Variations of (a) Vp anisotropy and the maximum Vs anisotropy, (b) Vp, (c) S-wave anisotropy, (d) average Vp, (e) deviation of average Vp, and (f) Vp/Vs as a function of mantle composition at a temperature of 1000 ºC and pressure of 0.8 GPa. Solid lines represent compositions ranging from 50% olivine + 50 % clinopyroxene to 100% olivine; broken lines represent compositions ranging from 50% olivine + 50 % orthopyroxene to 100% olivine. Contours are shown for three geodynamic models: red for horizontal extension, green for lateral shear, and blue for upwelling. Within the box, the shaded area represents the plane of the foliation, and lines indicate lineation. Circles indicate the mean composition of the Oki-Dogo harzburgites. Gray shaded areas represent the range of modal composition of peridotites.

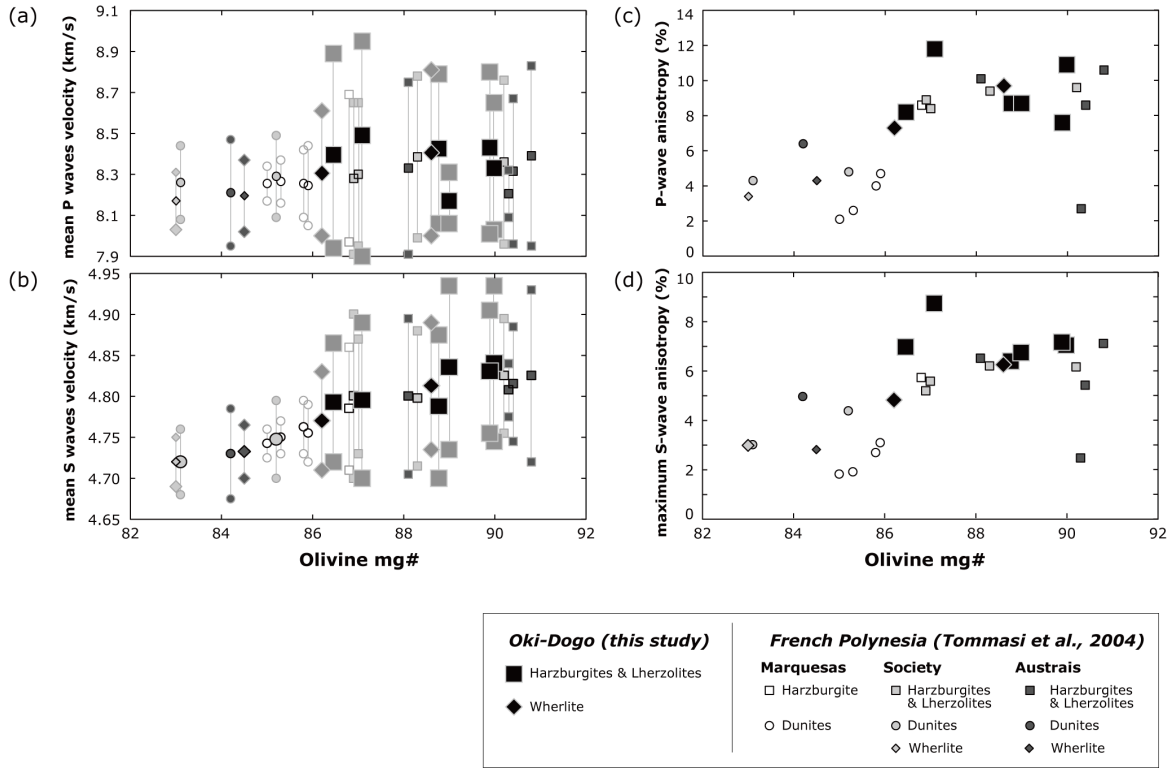

Figure 11. P-wave velocity (a), S-wave velocity (b), P-wave anisotropy (c), and maximum S-wave anisotropy (d) as a function of the forsterite content of olivine in Oki-Dogo samples, compared to samples from French Polynesia (Tommasi et al., 2004). The maximum and minimum P-wave velocities (a) or the mean fast and slow S-wave velocities (b) calculated for the anisotropic samples are represented as light gray symbols.

Table 1. Seismic velocity and anisotropy in Ichinomegata and Oki-Dogo peridotite xenoliths.

Sample #	Vp Max (km/s)	Vp Min (km/s)	AVp (%)	AVs Max (%)	Vs1 max (km/s)	Vs1 min (km/s)	Vs2 max (km/s)	Vs2 min (km/s)
Ichinomegata								
I667	8.25	7.71	6.80	5.90	4.67	4.52	4.60	4.38
I702	8.31	7.73	7.20	4.89	4.69	4.57	4.59	4.41
I708	8.58	7.61	12.00	7.83	4.77	4.58	4.58	4.31
I738	8.79	7.92	10.40	6.18	4.95	4.81	4.86	4.61
I764	8.45	7.68	9.50	6.87	4.74	4.55	4.60	4.36
I777	8.45	7.93	6.30	4.57	4.93	4.75	4.79	4.71
I892	8.74	8.03	8.40	5.69	4.98	4.81	4.88	4.64
I906	8.44	7.62	10.30	6.97	4.75	4.56	4.61	4.36
I909	8.51	7.60	11.20	8.21	4.75	4.53	4.60	4.34
TSI03	8.31	7.68	7.90	6.20	4.70	4.52	4.60	4.38
TSI06	8.24	7.75	6.10	4.34	4.70	4.59	4.62	4.47
TSI07	8.64	8.09	6.60	4.42	4.95	4.82	4.86	4.69
Oki-Dogo								
OKD04	8.36	7.61	9.29	7.35	4.72	4.53	4.55	4.31
OKD07	8.42	7.62	10.03	7.18	4.70	4.52	4.56	4.29
OKD39	8.81	8.00	9.70	6.26	4.98	4.80	4.86	4.61
OKD45-2	8.24	7.62	7.84	7.46	4.72	4.51	4.56	4.38
OKD57	8.54	7.61	11.49	7.99	4.74	4.53	4.58	4.30
OKD64	8.54	7.53	12.55	9.51	4.75	4.52	4.61	4.28
OKD69	8.25	7.64	7.63	5.16	4.64	4.51	4.56	4.36
KRB15	8.25	7.59	8.39	7.51	4.73	4.50	4.57	4.37

AVp: P-wave anisotropy; AVs: S-wave anisotropy.

Chapter 4

Seismic anisotropy of the uppermost mantle beneath the Rio Grande rift: Evidence from Kilbourne Hole peridotite xenoliths, New Mexico

Originally Published in modified form as "Seismic anisotropy of the uppermost mantle beneath the Rio Grande rift: Evidence from Kilbourne Hole peridotite xenoliths" by T. Satsukawa, K. Michibayashi, E. Y. Anthony, R. J. Stern, S. G. Stephen and H. L. Kelly, *Earth and Planetary Science Letters*, **331**, 172-181, 2011,

Abstract

Peridotite xenoliths from the Kilbourne Hole maar, New Mexico, consist of spinel lherzolite, harzburgite, and dunite. Because Kilbourne Hole erupted approximately 10 ka ago, these xenoliths represent essentially current conditions beneath the Rio Grande rift. In this study, we present detailed petrofabric data and seismic properties obtained from peridotite xenoliths from Kilbourne Hole to illuminate the origin and significance of shear-wave splitting in the uppermost mantle beneath this active rift. Using phase relations and the temperature of equilibration, we infer that these xenoliths were derived from the uppermost mantle, from depths of 35 – 60 km. Their crystallographic preferred orientations indicate the preservation of olivine b-axis fiber fabrics with a strong concentration of [010] with girdles of [100] and [001]. We consider three geodynamic models for the source region of these xenoliths: horizontal extension, lateral shear, and upwelling. After calculating seismic properties using a volume fraction of olivine, orthopyroxene and clinopyroxene appropriate to each model, we conclude that these xenoliths are derived from a lateral shear zone (vertical foliation (XY plane) and horizontal lineation within the plane of the foliation (X-axis)). However, the degree of seismic anisotropy generated by peridotite xenoliths alone is limited, so that the existence of melt in thin cracks or dikes could be required; the orientation of such melt pockets parallel to the XY plane in either model would result in an increase in anisotropy. These results indicate that the shear-wave splitting observed in the Rio Grande rift is a reflection of the lithospheric fabric, and the presence of melts as thin cracks or dikes.

Key words: peridotite xenolith; Kilbourne Hole maar; Rio Grande rift; rifting; mantle flow;

crystallographic preferred orientation (CPO); seismic anisotropy.

4-1. Introduction

Continental rifting is a complex process involving deformation of the lithosphere, asthenospheric flow, and partial melting; each of these processes can result in seismically anisotropic structures. As such, the significance of shear-wave splitting, in particular whether it represents lithospheric fabric or asthenospheric flow, remains controversial (e.g., Gao et al., 2008). Recent passive seismological investigations, combined with CPO (crystallographic preferred orientation) studies of xenolith fabrics, have provided an inexpensive and fruitful avenue for addressing this question (e.g., Satsukawa et al., 2010). Measurements of shear-wave splitting using P-to-S converted phase (SKS, SKKS, and PKS) play a crucial role in imaging the orientation and degree of polarization of mantle fabrics and in constraining models for the formation of these fabrics (Silver, 1996; Savage, 1999; Liu, 2009). Numerous laboratory and field studies suggest that seismic anisotropy in the uppermost mantle results mainly from olivine CPO, which tends to show a maximum seismic velocity parallel to the direction of plastic flow within the upper mantle (Nicolas and Christensen, 1987). This study is aimed at understanding mantle fabrics and their formation mechanisms beneath the Rio Grande rift by combining petrological and seismological measurements (Fig. 1).

The upwelling of asthenospheric mantle in rift zones provides an abundance of melts. Recent petrophysical studies of both natural (e.g., Le Roux et al., 2008) and experimentally generated (e.g., Holtzman et al., 2003) partially molten peridotites indicate that partial melting and refertilization processes may affect CPO. CPOs of peridotite xenoliths from the Kerguelen Islands, which are strongly affected by the

Kerguelen plume, differ between harzburgites and dunites as a result of melt–rock interaction; these petrographic differences correspond with the distribution of CPO-induced S-wave anisotropy (Bascou et al., 2008). The effect of melt on CPO is also addressed in ultramafic rocks from ultramafic complex in Far-East Russia (Burg et al., 2009) and in olivine-rich troctolites from IODP Hole U1309D in the Mid-Atlantic ridge (Drouin et al., 2009).

Previous studies have highlighted correlations between seismic properties and the modal composition of orthopyroxene and olivine, based on modeling (e.g., Mainprice, 1997), and analyses of natural sample of continental peridotite (e.g., Lee, 2003; Matsukage et al., 2005) and natural peridotite xenoliths (e.g., Pera et al., 2003; Soustelle and Tommasi, 2010). However, the effect of clinopyroxene on seismic properties remains poorly described, despite it having the third-highest modal abundance in peridotite.

Based on their observation of olivine CPO in Kilbourne Hole peridotite xenoliths from the Rio Grande rift, Bussod and Irving (1981) proposed that deformation was accompanied by syntectonic recrystallization in the presence of intercrystalline fluid. However, these samples were analyzed using a universal stage, and the seismic properties of the mantle beneath the Rio Grande rift were not considered. In this study, we present detailed petrofabric data for spinel peridotite xenoliths from Kilbourne Hole, New Mexico, determined using electron backscatter diffraction. Using these results, we illuminate the origin and significance of shear-wave splitting in the upper mantle beneath this active rift (Fig. 1).

4-2. Geological setting

The Kilbourne Hole maar exposes Quaternary basanites containing both

crustal and mantle xenoliths (Hamblock et al., 2007). It is roughly elliptical in shape, almost 3 km in length, and from 100 to 125 m deep. Using ^{3}He surface exposure methods, the age of eruption has been constrained to 10–20 ka (Anthony and Poths, 1992; Williams, 1999); thus, the xenoliths represent essentially ambient conditions for the Rio Grande rift. Kilbourne Hole is a part of the Potrillo volcanic field (Anthony et al., 1992; Thompson et al., 2005), which consists of cinder cones, maars, and fissure flows of basanitic and alkalic basalt composition. The Potrillo volcanic field is one of the largest silica-undersaturated volcanic fields in the Rio Grande rift, and has been interpreted as representing the products of small-degree partial melting of a volatile-charged asthenosphere.

4-3. Seismic data

For the study, we use all available broadband seismic data recorded in the 2^{o} by 2^{o} area approximately centered at Kilbourne Hole. The data were recorded by 7 stations (Fig. 1) and were archived at the IRIS (Incorporated Research Institutions for Seismology) Data Management Center. Station KIDD is operated by the University of Texas at El Paso (UTEP) and is located near the UTEP campus, and the rest of the stations belong to the Transportable Array of the USArray. A robust shear-wave splitting parameter measuring and ranking procedure (Liu et al., 2008; Liu, 2009; Gao and Liu, 2009; Gao et al., 2010), developed based on the approach of Silver and Chan (1991), was applied to the broadband seismograms to obtain the polarization direction of the fast wave and the splitting time. A total of 84 pairs of well-defined splitting parameters were obtained (Fig. 1). The average fast direction is 22.0 ± 11.7^{o} from the North, which is sub-parallel to the strike of most regional tectonic features including the Rio Grande rift and Cenozoic faults in the area (Fig. 1). The average splitting time

is 1.2 ± 0.3 s that is similar to the global average for continental areas (Silver, 1996). The waveforms, particle motion patterns and all the other related information for each of the measurements can be found at http://web.mst.edu/~sgao/XKS/KilHole/all/meas.html.

4-4. Mineral compositions, microstructures, and fabric analyses

We have studied six Kilbourne Hole peridotites, which span the modal ranges of lherzolite and harzburgite. In all samples the aluminous accessory phase is spinel, as is common for Cenozoic North American peridotite xenoliths (Wilshire et al., 1988). The silicate minerals have high Mg# ($Mg^{2+}/(Mg^{2+} + Fe^{2+})$), with Fo = 89–91 for olivine, En = 89–92 for orthopyroxene, and Mg# = 90–93 for clinopyroxene. Spinels exhibit a moderate depletion in Cr# ($Cr^{3+}/(Cr^{3+} + Al^{3+})$), ranging from 0.06 to 0.21 for lherzolite and from 0.22 to 0.51 for harzburgite. Based on texture, modal mineralogy, and chemical composition, the samples can be divided into three distinct groups. The first group comprises fine-grained (<2 mm) lherzolite with a tabular, equigranular texture (Fig. 2a). The second group consists of protogranular lherzolite (Fig. 2b); although its chemistry is still fertile, the fabric of these rocks is different from those of the first group. Although most previous studies of Kilbourne Hole xenoliths (e.g., Bussod and Irving, 1981) have considered only these two groups, we also identified a third group comprising porphyroclastic harzburgite (Fig. 2c). Xenoliths in this group are characterized by a strong foliation, and the whole-rock and mineral chemistries (Cr# in spinel) are consistent with melt depletion (Perkins and Anthony, 2011; Table 1). Using the thermometers of Brey and Köhler (1990), the equilibration temperatures (calculated at 2 GPa) of the three groups are also distinct: fine-grained lherzolite (KH41, KH29) has the lowest temperature (1009–1040°C),

protogranular to porphyroclastic lherzolite (KH43, KH54) has temperatures of 1049–1102°C, and porphyroclastic olivine-rich peridotites (KH22, KH25) have the highest temperatures (1094–1152°C; Table 1). Together with phase relations (Perkins and Anthony, 2011; Takahashi et al., 1993), these temperature ranges imply that Kilbourne Hole xenoliths were derived from depths of 35 – 60 km, within the uppermost mantle. The difference in temperature in three textural types suggests that the subcontinental mantle beneath Kilbourne Hole is rheologically and chemically layered.

The peridotite xenoliths contain a foliation and a lineation defined by the alignment of spinel crystals; we have analyzed their microstructures using thin sections cut perpendicular to the foliation and parallel to the lineation (i.e., XZ sections). To examine the conditions of deformation in more detail, and to evaluate the effects of the seismic properties on rocks beneath the rift zone, we have focused on the CPOs of three common mineral phases: olivine, orthopyroxene, and clinopyroxene. These observations were obtained by electron backscatter diffraction (EBSD) using the SEM-EBSD facility at Géosciences Montpellier, France. The EBSD patterns were generated by the interaction of a vertical incident electron beam with a polished thin section, tilted at 70°, in a scanning electron microscope (JEOL JSM 5600). The diffraction pattern was projected onto a phosphor screen and recorded using a digital CCD camera. The resulting image was then processed and indexed in terms of crystal orientation using the CHANNEL5 software distributed by Oxford Instruments HKL. For each sample, we obtained CPO maps covering almost the entire thin section (usually 35 mm long and 20 mm wide), with sampling steps of 30 or 35 μm, depending on grain size; rates of indexation in the raw maps range from 50% to 80%. The measured CPOs are presented on equal-area, lower-hemisphere projections (Fig.

3). Most of the analyzed samples show a strong concentration in [010], with weak girdle of [100] and [001] in olivine. For orthopyroxene, although most of CPO patterns are weak, a (010)[001] pattern (shear direction is [001] and shear plane is (010)) occurs in two oriented samples (i.e. KH22 and 25). Clinopyroxene CPO data show nearly random fabrics, except for KH22, which show a weak (010)[001] slip.

To characterize CPOs, we determined the fabric strength (*J*-index) and distribution density (*pfJ*-index) of the principal crystallographic axes (for definitions of the *J*-index and *pfJ*-index, see Mainprice et al., 2000; Michibayashi and Mainprice, 2004). Table 1 lists the number of measured olivine grains, the *J*-index values calculated for each xenoliths, and the maximum density and *pfJ*-index value for each pole Figure. The *J*-index is the volume-averaged integral of the squared orientation densities; it has a value of unity for a random CPO, and is infinite for a single crystal. Most natural peridotites yield values between 2 and 20 (Ben Ismaïl and Mainprice, 1998), and those of the present study range from 2.81 to 9.65 (Table 1).

To maximize the average seismic anisotropy, the orientation data for each sample were adjusted to an external reference frame in which the maximum Vp is parallel to the reference direction X, and the minimum Vp is parallel to the Z-axis (see also Fig. 4). Seismic properties for each sample are shown in Fig. 5. By combining data from each of the six xenoliths, the average of the sample was then calculated from the sum of all measurements, giving the same weight from each xenolith (Fig. 6a). Using this approach, olivine CPO data show b-axis fiber patterns characterized by a strong concentration in [010], with a weak girdle of [100] and [001]. For orthopyroxene, CPO data may indicate either or both (100)[001] and (010)[100] slip; the (100)[010] slip is the most readily activated, and thus the most common slip system (Naze et al., 1987). In contrast, clinopyroxene CPO data suggest a nearly

random fabric, with a weak concentration in (010) normal to the foliation (Fig. 6a).

4-5. Rock seismic properties

Seismic properties were computed by averaging individual grain elastic-constant tensors as a function of the CPO and modal composition of a sample. This method enables the calculation of the three-dimensional distribution of seismic velocities in an anisotropic polycrystalline aggregate (Mainprice and Humbert, 1994). In the present calculations, we used Voigt–Reuss–Hill averaging of single-crystal elastic constants at ambient conditions (Abramson et al., 1997; Chai et al., 1997; Collins and Brown, 1998). Because the geothermobarometric analysis in this study yielded temperatures of 950–1200°C and pressures of 1.3–1.8 GPa (Perkins and Anthony, 2011), we calculated the seismic properties assuming conditions of 1000°C and 1.5 GPa (Fig. 6b). This method has been described in detail previously (Pera et al., 2003; Tasaka et al., 2008).

Olivine CPOs result in P-wave propagation being fastest parallel to the highest density of [100], and slowest parallel to the highest density of [010]; polarization anisotropies are highest in directions approximately normal to the highest density of [010]. The orientation of the polarization plane of the fastest S-wave (Vs_1) indicates the orientation of the great circle containing the [100] maximum. The Vp of olivine range from 7.58 to 8.24 km/s; Vp anisotropy is 8.4% and AVs_{max} is 6.88%. For orthopyroxene, the average anisotropies are small: Vp range between 7.72 and 7.78 km/s, Vp anisotropy is 0.8%, and AVs_{max} is 1.72%. Although clinopyroxene has weaker CPOs and smaller amount of measured values than orthopyroxene, its seismic anisotropy is larger: Vp range between 8.28 and 8.61 km/s, Vp anisotropy is 3.9%, and AVs_{max} is 2.22%.

To assess the effect of grain size heterogeneity, we also calculated seismic properties from gridded data obtained from CPO maps (Fig. 6c). The distributions of seismic properties calculated in this way are very similar to those described above based on a single measurement per grain (Fig. 6b), although individual velocity and anisotropy values calculated from gridded data are higher (e.g., for olivine, Vp ranges from 7.45 to 8.42 km/s, Vp anisotropy is 12.3%, and AVs_{max} is 9.17%). In this paper, we favour using the seismic properties based on grided data (Fig. 6c) for the following discussion, because it contains the effect of grain size, hence it provides more realistic seismic properties.

4-6. Variation of seismic properties as a function of modal composition

Based on the modal composition of peridotites (four lherzolites and two harzburgites), we recalculated the seismic properties for mean compositions of dunite (Ol_{100}), harzburgite ($Ol_{78}Opx_{16}Cpx_{6}$), and lherzolite ($Ol_{64}Opx_{23}Cpx_{13}$; Fig. 7). Using this approach, P-wave propagation is fastest parallel to the highest density of olivine [100] and is slowest parallel to the highest density of [010], and polarization anisotropies are highest at directions approximately normal to the highest density of [010]. Vp/Vs_1 and Vp/Vs_2 ratios are highest for propagation directions that are normal and parallel, respectively, to the highest density of [100] of olivine. Although these anisotropy patterns do not change significantly as olivine volume fraction decreases, P- and S-wave velocities and anisotropies decrease. Because olivine is the primary mineral in peridotites, peridotite anisotropy is dominated by the elastic properties of olivine.

We have calculated variations in seismic properties as a function of modal composition for the structural planes of XY for horizontal shear, XZ for lateral shear,

and YZ for vertical shear (Fig. 8); in these figures, gray shaded squares represent ranges in the modal compositions of peridotite xenoliths from this study. To estimate the effect of modal composition on seismic properties, we varied the mineral composition from 100% olivine to 50% olivine + 50% pyroxene, by the alternating stepwise addition of 10% orthopyroxene or clinopyroxene. In Fig. 8, we have extrapolated variations in Vp anisotropy, the maximum Vs anisotropy, Vp, the anisotropy of Vs, the average of Vp, the deviation of Vp, and Vp/Vs with respect to the olivine volume fraction, assuming propagation direction of seismic wave is vertical. As a result, the effect of the second most abundant phase on seismic properties is highly dependent on structural orientation. Vp anisotropy decreases as the volume fraction of olivine decreases and orthopyroxene increases (Fig. 8a), whereas average Vp, unlike other factors, increases with the addition of clinopyroxene (i.e., decreasing olivine abundance; Fig. 8b, d). Vp/Vs does not differ significantly as a function of modal olivine abundance.

4-7. Discussion: Seismic anisotropies beneath the Rio Grande rift

Because the peridotite xenoliths in this study erupted recently (10 ka), they provide a snapshot of the "present" mantle composition and structure beneath the region in central New Mexico known as the Rio Grande rift. Isotopic studies suggest that all lithosphere that formed or was reworked during past tectonic events is preserved (Anthony, 2005). Kilbourne Hole peridotite xenoliths come from a depth range of 35 – 60 km, the lowest-temperature samples potentially represent lithospheric mantle, whereas those from higher temperatures may represent the asthenosphere. CPO patterns are characterized by a strong concentration of [010], which is a different distribution compared to that in other peridotite xenoliths from a continental margin

setting in Knippa, Texas (Satsukawa et al., 2010). Consequently, some seismic properties are different between the two sets of xenoliths, such as polarization anisotropies, which have maximums approximately parallel to the foliation for Kilbourne Hole peridotite xenoliths, but normal to foliation for Knippa peridotite xenoliths (Satsukawa et al., 2010).

The geometry and strength of seismic anisotropy are generally estimated using measurements of shear-wave splitting, which can place constraints on both the delay time and polarization direction of fast shear-wave propagation. Shear-wave splitting results indicate a delay time of 0.45–2.13 s with the average splitting time 1.2 ± 0.3 s within the Rio Grande rift (Fig. 1).

Continental rifting is a complex process involving deformation of the lithosphere, asthenospheric flow, and partial melting. Because each of these processes may result in seismically anisotropic structures, it is difficult to discriminate between the effects of rock anisotropy, recent mantle flow, and aligned cracks (Gao et al., 1997). In addition, Vauchez et al. (2000) showed that an anisotropy due to preferentially oriented anisometric melt pockets may add to the asthenospheric CPO-induced anisotropy beneath the active part of a rift.

Lherzolite xenoliths generally contain orthopyroxene in higher abundances than clinopyroxene, which is a result of the selective removal of clinopyroxene from primary mantle lherzolite by partial melting. In spite of its small volume fraction, clinopyroxene has a significant effect on seismic properties (see 4-6. Variation of seismic properties as a function of modal composition and Fig. 8). It is also interesting to note that in the case of harzburgite ($Ol_{78}Opx_{16}Cpx_{6}$) and lherzolite ($Ol_{64}Opx_{23}Cpx_{13}$) mineral compositions, S-wave anisotropy is lower than results calculated from either aggregate of orthopyroxene or clinopyroxene alone, even

though P-wave anisotropy is higher than that of orthopyroxene or clinopyroxene (Fig. 8c). This may reflect an offset of the S-wave anisotropy (AVs) caused by interactions between orthopyroxene and clinopyroxene (Fig. 6b, c).

The magnitude of the delay time depends on the strength of the anisotropy and the thickness of the anisotropic layer. To explain the variability in splitting times near Kilbourne Hole, the thickness (T) of an anisotropic layer can be described by T = (100 dt<Vs>)/AVs (e.g., Pera et al., 2003). Although the original orientation of the Kilbourne Hole xenoliths was lost during transport to the surface, we know from their mineral compositions that they were derived from the uppermost lithospheric mantle (Perkins and Anthony, 2011). We have calculated the thickness of the anisotropic layer with our averaged sample (Fig. 6) using the average splitting time (1.2 s) for three different structural orientations. This allowed us to assess the degree to which the CPO data are consistent with models in which horizontal extension, lateral shear, or upwelling are invoked to explain the observed delay times (Fig. 9). Using this approach, we obtain anisotropic layer thicknesses (for models of lateral shear, upwelling, and horizontal extension, respectively) of 70-110, 100-180 and 260-350 km for a delay time of 1.2 s (Fig. 9). Of these results, only the lateral shear and upwelling models yield thicknesses consistent with geothermobarometric evidence that the peridotite xenoliths came from a depth of 35 – 60 km. Because the study region is an active rift zone, these two models are also suitable from a geological perspective. For example, Vauchez et al. (2000) proposed that anisotropies measured in the Rio Grande rift were caused by a transtensional deformation of the lithospheric mantle during rifting, as indicated by the consistent obliqueness of the polarization direction of the fast shear wave to the rift trend. However, it should be noted that when a delay time of 1.2 s is used, our calculated thicknesses of the anisotropic layer are still greater than

those indicated by geothermobarometric evidence (25 km; Fig. 9).

Other factors, such as the alignment of melt lenses in the low-velocity zone, or cracks infilled by fluid, may provide a likely complementary explanation for the observed seismic anisotropy, and seismological studies do favor the existence of melts beneath the Rio Grande rift. A wide zone of low velocity situated beneath the Rio Grande rift, at a depth of 65 to 125 km, is clearly visible in LA RISTRA data obtained using both surface wave inversions (West et al., 2004) and tomography (Gao et al., 2004). Velocities from depths of 55 to 90 km beneath the rift axis are 10% slower than those beneath the Great Plains, which is consistent with the presence of small amounts of partial melt (West et al., 2004). Thus, SKS splitting measurements in the Rio Grande rift could also be caused by magma-filled cracks (e.g., Gao et al., 1997).

Seismological studies using travel-time tomography reveal the existence of a low-velocity zone within the mantle wedge (e.g., Nakajima and Hasegawa, 2004). The Vp/Vs ratio provides constraints on mantle composition, in particular for low-velocity zones in the mantle wedges (e.g., Nakajima et al., 2001). Several models have been proposed to explain spatial variation of Vp/Vs ratios, including the presence of fluids or melts for high ratios of Vp/Vs (Takei, 2002), or changes in mineralogical composition (e.g., orthopyroxene enrichment) for low ratios of Vp/Vs (Wagner et al., 2006).

Enrichment in orthopyroxene is widely reported for peridotite xenoliths (Griffin et al., 2008; Soustelle et al., 2010); Vp/Vs ratios calculated from spinel peridotite xenoliths from Avacha volcano in Kamchatka, vary from 1.72 to 1.75, and decrease with increasing orthopyroxene content (Soustelle and Tommasi, 2010). In addition, Vp/Vs ratios from different tectonic settings show a better correlation with the abundance of orthopyroxene than that of olivine (Afonso et al., 2010). In our

model, Vp/Vs ratios vary from 1.68 to 1.78 (Fig. 8f) and decrease with increasing orthopyroxene content, but the ratios are almost insensitive to the degree of clinopyroxene enrichment in all of our models (upwelling, lateral shear, and horizontal extension). As a result, the variability in Vp/Vs ratios is minimal for our natural peridotite compositions (harzburgite: $Ol_{78}Opx_{16}Cpx_{6}$; lherzolite: $Ol_{64}Opx_{23}Cpx_{13}$). Thus, we predict that for most of the upper mantle, compositional variations in peridotites are unlikely to alter Vp/Vs ratios to a detectable degree in terms of current seismological methods.

As discussed above, the use of models that consider only mineral CPOs makes it difficult to produce realistic thicknesses for the anisotropic layer, or meaningful Vp/Vs ratios from rock seismic anisotropies. Another possibility is to use the preferential orientation of melt-lenses as an additional phase in the models. By applying the approach developed by Mainprice (1997), Vauchez et al. (2000) used simulations to show that if melt is contained in isometric or weakly anisometric pockets, an increase in melt fraction alone does not significantly increase the anisotropy of an aggregate. In contrast, if even small amounts of melt (e.g., 4%) collect in thin lenses parallel to the foliation, they can double the anisotropy produced by the mineral CPO, indicating that melt lenses may contribute significantly to seismic anisotropy within the rift itself. Nakajima et al. (2005) evoked the existence of melt-filled pores, combined with a specific effective aspect ratio and volume fraction for the pores, to explain the observed low-velocity anomalies in NE Japan, which cannot be explained by the thermal effect alone. For a depth of 40 km, this approach results in 1–2 vol.% melts, present as thin cracks or dikes with aspect ratios of 0.02–0.04, whereas a depth of 65 km yields 0.04–0.05 vol.% melt with an aspect ratio of ~0.001.

We can compare the shear wave splitting of dt = 1.2 (± 0.3) s for the Rio Grande rift to another well-studied rift zone in Ethiopia (where the splitting is greater and varies from 1.7 to 2.5 s; Kendall et al., 2005). In addition, the APM (absolute plate motion) direction is nearly parallel to the rift for the Rio Grande, whereas in Ethiopia, it is almost perpendicular. Considering these observations and that degree of melting is rather small in the Rio Grande rift, the model that has the maximum CPO related shear wave splitting with Y vertical (i.e., the lateral shear model) is more realistic for the Rio Grande, even if a small amount of melt is present. The orientation of APM direction with respect to the rift axis is also more compatible with lateral shear.

In this study, we propose a schematic model for the structure of the uppermost mantle beneath the Rio Grande rift, based on evidence from peridotite xenoliths from the Kilbourne Hole maar, derived from depths of 35 – 60 km (Fig. 10). Model of lateral shear is likely to contribute to the thickness of the anisotropic layer (Fig. 9). Moreover, the vertically planar structure of these models is in good agreement with the observed high concentrations of [010] in olivine, parallel to the Z direction. In the lateral shear model (considered relative to the XZ plane), the polarization direction of Vs_1 (the fastest S-wave) is in the XY plane (Fig. 4). Because the shear-wave splitting direction is parallel to the rift axis, we assume that the Z direction is normal to the rift axis (Fig. 10), which is most reasonable from a geological perspective.

The degree of S-wave anisotropy generated by peridotite xenoliths alone is limited; it is 4.81 to 8.82 %, however it requires approximately 13 to 17 % to produce the realistic thickness (25km). Therefore the existence of melt in thin cracks or dikes could be invoked to cause a significant increase. It is well established that melt reduces shear-wave velocity; consequently, seismic anisotropy is sensitive to the orientation of melt pockets. It is likely that melt pockets could be ideally oriented

parallel to the XY plane in either model, so that the velocity of S2 may be lower, resulting in an increase in anisotropy (Fig. 10). In contrast, the orientation of such melt pockets parallel to the YZ plane would reduce the velocity of S1 but would not affect S2 velocities (Fig. 10), resulting in lower anisotropies. We can estimate the melt fractions and shape of melts pocket to produce high S-wave anisotropy (13 to 17 %) if we apply the result of simulation by Vauchez et al. (2000) to this study. In the case of a shape ratio of 20 (20:20:1), melt fraction is 1.5 to 2.5%. Up to 6 to 9 % of melt fraction is required if the shape ratio is 5 (5:5:1).

4-8. Conclusions

Continental rifting is a complex process involving deformation of the lithosphere, asthenospheric flow, and partial melting. Because each of these processes may result in seismically anisotropic structures, it is difficult to discriminate between the effects of rock anisotropy, recent mantle flow, and aligned cracks. In this paper, we present detailed petrofabric data from Kilbourne Hole peridotite xenoliths, and seismic properties calculated from these petrofabrics to illuminate the origin and significance of shear-wave splitting in the uppermost mantle beneath this active rift. Peridotite xenoliths from the Kilbourne Hole maar consist of spinel lherzolite, harzburgite, and dunite, which were derived from the uppermost mantle, from depths of 35 to 60 km. Since Kilbourne Hole erupted at approximately 10 ka, these xenoliths represent essentially current conditions beneath the Rio Grande rift. Their crystallographic preferred orientations indicate the preservation of olivine b-axis fiber fabrics with a strong concentration of [010] with girdles of [100] and [001].

We consider three geodynamic models for the source region of these xenoliths: horizontal extension, lateral shear, and upwelling, using a volume fraction

of orthopyroxene and clinopyroxene appropriate to each model. Although lherzolite xenoliths generally contain orthopyroxene in higher abundances than clinopyroxene, clinopyroxene has a significant effect on seismic properties originated in its high anisotropy of single crystal itself, in spite of its small volume fraction. After calculating seismic properties and consideration of absolute plate motion direction, we conclude that these xenoliths are derived from a lateral shear zone (vertical foliation (XY plane) and horizontal lineation within the plane of the foliation (X-axis)). However, the degree of seismic anisotropy generated by peridotite xenoliths alone is limited, so that the existence of melt in thin cracks or dikes could be required. If melt pockets are oriented parallel to the XY plane in either model, the velocity of S2 may be lower, resulting in an increase in anisotropy. In contrast, the orientation of such melt pockets parallel to the YZ plane would reduce the velocity of S1 but would not affect S2 velocities, resulting in lower anisotropies.

Overall, the peridotite xenoliths demonstrate the possible presence of an anisotropic layer within the uppermost mantle lithosphere, which could be related to ‘frozen’ deformation. We have calculated the maximized seismic properties of peridotite xenoliths in order to determine their contribution to seismic observations of the active region of the Rio Grande rift. In summary, the seismic properties determined for the mantle beneath the rift suggest that the region has a complex tectonic pattern, with probable lateral shear, in addition to the presence of melt as thin cracks or dikes.

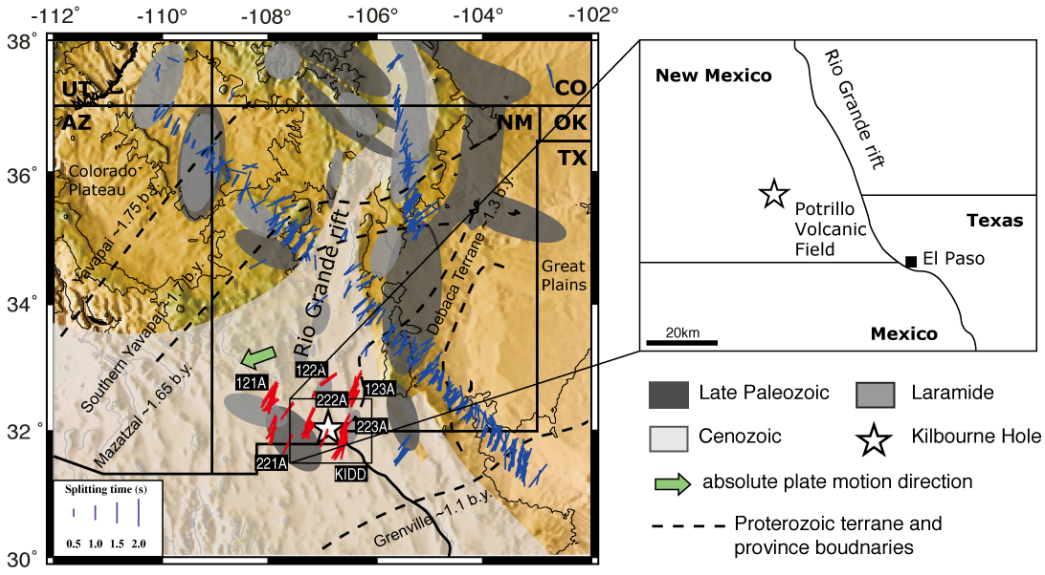

Figure 1. Location of Kilbourne Hole maar in New Mexico, USA and shear-wave splitting parameters plotted above the XKS ray-piercing points at 100 km depth. The red bars are new splitting data in this study, and the blue bars are from the first uniform shear-wave splitting database (Liu, 2009). Note that in the original paper (Liu, 2009), the data were plotted above 200 km piercing points. To be consistent with the new results, we re-calculated the locations to 100 km depth. Absolute plate motion direction (green arrow) of North America calculated based on the HS3-NUVEL1A model (Gripp and Gordon, 2002). The orientation of the red bars represents the polarization direction of the fast wave, and the length of the bars is proportional to the splitting time which ranges from 0.45 s to 2.13 s, and the average splitting time is 1.2 ± 0.3 s. Uplift traces are modified from Wilson et al. (2003).

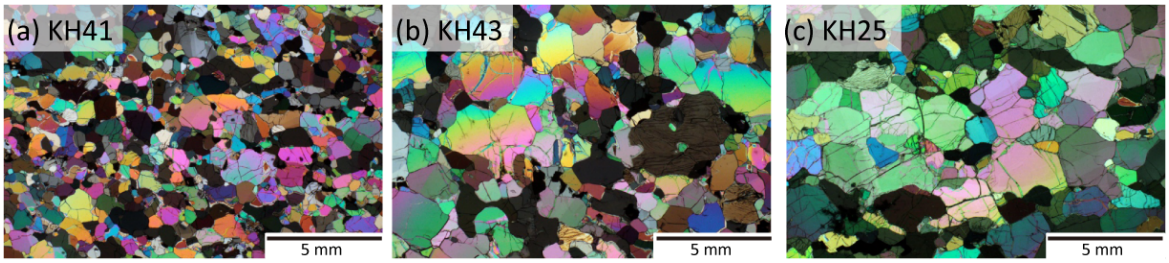

Figure 2. Photomicrographs of peridotite xenoliths from Kilbourne Hole (scale bar is 5 mm). (a) KH41, fine grained lherzolite. (b) KH43, protogranular lherzolite. (c) KH25, porphyroclastic harzburgite.

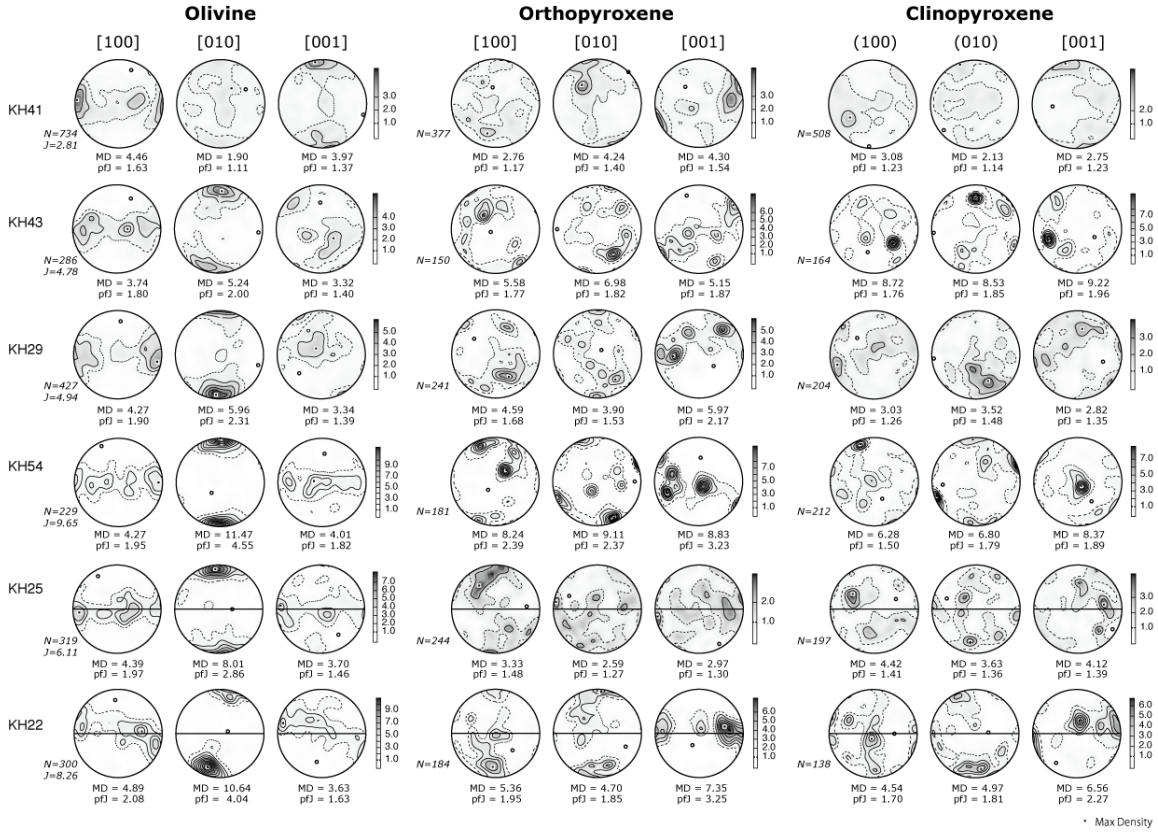

Figure 3. Crystallographic preferred orientations (CPOs) of olivine, orthopyroxene and clinopyroxene. Lower hemisphere, equal-area stereographic projections, contours at one multiple of uniform distribution. N is the number of measured grains. *J* and *pfJ* are indexes of fabric intensity, and MD is the maximum density.

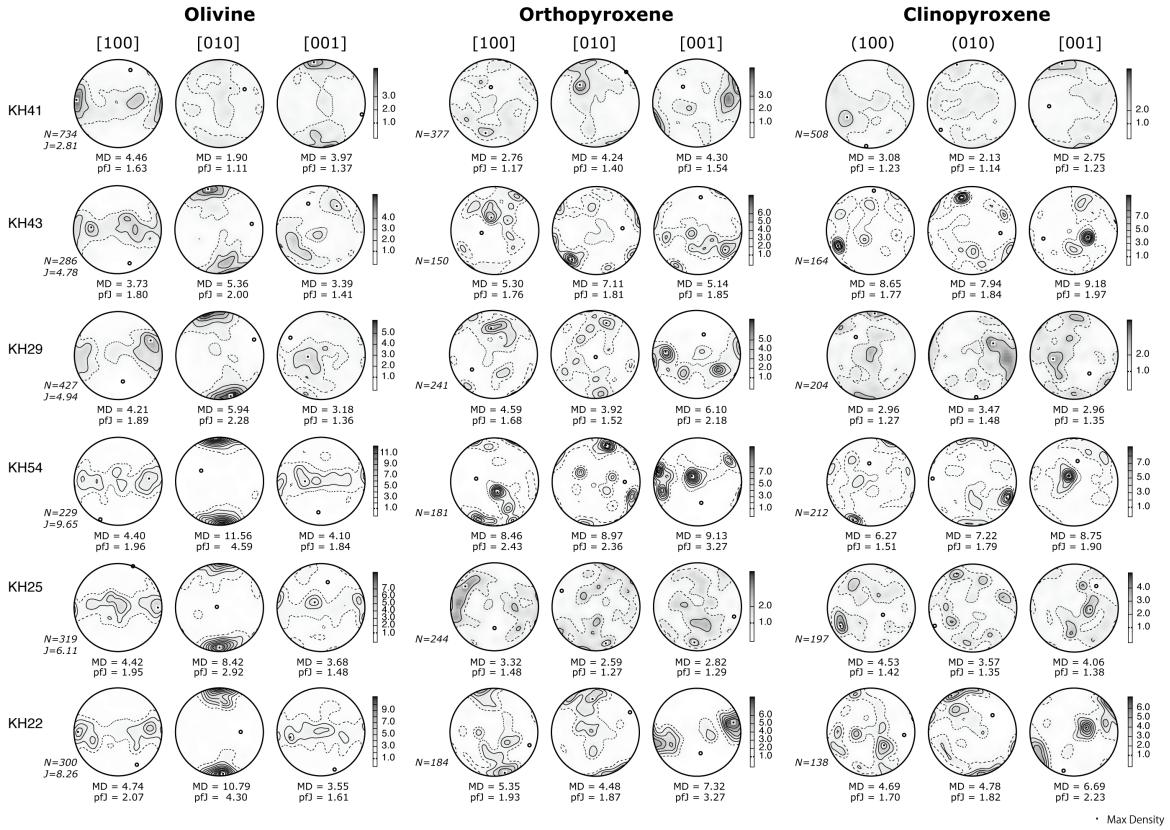

Figure 4. Olivine, orthopyroxene and clinopyroxene CPOs. To maximize the average seismic anisotropy in Figure 6, the orientation data for each sample were rotated to align the maximum calculated Vp with to the reference direction X (east or west in the pole figure) and the minimum calculated Vp with Z (north or south in the pole figure).

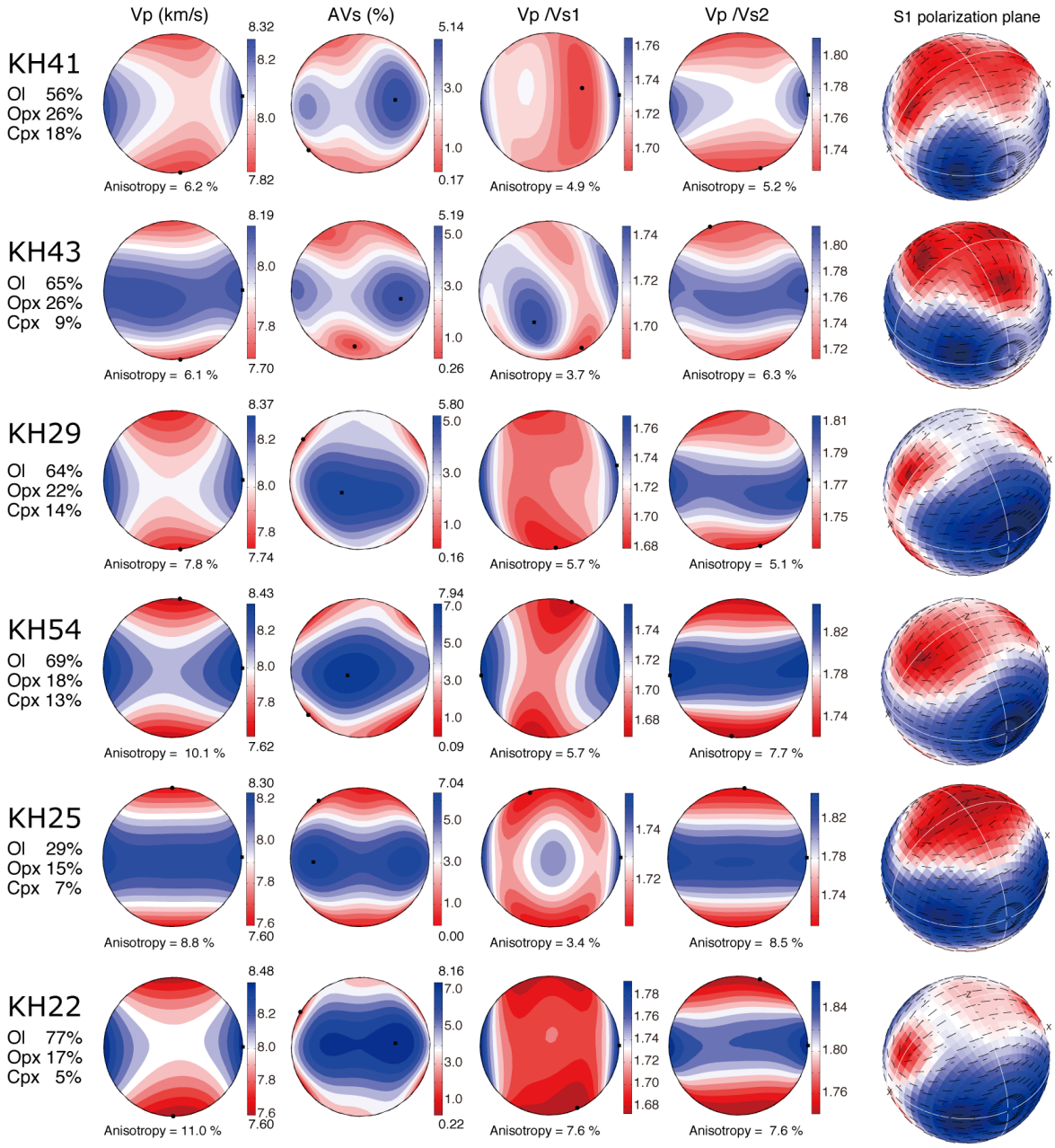

Figure 5. Calculated seismic properties of xxx. From left to right: P-wave velocity and anisotropy, S-wave anisotropy, Vp/Vs_1, Vp/Vs_2, and polarization of the fast shear wave S_1.

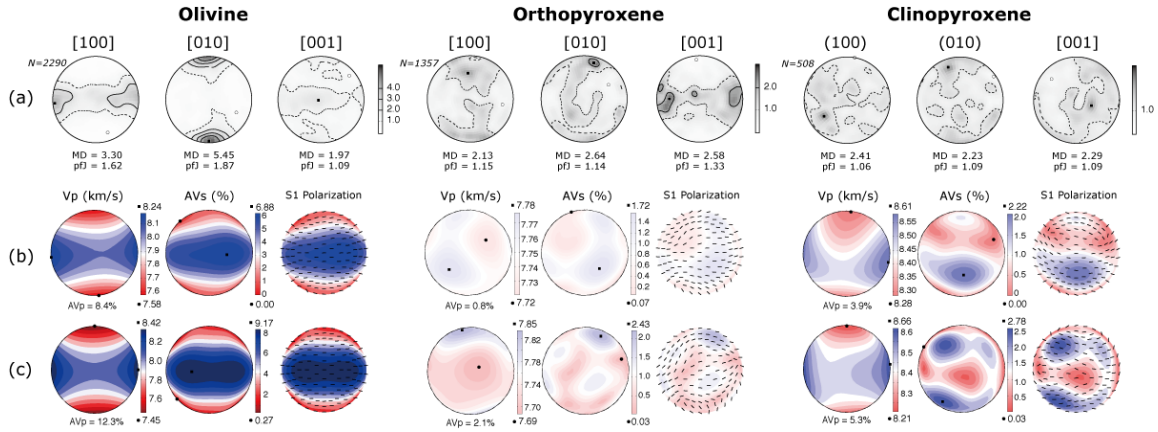

Figure 6. (a) Crystallographic preferred orientation (CPO) data for the average sample, obtained by summing the CPO of six peridotite xenoliths. CPOs are plotted on equal-area, lower-hemisphere projections, contours are multiples of the uniform distribution, N is the number of measurements, *pfJ* is an index of fabric intensity, and MD is the maximum density. (b, c) Seismic properties of the average sample for each mineral (olivine, orthopyroxene, and clinopyroxene) computed from the average CPOs based on one-point-per grain data (b), and gridded data (c), at a temperature of 1000 °C and pressure of 1.5 GPa. Contours are multiples of uniform density. The Vp plot shows the three-dimensional distribution of the P-wave velocity, anisotropy is $(Vp_{max} - Vp_{min})/(Vp_{mean})$; AVs is the three-dimensional distribution of the polarization anisotropy of S-waves due to S-wave splitting; S1 is the polarization plane of the fast split S-wave (S1), as a function of the orientation of the incoming wave relative to the structural frame of the sample. Each small segment represents the trace of the polarization plane at the point at which S1 penetrates the hemisphere.

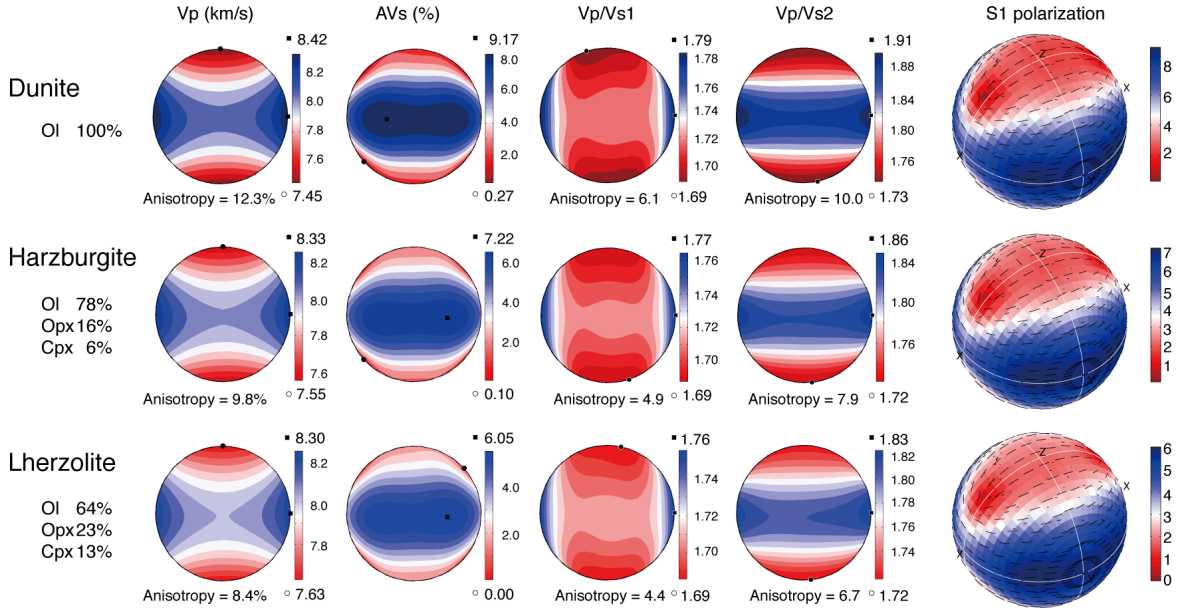

Figure 7. Seismic properties of the average dunite, harzburgite, and lherzolite (from Fig. 6a) at a temperature of 1000 °C and a pressure of 1.5 GPa. From left to right: P-wave velocity and anisotropy, S-wave anisotropy, Vp/Vs_1, Vp/Vs_2, and polarization of the fast shear wave S_1.

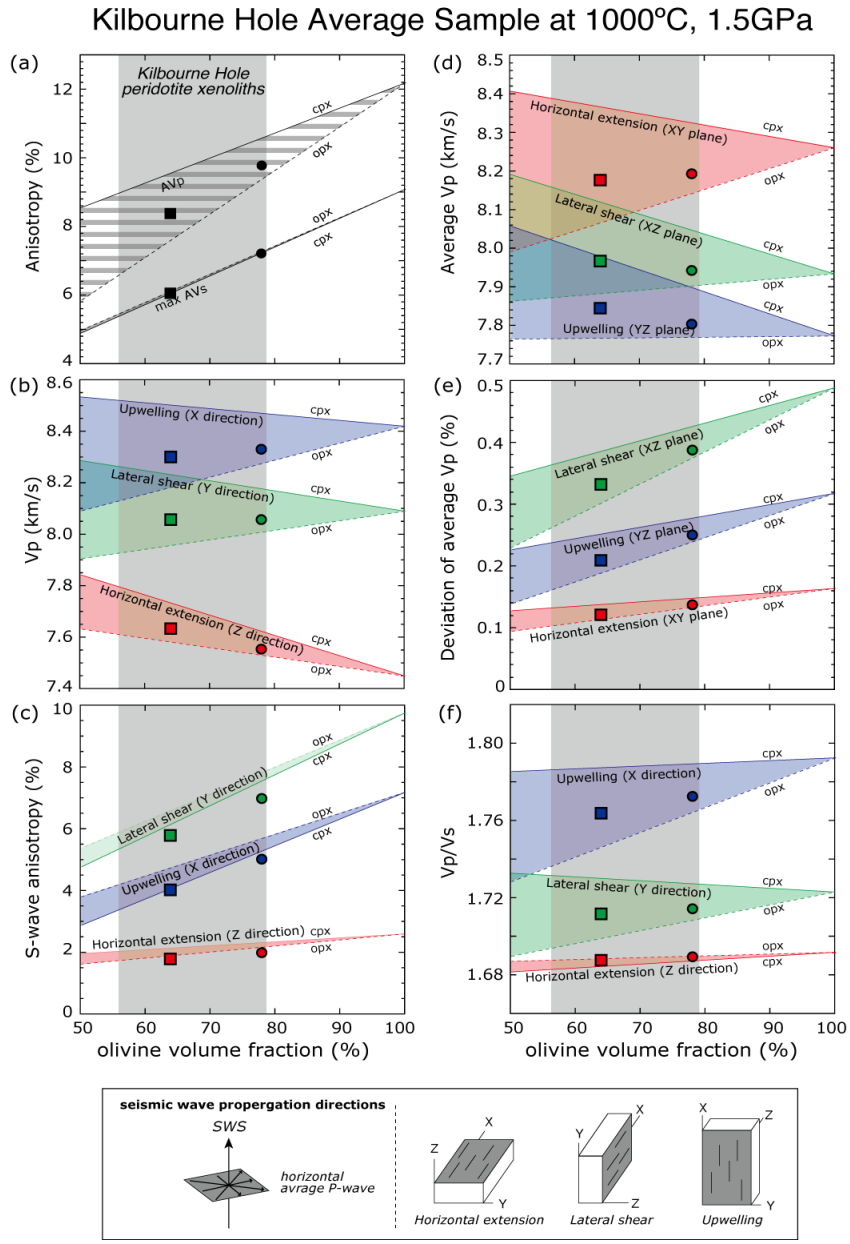

Figure 8. Variations in (a) Vp anisotropy and the maximum Vs anisotropy, (b) Vp, (c) S-wave anisotropy, (d) average Vp, (e) deviation of average Vp, and (f) Vp/Vs as a function of mantle composition at a temperature of 1000 ºC and pressure of 1.5 GPa. Solid lines represent compositions ranging from 50% olivine + 50 % clinopyroxene to 100% olivine; broken lines represent compositions ranging from 50% olivine + 50 % orthopyroxene to 100% olivine. Contours are shown for three geodynamic models: red for horizontal extension, green for lateral shear, and blue for upwelling. Within the box, the shaded area represents the plane of the foliation, and lines indicate lineation. Symbols relate to the mean composition of the peridotites: squares for lherzolite and circles for harzburgite. Gray shaded areas represent the range of modal composition of peridotites.

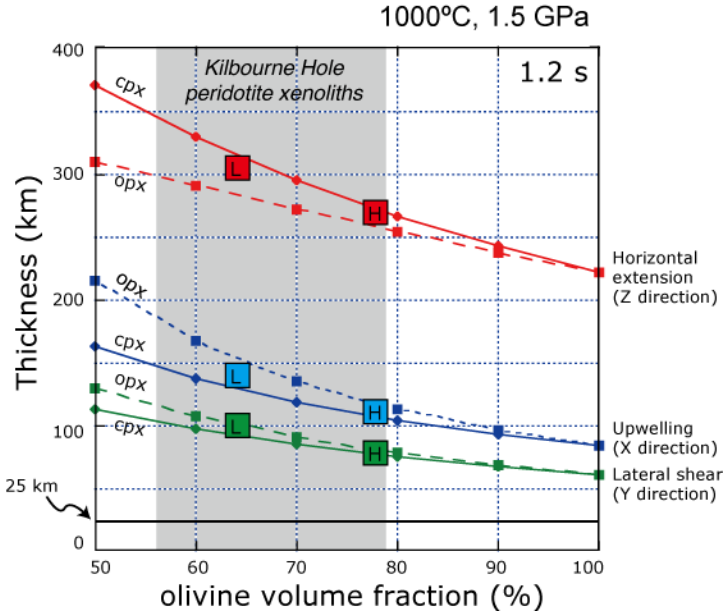

Figure 9. Relationship between the olivine volume fraction and the required anisotropic layer thickness in Kilbourne Hole, as inferred from peridotite xenoliths. Delay times is 1.2 s. H and L are the harzburgite and lherzolite shown in Fig. 7, respectively.

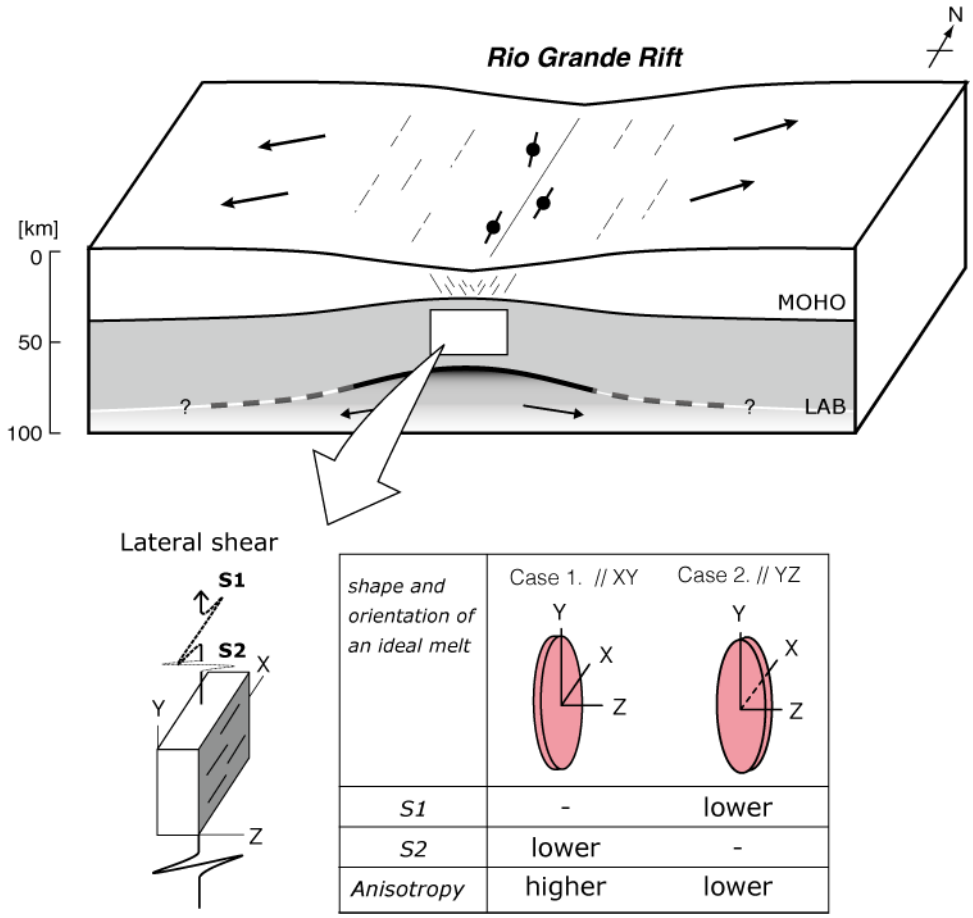

Figure 10. Schematic summary of the results, showing the possible tectonic model (lateral shear zone), and the shape and orientation of a representative average melt distribution beneath the Rio Grande rift.

Table 1. Lithology, modal composition (%), number of measurements, J-index values (calculated after Mainprice et al., 2000), max density (MD), pfJ values, and equilibrium temperature (Na/Opx-Cpx) for the six Kilbourne Hole peridotite xenoliths studied here.

Sample number	lithology	mode (%)			grain size (mm)	CPO olivine								T (ºC)	Ol Mg#	Sp Cr#
		ol	opx	cpx		N	J	[100] axis		[010] axis		[001] axis				
								MD	pf*J*	MD	pf*J*	MD	pf*J*			
KH41	fine-grained lherzolite	56	26	18	0.52	734	2.81	4.46	1.63	1.90	1.11	3.97	1.37	1009	0.90	0.10
KH29	fine-grained lherzolite	64	22	14	0.49	286	4.78	3.74	1.80	5.24	2.00	3.32	1.40	1040	0.89	0.07
KH43	protogranular lherzolite	65	26	9	0.69	427	4.94	4.94	1.90	5.96	2.31	3.34	1.39	1049	0.89	0.10
KH54	protogranular lherzolite	69	18	13	0.91	229	9.65	4.27	1.95	11.47	4.55	4.01	1.82	1102	0.89	0.11
KH22	porphyroclastic harzburgite	77	17	5	1.20	319	6.11	4.39	1.97	8.01	2.86	3.70	1.46	1152	0.91	0.32
KH25	porphyroclastic harzburgite	78	15	7	1.02	300	8.26	4.89	2.08	10.64	4.04	3.63	1.63	1094	0.91	0.22

Ol: olivine; Opx; orthopyroxene; Cpx: clinopyroxene; Sp: spinel; N: Number of measurements; J*:* *J*-index; MD: Maximum density; T: temperature, respectively.

Chapter 5

Uppermost mantle anisotropy beneath the southern Laurentian margin: Evidence from Knippa peridotite xenoliths, Texas

Originally Published in modified form as "Uppermost mantle anisotropy beneath the southern Laurentian margin: Evidence from Knippa peridotite xenoliths" by T. Satsukawa, K. Michibayashi, R. Urmidola, E. Y. Anthony, J. Pulliam and R. Stern, *Geophysical Research Letters*, **37** (L20312), doi:10.1029/2010GL044538, 2010,

Abstract

Peridotite xenoliths from southern Texas consist of spinel lherzolite, harzburgite and minor dunite. Based on phase relations and temperature of equilibration, Knippa xenoliths come from the uppermost mantle, 40-70 km deep. Knippa xenoliths provide rare snapshots of upper mantle processes and compositions beneath south-central Laurentia. They preserve olivine a-axis fiber fabrics with a strong concentration of (100) and girdles of (010) and (001). Assuming a lithospheric mantle that recorded a horizontal flow direction parallel to fast directions, the mantle lithospheric fabric revealed by the xenoliths mostly explains the magnitude of shear-wave splitting observed along the southern margin of the Laurentian craton.

Key words: peridotite xenoliths; Texas, mantle flow; crystallographic preferred orientation; seismic anisotropy

5-1. Introduction

The nature of ocean-continent transitional lithosphere is one of the complicated sites in the point of the evolution of ocean basins, which contains fundamental components of plate tectonics, and the presence of continental break-up remains controversial (e.g., Kendall et al., 2005). Recent passive seismological investigations provide fruitful avenues of inexpensive research to begin interrogating the lithosphere. Measuring shear-wave splitting (SKS) images the orientation and degree of polarization of mantle fabrics, and constrain models for the formation of these fabrics, including the mantle beneath south central North America (Gao et al., 2008). In spite of the robustness of SKS measurements, it is often not clear if

anisotropy inferred from these measurements resides in the mantle lithosphere or asthenosphere (e.g., Fouch and Rondenay, 2006). Here we are interested in understanding fabrics for mantle xenoliths from southern Texas, and use this information to interpret shear-wave splitting for upper mantle beneath the northern margin of the Gulf of Mexico (GoM) (Fig. 1). A previous study documented significant shear wave splitting beneath this region, with fast directions parallel to the Texas GoM continental margin (Fig. 1; Gao et al., 2008). They noted that SKS splitting reached an apparent maximum where the crust was thinnest and discussed the parallelism of the observed mantle anisotropy and the SE edge of the Laurentian cratonic keel.

In this study, we present new SKS results, and petrofabric data for spinel peridotite xenoliths from Knippa, Texas, and use these results illuminate the origin and significance of shear wave splitting beneath southern Laurentia (Fig. 1). The seismic anisotropy resulting mainly from olivine crystallographic preferred orientations (CPO) tends to show a maximum seismic velocity parallel to the direction of plastic flow within the upper mantle (Nicolas and Christensen, 1987). Assuming that shear-wave splitting reflects mineral CPO, we can use CPO measured in mantle xenoliths to better understand uppermost mantle structure beneath south central North America, and the elastic coefficients of minerals to evaluate the delay time along ray paths.

5-2. Geological setting

A quarry near Knippa, Texas (Fig. 1) exposes Late Cretaceous basanites containing upper mantle xenoliths. This is the only known mantle peridotite locality in Texas (Young and Lee, 2009). Mantle xenoliths were carried up by Late Cretaceous

(~87 Ma) quite primitive nephelinites of the Balcones Igneous Province (BIP) (Griffin et al., 2010). BIP volcanoes approximate the boundary between the ~1.1-1.4 Ga southernmost Laurentian (Texas) craton and Jurassic age transitional lithosphere along the GoM margin. The transitional lithosphere also involves the deformed rocks of the Ouachita fold belt (Keller et al. 1989).

Knippa peridotites are spinel lherzolite and harzburgite (plus minor dunite) consisting of olivine (Ol), orthopyroxene (Opx), clinopyroxene (Cpx) and spinel (Sp). Minerals have high Mg#: Ol ($Fo_{89-91.6}$), Opx ($En_{89.3-92.3}$) and Cpx (Mg#=90.4-93.4). Cr# (atomic Cr/(Cr+Al)) in Sp show moderate depletion, ranging from 0.14-0.21 for lherzolite to 0.25-0.36 for harzburgite, indicating that lherzolite experienced 5-9% melt depletion compared to 11-14% for harzburgite. Temperatures determined using the Ca in Opx thermometer (Brey and Köhler, 1990) range between 900 and 1000 °C. Based on the ubiquitous presence of spinel and absence of garnet (Takahashi et al., 1993), and on the equilibrium temperatures, Knippa xenoliths come from the uppermost mantle, from depths of 40-70 km. The temperatures are high for a steady-state geotherm, except for a lithosphere enriched in heat-producing elements (HPE) near its base (Stein et al., 1993). Alternatively, the temperatures may represent transient conditions associated with BIP magmatism. Young and Lee (2009) note that Knippa peridotites are enriched in fluid-mobile trace elements (e.g., La) relative to fluid-immobile trace elements (e.g., Nb). They inferred that such fractionation reflects subduction-related metasomatism of Laurentian lithospheric mantle due to ~1 Ga plate convergence.

5-3. Microstructural and Fabric Analyses

In this study, we selected eight peridotite xenoliths for detailed petrophysical

analyses to evaluate the effect of olivine CPO on seismic-wave properties. The xenoliths are coarse-grained and equigranular, with grain boundaries that range from triple junctions to smoothly curving boundaries. The spinels are elongate, bleb-shaped and dark brown in plane-polarized light. Some spinels and Cpx show corroded rims. Olivine grains are large and commonly contain subgrain boundaries (Fig. 2a). Serpentine veins occur in two peridotite xenoliths and cut olivine grains (Fig. 2a). These serpentine veins are identified as lizardite by Raman spectroscopy at the University of Tokyo, Japan.

To examine deformation conditions in more detail, we measured the CPOs of olivine grains from highly polished thin sections using a scanning electron microscope equipped with an electron backscatter diffraction system (EBSD), housed at the Center for Instrumental Analysis, Shizuoka University, Japan. We determined Ol, Opx and Cpx crystal orientations, and visually checked the computerized indexation of the diffraction pattern for each crystal orientation.

The dominant slip system in olivine was determined from the orientations of the axes of subgrain rotation and CPO data (see 2-5-3. Analysis of subgrain rotation axes in Chapter 2 for details). We rotated the CPO data such that the “foliation” became horizontal and the “lineation” became E-W. Subsequently, using data from the eight xenoliths, we compiled the CPO of an average sample (1740, 533 and 282 measurements for Ol, Opx and Cpx, respectively), giving the same weight to each measurement, independently of the number of measurements in each xenoliths (Fig. 2b, Table 1). The average olivine CPO data show an a-axis fiber pattern characterized by a strong concentration in (100) with weak girdles of (010) and (001), whereas the CPOs of enstatite and diopside show nearly random fabrics (Fig. 2b).

5-4. Rock Seismic Properties

We calculated the seismic properties of the peridotite xenoliths from single crystal elastic constants, crystal density, and the CPO of Ol, Opx, and Cpx, assuming different scenarios: either a composition of 100 % Ol (for each sample as well as the average sample), or the actual modal composition of the rock (dunite, lherzolite and harzburgite). The elastic constants and averaging scheme used in our calculations are described in *Michibayashi et al.* (2009).

Fig. 2(c) and Table 1 presents the seismic properties of the peridotite xenoliths. The maximum seismic anisotropy of S-waves varies between 5.09 and 8.26% for 100% olivine, whereas average samples vary between 4.35 and 6.12% along with variations of mineral composition (Table 1). Polarization anisotropies of most samples have two maxima girdles on each side of a plane normal to the (100) maximum, whereas the minimum birefringence occurs for propagation directions close to the (100) maximum (Fig. 2c). The orientation of the polarization plane of the fastest S-wave systematically marks the orientation of the great circle that contains the maximum concentration of (100) (Fig. 2b). These anisotropic patterns are quite common globally, as previously reported (e.g., Mainprice et al., 2000).

5-5. Seismic data

Five broadband, three-component seismographs were deployed between Junction and San Antonio, TX from February through August 2008 at an average spacing of 28 km (Table 2) (Pulliam et al., 2009). The transect extended form the Laurentian craton to the edge of the craton and, possibly, onto the stretched and thinned transitional crust of the Texas Gulf Coastal Plain. Receiver function results for

the same stations indicate crustal thickness of 32 km at GCP05 vs. 45 km at GC01 (Pulliam et al., 2009).

For each temporary station, as well as for the permanent ANSS station JCT, SKS splitting measurements were made for 22 deep-focus (h>50 km) teleseismic events with magnitudes greater than 6.0 using the Matlab-based SplitLab software (Wüstefeld et al., 2008). SplitLab simultaneously computes splitting parameters via three independent techniques: (a) the rotation-correlation method (e.g. Bowman and Ando, 1987), which maximizes the cross-correlation between the radial and transverse component of the SKS phase, (b) the minimum energy method (Silver and Chan, 1991), which minimizes the energy on the transverse component, and (c) the minimum eigenvalue method (Silver and Chan, 1991).

For measurements to be accepted, we required that results for both the minimum energy and rotation-correlation methods each display clear minima in their error surfaces and be consistent with each other, i.e., within 0.2 s of delay time and 20° with respect to fast polarization direction. On average, only five events satisfied these criteria for our stations during their seven-month deployment. Fig. 1 shows averaged results for the best five events at each station, including the permanent station JCT, located near Junction, TX. Our results for Junction (Table 2) confirm the results reported previously by Gao et al. (2008). Results from the five temporary stations show rapidly increasing delay times but only small changes in the fast polarization direction as one progresses from Junction toward the southeast.

5-6. Discussion and Conclusions

The region that spans the northern GoM margin underwent two complete cycles of continental rifting (ca. 540 and 170 Ma) and collisional orogeny (ca. 1000

and 350 Ma) along the southern flank of Laurentia (e.g., Thomas, 2006). These events include the late Mesoproterozoic Grenville orogeny, early Cambrian rifting and passive margin formation, late Paleozoic Ouachita orogeny during the final stages of assembly of Pangaea, and formation of the modern continental margin accompanied by brief seafloor spreading and oceanic crust formation during the Jurassic (ca. 165 Ma).

The lithosphere that formed or was reworked during these tectonics events is preserved across a region that extends from the Grenville province of the craton (Anthony, 2005) to Jurassic oceanic crust in the GoM. The Moho beneath the Texas passive margin is approximately 40 km deep (Gao et al., 2008). As described above, Knippa peridotites come from 40-70 km deep (Raye et al., 2009). Therefore, we consider it likely that the Knippa peridotite xenoliths are derived from the uppermost mantle lithosphere. We note that the region is dominated by alternate episodes of extension and compression (Fig. 1). The associated mantle fabric could preserve some of this deformation, suggesting an important potential for tectonic inheritance and overprinting.

The strong gradient in shear wave splitting observed along the traverse near Knippa implies a shallow, i.e. lithospheric, source for the anisotropy. One possible explanation invokes flow in the lithospheric mantle as a mechanism for aligning olivine fast axes: the Coastal Plain appears to have a crust that is on the order of 10 km thinner than the craton (Mickus et al., 2009). This would allow a correspondingly thicker lithospheric mantle and, therefore, longer paths for SKS to accumulate splitting times, assuming flow channeled around the cratonic keel aligns crystals' a-axes effectively.

Gao et al. (2008) argued that the magnitude of anisotropy must be 5.5–10%

(Fig. 3) in order to produce the observed 0.9 to 1.6 s splitting time, assuming that the lithosphere beneath the region is 70 km thick (Fig. 1). Our measurements constrain the intrinsic anisotropy within the lithospheric mantle, although the original orientations of the peridotite xenoliths were lost during their volcanic transport to the surface (e.g. Michibayashi et al., 2009). As noted above, the average Knippa peridotite shows 4.35 to 6.12% anisotropy depending on mineral compositions, whereas individual samples vary range from 5.09 to 8.26% in case of Ol 100% (Fig. 3). Consequently, the observed delay times are mostly explained by the seismic properties of the mantle lithosphere sampled by Knippa peridotite xenoliths.

To explain the variation of splitting time near station JCT is complicated. The thickness (T) of an anisotropic layer is given by T = (100dt<Vs>)/AVs, (e.g., Pera et al., 2004). Accordingly, the observed delay time (0.5 – 1.5 s at JCT) can be explained by the seismic properties of our peridotite xenoliths for an approximately 50 to 150 km thickness. However, it is difficult to produce the observed variation in split times over lateral distances of a few tens of km with this explanation alone. For example, if we use the AVs of a highly deformed sample (sample number; 10 shown in Table 1), the long delay time (1.5 s) requires 85 km thickness. Therefore, a more likely candidate is deformation caused by collision between Laurentia and Gondwana during the late Paleozoic, which produced large amounts of deformation, including the folded Ouachita mountain chain. Varying amounts of deformation would produce corresponding variations in the alignment of olivine fast directions in the lithospheric mantle. Such deformation can both vary significantly over short distances and can vary in its effectiveness in aligning crystals. In the case of Oman ophiolites, major shear zones seem to have developed at the contact between a flowing asthenosphere (young) and a frozen lithospheric (old) wall, a thermal boundary inducing a

characteristic asymmetry (Nicolas and Boudier, 2008). Consequently, the long delay time can be explained by fabric variation, that is, peridotites beneath the transitional crust could preserve greater deformation from the Paleozoic Ouachita orogeny (young) rather than the lithosphere beneath the Mesoproterozoic craton (old). Overall, the Knippa peridotite xenoliths demonstrate the possible occurrence of an anisotropic layer in the uppermost mantle lithosphere that could be related to 'frozen' deformation associated with the alternate processes of extension and compression beneath the southern Laurentian margin.

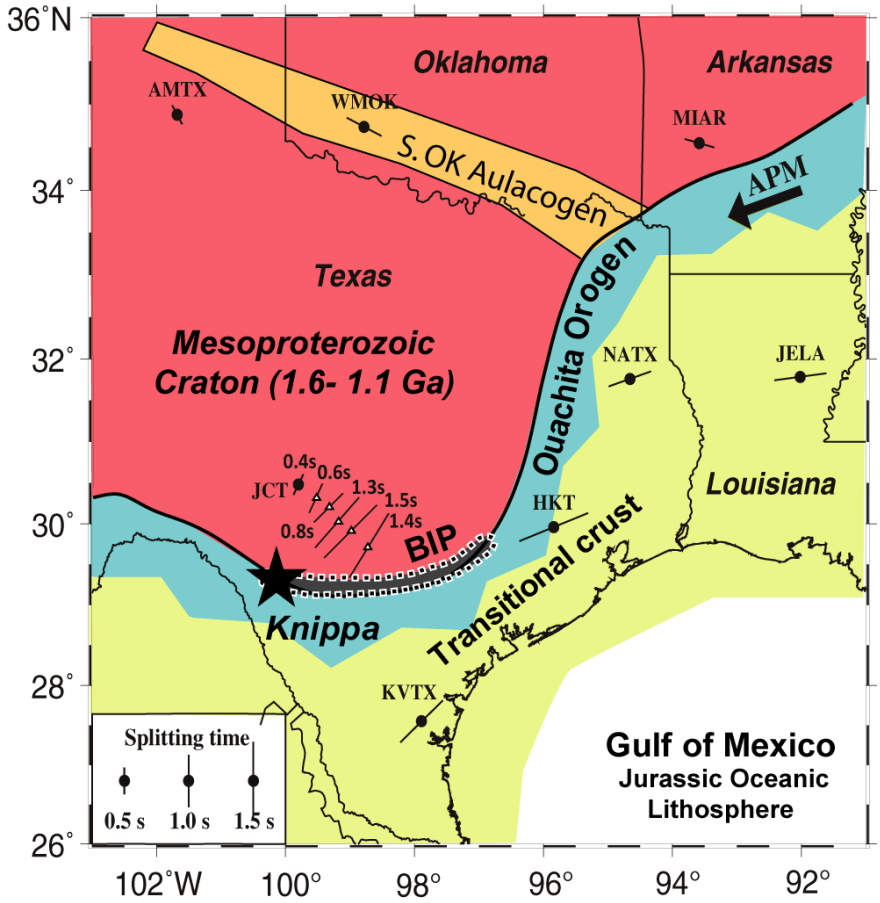

Figure 1. Location of Knippa and principal tectonic features of the south central USA. The peridotite xenoliths are from the Knippa quarry in Uvalde County, TX (star). SKS results shows shear-wave splitting time and shear-wave fast directions. Circles: results of Gao et al. (2008), triangles: results from this study (Table 2). The arrow represents the absolute plate motion (APM).

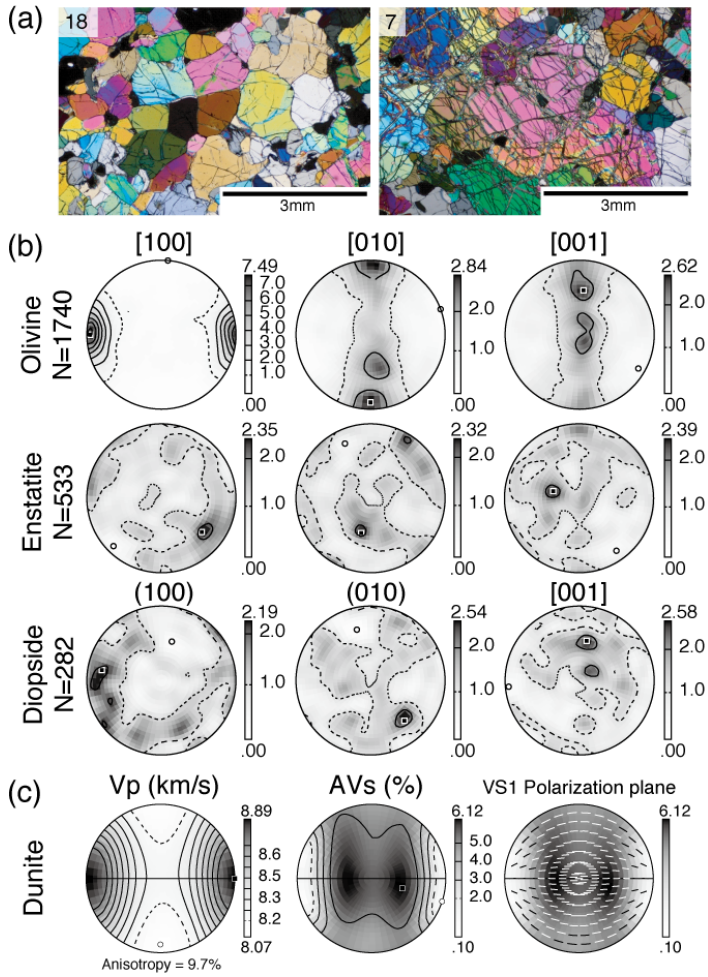

Figure 2. (a) Photomicrographs of Knippa peridotite xenoliths (cross-polarized light). In some samples, olivine is cut by serpentine veins. Scale bar is 3 mm, 18 and 7 are sample numbers. (b) CPO data of the average sample (Table 1) obtained by the EBSD technique. CPOs are plotted on equal-area, lower hemisphere projections. Contours are multiples of the uniform distribution. N is the number of measurements. (c) Seismic properties of the average sample computed from single crystal elastic constants, crystal density, and the average CPOs of olivine. Contours are multiples of uniform density. The Vp plot shows the 3D distribution of the P-wave velocity, anisotropy is (Vpmax-Vpmin)/Vpmean. AVs (seismic anisotropy of S-waves) is the 3D distribution of the polarization anisotropy of S-waves owing to S-wave splitting. Vs1 plane shows the polarization plane of the fast split S-wave (S1) as a function of the orientation of the incoming wave relative to the structural frame of the sample. Each small segment represents the trace of the polarization plane on the point at which S1 penetrates the hemisphere.

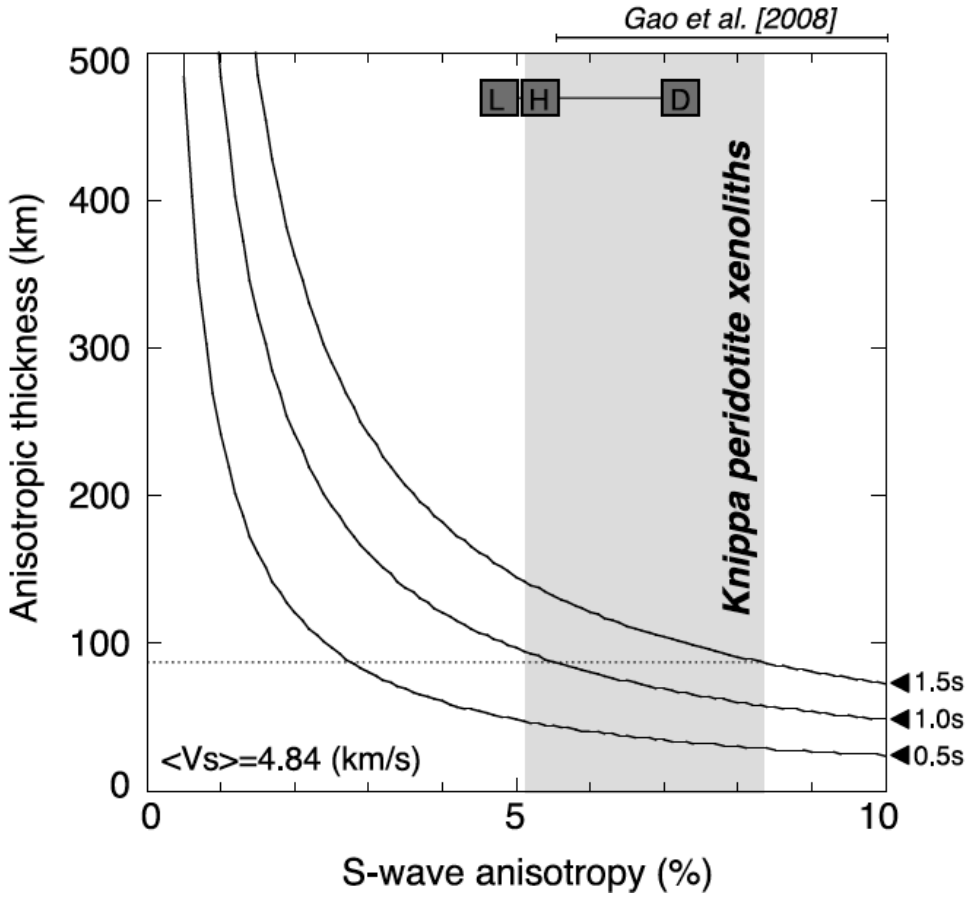

Figure 3. Relationship between the S-wave anisotropy (AVs) and the required anisotropic layer thickness in Knippa peridotite xenoliths calculated as 100% olivine. Shear-wave splitting time is 0.5 to 1.5 s, from Gao et al. (2008). Gray area shows the range of AVs obtained by individual samples. D, H and L are dunite harzburgite, and lherzolite average samples shown in Table 1.

Table 1. Modal composition (%), number of measurements, J-index values (calculated after Mainprice et al., 2000) and seismic properties (Vp, AVp, AVs, Vs_1, Vs_2) for the 8 Knippa peridotite xenoliths studied here. The last three lines report the crystallographic data and the seismic properties of average samples. The average samples are calculated from the sum of all measurements, giving the same weight to each measurement.

Sample number	Modal composition				CPO olivine		Seismic Anisotropy							
	ol	opx	cpx	sp	N	J	Vp (km/s)		AVp (%)	AVs (%)	Vs_1 (km/s)		Vs_2 (km/s)	
							Max	Min		Max	Max	Min	Max	Min
1	63	25	10	2	225	4.60	8.81	8.09	8.4	5.09	4.97	4.86	4.86	4.66
3	69	20	8	3	202	5.29	8.83	8.09	8.7	5.59	5.01	4.84	4.85	4.64
6	70	20	8	2	217	5.55	8.98	8.06	10.8	7.35	5.03	4.84	4.87	4.60
9	82	15	2	1	220	4.61	8.82	8.07	8.9	6.13	4.98	4.84	4.88	4.64
10	80	13	5	2	208	11.42	9.04	8.07	11.3	8.26	5.06	4.82	4.87	4.59
13	68	20	9	3	219	6.05	8.98	8.02	11.4	7.34	5.03	4.86	4.89	4.59
16	81	14	5	1	231	6.67	8.94	8.02	10.8	6.81	5.00	4.85	4.90	4.60
18	75	20	4	1	218	5.94	8.79	7.97	9.8	6.36	5.03	4.80	4.85	4.66
AS (D)	100	0	0	0	1740	-	8.89	8.07	9.7	6.12	5.01	4.84	4.87	4.63
AS (H)	80	15	5	0	-	-	8.75	8.08	7.9	4.92	4.97	4.84	4.86	4.67
AS (L)	70	18	12	0	-	-	8.89	8.07	7.1	4.35	4.95	4.83	4.85	4.68

Ol: olivine; Opx; orthopyroxene; Cpx: clinopyroxene; Sp: spinel; N: Number of measurements; J*:* *J*-index; MD: Maximum density; AS: Average sample. D, H and L are dunite, harzburgite, and lherzolite average samples, respectively.

Table 2. Station locations and SKS splitting results from the 2008 broadband deployment. Delay times between the fast and slow polarization directions are indicated by δt; the orientation of the fast polarization direction, with respect to north, is indicated by Φ.

Station	Latitude (°)	Longitude (°)	Elevation (m)	Sensor	δt	Φ
JCT	30.48	-99.8	581	Streckeisen STS2	0.42	28
GC01	30.33	-99.53	681	Guralp CMG-3ESP	0.57	24
GC02	30.2	-99.34	634	Guralp CMG-3ESP	0.8	44
GC03	30.02	-99.21	598	Guralp CMG-3T	1.3	42
GC04	29.91	-99.01	487	Guralp CMG-3ESP	1.5	46
GC05	29.73	-98.74	468	Guralp CMG-3ESP	1.44	34

Chapter 6

Mantle microstructure and seismic properties in spreading/rifting zones

6-1. Microstructural and petrological characteristics in the four studied peridotite xenolith localities: a summary

The uppermost mantle in back arc regions is the site of complex interactions between deformation, partial melting, fluid migration, and melts percolation. In order to constrain these interactions and their effects on olivine fabric, we have presented the detailed fabric analysis and calculated the seismic properties induced by rock anisotropies of 4 different localities (2 in the Japan sea back-arc; 2 in United States) in Chapters 2 to 5. Figure 1 shows the average olivine CPOs of each of the four localities.

In Chapter 2, I present the microstructures, geochemical analysis, crystallographic preferred orientations (CPOs), and water contents of spinel peridotite xenoliths from two localities in the back arc region of Japan arc: Ichinomegata (NE Japan) and Oki-Dogo (SW Japan).

The mineral chemistry of Ichinomegata peridotites show a typical residual peridotite trend, depleted in LREE (light rare earth element). Olivine CPO of Ichinomegata peridotites are consistent with slip on (010)[100] and {0kl}[100] (Fig. 1a), and the angle between the [100] maximum concentration and the foliation decrease with increasing fabric strength. By using those angles, shear strain is estimated to vary from 0.31 to 4.26, and temperature variation possibly suggest that *J*-index increases with decreasing depth. These observations suggest that a strain gradient revealed by the studied peridotite xenoliths could be related to back-arc spreading. Three structural markers are identified in samples and thin sections of Ichinomegata peridotites: foliation defined by pyroxene rich layers, the [100] maximum concentration of olivine, and shape preferred orientation of olivine. From the angular relationships between these three structures, the shear plane is considered

to be parallel to the [100] maximum concentration of olivine (not the foliation). These structural features are compatible with those described in the Oman ophiolite (e.g., Ceuleneer et al., 1988).

Oki-Dogo peridotites are affected by various degrees of metasomatism by melt derived from the upwelling asthenosphere. Water content in pyroxenes is low, suggesting that water in peridotites was easily moved in melts if water was contained in rocks before the metasomatism. Pyroxenes coexisting with olivine appear to retain their initial OH contents better than olivine even though the main minerals in the mantle (olivine, orthopyroxene and clinopyroxene) are nominally anhydrous (e.g., Peslier et al., 2002). Olivine CPOs of Oki-Dogo peridotites are consistent with the (010)[100] slip system (Fig. 1b). Samples have low Mg# and show relatively high concentration in [010]. Although peridotite xenoliths from Oki-Dogo Island could be deformed in the presence of melt as indicated by chemistry, there is no strong interaction between deformation and melt percolation recorded by the crystallographic fabrics.

In Chapter 3, we present the seismic properties caclulated for peridotite xenoliths from Ichinomegata and Oki-Dogo to illuminate the origi n and significance of shear-wave splitting in the uppermost mantle in the back arc region of Japan arc. Ichinomegata peridotite xenoliths demonstrate the possible occurrence of an anisotropic layer in the uppermost mantle lithosphere, with an estimated thickness of about 20 km. Olivine forsterite contents in Oki-Dogo peridotites varied continuously from 86 to 90, so that seismic properties were calculated by taking into account variable elastic constants and mineral density. Although the rock density and S-wave velocity decrease with increasing of olivine forsterite content, P-wave and S-wave anisotropies do not show significant changes.

In Chapter 4, we present detailed petrofabric data and seismic properties calculated for peridotite xenoliths from Kilbourne Hole maar, New Mexico, to illuminate the origin and significance of shear-wave splitting in the uppermost mantle beneath the Rio Grande rift. Peridotite xenoliths consist of spinel lherzolite, harzburgite, and dunite. Olivine CPOs indicat the preservation of b-axis fiber fabrics with a strong concentration of [010] with girdles of [100] and [001] (Fig. 1c). Three geodynamic models are considered for the source region of these xenoliths: horizontal extension, lateral shear, and upwelling. After calculating seismic properties, I conclude that these xenoliths were derived from a lateral shear zone (vertical foliation (XY plane) and horizontal lineation within the plane of the foliation (X-axis)). However, the degree of seismic anisotropy generated by peridotite xenoliths alone is limited, so that the existence of melt in thin cracks or dikes may be invoked; the orientation of such melt pockets parallel to the XY plane in either model would result in an increased anisotropy. As a result, the shear-wave splitting observed in the Rio Grande rift is inferred to be a reflection of both the lithospheric structural fabric and the presence of melts as thin cracks or dikes.

Knippa xenoliths provide rare snapshots of upper mantle processes and compositions beneath south-central Laurentia. In Chapter 5, we present new SKS results and petrofabric data for spinel peridotite xenoliths from Knippa, Texas, and use these results to interpret for the understanding of the origin and significance of shear wave splitting beneath southern Laurentia. Peridotite xenoliths consist of spinel lherzolite, harzburgite and minor dunite. They preserved olivine a-axis fiber fabrics with a strong concentration of [100] and girdles of [010] and [001] (Fig. 1d). Assuming a lithospheric mantle with a horizontal flow direction parallel to fast directions, the mantle lithospheric fabric revealed by the xenoliths mostly explain the

magnitude of shear-wave splitting observed along the southern margin of the Laurentian craton. Consequently, the long delay time could be explained by fabric variation of peridotites beneath the transitional crust, which could preserve greater deformation from the Paleozoic Ouachita orogeny (young) rather than representing the lithosphere beneath the Mesoproterozoic craton (old). Overall, the Knippa peridotite xenoliths demonstrate the possible occurrence of an anisotropic layer in the uppermost mantle lithosphere that could be related to 'frozen' deformation associated with the alternate processes of extension and compression beneath the southern Laurentian margin.

6-2. The evolution of the uppermost mantle during back-arc spreading

The four localities investigated in this study overall contribute to the understanding of lithospheric extension, more specifically of back-arc spreading. Schematic models showing the uppermost mantle behavior during back-arc spreading are presented in Fig. 2 and 3. Ichinomegata and Oki-Dogo peridotite xenoliths document distinct stages of spreading of the Japan Sea back-arc region.

Ichinomegata peridotites xenoliths recorded normal seafloor spreading (Fig. 2) (Chapter 2), whereas Oki-Dogo peridotites recorded the extension and the thinning of continental crust during incipient continental break-up (Fig. 3) (Chapter 2). For comparison, we have studied spinel peridotite xenoliths from other extensional tectonic settings: Kilbourne Hole (New Mexico, USA; Chapter 4) and Knippa peridotites (Texas, USA; Chapter 5) (Fig. 4). Peridotite xenoliths from Kilbourne Hole represent the early stages of spreading in an active rift zone (Fig. 4a and Chapter 4), whereas Knippa peridotites xenoliths come from the mantle lithosphere that could have recorded deformations in relation to the thinning of continental crust (Fig. 4b and

Chapter 5).

The uppermost mantle evolution recorded in Ichinomegata peridotite xenoliths is consistent with a vertical strain gradient during the latest geological event (seafloor spreading) of back-arc spreading (Chapter 2). Oki-Dogo peridotites show no clear change in microstructure and CPO with metasomatism, and the slip system is mostly (010)[100] rather than AG-type (Chapter 2). Thus, we do not observe pronounced changes in olivine CPO related to metasomatism, i.e., there is no strong interaction between percolation of melts and deformation recorded by fabrics (Chapter 2). In contrast, there is strong concentration of [010] in peridotites from Kilbourne Hole (Fig. 3a), which possibly documents the deformation in the presence of melts during continental rifting (Chapter 4).

The differences between the peridotite xenoliths from the Japan Sea and Kilbourne Hole in New Mexico, USA, may result from the different time scale and dimension between the two tectonic events (back-arc spreading and continental rifting). Whereas back-arc spreading covers several hundreds kilometers and continued for about 10 million years in the Japan Sea (Chapter 2), Kilbourne Hole is located in the Rio Grande rift, which underwent widespread extension in several hundreds kilometers during the past 35 million years (Chapter 4). The microstructural and geochemical characteristics of Oki-Dogo peridotite xenoliths were affected by the supply of upwelling-derived melts, at the end of the overall opening of the Japan Sea, which may trigger the termination of back-arc spreading (Chapter 2). Olivine CPO of Knippa peridotites is consistent with slip on {0kl}[100] with strong concentration in [100] (Chapter 5). Knippa is located in the Laurentian continental margin and records the deformation related to alternate extension and compression (Fig. 4b and Chapter 5). There are no samples in back-arc regions in Japan Sea that show strong fabrics like

Knippa, indicating that this strong CPO could have developed during these continuous deformations.

Overall, the active spreading starts (from the northeast parts in the case of Japan Sea) where the uppermost mantle deformed similar system to the mid ocean ridge spreading (Fig. 2). After that, passive extension, which depending on the surrounding environments, was induced in the southwest region (Fig. 3). There are no strong reactions between melt percolation and deformation in comparison with the continental rift zone, probably due to the relatively small size of the considered region, and to the relatively short period of time. In conclusion, this study document the uppermost mantle evolution during back-arc spreading, which is one of the key for to understanding the dynamics if this process.

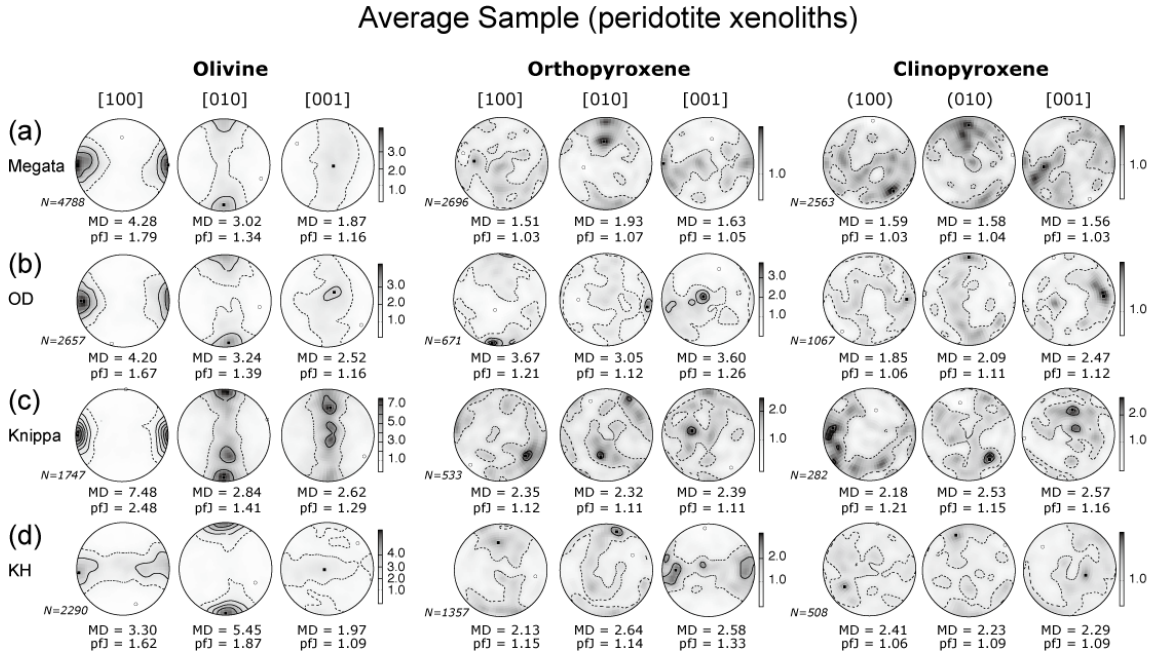

Figure 1. Crystallographic preferred orientation (CPO) data for average xenolith samples, obtained by summing the CPO of each peridotite xenolith from (a) Ichinomegata, (b) Oki-Dogo, (c) Knippa, and (d) Kilbourne Hole. CPOs are plotted on equal-area, lower-hemisphere projections, contours are multiples of the uniform distribution, N is the number of measurements, *pfJ* is an index of fabric intensity, and MD is the maximum density.

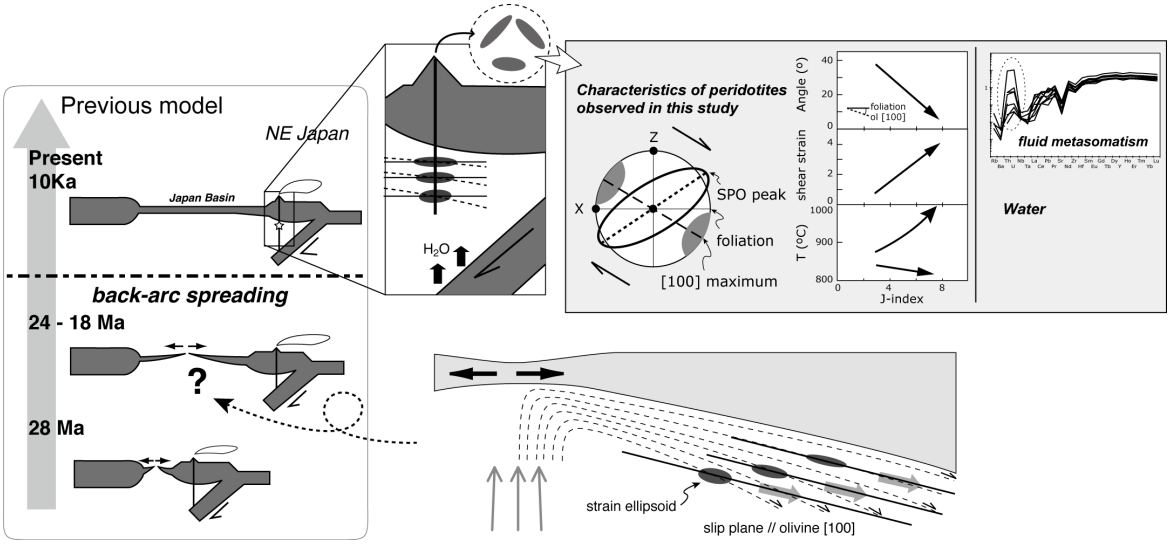

Figure 2. A summary of microstructural and petrological characteristics of the Ichinomegata peridotite xenoliths, and a schematic model of the uppermost mantle evolution during back-arc spreading. Previous model of the opening of the Japan Sea was modified after Tamaki (1995).

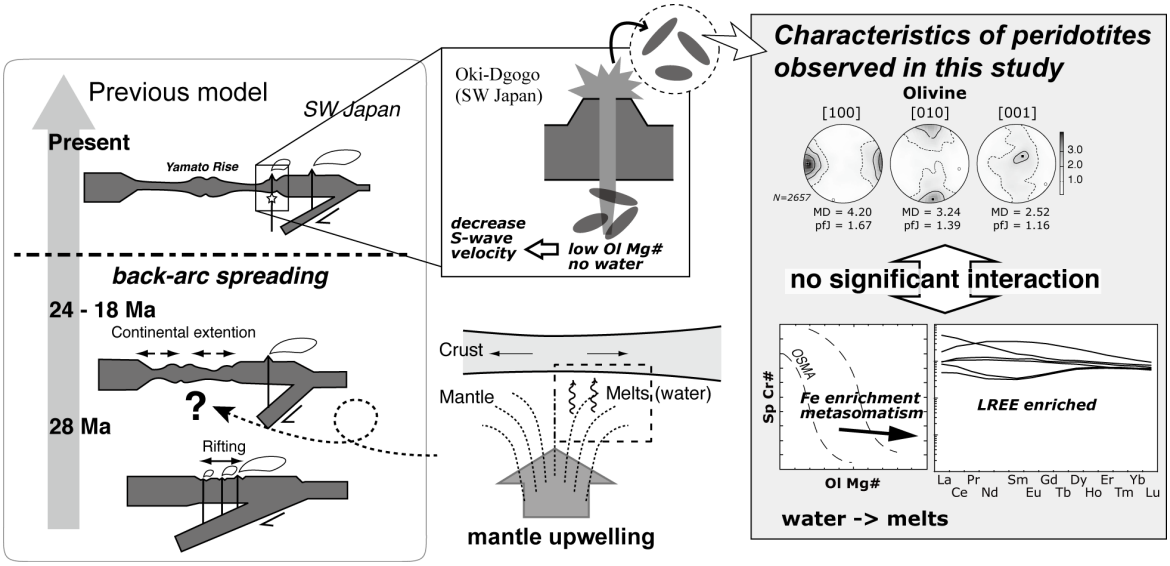

Figure 3. A summary of microstructural and petrological characteristics of the Oki-Dogo peridotite xenoliths, and a schematic model of the uppermost mantle evolution during back-arc spreading. Previous model of the opening of the Japan Sea was modified after Tamaki (1995).

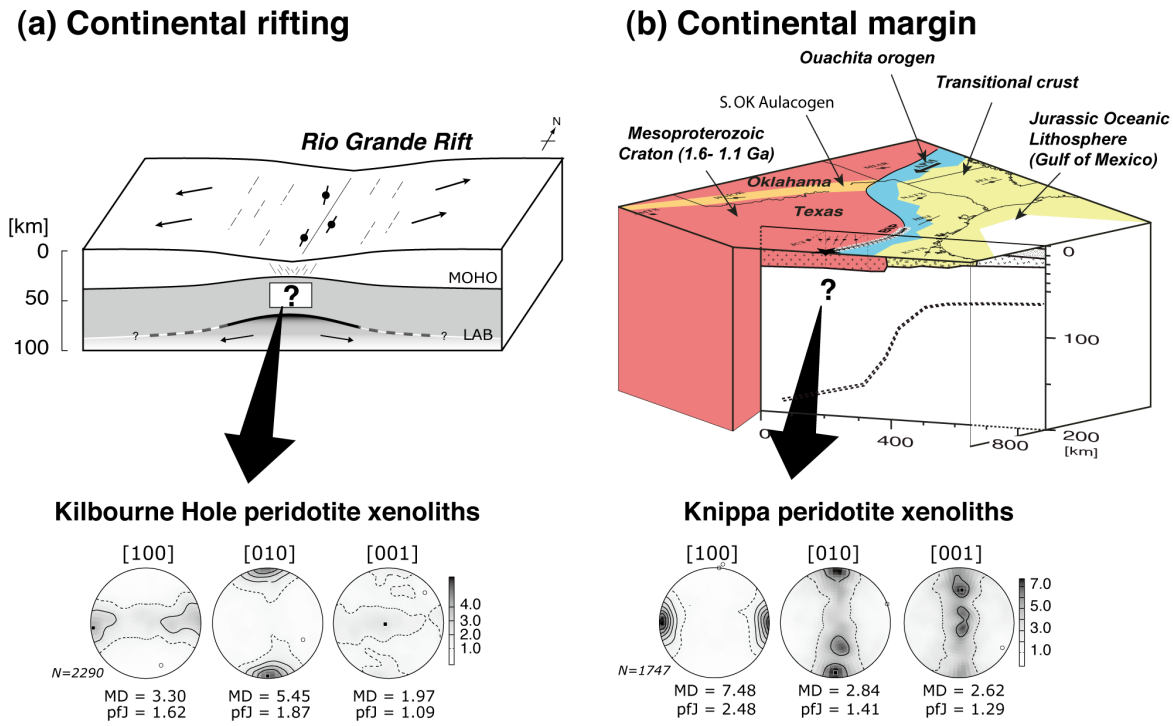

Figure 4. Fabric characteristics in the continental rifting (a) and continental margin (b) tectonic settings.

PART II

A plagioclase fabric database: Characterization of CPO and seismic properties in the lower crust

Chapter 7

A plagioclase fabric database: Characterization of CPO and seismic properties in the lower crust

Abstract

This chapter presents a unique database of almost 200 plagioclase Crystallographic Preferred Orientations (CPO) of variously deformed gabbroic rocks. The CPO characteristics as a function of deformation regime (magmatic and crystal-plastic) are outlined and discussed. CPO of principal mineral phases are also used to calculate the seismic properties of variously deformed gabbroic rocks from the oceanic lithosphere. The studied samples are from slow- and fast-spread present-day ocean crust, as well as ophiolites. Plagioclase is the dominant mineral phase in most of the studied samples. Plagioclase CPO is grouped in three main categories: B) a strong alignment of (010) with a girdle distribution of [100], A) a strong point maximum concentration of [100] with parallel girdle distributions of (010) and (001), and P) point maxima of [100], (010), and (001). A majority of CPO patterns are type B and type P, in samples showing both magmatic and crystal-plastic deformation textures. Type A CPO are less common; they represent 24 % of the samples deformed by crystal-plastic flow. Calculated seismic properties (P-wave and S-wave velocities and anisotropies) show that anisotropy (up to 11% for P-wave and 15% for S-wave) tends to increase as a function of fabric strength. Despite of a large variation of fabric patterns and geodynamic setting, seismic properties of plagioclase-rich rocks have similar anisotropies in magnitude. In most of the samples, P-wave propagation is fastest parallel to the highest density of (010) and slowest normal to the highest density of (010). The polarization plane of the fastest S-wave (Vs_1) is parallel to the great circle containing the (010) maximum. The *J*-index does not show any consistent variation as a function of the CPO patterns. However, the [100] concentration has an influence on the seismic anisotropies in crystal-plastic

deformed samples. On the other hand, the (010) plane alignment has a strong influence on seismic anisotropies in samples deformed by magmatic flow.

Key words: plagioclase; gabbro; fabric strength; crystallographic preferred orientation; EBSD; seismic anisotropy

7-1. Introduction

Studies of the crystallographic preferred orientations (CPO) of naturally deformed materials provides crucial insight into geodynamic processes (e.g., Nicolas and Christensen, 1987; Karato, 2008). They are a key component of our understanding of the physical properties (e.g., rheology, seismic velocities and its anisotropy) of mantle or crustal rocks. Plagioclase is the dominant phase in the lower crust, and the rheology of plagioclase-rich rocks controls the mechanical behavior of the lower oceanic and lower continental crust. However, in contrast with olivine CPO in peridotites (e.g., Ben Ismaïl and Mainprice, 1998), the plagioclase CPO in gabbros have rarely been studied in the past, because of the difficulty of measuring low-symmetry crystal orientations using the universal stage.

From natural samples, Montardi and Mainprice (1987) studied the crystal-plastic deformation of calcic plagioclase (An 68 - 70) using transmission electron microscopy (TEM). They observed four kinds of slip system; (010)[001], (001)[100], 1/2[111](011) and |101|(101). Harigane et al. (2008), based on CPO analysis of gabbroic rocks from the Godzilla megamulliion, reported that the dominant slip system depends on the sample texture; (010)[100] for coarse-grained texture, (010)[100] and (001)[100] for medium-grained type, and fine-grained texture have (001)[100] or random fabric. In layered mylonites from ODP Hole 735B, Mehl and

Hirth (2008) also showed that (010)[100] and (001)[100] are the dominant active slip systems. The (010)[001] slip system was observed in medium to high grade metamorphic condition (e.g., Kruhl, 1987; Zhao. 1997), and from optical and TEM investigation in experimentally deformed aggregated and single crystal (e.g., Olsen and Kohlstedt, 1984; Ji and Mainprice, 1988). Stünitz et al. (2003) performed deformation experiments of single crystals of labradorite under the condition of 900ºC and 1.0 GPa, and identified two dominant slip systems, (010)[001] and <110>(001). Svahnberg and Piazolo (2010) used natural plagioclase rich rocks under lower to mid crustal transition condition (675 – 700ºC, 350 – 450 MPa). From the observation of CPO in continuous recrystallized bands, they concluded that strain was localized and deformation system shifted from dislocation creep to dislocation-accommodated grain boundary sliding, with a single dominant (001)[110] slip system. Barreiro et al. (2007) observed that dominant slip system was (010)[100], with subsidiary (010)[001] and (001)[100] with torsion and axial compression experiment under 950 – 1200 ºC and 400 MPa. Pearce et al. (2011) investigated the mafic dykes intrusions in the Lewisian Complex (NW Scotland). The CPO of plagioclase was developed by dislocation creep with four slip system; (112)[110], (112)[110], (001)[110] and (001)[110]. However, these CPO patterns are very weak and they show relatively strong concentration in (010) and (001).

The seismic anisotropy of plagioclase aggregate is still poorly documented. Kono et al. (2009) measured P- and S-wave velocities of the lower crust rocks from the Kohistan arc under the condition of 25 – 400 ºC and 0.1 – 1.0 GPa. They found that plagioclase-free garnet pyroxenite showed significantly higher Vp and Vs than plagioclase-rich garnet granulite mainly due to the low Vp and Vs of plagioclase, even though Vp and Vs increased with increasing volume percent of garnet.

The database of plagioclase CPO presented herein would provide a significant understanding for the implication for the interpretation of seismic data in gabbroic rocks, in which plagioclase is the dominant phase. In the recent ~10 years, the use of the EBSD (Electron Back-Scattered Diffraction) technique to characterize crystallographic textures of Earth materials made the measurements of plagioclase much easier. We present here a large (183 samples) database of plagioclase CPO that documents various geodynamic settings and various deformation conditions. CPO data are used to calculate and discuss seismic properties of gabbroic rocks. The samples have been measured using the EBSD facilities at Géosciences Montpellier.

7-2. Sample locations and Geological Background

Table 1 lists the 183 gabbro samples compiled in this study, which represent various geodynamic settings. Most of the data presented herein are unpublished data; References to published data are given in Table 1. A majority of samples (82.1 %) are from present-day or ophiolitic ocean crust.

7-2-1. Fast-spreading ocean crust samples

54.7 % of the samples are from gabbroic rocks formed in fast-spreading environments (Oman ophiolite, Hess Deep, and ODP Hole 1256D). Although the precise initial geodynamic setting of the Oman ophiolite remains debated, the nearly continuous ocean crust present in this ophiolite makes it a classical analogue for present-day fast-spreading crust (e.g., Nicolas et al., 2000; MacLeod and Yaouancq, 2000). Hess Deep (2º14’N, 101º33’W; Hey et al., 1972) is the deepest part of a westward-propagating rift valley that is opening up the eastern flank of the equatorial EPR in advance of the westward-propagating Cocos-Nazca spreading center. The

gabbros used herein were sampled on the intra-rift ridge during ODP Leg 147 (Gillis et al., 1993), and with the UK ROV ISIS during the RSS James Cook JC21 Cruise in Jan-Feb 2008 (MacLeod et al., 2011). ODP Hole 1256D (6°44.2′ N, 91°56.1′ W) is located in an area of the Cocos plate crust that formed 15 m.y. ago on the eastern flank of the EPR at a superfast spreading rate (~220 mm/y full rate; Wilson, 1996). ODP Site 1256 formed on a ridge segment at least 400 km in length, ~100 km north of the triple ridge junction between the Cocos, Pacific, and Nazca plates. The samples presented in this compilation are from the petrologically complex sheeted dike – gabbro transition zone (Wilson et al., 2006; Koepke et al., 2011).

7-2-2. Slow spreading ocean crust samples

27.4% of the studied samples come from slow-spreading ocean crust. Most of them were collected in ODP Hole 735B, close to the Southwest Indian ridge. ODP Site 735 is located on the Atlantis Bank, a 11 m.y. old shallow oceanic core complex located 18 km east of the Atlantis II Transform Fault. Hole 735B was drilled to the depth of 1503 meter below seafloor, over two ODP Legs (118 and 176, in 1987 and 1997, respectively; Robinson et al., 1989; Dick et al., 1999, 2000). It recovered dominantly medium- to coarse-grained crystalline gabbroic rocks from a tectonically exposed lower crustal section, 23% of which are deformed the crystal-plastic, dislocation creep regime (Dick et al., 2000). A few samples presented herein come from ODP Holes 1270B, 1275B and 1275D, drilled during Leg 209 at the Mid-Atlantic Ridge in the 15°20' N fracture zone area (Kelemen et al., 2004).

7-2-3. Other samples

The remaining of the samples compiled herein (17.9) are from various

locations, representing a variety of gabbroic rocks (*sensu lato*) from different geodynamic settings. They include gabbros and charnockites from igneous intrusions in the Itabuna belt (Sao Francisco craton, Bahia, Brazil; Burgos, 2005), granulites from the Neoproterozoic Ribeira belt (Southeastern Brazil; Egydio-Silva et al., 2002), layered gabbros from La Réunion (Piton des Neiges volcano, Cirque de Salazie), one foliated anorthosite sample from the Precambrian Grenvillian basement in Oklahoma (USA; Seront et al., 1993), and basaltic lava flow samples from Saint Thibéry (Southern France; Bascou et al., 2005).

7-3. Methods

7-3-1. CPO measurements

To evaluate the plagioclase fabric characteristics, and the effects of these fabrics on the seismic properties of gabbroic rocks, CPO were obtained by electron backscatter diffraction (EBSD) using the SEM-EBSD facility at Géosciences Montpellier, France. Kikuchi patterns were indexed manually or automatically using Channel software by Oxford Instruments HKL. The EBSD patterns were generated by the interaction of a vertical incident electron beam with a polished thin section, tilted at 70°, in a scanning electron microscopes (JEOL JSM 5600; CamScan X500FE Crystal Probe) equipped with an EBSD system at Geosciences Montpellier (France). For most measured sample, we obtained CPO maps covering almost the entire thin section (usually 35 mm long and 20 mm wide), with varying sampling resolution (generally 30 or 35 μm, depending on grain size). The indexation rates in the raw maps range from 50% to 80%. Other CPO, that were measured more than 10 years ago, when the automatic mapping was not yet fully functional, were obtained manually, in an interactive mode (i.e., the user can select the appropriate indexation pattern for

each measured point). The automatic mode allows one to acquire a data set (herein called gridded data) that is volumetrically representative of the analyzed sample. From each gridded data set, a new data can be extracted using the hkl software after identification of individual grains using misorientations between adjacent points, with one data per grain (herein called 1 point-per-grain data, or 1ppg data), thus allowing us to eliminate bias due to grain size heterogeneity. The 1ppg data are used below to plot the CPO pole figures and calculate their strength and symmetry.

7-3-2. CPO strength

We determined the fabric strength and distribution density of the principal crystallographic axes by calculating the *J*-index and *pfJ*-index (e.g., Mainprice et al., 2000; Michibayashi and Mainprice, 2004). The rotation matrix between crystal and sample co-ordinates is used to describe the orientation *g* of a crystal in sample co-ordinates. In practice, it is convenient to describe the rotation by a triplet of Euler angles (φ1, Φ, φ2; Bunge, 1982). The orientation distribution function (O.D.F.), *f(g)* is defined as the volume fraction of orientations with an orientation in the interval between *g* and *g*+*dg* in a space containing all possible orientations given by:

$$\Delta V/V = \int f(g)dg$$

Where $\Delta V/V$ is the volume fraction of crystals with orientation *g*, *f(g)* is the texture function $dg=1/8\pi^2 sin\Phi d\varphi_1 d\Phi d\varphi_2$ and is the volume of the region of integration in orientation space. To quantify the strength of CPO, Mainprice and Silver (1993) used the *J*-index, defined by Bunge (1982) as:

$$J = \int f(g)^2 dg$$

The *J*-index ranges from 1 for a random distribution to infinity for a single crystal (or perfectly aligned crystals). In a similar manner, the strength of a pole figure can be analytically defined by the PfJ index as:

$$pf\ J = \int P_{hkl}^{2}(\alpha,\beta)d\omega$$

Where α and β are the spherical co-ordinates of the considered direction in the pole figure, $P^2_{hkl}\ (\alpha, \beta)$ is the density in that direction for a given crystallographic pole defined by *hkl* and $d\omega = 1/2 \sin\alpha d\alpha d\beta$ is the volume of the region of integration. The index has a value of 1 for a random distribution and infinity for a single crystal (or an aggregate of perfectly aligned crystals). The recent MTEX MatLab toolbox (Hielscher and Schaeben, 2008) now allows one to calculate *J* for aggregates of triclinic minerals.

7-3-3. Calculation of seismic properties

Seismic properties of the polycrystal minerals are computed by averaging individual grain elastic-constant tensors as a function of the CPO and modal composition of a sample. Whenever available, the gridded data were used to calculate the seismic properties of the samples. This method enables the calculation of the three-dimensional distribution of seismic velocities in an anisotropic polycrystalline aggregate (Mainprice and Humbert, 1994). The calculated seismic velocities are an average of the contributions of the different mineral phases; in the present calculations, we used Voigt–Reuss–Hill averaging of single-crystal elastic constants at ambient conditions (plagioclase: Wenk and Kroll, 1985; clinopyroxene: Collins and Brown, 1998; orthopyroxene: Chai et al., 1997; olivine: Abramson et al., 1997; Amphibole: Aleksandrov and Ryzhova, 1961). Anisotropy of seismic velocities (AVp and AVs) is defined (in percent) as $(V_{max} - V_{min})/ (V_{max} + V_{min})$.

7-4. Sample Microstructures

Rock types, modal compositions and microstructural observations are listed in Table 2 for all samples in this study. Mineral composition is plagioclase + clinopyroxene ± olivine ± amphibole (± orthopyroxene). Typical plagioclase microstructures in this study are shown in Fig. 1. The samples can be classified into two types, magmatic flow texture (Fig. 1a-d) and crystal-plastic deformed texture (Fig. 1c, f). The magmatic flow samples consist of coarse-grained aggregates with straight or curvilinear grain boundaries (Fig. 1a, b). Plagioclase grains are commonly oriented and define a foliation (Fig. 1a). In some samples grain boundaries have more irregular shapes (Fig. 1c, d). These microstructures are characteristics of incipient high temperature plastic deformation, which overprint magmatic flow textures. Samples deformed by significant crystal-plastic flow (Fig. 1e, f) are commonly characterized by the joint occurrence of porphyroclasts and neoblasts. Porphyroclasts consist of plagioclase and clinopyroxene, whereas neoblast are commonly only plagioclase. Some ultramylonitic samples from Hole 735B also show recrystallized olivine and clinopyroxene. Small-grained size textures (Fig. 1e, f) are from localized shear zones, resulting from enhanced strain rate and/or decreasing lithospheric temperature. For all samples in this study, deformation type was defined for each sample (Table 2). More than 60 % of samples have magmatic flow texture.

7-5. Crystallographic preferred orientation (CPO) of plagioclase

Measured CPOs are presented in equal-area, lower-hemisphere stereographic projections (Figs 2-4, Supplementary Figs. 1 – 7 in Appendix A). To obtain a representative CPO of the rock, the number of measured crystals must be at least 100

grains (Ben Ismaïl and Mainprice, 1998); Automatic mapping allows one to measure much more than this in general (Table 3).

Fast-spreading ocean crust samples

Gabbroic samples from fast-spreading environments are from the Oman ophiolite, Hess Deep, and ODP Hole 1256D. 49 plagioclase CPOs from Oman ophiolite gabbros and anorthosites (34 samples in Supplementary Fig. 1 and 15 samples in Morales et al., 2011) show relatively high concentrations of (010) poles with girdle concentration of [100] axes. Some samples show CPO patterns with concentration of both (010) and (001) poles perpendicular to the foliation, and with [100] axes distributed along the foliation plane (e.g., 95OB4, 98OB10G, 90OA77). From East Pacific crust Hole 1256D, we have 12 samples (Supplementary Fig. 4). Though the CPO is too weak to identify the slip system(s), (010) poles show relatively high concentrations (1256D_108_a, 1256D_109_b, and 1256D_112_a). The CPO of 38 samples from Hess Deep (Supplementary Fig. 5) are also weak and they also have relatively high concentration in (010) pole.

Slow-spreading ocean crust samples

Samples (56 samples) collected in ODP Hole 735B is the largest dataset in this compilation. They display various types of CPO (Supplementary Fig. 2). The majority of samples shows CPO patterns with girdle concentration of both (010) and (001) poles and with [100] axes distributed normal to them. Another type of pattern shows no girdle concentration, [100] and (010) are concentrated as point maxima (e.g., 735B-32, 735B-BI-82b). A few samples have the pattern commonly described in fast-spread crust, with strong (010) concentration (735B-BI-64a2). The three samples

from the Mid-Atlantic Ridge have CPO with no girdle concentration (Supplementary Fig. 7).

Other samples

The remaining of the samples compiled herein is from various locations (Supplementary Fig. 3). Samples of gabbros and charnockites from igneous intrusions in the Itabuna belt (Sao Francisco craton, Bahia, Brazil) and granulites from the Neoproterozoic Ribeira belt (Southeastern Brazil) show weak plagioclase CPO, do not show strong concentration in particular axes. The CPO of layered gabbros from La Réunion (Piton des Neiges volcano, Cirque de Salazie) show the same common type as in fast-spread ocean crust : (010) poles are strongly concentrated with girdle concentration of [100] and/or (001). Three samples of basaltic lava flow samples from Saint Thibéry (Southern France; Supplementary Fig. 7) show weak plagioclase CPO with (010) weak maximum. One foliated anorthosite sample from the Precambrian Grenvillian basement in Oklahoma (USA; Supplementary Fig. 7) shows a very strong concentration of (010) with clear girdle concentration of [100] and (001).

7-5-1. Typical CPO patterns

The measured samples overall show a large variability of fabric patterns. We can, however, classify them in three main groups (Fig. 2). **Type B** is defined by a strong concentration of (010) and a girdle distribution of [100], and it can be also called (010)-fiber pattern. **Type P** CPO shows point maxima of the three axes, however the concentration in (001) is often weak. **Type A** CPO has a strong point maximum concentration of [100] with parallel girdle distributions of (010) and (001). All of the plagioclase fabrics compiled in this study fall into one of these three groups,

as reported in the last column of Table 3.

7-5-2. Plagioclase CPO and microstructure

Figures 3 and 4 show typical examples of plastic flow and magmatic flow textures, respectively, with corresponding CPO's. Samples with typical magmatic textures systematically show, when they have a fabric, B type CPO with a strong concentration in (010), which indicates that the foliation is primarily marked by aligned plagioclase (010) planes (Fig. 3). The systematic relationship between plagioclase (010) concentration and magmatic foliation is already described in other studies (e.g., Morales et al., 2011). The CPO of 735B-BI-34 show A type CPO that [100] is sub-parallel to the foliation and (010) is normal to foliation (Fig. 4a), consistent with the classically described (010)[100] slip system (e.g., Montardi and Mainprice, 1987; Rosenberg and Stünitz, 2003). The CPO of other samples of plastically deformed samples show high concentrations of [100], consistent with the lineation direction, indicating that the activated plagioclase slip direction is [100] and slip plane might be from (010) to (001) (Fig. 4), which consistent with the Mehl and Hirth (2008).

7-5-3. Fabric strength

The literature on olivine CPO is abundant (e.g., Ben Ismail and Mainprice, 1998; Dijkstra et al., 2002; Tommasi et al., 2004; Linckens et al., 2011); and their relationships with deformation processes and intensity is well documented. In contrast, because of the inherent difficulty to measure low-symmetry crystal orientations in pre-EBSD times, the literature on plagioclase CPO is much less abundant (e.g., see references in introduction on slip-systems), and relationships with deformation

processes remain poorly documented. The calculated *J*-index of all plagioclase fabrics reported in this study is shown in Figs. 5, 6 and Table 3. We have removed the files with less than 100 measurements as *J* is then abnormally high. The files of the samples with $J > 20$ contain sequences of repeating euler angles phi1, PHI, and phi2, which suggests that grain detection must have failed on these two sets of measurements. The *J*-index ranges from 1.12 to 13.63, with a mean value of 4.05 and a standard deviation of 2.19. The fabric strength of samples with magmatic flow textures is very variable; in contrast, plastically deformed samples have relatively weak *J* (Fig. 6a). There are no strong relationships with the variation of *J*-index and CPO types (Fig. 6b).

7-5-4. Eigenvalue analysis of [100] and (010) pole figure symmetry

To characterize [100] and (010) pole figure symmetry, as it is important to identify the differences between B type and A type, we use the LS-index defined by eigenvalue analysis, which does not depend on contouring methods and is independent on the sample reference frame. This method is based on well-established technique of eigenvalue analysis of pole figures, and is presented in detail by Ulrich and Mainprice (2005), who used it to quantify CPO variations in omphacite. In the present study, there is a clear variation of the [100] and (010) from point maxima to girdle distributions. The LS-index is useful to characterize this variation. The three eigenvalues ($\lambda_1 \geq \lambda_2 \geq \lambda_3$, with $\lambda_1+\lambda_2+\lambda_3 = 1$) are used to define three fabric indices proposed by Vollmer (1990), point maximum ($P = \lambda_1 - \lambda_2$, P has a high value when $\lambda_1 > \lambda_2 \approx \lambda_3$), girdle ($G = 2(\lambda_2 - \lambda_3$, G has a high value when $\lambda_1 \approx \lambda_2 > \lambda_3$) and random ($R = 3\lambda_3$, R has a high value when $\lambda_1 \approx \lambda_2 \approx \lambda_3$). These indices range from 0 to 1, and $P + G + R = 1$.

The LS-index is defined as $1/2[2-\{P_{010}/(G_{010}+P_{010})\}-\{P_{100}/(G_{100}+P_{100})\}]$. In

this case, to determine if the plagioclase CPO is [100]-fiber pattern (type A) or (010)-fiber pattern (type B), we need to combine the eigenvalue analyses of the [100] and (010) pole figures as described above. Theoretically, the LS-index has a value of 1 for an ideal [100]-fiber pattern (type A) and 0 for and ideal (010)-fiber pattern (type B The LS-index of the studied samples is shown in Figure 7 and Table 3. It ranges from 0.12 to 0.89.). Figure 7b shows that our visual estimation of the CPO types (B, A, or P) are consistent with LS; the B-type CPO histogram is shifted toward the [010]-fiber end-member (LS=0), while the A-type CPO histogram is shifted toward the [100] fiber end-member (LS=1). The LS of samples which show type P CPO's clusters around 0.5. Samples with magmatic textures show a dominant type B signature (i.e., LS = 0; Fig. 7a), also consistent with our observation that magmatic sample CPOs are dominated by a strong maximum of (010). LS for CPOs of plastically deformed samples is more evenly distributed (Fig. 7a).

7-6. Seismic properties

We calculated four versions of the seismic properties, depending on the combination of CPO data (1ppg or gridded data) and modal composition (100% plagioclase or real composition) to show the effect of these parameters on the calculated properties :

1) 1ppg data with plagioclase 100% components (Table 4),

2) 1ppg data with real modal composition (Table 5),

3) gridded data with plagioclase 100% components (Table 6), and

4) gridded data with real modal composition (Table 7).

The results for some samples are shown in Figures 8 and 9.

Sample 86OA20A is an anorthosite, and contains dominantly plagioclase;

hence only plagioclase was measured (Fig. 8). Seismic properties are calculated from 1ppg data (Fig. 8a) and gridded data (Fig. 8b). P-wave propagation is fastest parallel to the highest density of (010) and slowest in the orthogonal direction (Fig. 4c). The polarization plane of the fastest S-wave (Vs_1) is parallel to the great circle containing the (010) maximum. Vp ranges from 6.50 to 7.04 km/s for the 1ppg version, and, from 6.44 to 7.06 km/s for the gridded data version. The differences between 1ppg data and gridded data of CPO reflect the effect of the heterogeneity of grain size. Gridded data of CPO in this case produces higher values of anisotropy for both P-wave and S-wave, but does not change the anisotropy patterns dramatically; P-wave anisotropy (AVp) changes from 8.0 % to 9.2 %, and maximum S-wave anisotropy (AVs_{max}) changes from 8.27 % to 16.68 % (Fig. 8).

Figure 9 shows an example of seismic properties calculated for a sample (735B-BI-15 from ODP Hole 735B) that contains several mineral phases (plagioclase, clinopyroxene, olivine, orthopyroxene and amphibole). Seismic properties were calculated either from the plagioclase CPO only (Figs. 9a, c), or from all CPO's and the modal composition (Figs. 9b, d). P-wave propagation is fastest parallel to the highest density of (010) and slowest normal to the highest density of (010) (Fig. 2). The polarization plane of the fastest S-wave (Vs_1) is parallel to the great circle containing the (010) maximum. The effect of additional mineral phases reduces the amount of anisotropy for both P-wave and S-wave to about half the value of the 100% plagioclase versions, but does not change the anisotropy patterns; AVp changes from 4.6 % to 2.6%, and AVs_{max} changes from 4.38 % and 2.87 % (Fig. 9a, b).

Figure 10 shows an example of seismic properties calculated for a sample (98OB10A from Oman ophiolite) that contains several mineral phases (plagioclase, clinopyroxene, olivine, orthopyroxene and amphibole). Seismic properties were

calculated either from the plagioclase CPO only (Fig. 10a), or from all CPO's and the modal composition (Fig. 10d). In contrast with 86OA20A (Fig. 8), P-wave propagation is fastest parallel to the highest density of [100] and slowest normal to the highest density of [100] (Supplementary Fig. 1). The polarization plane of the fastest S-wave (Vs_1) is parallel to the great circle containing the [100] maximum. As shown earlier (e.g., Siegesmund and Kruhl, 1991; Barruol and Mainprice, 1993), the shear wave splitting patterns are complicated, with no simple relationship to the macroscopic rock structure.

For the sake of a direct comparison of the effect of plagioclase with the olivine CPO database of Ben Ismaïl and Mainprice (1998), which proposed an analysis of peridotite seismic properties based only on olivine fabrics measured manually, we commonly use type 1) seismic properties for later discussion, although it does not realistically represent the seismic properties of gabbroic rocks. This also allows us to use those samples that were measured before the automatic mapping facility could be use in Montpellier. The P-wave velocity varies from 6.38 km/s to 7.30 km/s, the mean S-wave velocity varies from 3.29 km/s to 3.56 km/s, P-wave anisotropy varies from 1.00 % to 11.0 %, and the maximum S-wave anisotropy varies from 0.09 % to 13.58 %.

7-7. Discussion

7-7-1. Relationships between seismic anisotropy and fabric strength

In our database, the range of *J*-index for plagioclase CPO covers a much smaller range (1.1 to 13.6; Table 3) than that documented for olivine (3.2 to 27.0) by Ben Ismaïl and Mainprice (1998). Figure 11 shows the seismic properties as a function of *J* for both P-waves (Fig. 11a - d) and S-waves (Fig. 11e - h). As detailed in section

"5-6. Calculated seismic properties", seismic anisotropies are calculated different ways. In all cases, seismic anisotropy increases as a function of fabric strength, up to 11% for P-wave and 17% for S-wave. The seismic properties calculated for 100% plagioclase aggregates with 1ppg data can be directly compared with the olivine database of Ben Ismaïl and Mainprice (1998). AVp varies between 1.00 % and 11.0 %, with a mean value of 4.7% and a standard deviation of 2.00, AVs_{max} varies between 0.99 % and 13.85 %, with a mean value of 4.83 % and a standard deviation of 2.00 (Fig. 11a). Both anisotropies are smaller than those reported for olivine aggregates (AVp varies between 4.0 % to 21.4 % with mean value of 12.2 % and standard deviation of 3.9, AVs_{max} varies between 3.3 % to 17.4 % with mean value of 9.4 % and standard deviation of 2.6; Ben Ismaïl and Mainprice, 1998). Seismic anisotropy (for both P- and S-waves) increases as a function of fabric strength (Fig. 11a, e). This behaviour is similar to that reported for olivine aggregates, in which the value of AVp and AVs_{max} is also a function of fabric strength.

To compare the roles of fabric strength (J) and each crystallographic axis on the seismic anisotropy, we plotted seismic anisotropy as a function of J-index (Fig. 12a-d), pfJ index (Fig. 12e-h), and maximum density distribution (Fig. 12i-l) of each axis (Fig. 12). These anisotropies are calculated for plagioclase 100% with 1ppg data and data are plotted for the two different flow regimes (plastic flow and magmatic flow). The seismic anisotropy of both P- and S-waves increases with increasing pfJ and maximum density (Fig. 12e - l). It is clear that all three axes influence the magnitude of P- and S-wave anisotropy. In crystal-plastic deformed samples, the [100] have the strongest influence on the seismic anisotropies (Fig. 12e, g, i, k), whereas, (010) have a stronger influence on seismic anisotropies in magmatic flow samples (Fig. 12f, h, j, l).

7-7-2. The effect of CPO type on seismic anisotropy

Figure 13 shows the seismic anisotropy of both P- and S-waves as a function of fabric strength to compare the seismic signatures of the three CPO types B, P, and A. These anisotropies are calculated as plagioclase 100% with 1ppg data. Type B and P display a relatively wide range of both AVp and AVs, which covers almost the database. There is no obvious specific anisotropy signature for any of the three CPO type. (Fig. 13).

7-7-3. The effect of grain size heterogeneity on calculated seismic properties

The effect of the heterogeneity of grain size on seismic properties is significant, as illustrated by the differences between properties calculated with 1ppg and with gridded data (see section 5-6. "Calculated seismic properties"). This is further illustrated by figure 13, which compares the seismic properties calculated from 1ppg data and from gridded data for 100% plagioclase aggregates. Clearly the gridded data, in which the heterogeneity of grain size is taken into account, produces the higher seismic anisotropies. Some AVs_{max} data for magmatic flow samples plot very far away from the 1:1 correlation line (Fig. 14d), indicating that grain size distribution of these samples are more heterogeneous than others.

To compare with olivine, we calculated the seismic properties from the peridotite xenoliths studied in this thesis, using by 1ppg data and gridded data with olivine 100% (Fig. 15), because there is no gridded data in Ben Ismaïl and Mainprice (1998). As for plagioclase, the seismic anisotropy calculated from gridded data produces the higher seismic anisotropies. However, there is less deviation from the 1:1 correlation line than in the case of plagioclase, which likely reflects the fact that, in

the measured peridotite xenolith samples (Chapter 2 - 5), the grain size is less variable than in some of the plagioclase-bearing samples studied herein.

7-7-4. The effect of modal composition on seismic properties of gabbroic rocks

Plagioclase is the dominant phase in the lower crust and the rheology of plagioclase-rich rocks controls the mechanical behavior of the lower oceanic and lower continental crust. Plagioclase is therefore expected to be one of the dominant phases controlling the seismic properties in the lower crust. The result of our seismic modeling (e.g., Figs. 9 and 10) clearly shows that the effect of additional mineral phases in gabbroic rocks is to reduce the amount of anisotropy.

Figure 16 (Ildefonse et al., 2002), shows that the direction of fast propagation for Vp in a gabbroic rock depends on the modal composition. The seismic velocities are calculated for a foliated (magmatic texture) gabbro with a B-type CPO for the plagioclase, and a classical A-type CPO for Olivine (with a concentration of [100] parallel to the lineation). In 100% plagioclase aggregates, the fast direction is parallel to the direction orthogonal to (010), i.e., to the foliation (Z direction). In contrast, when the fraction of plagioclase is lower than 50%, the effect of olivine and clinopyroxene fast-direction (parallel to [100]) is to switch the fast propagation direction parallel to the lineation. When the rock contains about 50% of plagioclase, the anisotropy is null or very weak. This directly illustrates the competing effects of plagioclase and of olivine + clinopyroxene. This explains why the anisotropy is more scattered, when plotted as a function of the fabric strength *J* and when the calculated taking the modal composition into account (Fig. 11).

This effect of the modal composition of gabbroic rocks is further illustrated by figure 17, which shows the relation between the plagioclase content of the studied

samples and seismic anisotropy. The higher the plagioclase content, the higher the anisotropy; this effect is more particularly visible above 80% plagioclase, and less pronounced below that, with no visible effect of the flow regime. However, the relationship between the plagioclase content and seismic anisotropy is not as simple as predicted in the theoretical example of figure 16, with a higher anisotropy in plagioclase-poor aggregates. This is likely because the presence of amphibole in part of the studied samples, and also because the olivine CPO is in general very weak in most of the studied samples.

7-8. Conclusions

We present a compilation of 183 plagioclase CPO, and the corresponding calculated seismic properties for variously deformed gabbroic rocks from the oceanic lithosphere and continental lower crust. The studied oceanic samples are from both slow- and fast-spread crust environments. In most of the studied samples, plagioclase is the dominant mineral phase and forms a connected framework. About 37 % of the samples have been deformed by crystal-plastic flow.

CPO of plagioclase is classified in three main groups: B) a strong alignment of (010) with a girdle distribution of [100], A) a strong point maximum concentration of [100] with parallel girdle distributions of (010) and (001), and P) point maxima of the three axes. The Majority of the CPO patterns are type B and type P for both magmatic and crystal-plastic textures. The less common type A fabric is here reported for the first time. 24 % of samples deformed by crystal-plastic flow have type A fabric.

Most gabbros have relatively low seismic anisotropy (P- and S-waves) and complicated S-wave splitting patterns, with, in contrast to olivine, no simple

relationship to either flow regime or CPO-type. Seismic anisotropies generally increase as a function of fabric strength, up to 11% for P-wave and 15% for S-wave. However, this correlation is not as strong as for olivine. This partly explained by the average lower fabric strength. The seismic properties of plagioclase-bearing rocks contrast with those of peridotites, in which the seismic anisotropy (with the fast propagating direction parallel to the mineral lineation) primarily depends on the fabric strength. In gabbroic rocks, it depends also on the fabric strength, as well as on the plagioclase contents, because in foliated rocks, the plagioclase fast-direction is orthogonal to the olivine fast-direction. Despite a large variability of CPO patterns and geodynamic setting, seismic properties of plagioclase-bearing rocks have similar magnitudes of anisotropy. The fabric strength, characterized by the CPO *J*-index, does not show any consistent variation as a function of the CPO type. However, [100] seems to have a stronger influence on the seismic anisotropy in plastically deformed samples, while (010) dominantly controls seismic anisotropies in samples deformed by magmatic flow.

Although this database may be partly biased toward some specific series of samples (in particular Oman gabbros, and Hole 735B gabbros), it provides the first overview of plagioclase CPO from nearly 200 samples with variable texture, and from various geological setting. For a comprehensive understanding of plagioclase fabrics in an exhaustive range of geodynamic settings, we hope to make this plagioclase database available online in the future, so that it could be complemented by users worldwide.

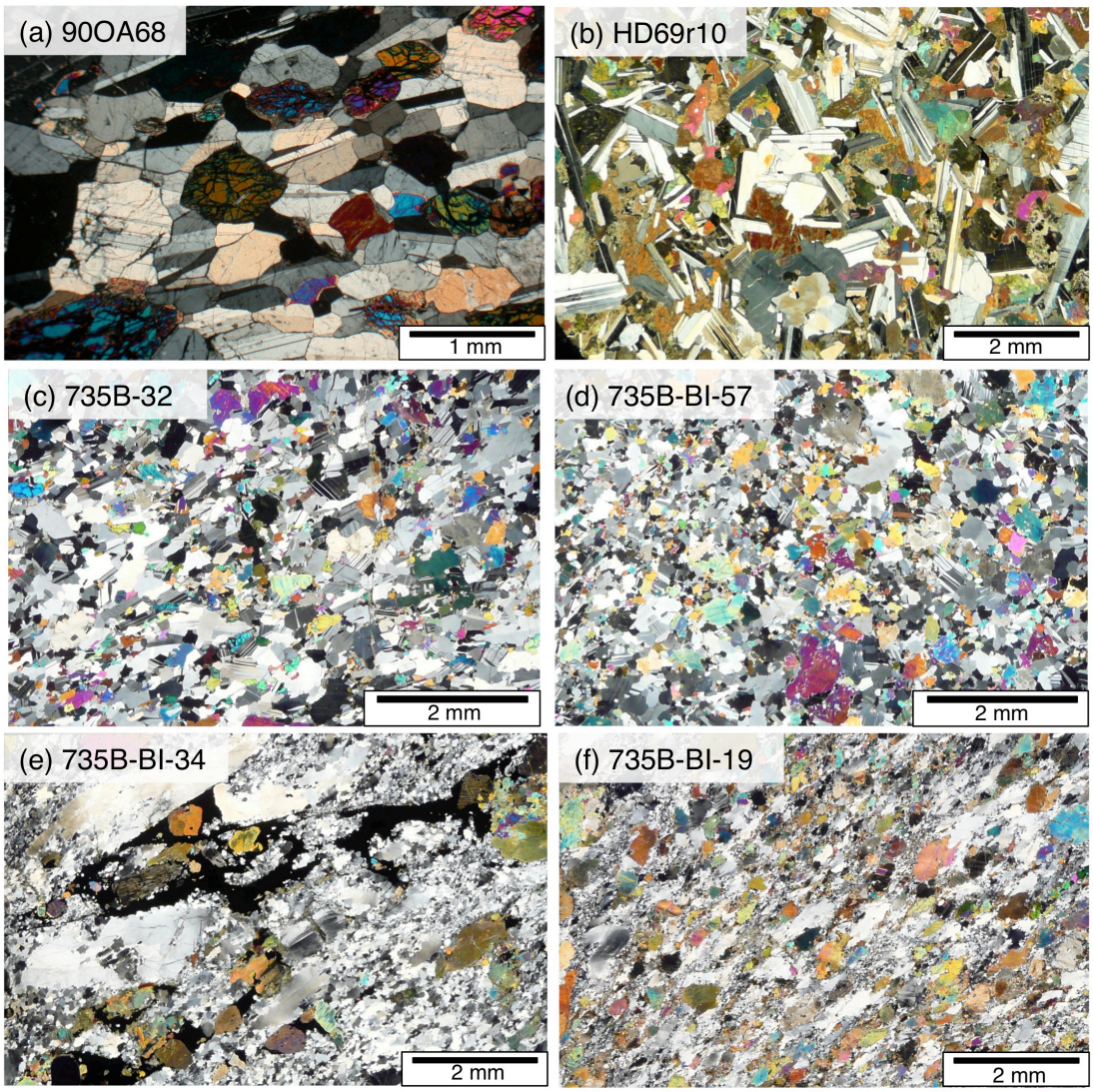

Figure 1. Photomicrographs (cross-polarized light) of plagioclase microstructure within gabbros from Oman ophiolite (a), Hess Deep (b), and ODP Hole 735B (c - f). (a, b) Magmatic flow textures. (c) Magmatic flow texture with moderate shape fabric. (d) Magmatic flow texture with weak shape fabric. Mylonitic texture (f) and porphyroclastic texture (e) are produced by crystal-plastic flow. Porphyroclasts consist of plagioclase and clinopyroxene, whereas neoblast are only plagioclase.

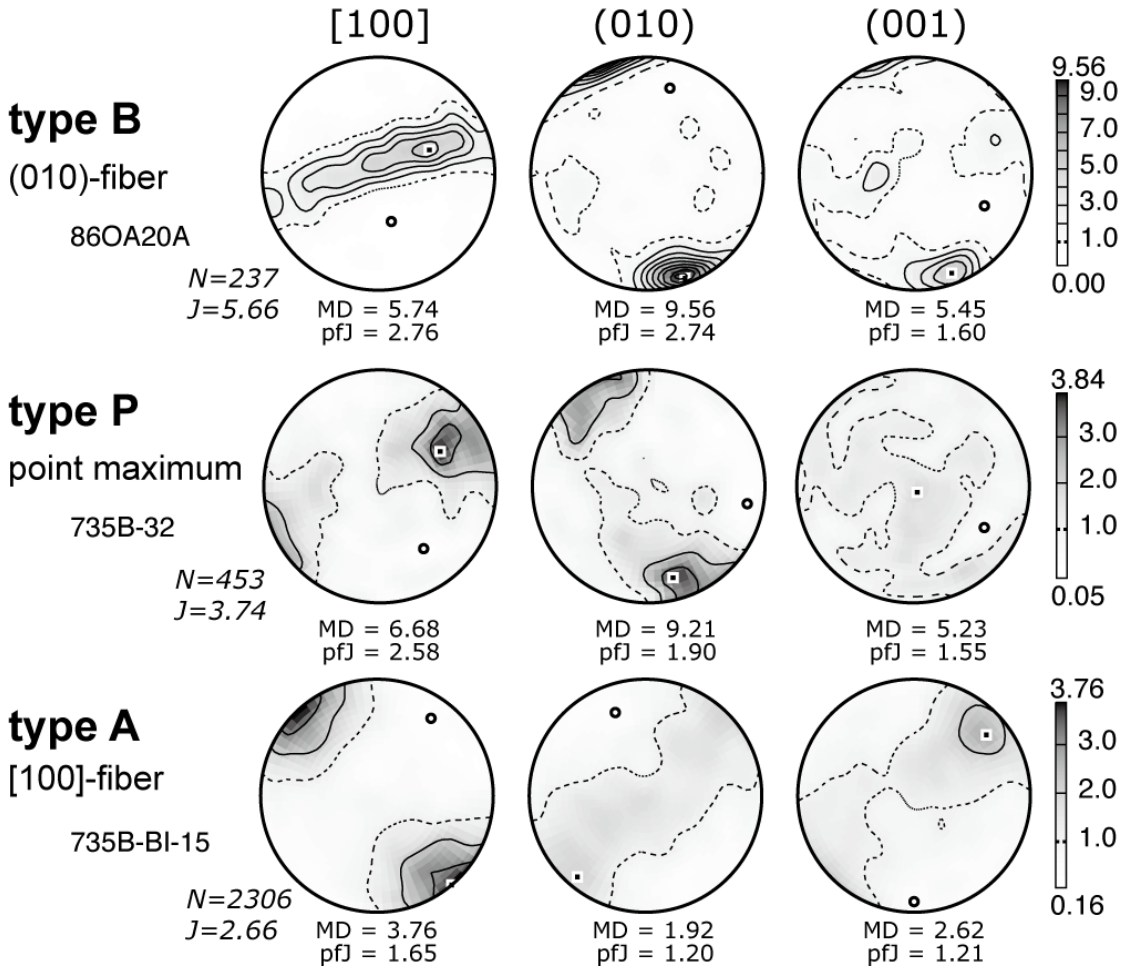

Figure 2. Typical plagioclase CPO patterns. All plagioclase CPOs are classified within these three main types. Type B is defined by a strong concentration of (010) and a girdle distribution of [100], and it can be also called (010)-fiber pattern. Type P CPO shows point maxima of the three axes. Type A CPO has a strong point maximum concentration of [100] and parallel girdle distributions of (010) and (001).

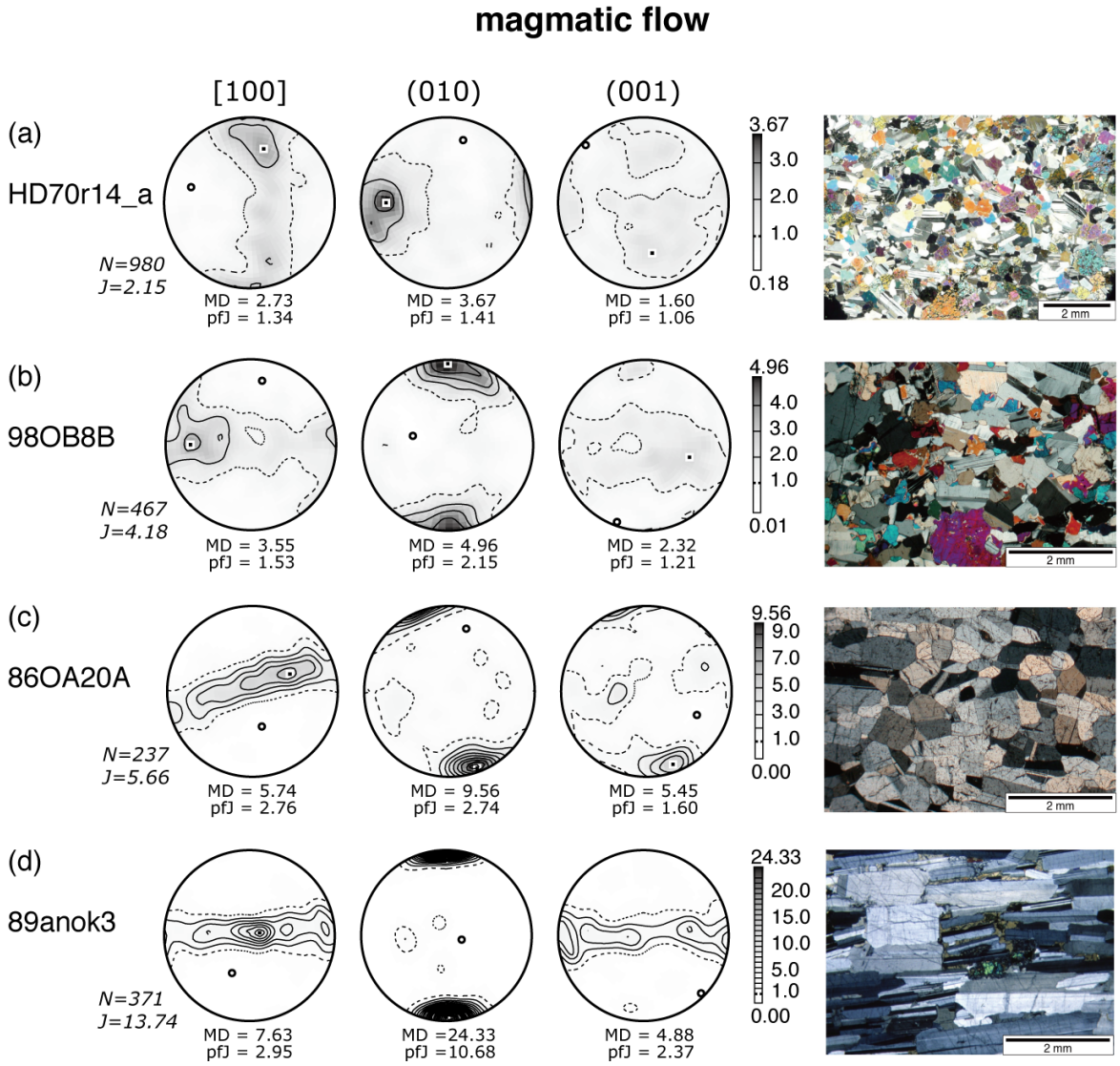

Figure 3. B-type CPOs of plagioclase and corresponding photomicrographs of magmatic deformed samples. (a) HD70r14a from Hess Deep, (b) 98OB8B from Oman ophiolite, (c) 86OA20A from Oman ophiolite, (d) 89anok3 from Oklahama.

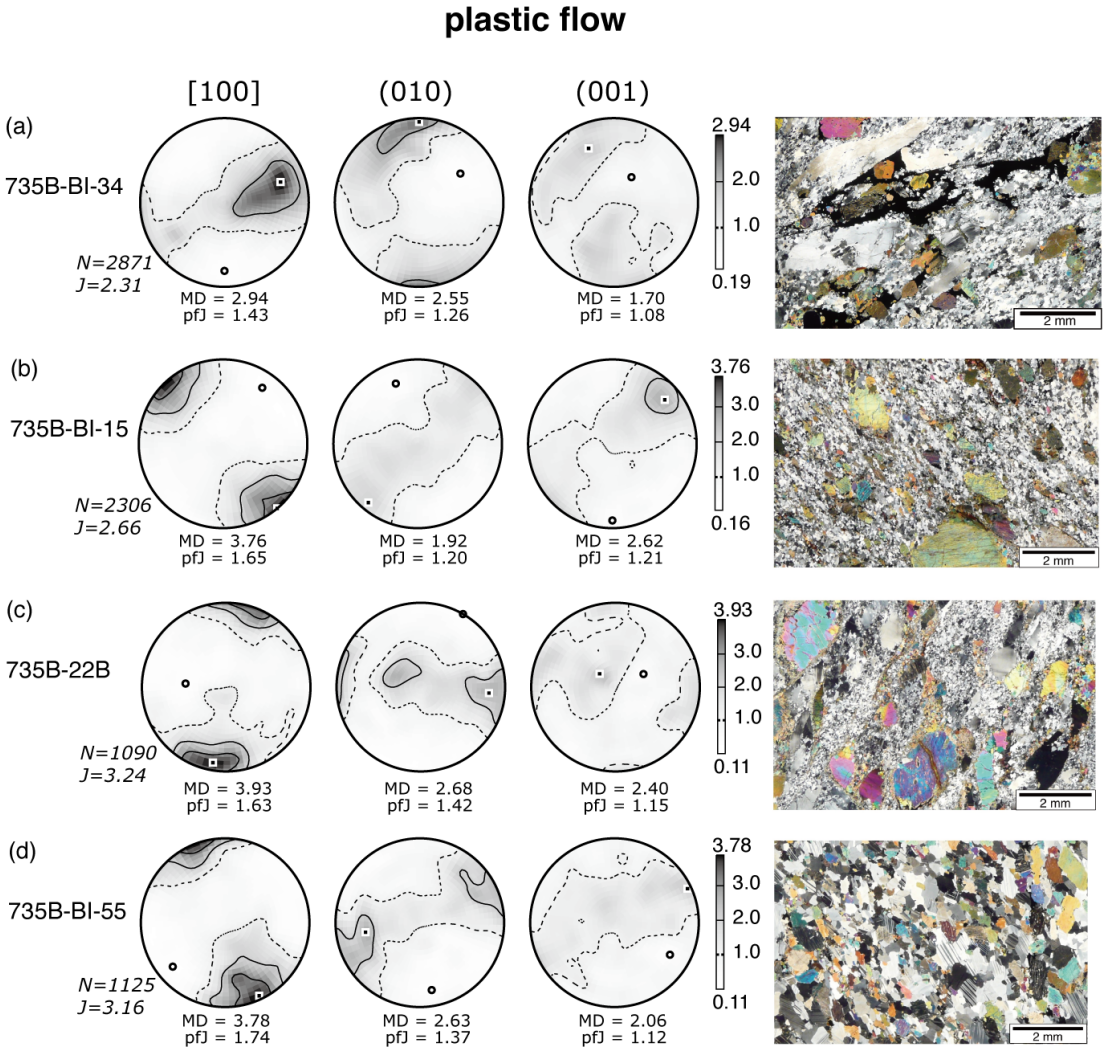

Figure 4. CPOs of plagioclase, and corresponding photomicrographs of plastically deformed samples from ODP Hole 735B. (a) P-type CPO and mylonitic texture deformed at low temperature, (b) A-type CPO and mylonitic texture deformed at low temperature, (c) P-type CPO and porphyroclastic texture deformed at low temperature, (d) A-type CPO and medium grained deformed at high temperature.

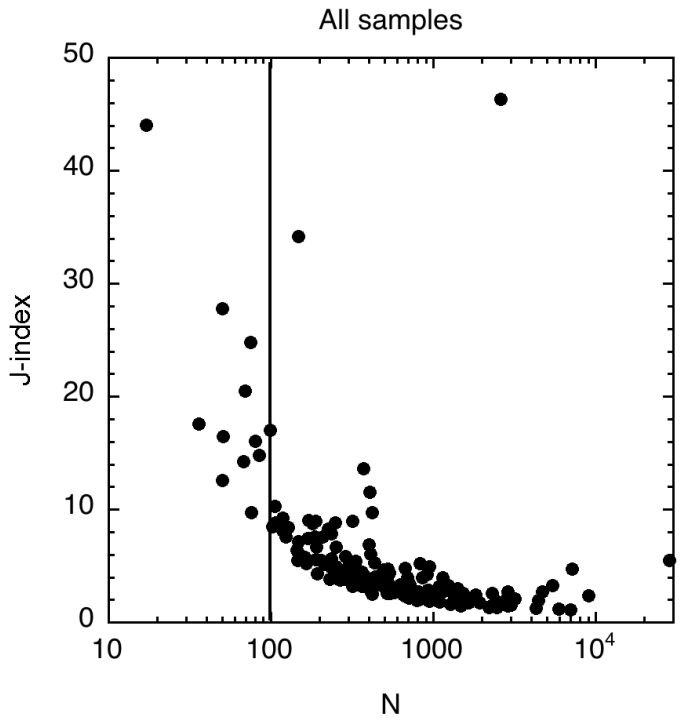

Figure 5. Relationship between the fabric strength (*J*-index) and the number of measured grains. CPOs with less than 100 measurements show abnormal high J values, and are not considered. The few samples that have J > 20 show sequences of repeating euler angles, which suggests that grain detection must have failed; they are discarded from further analysis.

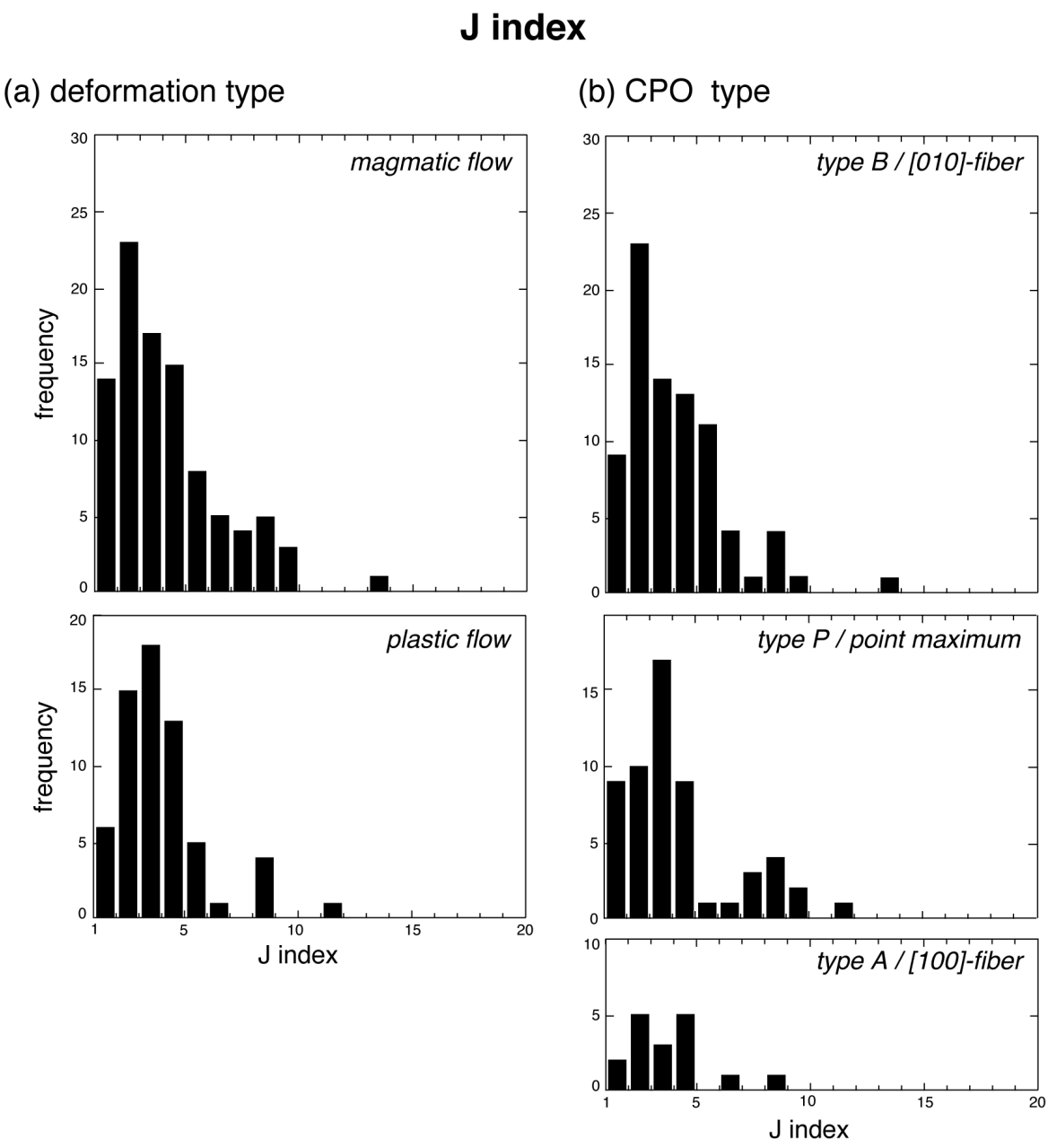

Figure 6. Histograms of *J*-index. Data are grouped as a function of deformation type (a) and CPO type (b). See text for further description

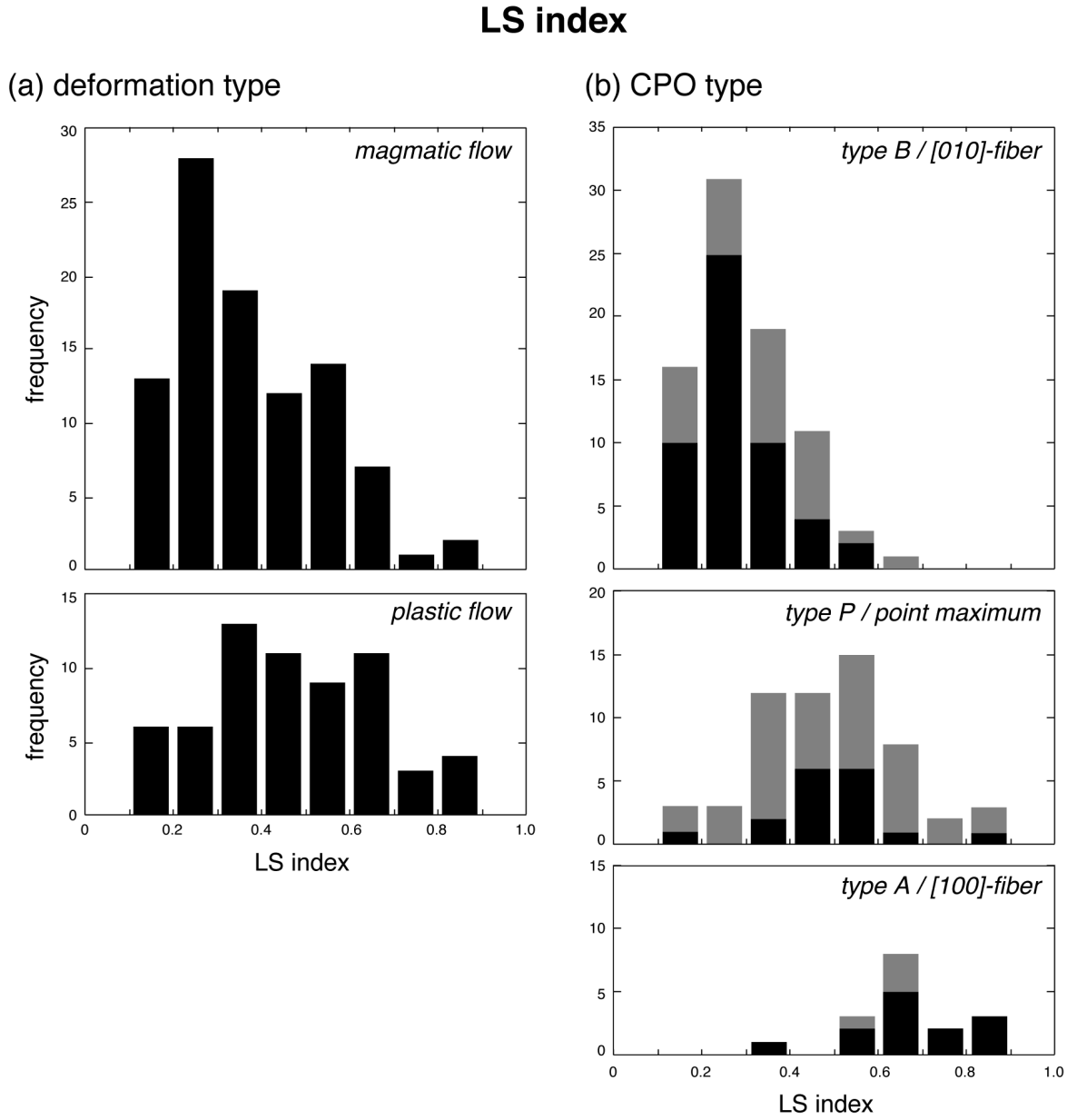

Figure 7. Histograms of LS index. Data are grouped as a function of deformation type (a) and CPO type (b). See text for further description. Data that correspond to weak fabrics are represented as gray color bars.

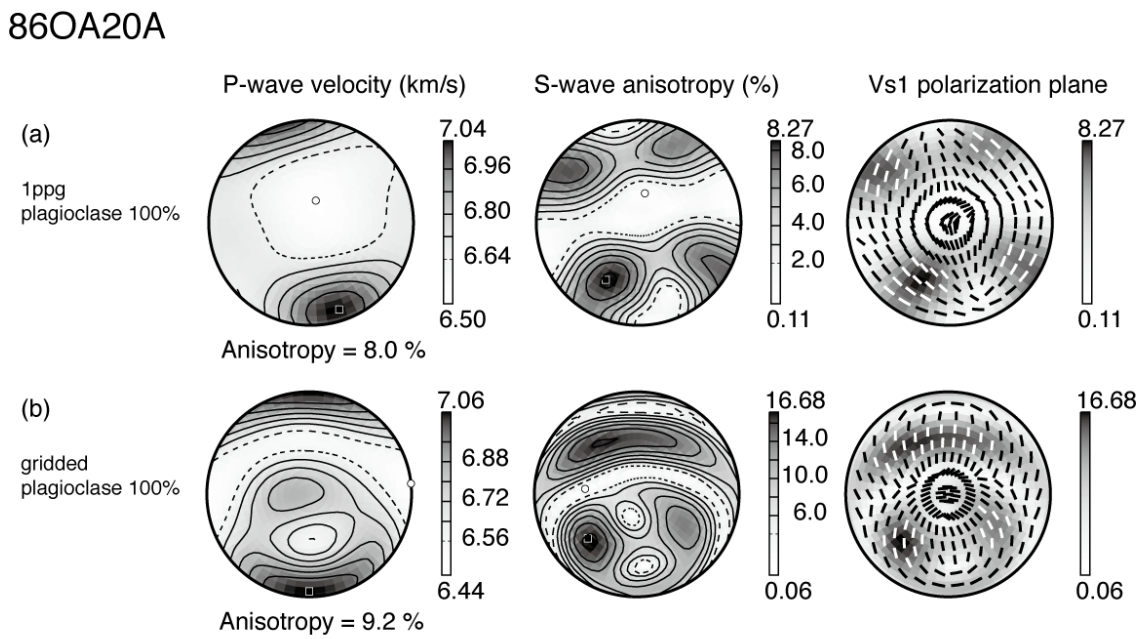

Figure 8. Seismic properties of sample 86OA20A (Oman ophiolite gabbro, magmatic texture). Seismic properties are calculated from 1ppg data (a) and gridded data (b). The differences between 1ppg data and gridded data of CPO reflect the effect of the heterogeneity of grain size. See text for further description.

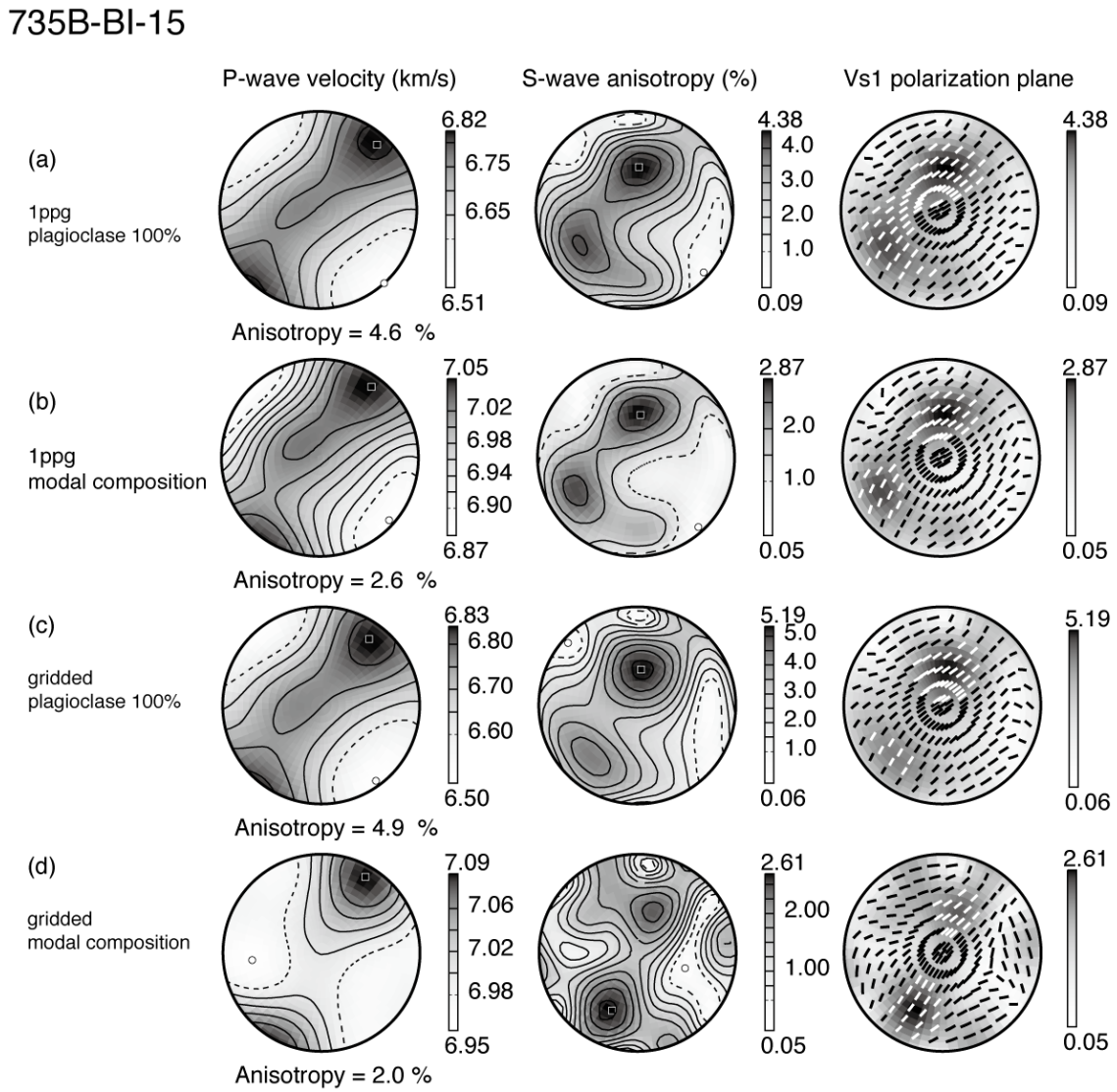

Figure 9. Seismic properties of sample 735B-BI-15 (ODP Hole 735B gabbro, crystal-plastic deformation texture). Seismic properties are calculated from 1ppg data with plagioclase 100% components (a), 1ppg data with real modal composition (b), gridded data with plagioclase 100% components (c), and gridded data with real modal composition (d). See text for further description.

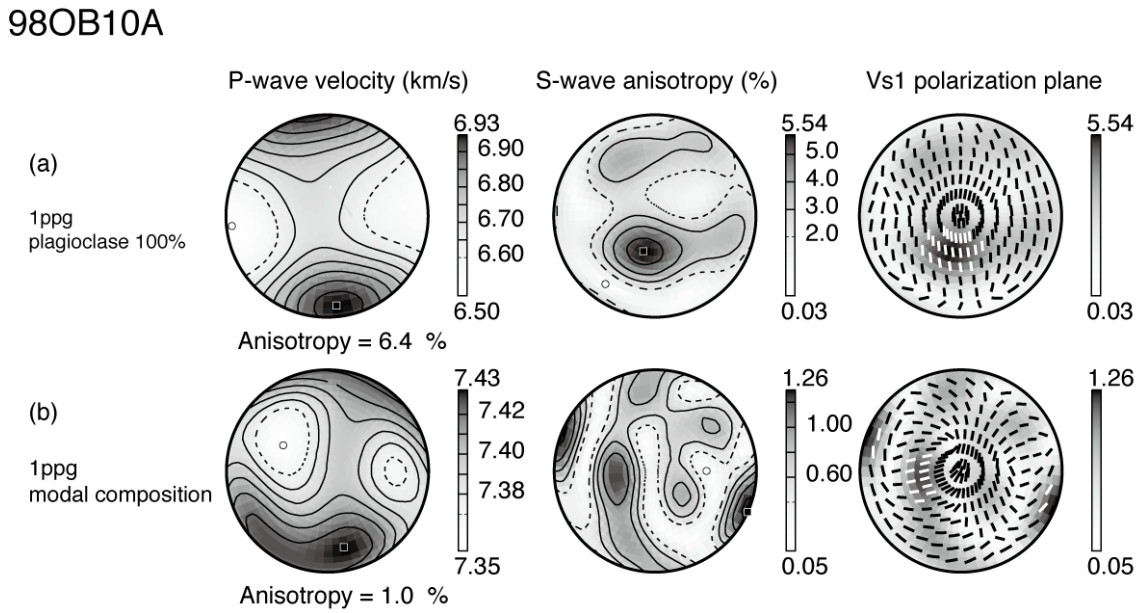

Figure 10. Seismic properties of sample 98OB10A (Oman ophiolite gabbro, magmatic texture). Seismic properties are calculated from 1ppg data with plagioclase 100% components (a), 1ppg data with real modal composition (b). See text for further description.

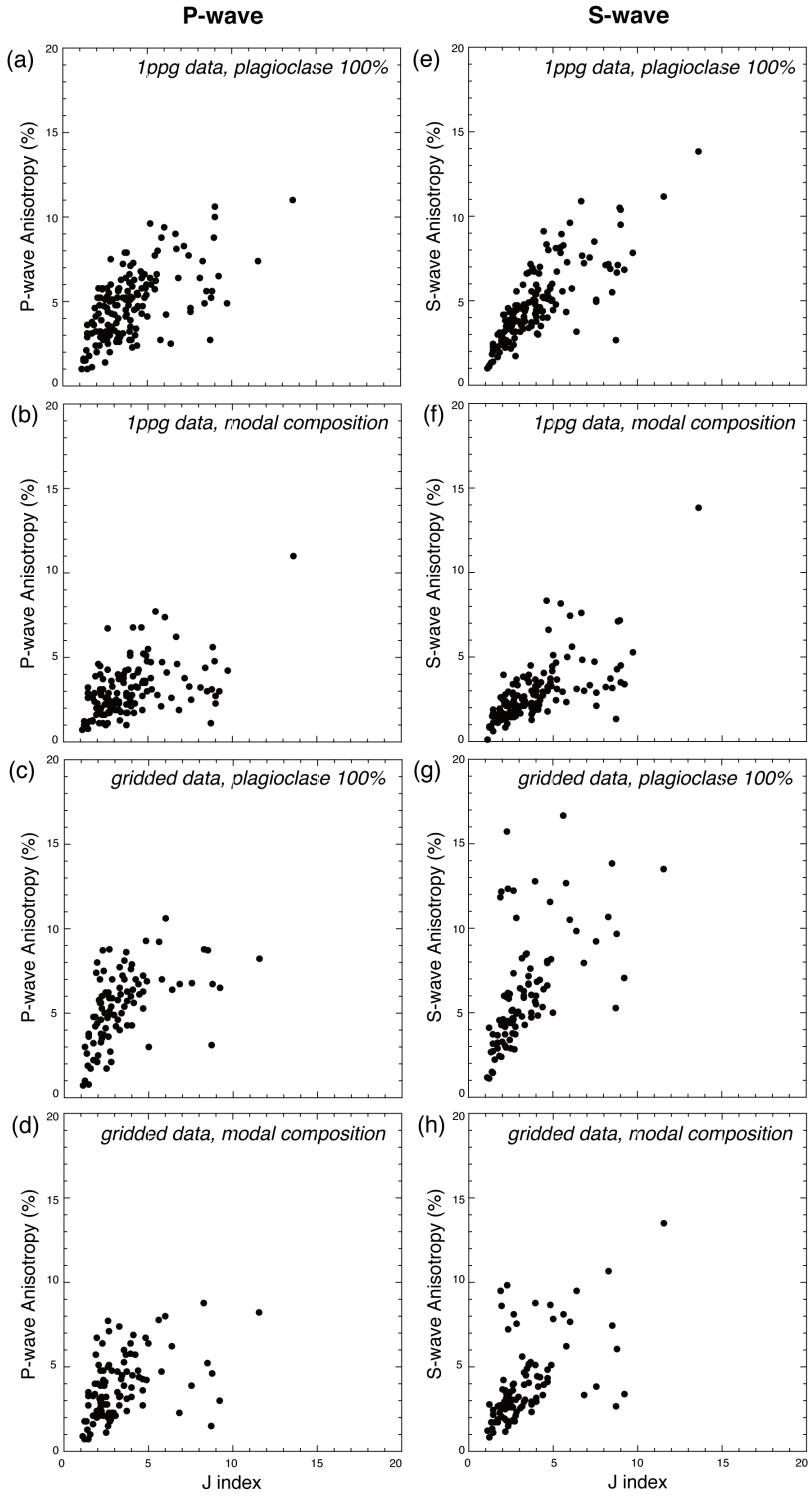

Figure 11. Seismic anisotropy as a function of fabric strength for Vp (a-d) and Vs (e-h) anisotropy. Seismic anisotropies are calculated in four different ways depending on CPO data and modal composition (see text for further explanation).

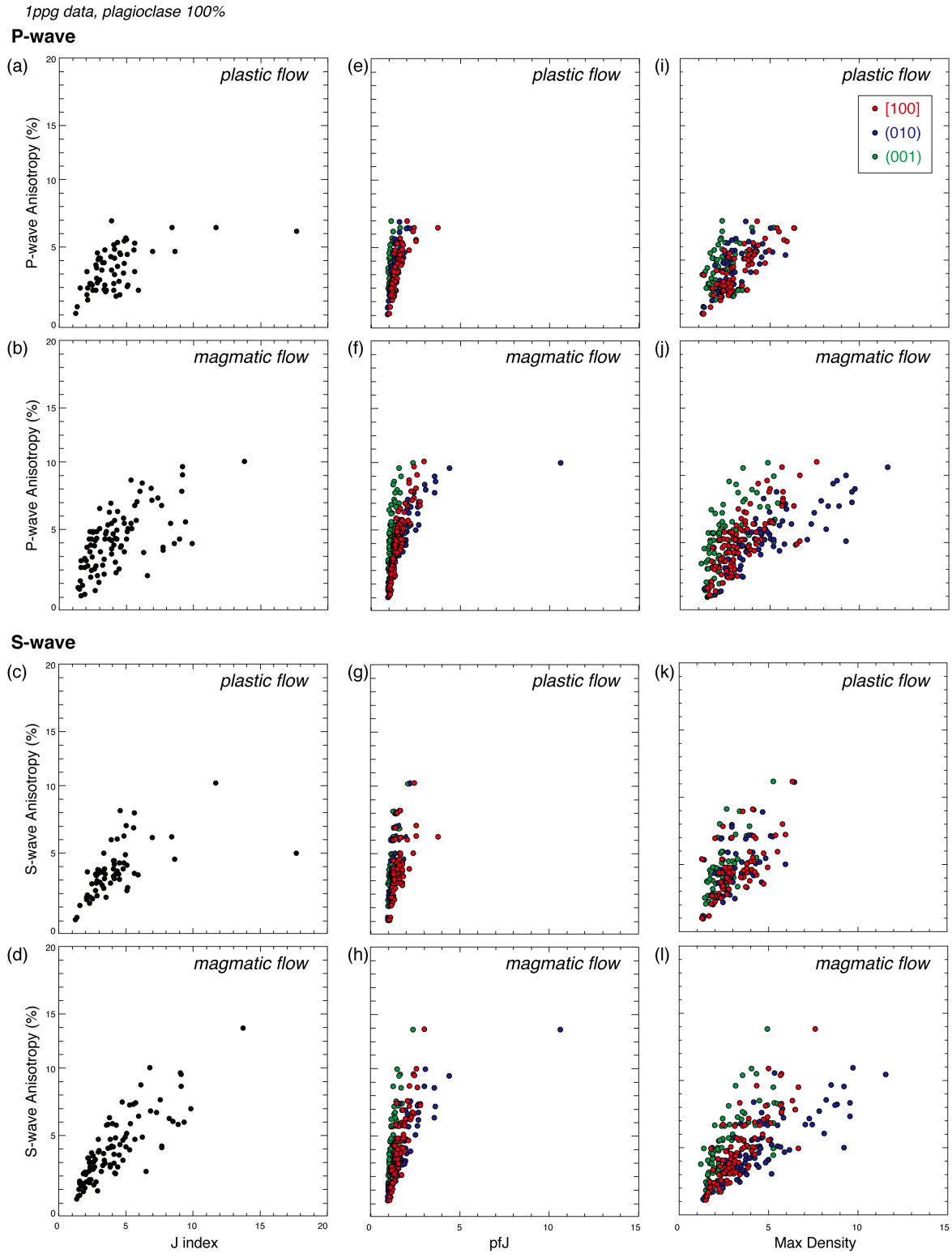

Figure 12. Relationship between seismic anisotropy and the fabric strength (a), pfJ index (b), and maximum density of each axes (c) for Vp and Vs anisotropy. Red, blue and green dots represent [100], (010), and (001), respectively.

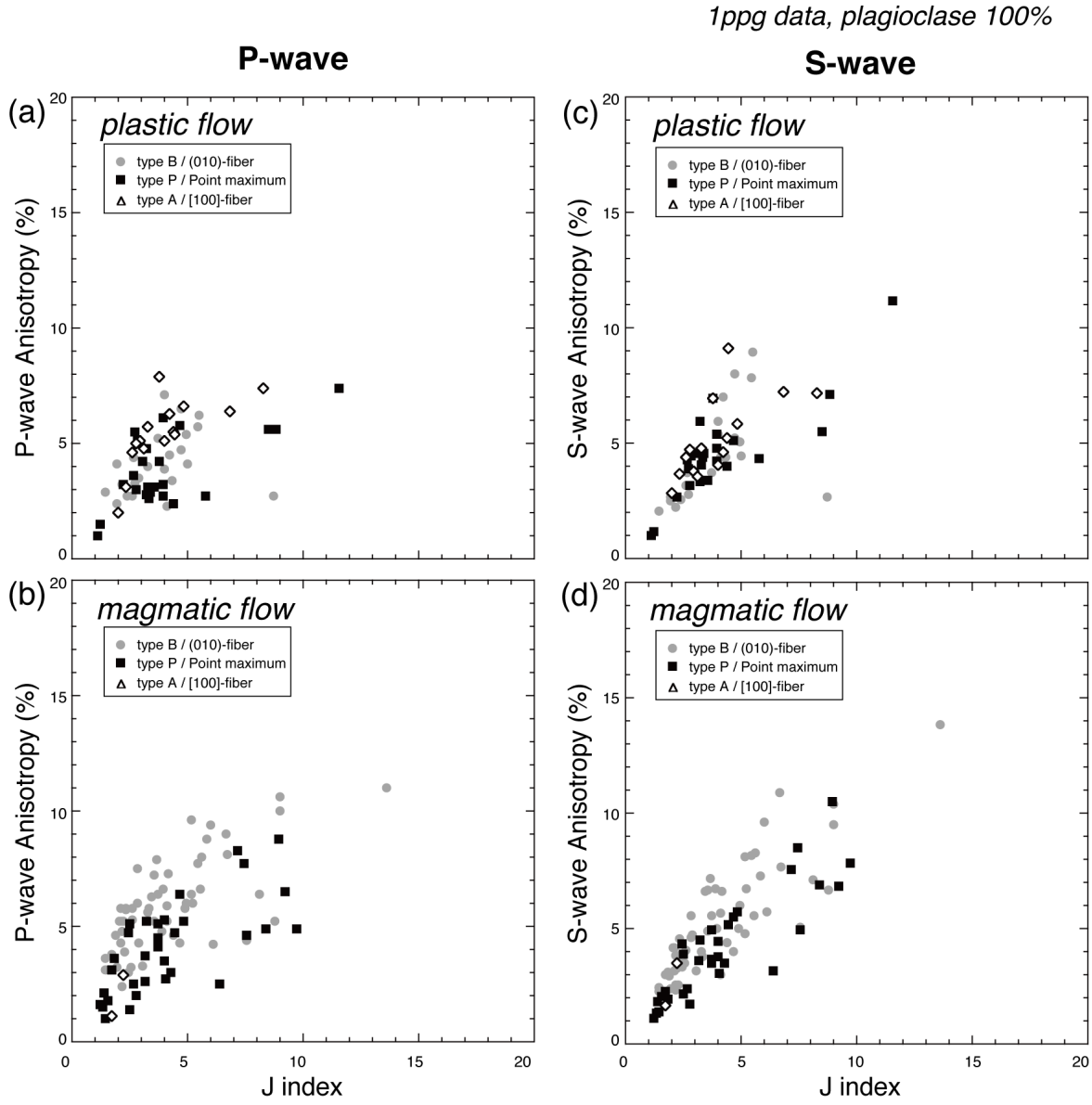

Figure 13. Relationship between seismic anisotropy and fabric strength for Vp (a, b) and Vs (c, d) anisotropy. These anisotropies are calculated as plagioclase 100% with 1ppg data (b, d). Data is plotted for the different CPO type (type B, P, A).

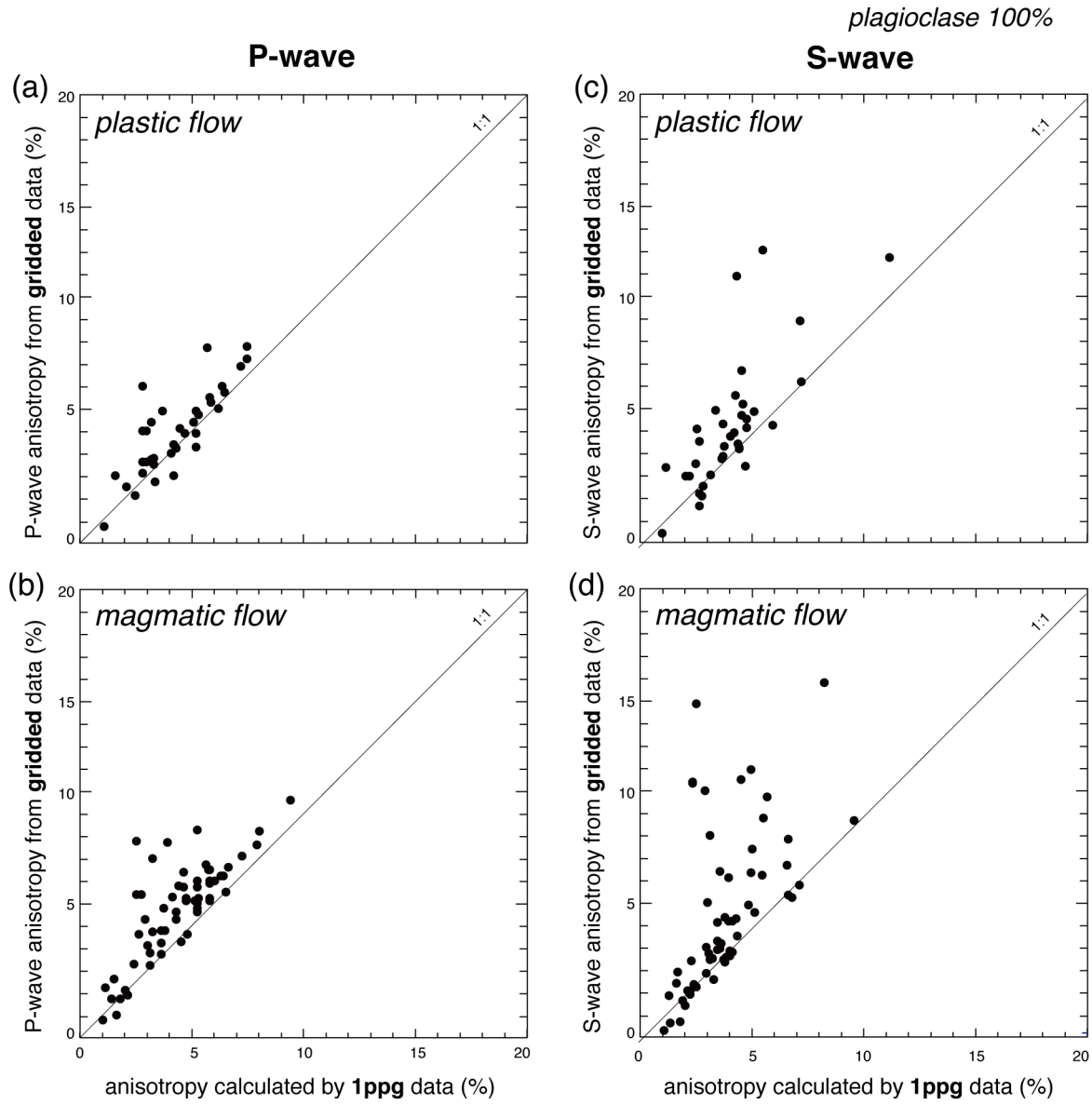

Figure 14. Comparison between seismic anisotropy calculated for 1PPG and gridded data in plagioclase aggregates.

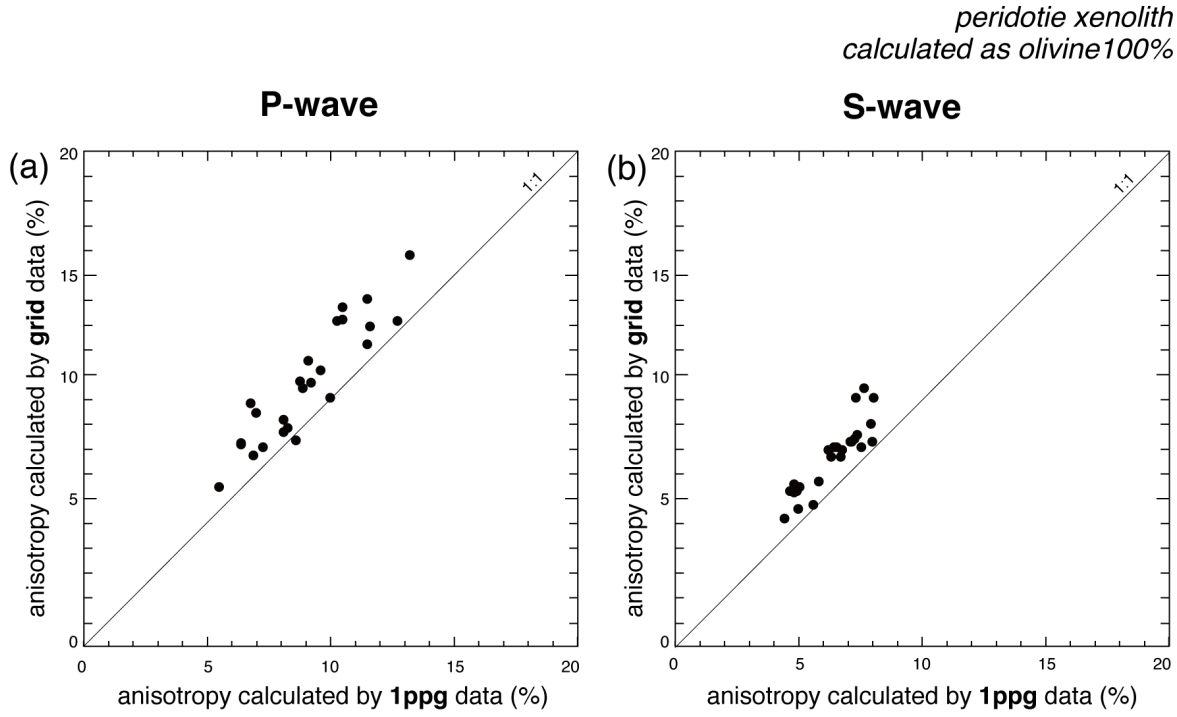

Figure 15. Comparison between seismic anisotropy calculated for 1PPG and gridded data in olivine aggregates. The seismic properties were calculated for the peridotite xenoliths studied in this thesis.

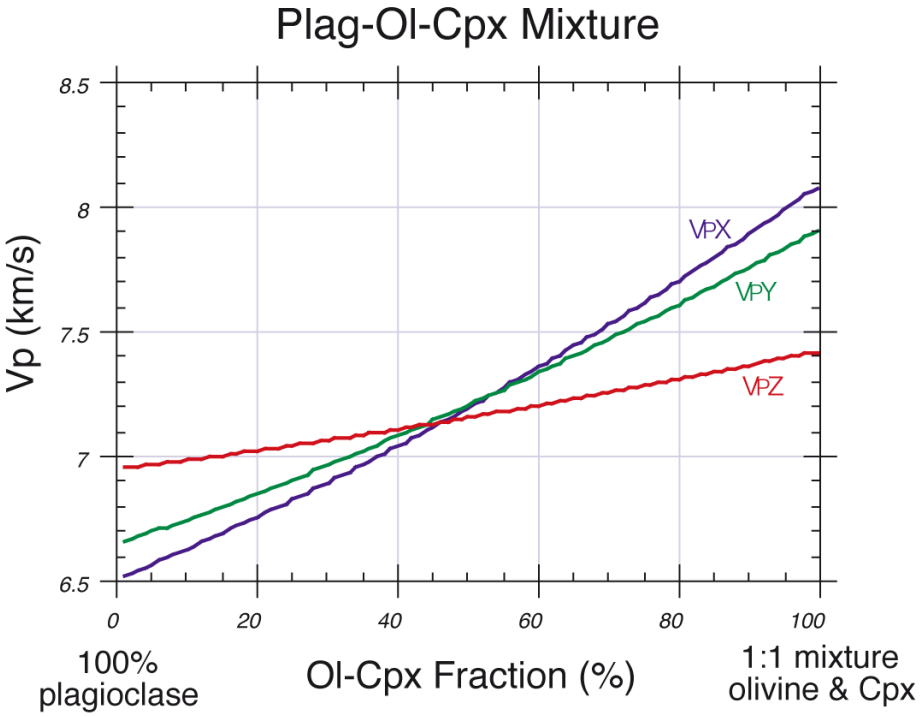

Figure 16. Variation of P-wave velocity as a function of modal composition (Ildefonse et al., 2002). X, Y and Z refer to the classical structural reference frame XYZ, in which X is the lineation, XY is the foliation, and Z the direction orthogonal to the foliation.

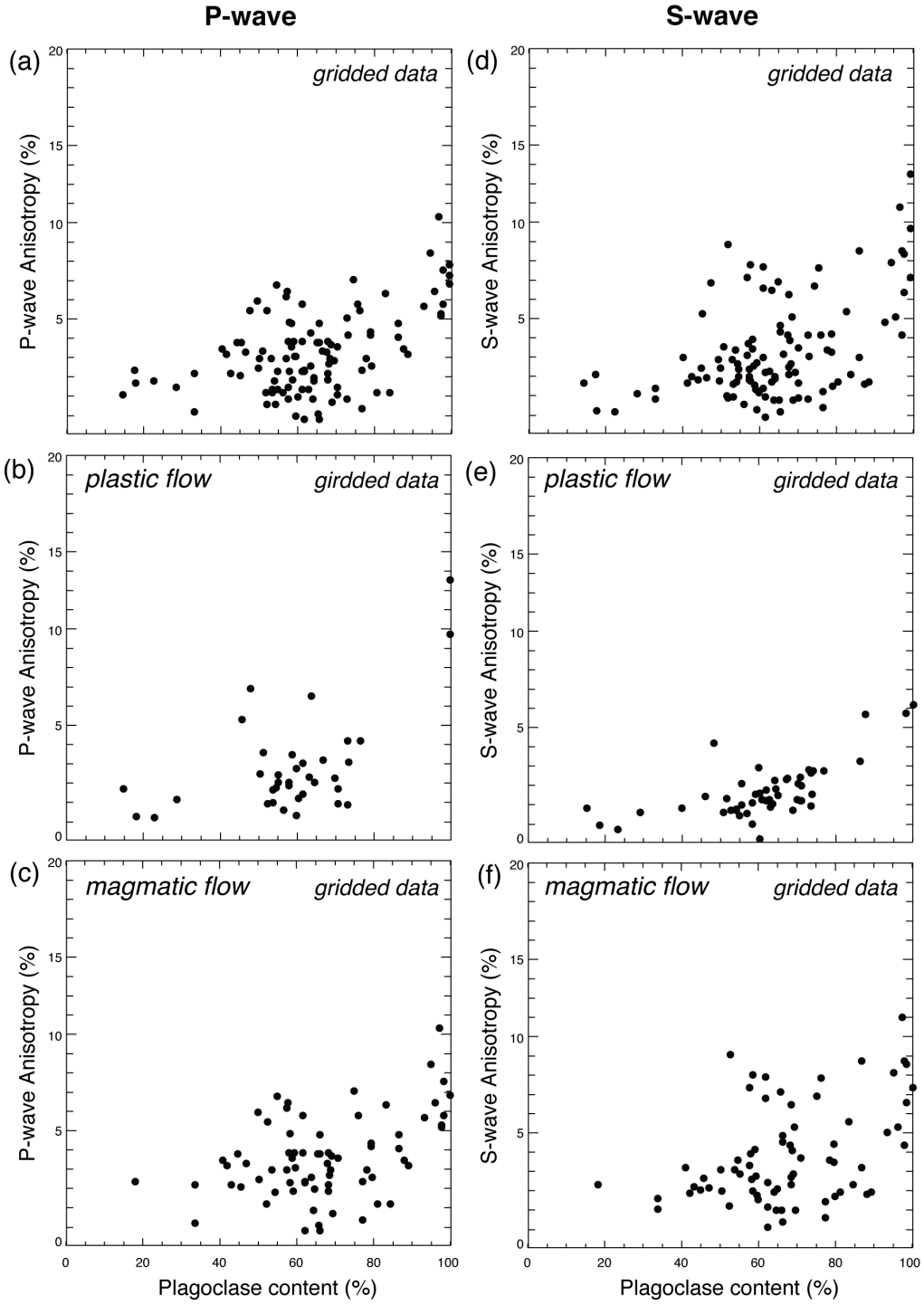

Figure 17. Relationship between seismic anisotropy and plagioclase content for Vp (a-c) and Vs (d-f) anisotropy. (a, d) all samples, (b, e) crystal-plastic deformed samples, (c, f) magmatic flow samples.

Table 1. Geodynamic environment, deformation type, CPO type, locality and related references of each sample in this study. B, P and A in the CPO type column are (010)-fiber pattern, point maximum pattern and [100]-fiber pattern, respectively.

Geodynamic environment of samples	Percentage of samples	Deformation type	CPO type	Locality and related references
Fast spreading ridge	54.7%	plastic 3.6% magmatic 96.4%	B 50.0%; P 46.9%; A 3.1%	Oman ophiolite (Morales et al., 2011; Nicolas et al., 2009; PhD thesis of Dr. B. Valsardieu), EPR (data from Dr. B. Ildefonse), Hess Deep (Data from K. Howard)
Slow spreading ridge	27.4%	plastic 77.2% magmatic 22.8%	B 32.1%; P 43.4%; A 24.5%	Southwest Indian ridge (data from Dr. L. Morales and T. Satsukawa), Mid Atlantic ridge (data from Dr. B. Ildefonse)
Massif and Lava	17.9%	plastic 58.8% magmatic 41.2%	B 63.6%; P 33.3%; A 3.05%	Brazil (PhD thesis of Dr. J. Bascou), Reunion (data from Dr. M. Drouin), St-Thibéry (Bascou et al., 2005), Nuvvuagittuq and Oklahama (data from Dr. B. Ildefonse)

Table 2. Modal composition (%), rock type, deformation type and related references for the gabbros studied here. Mode: modal composition; Pl: plagioclase; Cpx; clinopyroxene; Ol: olivine, Opx: orthopyroxene; Amp: amphibole, respectively.

sample#	Mode (%)					rock type	deformation	comment and references of the priginal works
	Pl	Cpx	Ol	Opx	Amp			
Oman ophiolite								
86OA20A	100	0	0	0	0	anorthosite	magmatic	thèse GL p77
86OA20B	100	0	0	0	0			
86OA20C	100	0	0	0	0		magmatic	
95OB4	63	10	27	1	0	gabbro	(magmatic +) faible déformation plastic	
97OB1C	46	14	0	41	0	gabbronorite	magmatic (recristallisée)	starting material of GABAT
98OB7A	86	14	0	0	0	gabbro	magmatic	GEOman (Bertrand Valsardieu)
98OB8B	55	38	7	0	0	gabbro	magmatic	GEOman (Bertrand Valsardieu)
98OB10A	46	50	4	0	0	cpx-ol gabbro	magmatic	GEOman (Bertrand Valsardieu)
98OB10E	30	64	6	0	0	cpx-ol gabbro	magmatic	GEOman (Bertrand Valsardieu)
98OB10G	40	38	23	0	0	cpx-ol gabbro	plastic	GEOman (Bertrand Valsardieu), oxide
88OA13	59	14	27	0	0		magmatic	Gwenaelle. modes p44
88OA14b	77	23	0	0	0		magmatic	Gwenaelle. modes p44 gwen322
90OA68	59	29	11	0	0		magmatic	Gwenaelle. modes p44 gwen1111
90OA77	47	37	16	0	0		magmatic	Gwenaelle. modes p44
90OF11	70	25	5	0	0		magmatic	Gwenaelle. modes p44 gwen2911
92OB100b	71	29	0	0	0		magmatic	Gwenaelle. modes p44 gwen1224
92OB101	59	41	0	0	0		magmatic	Gwenaelle. modes p44 gwen1123
92OB134	67	33	0	0	0		magmatic	Gwenaelle. modes p44
92OB139	46	43	11	0	0		magmatic	Gwenaelle. modes p44 gwen1521
92OB140a	59	22	19	0	0		magmatic	Gwenaelle. modes p44 gwen1621
92OB140c	54	46	0	0	0		magmatic	Gwenaelle. modes p44 gwen812
92OB142	80	20	0	0	0		magmatic	Gwenaelle. modes p44 gwen222
92OB143	55	37	7	0	0		magmatic	Gwenaelle. modes p44 gwen1023
93OB157	94	6	0	0	0		magmatic	Gwenaelle. modes p44 gwen221
94OB28	87	12	1	0	0		magmatic	Gwenaelle. modes p44 gwen1121
95OA129	100	1	0	0	0		magmatic	Gwenaelle. mode table1 Tectonophysics paper
06OA31b	64	36	0	0	0		plastic	Root Sheeted Dyke Oman
07OA20a	34	58	5	4	0		magmatic	Lyde. Nicolas et al. (2009, EPSL)
07OA20c1	77	28	0	0	0		magmatic	Lyde. Nicolas et al. (2009, EPSL)
07OA20d	77	23	0	0	0		magmatic	Lyde. Nicolas et al. (2009, EPSL)
07OA20e	80	20	0	0	0		magmatic	Lyde. Nicolas et al. (2009, EPSL)
07-2OA13	34	58	5	4	0		magmatic	Lyde. Nicolas et al. (2009, EPSL)
07_2_OA_10B	96	3	1	0	0	anorthosite	magmatic	anorthosite with steep foliation (subsidence)
07_2_OA_18b	98	2	0	0	0	anorthosite	magmatic	anorthosite with steep foliation (subsidence)
07_2_OA_18c	98	2	0	0	0	anorthosite	magmatic	anorthosite with steep foliation (subsidence)
07_2_OA_30b	98	0	2	0	0	anorthosite	magmatic	anorthosite with steep foliation (subsidence)
07_2_OA_30h	93	6	0	0	0	anorthosite	magmatic	anorthosite with steep foliation (subsidence)
07_2_OA_37	89	11	0	0	0	anorthosite		lower crust aanorthosite
07_2_OA_37b	100	0	0	0	0	anorthosite		lower crust aanorthosite
07_2_OA_41g	78	16	3	3	0	anorthosite	magmatic	anorthosite with flat-lying foliation (melt lenses)
07_2_OA_42c	89	9	1	0	0	anorthosite	magmatic	anorthosite with flat-lying foliation (melt lenses)

Table 2. *(continued)*

sample#	Mode (%)					rock type	deformation	comment and references of the priginal works
	Pl	Cpx	Ol	Opx	Amp			
07_2_OA_45c3	97	2	1	0	0	anorthosite	magmatic	anorthosite with flat-lying foliation (melt lenses)
07_2_OA_45c4	83	17	0	0	0	anorthosite	magmatic	anorthosite with flat-lying foliation (melt lenses)
07_2_OA_66	95	5	0	0	0	anorthosite	magmatic	anorthosite with flat-lying foliation (melt lenses)
07_OA_8g_2S	88	12	0	0	0	anorthosite	magmatic	anorthosite with steep foliation (subsidence)
GAVAT2	65	31	0	4	0			sample for attenuation measurements
ODP Hole 735B								
735B-5	59	33	8	0	0	disseminated oxide olivine gabbro	magmatic (mf2) (+ plastic (pf1))	
735B-22B	60	15	16	1	9	olivine gabbronorite	plastic (pf2)	coarse-grained, vertical foliation, mylonite, low T
735B-22C	100	0	0	0	0		plastic (pf2)	
735B-22D	100	0	0	0	0	olivine gabbronorite	plastic (pf2)	coarse-grained, vertical foliation
735B-22E	100	0	0	0	0		plastic (pf2)	
735B-22F	100	0	0	0	0	olivine gabbronorite	plastic (pf2)	coarse-grained, vertical foliation
735B-32	67	18	13	1	0	olivine gabbro	magmatic (Mf2)	
735B-32B	68	27	5	0	0	olivine gabbro	magmatic (Mf2)	
735B-BI-50	55	39	4	2	0	gabbro	plastic	base of thick shear zone (the biggest one, more than 20m), very fine grain, mylonite
735B-51	100	0	0	0	0	troctolite	plastic (pf2/4)	base of thick shear zone
735B-70	74	14	10	2	0	disseminated oxide olivine gabbro	plastic (Pf3)	
735B-79	58	34	5	3	0		magmatic	fine-grained intrusive subvertical layer in coarse-grained gabbro
735B-79B	69	30	1	0	0		magmatic	fine-grained intrusive subvertical layer in coarse-grained gabbro
116R4	68	16	11	2	3	opx-bearing gabbro	magmatic + plastic (pf1, faciès amphibolite)	116-127, low T
133R3	71	20	8	2	0	olivine gabbro	(magmatic +) plastic (pf2, HT)	133-3-0, coarse grain, high T plastic flow
133-3-0-7A	63	28	7	1	1			
142R5	73	13	13	1	0	olivine gabbro	magmatic (mf2) + plastic (pf1, HT)	142-5-6, high T recrystallized texture
142-5-6-8b	59	22	19	0	0			
147R6	71	18	7	1	3	gabbro	plastic (pf2, LT)	147-6-39
154R5	64	33	2	2	0	olivine gabbro	(magmatic (mf2) +) plastic (pf1, HT)	154-5-42, essentialy magmatic texture, but magmatic flow texture was pverprinted by plastic flow texture(small grains recrystalized), bending, undulose
154-5-42-44B	55	42	3	1	0			
167R6	68	22	8	2	0	gabbro	magmatic (mf1)	167-6-V

Table 2. *(continued)*

sample#	Mode (%)					rock type	deformation	comment and references of the priginal works
	Pl	Cpx	Ol	Opx	Amp			
179R5	75	15	10	0	1	olivine gabbro	magmatic	179-5-97, pas joli. Trop gros grains, well developed triple junction
190R4	64	27	6	2	0	troctolitic gabbro	magmatic (mf1-2- + faible plastic (pf0-1)	190-4-87
209R7	67	23	10	0	0	olivine gabbro	magmatic	209-7-H, pas joli. Trop gros grains
735B-BI-6	62	31	7	0	0	gabbro	plastic	low T, porphyroclastic texture
735B-BI-7	57	38	4	1	1		plastic	low T, mylonite
735B-BI-15	71	22	2	0	6	oxide gabbronorite	plastic	low T, mylonite-ultra mylonite
735B-BI-19	54	42	3	0	0	gabbro	plastic	low T, porphyroclastic texture
735B-BI-25	71	22	2	0	6	olivine gabbro	plastic	high T, fine grained porphyroclastic texture
735B-BI-26	52	18	29	1	0	olivine microgabbro	plastic	fine grained, foliation not clear
735B-BI-33	46	45	4	4	1	oxide gabbro olivine gabbro	plastic	low T, partly shear lozlized
735B-BI-34	74	18	3	1	4	oxide gabbro	plastic	low T, mylonite, neoblast:pl, porphyroclast:pl+cpx
735B-BI-38	73	13	10	3	1	leucocratic troctolitic microgabbro	plastic	high T
735B-BI-49	65	29	4	2	0	gabbro	plastic (pf2)	high T, mylonite, close to shear zone (similar to 735B-BI-50)
735B-50	88	7	3	3	0	troctolite	plastic (pf2)	base of thick shear zone
735B-BI-51	60	37	3	0	0	troctolite	plastic (pf2/4)	base of thick shear zone, ultra mylonite, oxide rich, low T
735B-BI-52	51	42	7	0	0	gabbro	plastic	
735B-BI-52a	55	35	9	0	0	gabbro	plastic	porphyroclastic texture, high T
735B-BI-52b	69	24	7	0	0	gabbro	magmatic (mf1) mf variably developed	
735B-BI-52c	51	43	5	1	0			
735B-BI-55	61	26	5	8	1	olivine gabbro	plastic	coarse-grained, equigranular texture, high T
735B-BI-57	54	36	9	0	0	olivine gabbro	magmatic (mf0)	high T, weak magmatic foliation
735B-BI-58	77	20	3	0	0	olivine gabbro	(magmatic (mf2) magmatic reverse SZ)+ plastic (pf1, 2)	high T, porphyroclastic texture
735B-BI-64a (coarse)	65	30	5	0	0	olivine microgabbro	plastic	
735B-BI-64a2 (fine)	58	32	7	2	0	olivine microgabbro	plastic	
735B-BI-64b	54	36	9	1	0	olivine gabbro	plastic	coarse grained zone exist within fine grained zone
735B-BI-70	62	14	23	1	0	disseminated oxide olivine gabbro	plastic (pf3)	ultramylonite, low T, px:porphyroclast, pl:neoblast
735B-BI-82a	61	32	4	3	0	gabbro		well foliated, fine grain, high T
735B-BI-82b	67	29	3	1	0	olivine gabbro		porphyroclastic texture, high T

Table 2. *(continued)*

sample#	Mode (%)					rock type	deformation	comment and references of the priginal works
	Pl	Cpx	Ol	Opx	Amp			
735B-BI-83a	73	19	6	1	0	leucocratic disseminated oxide microtroctolite	plastic	veriable grain size but not foliated
735B-BI-83b	70	22	6	2	0	olivine gabbro	plastic (pf2, 1), mf0	localized shear zone
735B-BI-92 (fine)	48	40	12	0	0	olivine microgabbro	plastic	strain localized area
735B-BI-92-2 (coarse)	55	32	8	4	0	olivine microgabbro	plastic	
Brazil, Itabuna and Ribeira belts								
CM19	86	6	0	7	0	charnokite	magmatic+plastic HT	Bahia, Carapussê massif, carapussê. Matrice recristallisée
CM20	70	16	0	14	0	charnokite	magmatic+plastic HT	Cristina. carapussê. Gros clastes + Matrice recristallisée
RMB20	99	0	1	0	0	gabbro	magmatic + brittle	Bahia, Potiraguá massif, Cristina, gros grains
CM08	67	14	0	15	3	charnokite	magmatic+plastic HT	Bahia, Samaritana massif, Cristina, Gros clastes + Matrice recristallisée
CM09	69	15	0	16	0	charnokite	magmatic+plastic HT	Samaritana, Cristina, Gros clastes + Matrice recristallisée
CM22	63	20	0	18	0	charnokite	magmatic+plastic HT	Samaritana, Cristina, Gros clastes + Matrice recristallisée
CM29	60	34	0	1	5		?	Rio Piau
RB5E						granulite	plastic	
RB538						granulite	plastic	thèse JB, almost single crystal, fine pl + big grian size single crystal ol
RB540						granulite	plastic	thèse JB, layered structure with pl+cpx
RB546						granulite	?	thèse JB
RB548						granulite	plastic	thèse JB
RB559						granulite	magmatic	thèse JB
RB566						granulite	plastic	thèse JB
RB607A						granulite	plastic	thèse JB
RB607B						granulite	plastic	thèse JB
RB609A						granulite	plastic	thèse JB
RB614						granulite	plastic	thèse JB
RB689						granulite	plastic	thèse JB
ODP Hole 1256D								
1256D_78_a	81	12	0	1	6		magmatic	
1256D_91_c	41	20	7	0	32		magamtic	no foliation
1256D_103_a	58	33	0	4	5		plastic	low T
1256D_108_a	33	54	0	7	6			fine grain
1256D_109_b	61	28	0	4	7			fine grain and coarse grain
1256D_112_a	68	22	0	6	4			opx + pl, cpx + pl
1256D_112_b	62	25	0	10	3		magmatic	magmatic flow by heat
1256D_115	65	20	0	10	6		magmatic	fine grain zone (opx+pl) within coarse grain zone (cpx+pl)
1256D_116_a	60	24	0	10	6		plastic	fine grain, no strong foliation
1256D_116_b	63	14	0	16	6		plastic?	fine grain
1256D_117_a	62	26	0	12	0		magmatic	fine grain, no strong foliation
1256D_117_b	66	25	0	3	5		magmatic	fine grain, no strong foliation

Table 2. *(continued)*

sample#	Mode (%)					rock type	deformation	comment and references of the priginal works
	Pl	Cpx	Ol	Opx	Amp			
Hess Deep								
HD69r6_a	84	2	13	0	0	oxide gabbro	magmatic	
HD69r10_a	57	39	0	2	2	oxide gabbro	magmatic	some big grains are orientated and have planer shape, which is related to b-axis concentration
HD69r16_a	69	28	0	1	1	oxide gabbro	magmatic	
HD70r2_a	53	19	28	0	0	oxide gabbro	magmatic	
HD70r14_a	52	19	28	0	1	oxide gabbro	magmatic	foliated but not porphyroclastic texture
HD70r15_a	58	30	0	1	11	oxide gabbro	magmatic	
HD70r17_a	87	10	0	0	3	oxide gabbro	magmatic	fine grain
HD70r18_a	54	46	0	0	0	oxide gabbro	magmatic	
HD70r20_a	62	30	0	0	8	oxide gabbro	magmatic	coarse grain
HD73r2_a	79	7	12	0	1	oxide gabbro	magmatic	
HD73r4_a	62	34	3	1	0	oxide gabbro	magmatic	
HD73r5_a	69	26	1	1	3	oxide gabbro	magmatic	
HD73r9_a	68	29	1	2	0	oxide gabbro	magmatic	
HD73r13_a	59	38	0	2	0	oxide gabbro	magmatic	
HD73r15_a	45	41	0	1	13	oxide gabbro	magmatic	coarse grain
HD73r16_a	87	1	11	0	1	oxide gabbro	magmatic	
HD73r18_a	58	25	12	2	3	oxide gabbro	magmatic	
HD73r20_a	79	13	1	0	7	oxide gabbro	magmatic	
HD75r5_a	68	21	7	1	3	oxide gabbro	magmatic	
HD75r8_a	50	49	0	0	0	oxide gabbro	magmatic	pl+cpx mixture, pl have subgrain boundary
HD75r11_a	58	40	0	1	1	oxide gabbro	magmatic	
HD76r1_a	66	34	0	0	0	oxide gabbro	magmatic	
HD76r3_a	75	24	0	0	0	oxide gabbro	magmatic	
HD76r8_a	58	41	0	1	0	oxide gabbro	magmatic	
HD76r10_a	68	31	0	0	1	oxide gabbro	magmatic	no strong foliation
HD76r11_a	76	21	0	0	3	oxide gabbro	magmatic	
HD76r14_a	58	22	0	0	20	oxide gabbro	magmatic	
HD78r1_a	60	38	0	0	2	oxide gabbro	magmatic	
HD78r2_a	98	2	0	0	0	oxide gabbro	magmatic	coarse grain

Table 2. *(continued)*

sample#	Mode (%)					rock type	deformation	comment and references of the priginal works
	Pl	Cpx	Ol	Opx	Amp			
HD78r5a	62	33	0	3	1	oxide gabbro	magmatic	
HD78r5b	71	26	0	1	2	oxide gabbro	magmatic	
HD78r5x4	64	32	0	2	3	oxide gabbro	magmatic	
HD78r6_a	62	26	9	3	0	oxide gabbro	magmatic	
HD78r7_a	66	19	0	6	9	oxide gabbro	magmatic	
4G11-2-5	66	27	0	0	7		magmatic	ODP147
4G-12-2	59	30	0	5	6		magmatic	ODP147
4G-12-3-8B	59	37	0	0	4		magmatic	ODP147
4G-13-1-9Ab	65	29	0	2	4		magmatic	ODP147
Reunion, Cirque de Salazie								
SaG1	56	44	0	0	0		magmatic	cpx+pl:porphyroclast, pl:neoblast
SaG2	55	45	0	0	0		magmatic	cpx+pl:porphyroclast, pl:neoblast
SaG3	42	58	0	0	0		magmatic	coarse part: cpx+pl
SaG4	18	76	6	0	0		magmatic	ol:porphyroclast, mode: pl<cpx
SaG5	84	14	2	0	0		plastic	high T, cpx:porphyroclast, pl:neoblast
SaG6	18	73	8	0	0		plastic	cpx rich fine grain + strain localized zone + pl+cpx+ol fine graine zone
SaG6b	23	69	8	0	0		plastic	
SaG7	50	50	0	0	0		magmatic	well planer structure
SaG8	47	43	10	0	0		magmatic	
SaG9	43	51	6	0	0		magmatic	equigranular texture
SaG10	15	56	29	0	0		plastic	shear localized, low T
SaG11	29	46	26	0	0		plastic	pl+cpx+ol:porphyroclast, pl:neoblast
St Thibéry lava flows								
005							magmatic	
016	98	1	1	0	0		magmatic	
029	100	0	0	0	0		magmatic	
074	60	40	0	0	0		magmatic	
Mid Atlantic ridge, ODP Leg 209								
114	98	2	0	0	0		plastic	Julia, pl+px: porphyroclast, pl: neoblast
121	64	28	5	4	0		magmatic	
137	55	45	0	0	0		magmatic	
Oklahama								
89ANOK	100	0	0	0	0		magmatic	foliation très marquée, pl tabulaires

Table 3. CPO characteristics for the gabbros studied here. I: data from interactive mode; M: data from mapping mode; N: number of measurements; LS: LS index, respectively.

sample#	EBSD	N	J	Max Density			pfJ			(010)		[100]		LS	CPO type	
				[100]	(010)	(001)	[100]	(010)	(001)	P	G	P	G			
Oman ophiolite																
86OA20A	I	236	5.62	5.74	9.56	5.45	2.71	2.74	1.60	0.31	0.14	0.17	0.54	0.27	B	
86OA20B	M	187	7.59	5.90	8.34	3.37	2.31	2.19	1.34	0.14	0.23	0.20	0.42	0.47	B	
86OA20C	I	334	5.43	5.69	8.83	4.87	2.75	2.69	1.55	0.35	0.07	0.13	0.58	0.18	B	
95OB4	I	1345	2.75	2.72	2.51	1.67	1.30	1.29	1.07	0.12	0.27	0.22	0.23	0.59	P	
97OB1C	M	1268	2.86	3.24	5.87	1.71	1.64	2.05	1.07	0.36	0.17	0.19	0.49	0.30	B	
98OB7A	I	823	5.18	4.85	8.70	2.73	2.09	3.65	1.32	0.55	0.16	0.33	0.44	0.33	B	
98OB8B	I	467	4.16	3.55	4.96	2.32	1.53	2.15	1.25	0.38	0.15	0.24	0.35	0.35	B	
98OB10A	I	518	3.75	3.59	4.13	2.37	1.61	1.92	1.19	0.38	0.09	0.15	0.46	0.22	B	
98OB10E	I	377	4.14	3.47	4.61	2.37	1.50	2.06	1.22	0.40	0.11	0.14	0.39	0.24	B	
98OB10G	I	466	3.78	4.29	3.69	2.32	2.01	1.69	1.16	0.10	0.54	0.41	0.08	0.84	A	
88OA13	I	118	8.13	4.74	7.27	3.43	2.16	2.75	1.46	0.42	0.18	0.08	0.65	0.20	B	
88OA14b	I	253	4.93	4.69	8.12	2.94	1.77	2.54	1.27	0.40	0.12	0.09	0.45	0.19	B	
90OA68	I	147	7.18	5.70	4.62	3.60	2.40	2.13	1.35	0.23	0.43	0.30	0.40	0.54	P	
90OA77	I	318	8.97	5.74	5.34	4.28	2.31	2.46	1.65	0.38	0.25	0.37	0.26	0.50	P	
90OF11	I	188	5.57	5.03	5.09	2.88	2.07	1.95	1.22	0.30	0.20	0.15	0.49	0.31	B	
92OB100b	I	212	5.15	4.05	6.15	2.18	1.82	2.28	1.19	0.42	0.12	0.13	0.53	0.20	B	
92OB101	I	165	5.20	3.73	4.75	3.13	1.58	1.88	1.29	0.33	0.09	0.11	0.42	0.21	B	
92OB134	I	165	5.20	3.73	4.75	3.13	1.58	1.88	1.29	0.33	0.09	0.11	0.42	0.21	B	
92OB139	M	118	9.25	5.12	4.93	5.23	1.86	1.90	1.55	0.27	0.23	0.17	0.38	0.38	P	weak
92OB140a	I	188	8.99	6.68	9.21	5.23	2.58	3.59	1.71	0.49	0.19	0.31	0.40	0.35	B	
92OB140c	I	169	7.47	6.33	8.21	4.47	2.03	2.30	1.42	0.25	0.27	0.30	0.22	0.55	P	
92OB142	I	252	6.67	4.99	9.70	4.00	2.50	3.12	1.53	0.39	0.20	0.21	0.52	0.31	B	
92OB143	I	170	9.01	5.66	11.55	3.53	2.41	4.42	1.61	0.58	0.20	0.34	0.48	0.34	B	
93OB157	I	191	6.70	5.70	7.86	3.49	2.29	2.72	1.37	0.42	0.11	0.24	0.45	0.28	B	
94OB28	I	287	5.82	4.93	9.58	3.23	2.25	3.64	1.37	0.53	0.12	0.17	0.59	0.20	B	
95OA129	I	427	3.25	4.24	3.36	3.07	1.48	1.39	1.19	0.17	0.22	0.18	0.19	0.53	P	weak
06OA31b	M	102	8.51	4.14	4.77	4.26	1.56	1.95	1.52	0.28	0.23	0.10	0.28	0.35	P	weak
07OA20a	M	418	2.52	1.92	2.20	2.15	1.10	1.08	1.08	0.02	0.02	0.01	0.13	0.30	P	n.i.
07OA20c1	M	2235	1.38	1.70	1.66	1.42	1.07	1.07	1.03	0.07	0.11	0.08	0.11	0.52	P	weak
07OA20d	M	2873	1.47	1.77	2.52	1.50	1.15	1.22	1.02	0.18	0.09	0.09	0.26	0.29	B	weak
07OA20e	M	2518	1.47	1.71	2.43	1.47	1.13	1.19	1.02	0.16	0.10	0.07	0.25	0.30	B	weak
07-2OA13	M	330	3.72	3.87	4.33	2.72	1.32	1.47	1.21	0.18	0.21	0.18	0.16	0.53	P	weak
07_2_OA_10B	M	5183	4.43				1.86	2.49	1.17						P	
07_2_OA_18b	M	5070	8.73				2.40	4.71	1.48						P	
07_2_OA_18c	M	3690	3.68				1.68	2.23	1.12						P	
07_2_OA_30b	M	1725	3.78				1.98	1.65	1.24						P	
07_2_OA_30h	M	2254	4.93				1.83	2.90	1.21						P	
07_2_OA_37	M	885	4.62				2.10	2.12	1.33						P	
07_2_OA_37b	M	1846	4.03				2.09	2.14	1.18						P	
07_2_OA_41g	M	1213	2.70				1.59	1.25	1.33						P	
07_2_OA_42c	M	3817	2.55				1.35	1.74	1.08						P	
07_2_OA_45c3	M	1392	11.91				2.14	4.54	1.46						P	
07_2_OA_45c4	M	2801	7.94				2.77	5.39	2.00						P	
07_2_OA_66	M	1961	9.07				2.26	5.11	1.52						P	
07_OA_8g_2S	M	3066	2.08				1.20	1.42	1.05						P	
GAVAT2	I	437	5.27	4.11	6.67	3.27	1.77	2.30	1.32	0.02	0.20	0.02	0.08	0.57	P	
ODP Hole 735B																
735B-5	I	124	7.55	1.76	1.81	1.31	1.66	1.61	1.10	0.33	0.05	0.07	0.48	0.12	P	
735B-22B	I	1090	3.22	3.93	2.68	2.40	1.63	1.42	1.15	0.05	0.46	0.26	0.04	0.89	P	
735B-22C	M						3.68	4.36	3.42	0.46	0.19	0.26	0.21	0.42	P	
735B-22D	M	225	8.29	5.37	5.08	4.00	3.70	2.04	1.65	0.28	0.36	0.50	0.18	0.65	A	
735B-22E	M															
735B-22F	M	404	11.56	6.34	6.38	5.24	2.39	2.29	2.13	0.28	0.23	0.44	0.09	0.64	P	
735B-32	I	452	3.72	6.68	9.21	5.23	1.56	1.55	1.11	0.18	0.29	0.20	0.22	0.54	P	
735B-32B	M	299	4.87	4.25	4.31	2.10	1.69	1.77	1.15	0.25	0.27	0.19	0.35	0.44	B	weak
735B-BI-50	M	403	6.85	5.94	3.82	3.09	2.52	1.52	1.29	0.08	0.06	0.11	0.04	0.57	A	
735B-51	I	250	8.85	4.19	5.15	3.73	1.62	1.72	1.58	0.26	0.14	0.14	0.28	0.34	P	weak

Table 3. *(continued)*

sample#	EBSD	N	J	Max Density			pfJ			(010)		[100]		LS	CPO type	
				[100]	(010)	(001)	[100]	(010)	(001)	P	G	P	G			
735B-70	I	321	3.94	2.85	3.00	2.69	1.21	1.23	1.17	0.12	0.02	0.05	0.19	0.16	P	n.i.
735B-79	I	313	4.03	2.93	4.13	5.23	1.51	1.63	1.14	0.27	0.13	0.15	0.36	0.30	P	weak
735B-79B	M	107	8.80	4.53	7.07	4.20	1.65	2.00	1.46	0.26	0.16	0.08	0.42	0.27	B	weak
116R4	I	855	3.99	1.30	1.31	1.20	1.30	1.32	1.26	0.11	0.15	0.01	0.18	0.31	B	weak
133R3	I	1079	3.13	4.71	2.47	1.98	1.71	1.37	1.12	0.07	0.40	0.24	0.14	0.74	A	
133-3-0-7A	M	1418	2.97	3.96	2.70	1.84	1.69	1.37	1.11	0.13	0.35	0.31	0.18	0.68	A	
142R5	I	670	4.81	4.71	3.10	2.29	1.60	1.40	1.23	0.03	0.42	0.30	0.13	0.82	A	
142-5-6-8b	M	913	4.24	4.04	2.68	2.52	1.70	1.40	1.23	0.01	0.50	0.31	0.12	0.85	A	
147R6	I	929	2.88	2.72	2.21	1.96	1.25	1.22	1.11	0.15	0.09	0.14	0.12	0.46	B	weak
154R5	I	536	4.39	4.15	3.45	2.72	1.74	1.46	1.20	0.13	0.34	0.26	0.22	0.63	A	
154-5-42-44B	M	441	4.01	3.62	2.86	2.37	1.56	1.41	1.13	0.11	0.34	0.22	0.24	0.61	A	
167R6	I	657	3.07	2.93	3.33	2.13	1.23	1.32	1.09	0.16	0.18	0.09	0.24	0.40	B	weak
179R5	I	420	9.72	6.49	5.76	6.46	1.71	1.99	1.80	0.05	0.09	0.05	0.37	0.39	P	weak
190R4	I	935	2.88	2.61	2.68	1.87	1.34	1.35	1.09	0.18	0.15	0.11	0.32	0.35	B	weak
209R7	I	489	4.30	3.01	3.29	2.56	1.30	1.29	1.20	0.07	0.20	0.16	0.03	0.80	P	n.i.
735B-BI-6	M	1173	2.81	2.99	3.56	1.78	1.53	1.57	1.08	0.24	0.24	0.15	0.33	0.40	P	
735B-BI-7	M	9010	2.36	2.35	2.10	1.55	1.21	1.20	1.05	0.06	0.31	0.16	0.15	0.67	A	weak
735B-BI-15	M	2305	2.61	3.76	1.92	2.62	1.65	1.20	1.21	0.04	0.35	0.24	0.11	0.80	A	
735B-BI-19	M	1098	3.07	3.64	2.40	2.51	1.50	1.29	1.14	0.15	0.24	0.14	0.23	0.50	P	
735B-BI-25	M	1531	2.25	2.14	2.04	1.56	1.15	1.19	1.04	0.13	0.17	0.12	0.17	0.50	P	weak
735B-BI-26	M	545	2.61	2.43	2.48	1.83	1.17	1.17	1.07	0.14	0.04	0.05	0.19	0.23	B	weak
735B-BI-33	M	161	5.80	2.90	2.92	3.42	1.26	1.22	1.34	0.06	0.10	0.09	0.14	0.49	P	n.i.
735B-BI-34	M	2871	2.68	2.94	2.55	1.70	1.43	1.26	1.08	0.14	0.23	0.11	0.25	0.46	P	
735B-BI-38	M	810	2.73	2.65	2.76	1.88	1.24	1.23	1.07	0.14	0.18	0.11	0.20	0.45	B	weak
735B-BI-49	M	5440	3.27	4.95	3.04	1.90	2.11	1.47	1.16	0.16	0.41	0.29	0.22	0.64	A	
735B-50	I	7144	4.73	5.78	2.88	2.24	2.48	1.65	1.46	0.19	0.31	0.26	0.30	0.55	B	
735B-BI-51	M	4448	1.98	2.20	1.76	1.93	1.15	1.06	1.11	0.12	0.06	0.06	0.16	0.31	A	
735B-BI-52	M	626	3.37	2.68	2.71	1.66	1.25	1.21	1.13	0.15	0.14	0.06	0.20	0.36	P	weak
735B-BI-52a	M	180	8.75	2.28	2.37	1.81	1.17	1.21	1.06	0.15	0.14	0.08	0.21	0.38	B	weak
735B-BI-52b	M	255	4.65	3.03	2.63	2.56	1.40	1.32	1.21	0.13	0.33	0.22	0.21	0.62	B	weak
735B-BI-52c	M	1823	2.41	2.34	2.13	1.83	1.15	1.14	1.08	0.11	0.10	0.10	0.14	0.44	B	weak
735B-BI-55	M	1124	2.77	3.78	2.63	2.06	1.74	1.37	1.12	0.16	0.33	0.23	0.29	0.55	A	
735B-BI-57	M	336	4.68	3.59	4.05	2.18	1.61	1.56	1.13	0.30	0.19	0.16	0.42	0.33	P	weak
735B-BI-58	M	693	3.95	4.31	4.09	2.09	1.77	1.72	1.10	0.30	0.19	0.19	0.46	0.33	P	
735B-BI-64a	M															
735B-BI-64a2	M	424	3.70	2.68	4.56	2.35	1.55	1.90	1.11	0.33	0.15	0.08	0.47	0.23	B	
735B-BI-64b	M	899	2.68	2.82	2.95	1.53	1.40	1.46	1.03	0.19	0.28	0.10	0.30	0.42	B	weak
735B-BI-70	M	1229	3.28	2.55	2.87	1.81	1.47	1.38	1.08	0.26	0.04	0.07	0.37	0.15	B	
735B-BI-82a	M	4683	2.68	4.01	3.29	1.85	1.71	1.52	1.10	0.22	0.27	0.26	0.19	0.56	p	
735B-BI-82b	M	498	4.68	3.83	4.24	2.32	1.71	1.79	1.14	0.29	0.24	0.18	0.38	0.38	P	
735B-BI-83a	M	524	3.57	2.45	2.31	2.61	1.15	1.24	1.24	0.15	0.11	0.07	0.20	0.35	P	weak
735B-BI-83b	M	1147	3.98	5.53	4.08	2.32	2.32	1.68	1.26	0.23	0.33	0.33	0.24	0.58	B	
735B-BI-92	M	310	5.03	4.25	3.97	2.74	1.44	1.61	1.18	0.20	0.20	0.08	0.26	0.37	B	weak
735B-BI-92-2	M	28367	5.52													
Brazil, Itabuna and Ribeira belts																
CM19	I	947	4.97	3.79	5.91	3.06	1.54	1.55	1.40	0.26	0.02	0.27	0.15	0.35	B	weak
CM20	I	490	3.20	3.75	3.73	3.24	1.31	1.20	1.21	0.10	0.02	0.07	0.18	0.23	P	weak
RMB20	I	148	6.11	3.25	3.10	3.03	1.44	1.47	1.43	0.17	0.21	0.08	0.32	0.37	B	weak
CM08	I	523	4.71	3.99	4.45	2.93	1.43	1.58	1.16	0.25	0.12	0.08	0.34	0.26	B	weak
CM09	I	538	2.78	2.77	2.73	2.52	1.23	1.19	1.12	0.06	0.23	0.09	0.19	0.56	P	weak
CM22	I	481	3.29	3.42	3.43	2.88	1.27	1.30	1.18	0.14	0.10	0.09	0.16	0.39	P	weak
CM29	I	193	4.33	3.12	2.49	2.83	1.25	1.16	1.23	0.03	0.06	0.08	0.05	0.61	P	n.i.
RB5E	I	306	4.22	2.97	2.85	2.14	1.31	1.30	1.18	0.20	0.03	0.09	0.27	0.19	B	weak
RB538	I	203	5.48	3.57	4.60	3.32	1.44	1.47	1.41	0.17	0.21	0.19	0.19	0.52	B	weak
RB540	I	256	4.39	2.66	2.76	2.98	1.29	1.31	1.19	0.10	0.17	0.11	0.05	0.67	P	n.i.
RB546	I	362	3.22	1.98	2.28	2.89	1.16	1.18	1.32	0.06	0.15	0.03	0.17	0.44	B	weak
RB548	I	282	3.80	1.98	2.28	2.89	1.20	1.15	1.23	0.03	0.10	0.06	0.06	0.62	P	n.i.
RB559	I	372	3.89	2.42	3.42	2.76	1.33	1.43	1.27	0.21	0.13	0.04	0.42	0.23	B	
RB566	I	289	3.95	2.38	2.37	3.22	1.22	1.16	1.43	0.02	0.17	0.10	0.19	0.61	P	n.i.
RB607A	I	505	4.34	2.41	3.46	2.60	1.34	1.48	1.21	0.23	0.13	0.01	0.43	0.20	B	weak

Table 3. *(continued)*

sample#	EBSD	N	J	Max Density			pfJ			(010)		[100]		LS	CPO type	
				[100]	(010)	(001)	[100]	(010)	(001)	P	G	P	G			
RB607B	I	351	3.33	2.79	2.18	2.32	1.19	1.18	1.21	0.05	0.10	0.09	0.15	0.52	P	n.i.
RB609A	I	146	5.47	2.46	2.88	3.89	1.33	1.36	1.54	0.14	0.05	0.02	0.34	0.17	B	n.i.
RB614	I	249	4.09	2.22	2.31	2.96	1.20	1.22	1.34	0.13	0.04	0.02	0.22	0.16	B	weak
RB689	I	362	4.44	4.10	4.09	2.64	1.60	1.65	1.26	0.20	0.30	0.28	0.14	0.63	A	weak
ODP Hole 1256D																
1256D_78_a	M	1925	1.73	1.64	1.91	1.73	1.05	1.07	1.05	0.03	0.08	0.03	0.03	0.64	A	weak
1256D_91_c	M	512	4.44	3.78	5.17	3.74	1.27	1.33	1.22	0.04	0.08	0.13	0.25	0.51	P	weak
1256D_103_a	M	4289	1.23	1.65	1.31	1.30	1.04	1.02	1.01	0.03	0.05	0.06	0.07	0.54	P	n.i.
1256D_108_a	M	633	2.67	2.36	3.03	2.80	1.18	1.32	1.17	0.10	0.18	0.10	0.11	0.56	B	weak
1256D_109_b	M	2632	1.57	1.87	2.26	1.53	1.12	1.17	1.03	0.14	0.12	0.10	0.19	0.41	B	weak
1256D_112_a	M	3007	1.54	2.24	2.92	1.46	1.17	1.23	1.04	0.16	0.13	0.10	0.15	0.42	B	weak
1256D_112_b	M	846	2.20	2.54	2.60	2.10	1.22	1.18	1.06	0.11	0.15	0.13	0.09	0.58	A	weak
1256D_115	M	2205	1.33	1.57	1.53	1.37	1.04	1.04	1.02	0.05	0.08	0.05	0.08	0.50	P	weak
1256D_116_a	M	6965	1.12	1.29	1.26	1.20	1.01	1.01	1.00	0.01	0.07	0.05	0.02	0.78	P	n.i.
1256D_116_b	M	2463	1.36	1.38	1.64	1.63	1.03	1.03	1.04	0.04	0.05	0.02	0.08	0.40	P	n.i.
1256D_117_a	M	5952	1.21	1.51	1.36	1.33	1.03	1.03	1.01	0.01	0.14	0.08	0.03	0.82	P	n.i.
1256D_117_b	M	1473	1.44	1.54	1.52	1.52	1.03	1.03	1.03	0.04	0.06	0.03	0.04	0.50	P	weak
Hess Deep																
HD69r6_a	M	412	2.77	2.36	2.34	2.19	1.12	1.15	1.09	0.04	0.17	0.04	0.06	0.60	P	n.i.
HD69r10_a	M	572	2.67	2.86	3.40	2.62	1.22	1.26	1.10	0.17	0.01	0.10	0.11	0.26	P	weak
HD69r16_a	M	1503	1.74	2.11	2.43	1.54	1.16	1.21	1.04	0.11	0.23	0.15	0.08	0.66	P	weak
HD70r2_a	M	674	2.27	2.31	3.29	2.10	1.20	1.41	1.11	0.24	0.13	0.08	0.30	0.28	B	
HD70r14_a	M	984	2.14	2.73	3.67	1.60	1.34	1.41	1.06	0.25	0.06	0.08	0.38	0.18	B	
HD70r15_a	M	245	4.41	3.18	3.73	3.09	1.35	1.67	1.26	0.29	0.08	0.06	0.39	0.18	B	
HD70r17_a	M	2437	1.89	2.35	3.80	1.57	1.34	1.54	1.04	0.27	0.12	0.09	0.39	0.24	B	
HD70r18_a	M	209	7.57	4.13	5.49	3.69	1.63	1.83	1.42	0.21	0.26	0.14	0.25	0.45	B	weak
HD70r20_a	M															
HD73r2_a	M	2916	2.05	2.19	4.23	1.84	1.31	1.76	1.10	0.33	0.15	0.10	0.41	0.25	B	
HD73r4_a	M	675	2.83	3.34	4.39	2.21	1.42	1.67	1.12	0.30	0.11	0.15	0.34	0.29	B	
HD73r5_a	M	1050	2.16	2.66	3.23	1.62	1.29	1.43	1.05	0.23	0.15	0.12	0.36	0.32	B	
HD73r9_a	M	1400	2.36	2.89	4.44	1.83	1.38	1.73	1.08	0.30	0.14	0.13	0.41	0.28	B	
HD73r13_a	M	824	2.15	3.04	3.15	1.67	1.41	1.35	1.05	0.18	0.18	0.15	0.35	0.40	B	
HD73r15_a	M	265	3.75	3.82	4.46	2.16	1.43	1.64	1.17	0.28	0.04	0.09	0.31	0.18	P	weak
HD73r16_a	M	1315	2.59	2.41	5.03	2.21	1.36	2.01	1.16	0.41	0.02	0.10	0.42	0.12	B	
HD73r18_a	M	445	3.26	3.09	4.92	2.15	1.49	1.71	1.10	0.30	0.11	0.14	0.40	0.26	B	
HD73r20_a	M	357	3.56	3.49	4.54	2.14	1.46	1.74	1.14	0.29	0.17	0.15	0.35	0.33	B	
HD75r5_a	M	1454	2.21	2.61	3.54	1.83	1.31	1.51	1.07	0.27	0.11	0.16	0.32	0.31	B	
HD75r8_a	M	943	1.86	2.25	2.42	1.84	1.15	1.25	1.06	0.18	0.11	0.11	0.21	0.36	P	weak
HD75r11_a	M	312	3.95	3.63	5.67	2.35	1.70	2.03	1.19	0.38	0.08	0.15	0.49	0.20	B	
HD76r1_a	M	486	3.66	3.87	5.82	2.41	1.87	2.09	1.19	0.31	0.22	0.27	0.35	0.43	B	
HD76r3_a	M	409	6.02	4.31	8.50	3.13	2.11	3.04	1.29	0.38	0.26	0.32	0.41	0.42	B	
HD76r8_a	M	1138	3.54	3.69	7.47	1.96	1.83	2.68	1.16	0.43	0.14	0.13	0.55	0.22	B	
HD76r10_a	M	517	2.57	2.79	2.84	1.90	1.23	1.20	1.07	0.13	0.06	0.08	0.27	0.27	B	
HD76r11_a	M	939	1.93	1.94	2.14	1.80	1.18	1.19	1.04	0.17	0.06	0.04	0.33	0.19	B	
HD76r14_a	M	706	2.52	3.32	3.19	1.65	1.40	1.44	1.07	0.17	0.28	0.22	0.21	0.56	P	
HD78r1_a	M	1091	1.82	2.50	2.40	1.81	1.25	1.23	1.05	0.15	0.11	0.06	0.31	0.29	B	
HD78r2_a	M	145	6.38	3.15	2.88	3.53	1.31	1.34	1.34	0.07	0.23	0.09	0.05	0.69	P	n.i.
HD78r5a	M	1650	1.71	2.22	2.61	1.57	1.22	1.27	1.03	0.20	0.08	0.08	0.30	0.25	B	
HD78r5b	M	250	4.04	2.81	2.54	3.00	1.27	1.30	1.25	0.14	0.13	0.14	0.05	0.62	P	n.i.
HD78r5x4	M	317	3.17	2.27	2.58	2.63	1.12	1.19	1.21	0.07	0.15	0.09	0.12	0.55	P	n.i.
HD78r6_a	M	235	4.86	4.20	4.66	2.71	1.79	1.74	1.19	0.23	0.24	0.19	0.30	0.45	P	
HD78r7_a	M	1276	1.57	1.75	1.72	1.55	1.07	1.05	1.03	0.02	0.14	0.10	0.01	0.88	P	n.i.
4G11-2-5	M	389	3.17	2.95	3.47	2.83	1.27	1.39	1.15	0.18	0.21	0.14	0.18	0.48	P	weak
4G-12-2	M	896	2.46	2.93	3.39	1.86	1.36	1.39	1.09	0.16	0.24	0.19	0.21	0.54	P	
4G-12-3-8B	M	442	3.46	3.10	5.49	2.53	1.51	2.18	1.18	0.34	0.20	0.10	0.44	0.27	B	
4G-13-1-9Ab	M	800	2.15	2.66	2.86	1.88	1.18	1.19	1.06	0.12	0.06	0.05	0.18	0.27	B	n.i.

Table 3. *(continued)*

sample#	EBSD	N	J	Max Density			pfJ			(010)		[100]		LS	CPO type	
				[100]	(010)	(001)	[100]	(010)	(001)	P	G	P	G			
Reunion, Cirque de Salazie																
SaG1	M	24														
SaG2	M	1529	2.61	2.44	3.73	1.57	1.42	1.67	1.04	0.32	0.08	0.10	0.48	0.19	B	
SaG3	M	656	2.43	1.88	3.03	2.16	1.11	1.28	1.13	0.15	0.19	0.08	0.18	0.43	B	weak
SaG4	M	715	3.34	2.75	3.69	2.19	1.47	1.86	1.12	0.37	0.11	0.11	0.51	0.20	B	
SaG5	M	50														
SaG6	M	705	2.15	2.00	2.37	1.62	1.17	1.22	1.05	0.17	0.09	0.04	0.30	0.24	B	weak
SaG6b	M	2323	1.47	1.76	1.85	1.45	1.09	1.12	1.02	0.11	0.11	0.07	0.21	0.37	B	weak
SaG7	M	279	4.14	3.41	5.18	2.20	1.65	1.80	1.14	0.32	0.05	0.10	0.44	0.16	B	
SaG8	M	2874	2.31	2.78	4.84	1.77	1.49	1.92	1.08	0.38	0.08	0.11	0.45	0.19	B	
SaG9	M	3178	2.11	2.90	3.92	1.82	1.47	1.67	1.07	0.31	0.12	0.13	0.41	0.27	B	
SaG10	M	1391	1.92	2.33	3.07	1.41	1.27	1.34	1.03	0.22	0.12	0.10	0.32	0.29	B	weak
SaG11	M	795	1.93	1.82	2.17	1.71	1.10	1.12	1.05	0.09	0.08	0.08	0.11	0.44	B	weak
St Thibéry lava flows																
005	I	19														
016	I	313		3.10	3.97	3.00	1.34	1.73	1.22	0.24	0.31	0.18	0.15	0.56	P	
029	I	264	4.64	3.41	4.15	5.29	1.38	1.68	1.80	0.20	0.32	0.23	0.07	0.69	P	
074	I	231	3.85	2.91	4.52	3.85	1.41	1.56	1.22	0.16	0.30	0.20	0.16	0.60	P	
Mid Atlantic ridge, ODP Leg 209																
114	I	93														
121	I	285	4.01	2.82	2.89	1.15	1.34	1.34	1.16	0.13	0.19	0.10	0.24	0.44	P	weak
137	I	127	8.39	4.25	4.52	3.85	1.67	1.91	1.45	0.25	0.24	0.20	0.22	0.49	P	weak
Oklahama																
89ANOK	I	370	13.63	7.63	24.33	4.88	2.95	10.68	2.37	0.76	0.14	0.07	0.81	0.12	B	

Table 4. Seismic properties (velocity and anisotropy) calculated as plagioclase 100% using one point per grain data for gabbros studied here. Vp: P-wave; AVp: P-wave anisotropy; AVs: S-wave anisotropy, respectively.

sample#	Vp Max (km/s)	Vp Min (km/s)	AVp (%)	AVs Max (%)	AVs Min (%)	Vs1 max (km/s)	Vs1 min (km/s)	Vs2 max (km/s)	Vs2 min (km/s)
Oman ophiolite									
86OA20A	7.04	6.50	8.00	8.27	0.11	3.75	3.47	3.51	3.43
86OA20B	6.93	6.57	5.40	7.57	0.11	3.77	3.49	3.53	3.44
86OA20C	7.05	6.53	7.70	8.18	0.03	3.76	3.48	3.51	3.45
95OB4	6.86	6.49	5.50	3.88	0.08	3.63	3.52	3.56	3.49
97OB1C	6.98	6.48	7.50	4.63	0.03	3.65	3.49	3.55	3.47
98OB7A	7.07	6.43	9.60	8.14	0.06	3.72	3.48	3.56	3.40
98OB8B	6.97	6.48	7.30	6.63	0.03	3.71	3.47	3.55	3.47
98OB10A	6.93	6.50	6.40	5.54	0.03	3.66	3.53	3.55	3.45
98OB10E	6.93	6.53	5.90	5.68	0.14	3.64	3.51	3.59	3.44
98OB10G	6.92	6.40	7.90	6.92	0.09	3.69	3.48	3.54	3.44
88OA13	6.98	6.55	6.40	7.13	0.03	3.71	3.49	3.61	3.43
88OA14b	6.95	6.54	6.00	5.99	0.17	3.71	3.50	3.54	3.43
90OA68	6.99	6.44	8.30	7.57	0.15	3.71	3.44	3.57	3.42
90OA77	7.01	6.41	8.80	10.52	0.14	3.79	3.47	3.56	3.40
90OF11	6.94	6.50	6.60	5.55	0.25	3.67	3.50	3.58	3.44
92OB100b	6.94	6.51	6.40	4.76	0.22	3.63	3.51	3.57	3.45
92OB101	6.95	6.55	6.00	6.72	0.17	3.71	3.48	3.56	3.45
92OB134	6.95	6.55	6.00	6.72	0.17	3.71	3.48	3.56	3.45
92OB139	6.94	6.51	6.50	6.86	0.17	3.71	3.48	3.59	3.41
92OB140a	7.05	6.38	10.00	9.49	0.06	3.79	3.47	3.53	3.41
92OB140c	6.94	6.42	7.70	8.51	0.00	3.77	3.49	3.54	3.43
92OB142	7.09	6.48	9.00	10.87	0.17	3.83	3.46	3.53	3.39
92OB143	7.12	6.40	10.60	10.41	0.09	3.78	3.48	3.56	3.35
93OB157	7.01	6.47	8.10	7.68	0.03	3.75	3.50	3.54	3.43
94OB28	7.07	6.47	8.80	7.29	0.06	3.74	3.48	3.52	3.45
95OA129	6.86	6.51	5.20	4.52	0.06	3.65	3.51	3.55	3.48
06OA31b	6.89	6.52	5.60	5.50	0.11	3.65	3.49	3.62	3.43
07OA20a	6.74	6.64	1.40	2.16	0.03	3.60	3.53	3.57	3.49
07OA20c1	6.75	6.60	2.10	1.81	0.03	3.58	3.53	3.55	3.51
07OA20d	6.81	6.60	3.10	2.29	0.06	3.59	3.52	3.56	3.50
07OA20e	6.82	6.59	3.60	2.45	0.11	3.60	3.52	3.55	3.51
07-2OA13	6.83	6.53	4.50	3.68	0.03	3.65	3.52	3.55	3.48
GAVAT2	7.01	6.51	7.40	7.82	0.11	3.74	3.49	3.52	3.44
ODP Hole 735B									
735B-5	6.88	6.57	4.60	4.96	0.20	3.64	3.53	3.58	3.46
735B-22B	6.82	6.50	4.80	5.96	0.03	3.68	3.50	3.55	3.45
735B-22C	7.07	6.31	11.30	21.34	0.32	4.07	3.39	3.65	3.19
735B-22D	6.86	6.38	7.40	7.18	0.23	3.74	3.49	3.55	3.40
735B-22E	7.08	6.30	11.70	14.52	0.17	3.94	3.41	3.53	3.33
735B-22F	6.96	6.46	7.40	11.19	0.20	3.81	3.47	3.59	3.34
735B-32	6.83	6.49	5.10	4.92	0.14	3.65	3.50	3.56	3.45
735B-32B	6.89	6.50	5.80	5.01	0.14	3.66	3.51	3.56	3.44
735B-BI-50	6.83	6.41	6.40	7.25	0.40	3.71	3.50	3.60	3.40
735B-51	6.91	6.54	5.60	7.14	0.14	3.72	3.48	3.56	3.43
735B-70	6.82	6.60	3.20	4.76	0.03	3.66	3.51	3.57	3.45
735B-79	6.90	6.54	5.30	4.46	0.23	3.62	3.50	3.58	3.46
735B-79B	6.90	6.55	5.20	6.68	0.09	3.71	3.49	3.58	3.46
116R4	6.81	6.55	3.90	5.37	0.03	3.69	3.49	3.56	3.45
133R3	6.81	6.48	4.80	3.57	0.03	3.63	3.51	3.53	3.47
133-3-0-7A	6.81	6.47	5.10	3.76	0.09	3.63	3.51	3.54	3.47
142R5	6.87	6.43	6.60	5.85	0.20	3.68	3.49	3.56	3.42
142-5-6-8b	6.85	6.43	6.30	4.61	0.09	3.67	3.52	3.54	3.45
147R6	6.80	6.57	3.50	4.69	0.06	3.67	3.51	3.56	3.48
154R5	6.85	6.48	5.50	5.25	0.14	3.66	3.50	3.55	3.46
154-5-42-44B	6.85	6.50	5.10	4.04	0.06	3.62	3.52	3.54	3.47
167R6	6.80	6.58	3.30	3.17	0.06	3.62	3.53	3.55	3.50
179R5	6.83	6.51	4.90	7.82	0.14	3.71	3.50	3.60	3.40

Table 4. *(continued)*

sample#	Vp Max (km/s)	Vp Min (km/s)	AVp (%)	AVs Max (%)	AVs Min (%)	Vs1 max (km/s)	Vs1 min (km/s)	Vs2 max (km/s)	Vs2 min (km/s)
190R4	6.84	6.55	4.30	4.73	0.11	3.64	3.52	3.58	3.46
209R7	6.76	6.56	3.00	3.52	0.03	3.63	3.52	3.56	3.48
735B-BI-6	6.87	6.53	5.10	4.47	0.08	3.64	3.51	3.56	3.46
735B-BI-7	6.78	6.57	3.10	3.68	0.03	3.62	3.52	3.59	3.46
735B-BI-15	6.82	6.51	4.60	4.38	0.09	3.64	3.50	3.55	3.46
735B-BI-19	6.81	6.53	4.20	4.58	0.14	3.65	3.50	3.57	3.46
735B-BI-25	6.78	6.57	3.20	2.66	0.06	3.58	3.52	3.56	3.49
735B-BI-26	6.78	6.60	2.70	3.18	0.00	3.61	3.52	3.57	3.49
735B-BI-33	6.77	6.59	2.70	4.31	0.06	3.63	3.51	3.58	3.45
735B-BI-34	6.80	6.56	3.60	4.30	0.08	3.63	3.51	3.59	3.48
735B-BI-38	6.80	6.58	3.30	2.76	0.06	3.60	3.53	3.56	3.49
735B-BI-49	6.83	6.45	5.70	4.79	0.26	3.65	3.51	3.57	3.45
735B-50	6.88	6.45	6.50	8.03	0.09	3.75	3.51	3.55	3.42
735B-BI-51	6.74	6.61	2.00	2.84	0.03	3.61	3.52	3.54	3.51
735B-BI-52	6.76	6.57	2.90	4.56	0.11	3.64	3.51	3.57	3.47
735B-BI-52a	6.79	6.60	2.70	2.67	0.06	3.61	3.52	3.56	3.49
735B-BI-52b	6.84	6.55	4.30	4.03	0.03	3.61	3.51	3.59	3.45
735B-BI-52c	6.75	6.57	2.70	2.54	0.14	3.59	3.52	3.57	3.49
735B-BI-55	6.83	6.50	5.00	4.73	0.03	3.64	3.50	3.53	3.47
735B-BI-57	6.90	6.47	6.40	5.51	0.06	3.67	3.51	3.55	3.45
735B-BI-58	6.90	6.49	6.10	4.21	0.20	3.62	3.52	3.56	3.45
735B-BI-64a2	6.91	6.56	5.20	3.74	0.03	3.63	3.51	3.56	3.46
735B-BI-64b	6.83	6.54	4.40	3.72	0.11	3.61	3.53	3.57	3.46
735B-BI-70	6.81	6.55	4.00	4.77	0.06	3.64	3.52	3.61	3.46
735B-BI-82a	6.83	6.47	5.40	4.31	0.20	3.63	3.51	2.54	3.47
735B-BI-82b	6.89	6.50	5.80	5.10	0.06	3.64	3.51	3.58	3.46
735B-BI-83a	6.78	6.57	3.10	3.41	0.03	3.61	3.50	3.57	3.49
735B-BI-83b	6.88	6.41	7.10	5.93	0.29	3.68	3.50	3.54	3.44
735B-BI-92	6.85	6.57	4.10	4.42	0.14	3.63	3.52	3.55	3.47
735B-BI-92-2									
Brazil, Itabuna and Ribeira belts									
CM19	6.85	6.48	5.40	5.04	0.00	3.64	3.52	3.56	3.46
CM20	6.79	6.61	2.80	3.36	0.03	3.63	3.52	3.56	3.47
RMB20	6.87	6.59	4.20	5.74	0.20	3.64	3.51	3.59	3.43
CM08	6.57	6.89	4.70	5.22	0.06	3.66	3.50	3.58	3.46
CM09	6.79	6.59	3.00	3.16	0.14	3.61	3.53	3.57	3.48
CM22	6.79	6.58	3.10	4.08	0.08	3.64	3.52	3.56	3.47
CM29	6.79	6.62	2.50	5.16	0.00	3.66	3.51	3.55	3.46
RB5E	6.87	6.57	4.50	7.03	0.31	3.69	3.48	3.56	3.42
RB538	6.95	6.54	6.20	8.93	0.06	3.79	3.44	3.55	3.38
RB540	6.77	6.61	2.40	4.02	0.06	3.64	3.52	3.57	3.45
RB546	6.85	6.58	4.20	6.95	0.03	3.72	3.46	3.58	3.39
RB548	6.86	6.58	4.20	6.95	0.03	3.72	3.46	3.58	3.39
RB559	6.89	6.57	4.80	6.71	0.11	3.72	3.50	3.58	3.40
RB566	6.75	6.57	2.70	5.37	0.14	3.66	3.51	3.58	3.46
RB607A	6.84	6.61	3.40	4.40	0.14	3.65	3.50	3.58	3.48
RB607B	6.78	6.60	2.60	4.38	0.06	3.66	3.50	3.57	3.47
RB609A	6.96	6.58	5.70	7.82	0.08	3.73	3.48	3.55	3.40
RB614	6.77	6.61	2.30	4.37	0.03	3.62	3.50	3.57	3.46
RB689	6.89	6.53	5.40	9.09	0.09	3.77	3.47	3.55	3.44
ODP Hole 1256D									
1256D_78_a	6.72	6.64	1.10	1.69	0.06	3.58	3.52	3.56	3.51
1256D_91_c	6.88	6.56	4.70	5.18	0.03	3.67	3.50	3.56	3.47
1256D_103_a	6.72	6.62	1.50	1.19	0.03	3.57	3.54	3.55	3.52
1256D_108_a	6.79	6.56	3.50	4.33	0.11	3.62	3.50	3.57	3.45
1256D_109_b	6.81	6.60	3.10	2.80	0.03	3.59	3.52	3.57	3.49
1256D_112_a	6.78	6.59	2.80	2.25	0.00	3.60	3.53	3.55	3.51
1256D_112_b	6.77	6.58	2.90	3.48	0.06	3.60	3.51	3.56	3.46
1256D_115	6.73	6.63	1.50	1.35	0.03	3.57	3.53	3.55	3.52

Table 4. *(continued)*

sample#	Vp Max (km/s)	Vp Min (km/s)	AVp (%)	AVs Max (%)	AVs Min (%)	Vs1 max (km/s)	Vs1 min (km/s)	Vs2 max (km/s)	Vs2 min (km/s)
1256D_116_a	6.71	6.64	1.00	0.99	0.00	3.56	3.54	3.55	3.53
1256D_116_b	6.73	6.65	1.20	1.44	0.03	3.58	3.53	3.56	3.52
1256D_117_a	6.72	6.61	1.60	1.13	0.00	3.57	3.53	3.55	3.52
1256D_117_b	6.71	6.65	1.00	1.41	0.00	3.58	3.53	3.56	3.52
Hess Deep									
HD69r6_a	6.76	6.62	2.00	1.72	0.03	3.58	3.53	3.56	3.52
HD69r10_a	6.76	6.59	2.50	2.40	0.06	3.59	3.53	3.56	3.48
HD69r16_a	6.78	6.57	3.10	2.28	0.00	3.59	3.52	3.55	3.51
HD70r2_a	6.83	6.57	3.90	2.58	0.06	3.61	3.53	3.56	3.48
HD70r14_a	6.86	6.57	4.30	3.16	0.06	3.61	3.52	3.57	3.48
HD70r15_a	6.89	6.58	4.60	4.41	0.14	3.65	3.50	3.57	3.47
HD70r17_a	6.89	6.57	4.60	2.96	0.11	3.61	3.50	3.56	3.50
HD70r18_a	6.81	6.52	4.40	5.06	0.14	3.66	3.51	3.58	3.45
HD73r2_a	6.92	6.57	5.20	4.15	0.03	3.64	3.50	3.55	3.49
HD73r4_a	6.91	6.51	6.00	5.54	0.11	3.65	3.52	3.55	3.45
HD73r5_a	6.87	6.55	4.80	2.57	0.06	3.59	3.52	3.57	3.49
HD73r9_a	6.93	6.55	5.70	4.57	0.03	3.64	3.49	3.54	3.48
HD73r13_a	6.87	6.53	5.20	3.84	0.06	3.62	3.52	3.56	3.47
HD73r15_a	6.83	6.56	4.10	3.50	0.08	3.61	3.53	3.58	3.48
HD73r16_a	6.92	6.56	5.30	4.07	0.03	3.64	3.51	3.54	3.49
HD73r18_a	6.91	6.53	5.60	3.99	0.11	3.63	3.50	3.56	3.49
HD73r20_a	6.89	6.54	5.20	4.87	0.12	3.64	3.48	3.57	3.46
HD75r5_a	6.88	6.53	5.20	3.29	0.03	3.62	3.50	3.57	3.49
HD75r8_a	6.80	6.56	3.60	1.95	0.08	3.59	3.54	3.55	3.50
HD75r11_a	6.97	6.52	6.60	5.00	0.03	3.65	3.49	3.56	3.47
HD76r1_a	6.99	6.46	7.90	7.19	0.06	3.70	3.49	3.55	3.43
HD76r3_a	7.09	6.45	9.40	9.62	0.03	3.79	3.47	3.52	3.40
HD76r8_a	7.03	6.54	7.20	6.67	0.11	3.70	3.49	3.54	3.44
HD76r10_a	6.81	6.59	3.20	3.53	0.03	3.61	3.53	3.56	3.48
HD76r11_a	6.81	6.60	3.20	2.40	0.11	3.59	3.53	3.57	3.50
HD76r14_a	6.86	6.52	5.10	3.88	0.06	3.62	3.49	3.57	3.48
HD78r1_a	6.84	6.60	3.60	3.13	0.17	3.61	3.53	3.55	3.49
HD78r2_a	6.77	6.60	2.50	3.19	0.03	3.62	3.51	3.57	3.45
HD78r5a	6.83	6.58	3.80	2.99	0.06	3.59	3.52	3.57	3.49
HD78r5b	6.75	6.57	2.70	3.04	0.06	3.62	3.52	3.55	3.48
HD78r5x4	6.76	6.59	2.60	3.63	0.11	3.62	3.53	3.57	3.46
HD78r6_a	6.87	6.52	5.20	5.70	0.08	3.66	3.52	3.58	3.42
HD78r7_a	6.74	6.62	1.80	2.08	0.00	3.60	3.53	3.55	3.52
4G11-2-5	6.82	6.57	3.70	3.64	0.11	3.65	3.52	3.56	3.48
4G-12-2	6.85	6.54	4.70	4.35	0.06	3.64	3.50	3.56	3.48
4G-12-3-8B	6.97	6.55	6.30	6.59	0.17	3.68	3.47	3.55	3.43
4G-13-1-9Ab	6.77	6.61	2.40	2.36	0.06	3.58	3.53	3.56	3.49
Reunion, Cirque de Salazie									
SaG2	6.93	6.54	5.80	4.08	0.25	3.63	3.51	3.56	3.47
SaG3	6.80	6.61	3.00	3.33	0.03	3.61	3.52	3.58	3.48
SaG4	6.91	6.53	5.80	3.78	0.17	3.62	3.52	3.58	3.46
SaG6	6.80	6.59	3.20	2.20	0.03	3.59	3.55	3.56	3.50
SaG6b	6.78	6.59	2.90	2.04	0.03	3.58	3.53	3.56	3.50
SaG7	6.89	6.54	5.20	3.03	0.14	3.62	3.54	3.57	3.47
SaG8	6.92	6.53	5.80	3.84	0.06	3.64	3.53	3.54	3.49
SaG9	6.92	6.53	5.80	4.17	0.03	3.65	3.51	3.54	3.49
SaG10	6.83	6.55	4.10	2.52	0.08	3.59	3.54	3.56	3.48
SaG11	6.78	6.61	2.40	2.68	0.08	3.59	3.53	3.56	3.50
St Thibéry lava flows									
016	6.84	6.53	4.60	4.12	0.14	3.64	3.50	3.56	3.46
029	6.89	6.44	6.80	8.36	0.17	3.76	3.48	3.58	3.40
074	6.86	6.48	5.60	5.05	0.11	3.68	3.50	3.57	3.43

Table 4. *(continued)*

sample#	Vp Max (km/s)	Vp Min (km/s)	AVp (%)	AVs Max (%)	AVs Min (%)	Vs1 max (km/s)	Vs1 min (km/s)	Vs2 max (km/s)	Vs2 min (km/s)
Mid Atlantic ridge, ODP Leg 209									
114	6.82	6.53	4.40	7.78	0.06	3.71	3.49	3.60	3.38
121	6.81	6.57	3.50	3.79	0.11	3.61	3.52	3.59	3.46
137	6.86	6.53	4.90	6.88	0.28	3.69	3.50	3.62	3.42
Oklahama									
89ANOK	7.30	6.54	11.00	13.85	0.06	3.94	3.39	3.53	3.29

Table 5. Seismic properties (velocity and anisotropy) calculated based on modal composition of each samples using one point per grain data for gabbros studied here. Vp: P-wave; AVp: P-wave anisotropy; AVs: S-wave anisotropy, respectively.

sample#	Vp Max (km/s)	Vp Min (km/s)	AVp (%)	AVs Max (%)	AVs Min (%)	Vs1 max (km/s)	Vs1 min (km/s)	Vs2 max (km/s)	Vs2 min (km/s)
Oman ophiolite									
86OA20C	7.05	6.53	7.70	8.18	0.03	3.76	3.48	3.51	3.45
95OB4	7.24	7.12	1.70	1.80	0.00	3.98	3.93	3.95	3.91
97OB1C	7.49	7.31	2.40	1.69	0.02	4.18	4.11	4.13	4.09
98OB7A	7.33	6.99	4.70	4.66	0.10	4.03	3.88	3.91	3.82
98OB8B	7.43	7.31	1.70	2.16	0.07	4.17	4.08	4.13	4.06
98OB10A	7.41	7.33	1.00	1.27	0.02	4.14	4.10	4.13	4.08
98OB10E	7.71	7.41	3.90	1.91	0.05	4.34	4.26	4.28	4.25
98OB10G	7.62	7.49	1.70	1.70	0.02	4.28	4.22	4.25	4.20
88OA13	7.91	7.65	3.20	3.20	0.02	4.48	4.35	4.40	4.34
88OA14b	7.49	7.26	3.00	4.47	0.02	4.22	4.08	4.17	4.00
90OA68	7.49	7.21	3.80	3.36	0.17	4.19	4.07	4.14	4.02
90OA77	7.16	6.82	4.80	7.19	0.16	3.95	3.73	3.80	3.66
90OF11	7.28	7.08	2.80	2.96	0.05	4.02	3.93	3.96	3.87
92OB100b	7.50	7.22	3.80	2.47	0.02	4.14	4.06	4.11	4.03
92OB101	7.70	7.46	3.10	3.11	0.07	4.35	4.24	4.30	4.20
92OB134	7.43	7.20	3.10	3.65	0.10	4.16	4.04	4.09	3.99
92OB139	7.52	7.30	3.00	3.37	0.02	4.21	4.11	4.17	4.05
92OB140a	7.46	7.26	2.70	4.53	0.07	4.18	4.03	4.09	3.99
92OB140c	7.38	7.14	3.30	4.70	0.00	4.12	3.95	4.03	3.93
92OB142	7.31	6.87	6.20	7.59	0.08	4.02	3.73	3.80	3.69
92OB143	7.57	7.39	2.30	3.52	0.00	4.27	4.16	4.19	4.06
93OB157	7.51	7.17	4.60	4.81	0.12	4.19	4.03	4.10	3.98
94OB28	7.19	6.86	4.70	5.03	0.08	3.92	3.74	3.77	3.71
06OA31b	7.29	7.07	3.00	3.18	0.03	4.00	3.90	3.97	3.87
07OA20a	6.20	6.14	1.00	1.45	0.00	3.35	3.30	3.31	3.29
07OA20c1	6.92	6.84	1.10	1.52	0.05	3.78	3.75	3.76	3.71
07OA20d	7.06	6.86	2.90	1.68	0.11	3.80	3.74	3.77	3.72
07OA20e	7.12	6.89	3.20	1.90	0.05	3.83	3.78	3.79	3.75
07-2OA13	7.61	7.48	1.70	1.64	0.02	4.30	4.24	4.26	4.21
GAVAT2	7.36	7.03	4.50	4.75	0.05	4.04	3.88	3.91	3.84
ODP Hole 735B									
735B-5	7.30	7.12	2.50	2.11	0.05	4.02	3.96	4.00	3.93
735B-22B	7.26	6.98	4.00	3.83	0.08	4.00	3.87	3.91	3.83
735B-32	7.22	7.01	2.90	2.98	0.08	3.96	3.86	3.91	3.83
735B-32B	7.31	6.94	5.10	3.30	0.08	3.98	3.85	3.95	3.82
735B-BI-50	7.33	7.20	1.90	2.99	0.05	4.10	4.02	4.07	3.94
735B-51	6.91	6.54	5.60	7.14	0.14	3.72	3.48	3.56	3.43
735B-70	7.14	6.96	2.50	3.65	0.05	3.91	3.79	3.84	3.76
735B-79	7.32	7.16	2.30	2.03	0.13	4.03	3.96	4.00	3.94
735B-79B	7.20	6.98	3.10	4.28	0.10	3.99	3.85	3.91	3.80
133R3	7.11	6.94	2.50	2.13	0.05	3.90	3.83	3.84	3.80
133-3-0-7A	7.23	7.07	2.30	1.96	0.03	3.98	3.91	3.93	3.89
142R5	7.15	6.89	3.60	3.75	0.08	3.92	3.80	3.85	3.76
142-5-6-8b	7.34	7.17	2.30	2.43	0.02	4.05	3.97	4.01	3.94
147R6	7.26	7.02	3.30	3.34	0.10	3.97	3.86	3.89	3.82
154R5	7.24	7.02	3.20	2.70	0.05	3.99	3.89	3.94	3.87
154-5-42-44B	7.20	7.05	2.10	1.91	0.03	3.96	3.90	3.93	3.88
167R6	7.18	7.02	2.30	1.67	0.03	3.93	3.88	3.88	3.86
179R5	7.17	6.87	4.20	5.30	0.10	3.97	3.79	3.85	3.70
190R4	7.23	7.07	2.20	2.72	0.00	3.98	3.89	3.94	3.87
209R7	7.22	6.99	3.30	3.48	0.10	3.95	3.88	3.93	3.81
735B-BI-6	7.28	7.12	2.20	2.12	0.03	4.00	3.93	3.97	3.90
735B-BI-7	7.26	7.18	1.10	1.43	0.03	4.02	3.98	4.01	3.95
735B-BI-15	7.05	6.87	2.60	2.87	0.05	3.86	3.76	3.80	3.73
735B-BI-19	7.40	7.26	1.90	1.66	0.02	4.09	4.03	4.06	4.00
735B-BI-25	7.05	6.85	2.90	2.14	0.13	3.83	3.77	3.80	3.74
735B-BI-26	7.42	7.33	1.10	1.59	0.02	4.11	4.05	4.09	4.04

Table 5. *(continued)*

sample#	Vp Max (km/s)	Vp Min (km/s)	AVp (%)	AVs Max (%)	AVs Min (%)	Vs1 max (km/s)	Vs1 min (km/s)	Vs2 max (km/s)	Vs2 min (km/s)
735B-BI-33	7.46	7.30	2.10	2.34	0.05	4.16	4.09	4.15	4.06
735B-BI-34	7.13	6.93	2.90	2.47	0.03	3.86	3.78	3.84	3.75
735B-BI-38	7.12	6.97	2.20	1.85	0.10	3.87	3.82	3.84	3.80
735B-BI-49	7.21	7.04	2.40	2.37	0.13	3.97	3.90	3.94	3.86
735B-50	7.02	6.67	5.20	6.59	0.08	3.86	3.66	3.70	3.59
735B-BI-51	7.32	7.15	2.30	2.52	0.03	4.04	3.95	3.98	3.91
735B-BI-52	7.41	7.29	1.80	2.20	0.02	4.14	4.05	4.07	4.03
735B-BI-52a	7.35	7.27	1.10	1.34	0.05	4.08	4.03	4.05	4.01
735B-BI-52b	7.21	7.02	2.70	3.00	0.00	3.93	3.86	3.91	3.81
735B-BI-52c	7.39	7.27	1.60	1.49	0.00	4.11	4.05	4.08	4.05
735B-BI-55	7.23	7.07	2.30	2.17	0.08	4.00	3.92	3.95	3.91
735B-BI-57	7.40	7.26	1.90	1.77	0.00	4.10	4.04	4.05	4.02
735B-BI-58	7.20	6.83	5.30	3.66	0.05	3.87	3.77	3.81	3.72
735B-BI-64a2	7.38	7.18	2.70	2.02	0.05	4.06	3.98	4.02	3.96
735B-BI-64b	7.37	7.24	1.80	1.64	0.00	4.07	4.03	4.05	4.00
735B-BI-70	7.30	7.14	2.30	2.67	0.05	4.02	3.94	4.01	3.91
735B-BI-82a	7.25	7.11	2.00	1.76	0.00	4.01	3.95	3.97	3.93
735B-BI-82b	7.25	7.00	3.50	3.21	0.05	3.96	3.87	3.93	3.83
735B-BI-83a	7.23	6.94	4.00	3.54	0.10	3.91	3.82	3.86	3.77
735B-BI-83b	7.18	6.96	3.20	2.99	0.05	3.95	3.85	3.88	3.82
735B-BI-92	7.60	7.19	5.50	5.14	0.12	4.22	4.07	4.14	4.00
735B-BI-92-2									
Brazil, Itabuna and Ribeira belts									
CM19	7.01	6.68	4.80	4.16	0.00	3.78	3.67	3.72	3.63
CM20	7.15	7.02	1.90	2.19	0.08	3.94	3.87	3.89	3.83
RMB20	6.87	6.60	4.10	5.59	0.03	3.65	3.52	3.60	3.44
CM08	7.22	6.97	3.60	3.29	0.08	3.96	3.84	3.90	3.82
CM09	7.17	7.02	2.10	1.64	0.10	3.93	3.87	3.91	3.86
CM22	7.22	7.09	1.90	2.17	0.05	4.01	3.93	3.98	3.91
CM29	7.20	7.08	1.80	2.96	0.03	3.98	3.90	3.95	3.85
ODP Hole 1256D									
1256D_78_a	6.89	6.81	1.20	1.36	0.03	3.72	3.67	3.70	3.66
1256D_91_c	7.45	7.11	4.30	4.08	0.03	4.05	3.91	3.95	3.88
1256D_103_a	7.20	7.13	1.00	0.89	0.00	3.97	3.94	3.95	3.93
1256D_108_a	7.56	7.44	1.60	2.07	0.02	4.25	4.20	4.24	4.16
1256D_109_b	7.18	7.05	1.70	1.52	0.00	3.92	3.38	3.91	3.86
1256D_112_a	7.11	6.99	1.70	1.11	0.00	3.88	3.84	3.86	3.84
1256D_112_b	7.22	7.07	2.00	2.22	0.05	3.97	3.91	3.94	3.87
1256D_115	7.08	7.01	1.10	0.78	0.03	3.88	3.85	3.86	3.84
1256D_116_a	7.14	7.10	0.70	0.09	0.00	3.94	3.92	3.93	3.90
1256D_116_b	7.15	7.09	0.90	1.28	0.03	3.93	3.89	3.91	3.88
1256D_117_a	7.20	7.12	1.20	0.86	0.05	3.98	3.95	3.96	3.94
1256D_117_b	7.12	7.06	0.80	1.11	0.03	3.90	3.86	3.88	3.85
Hess Deep									
HD69r6_a	7.26	7.13	1.90	1.49	0.05	3.86	3.81	3.84	3.79
HD69r10_a	7.28	7.15	1.70	1.46	0.03	4.01	3.97	4.00	3.95
HD69r16_a	7.14	7.05	1.30	1.11	0.00	3.90	3.86	3.88	3.85
HD70r2_a	7.39	7.28	1.60	1.06	0.00	4.09	4.06	4.07	4.04
HD70r14_a	7.39	7.31	1.10	1.38	0.02	4.10	4.05	4.08	4.03
HD70r15_a	7.28	6.99	4.10	2.95	0.13	3.97	3.86	3.90	3.84
HD70r17_a	7.00	6.73	3.90	2.60	0.08	3.71	3.62	3.67	3.61
HD70r18_a	7.38	7.20	2.50	2.87	0.07	4.11	4.02	4.06	3.95
HD73r2_a	7.21	6.89	4.60	3.96	0.03	3.86	3.74	3.78	3.71
HD73r4_a	7.32	7.06	3.60	3.67	0.05	4.03	3.93	3.97	3.88
HD73r5_a	7.22	6.93	4.00	2.76	0.05	3.90	3.83	3.87	3.79
HD73r9_a	7.27	7.01	3.70	2.92	0.03	3.96	3.86	3.88	3.84
HD73r13_a	7.44	7.11	4.50	2.40	0.05	4.05	3.97	4.00	3.94
HD73r15_a	7.32	7.16	2.20	2.27	0.02	4.06	3.99	4.04	3.96

Table 5. *(continued)*

sample#	Vp Max (km/s)	Vp Min (km/s)	AVp (%)	AVs Max (%)	AVs Min (%)	Vs1 max (km/s)	Vs1 min (km/s)	Vs2 max (km/s)	Vs2 min (km/s)
HD73r16_a	7.06	6.76	4.30	3.41	0.03	3.76	3.65	3.68	3.63
HD73r18_a	7.39	7.13	3.70	2.11	0.05	4.03	3.95	3.98	3.92
HD73r20_a	7.05	6.79	3.80	3.97	0.05	3.78	3.65	3.73	3.63
HD75r5_a	7.19	6.99	2.80	2.35	0.10	3.91	3.83	3.88	3.82
HD75r8_a	7.44	7.28	2.40	1.96	0.02	4.12	4.06	4.10	4.04
HD75r11_a	7.44	7.07	5.10	3.28	0.05	4.06	3.95	3.99	3.92
HD76r1_a	7.32	7.03	4.20	4.48	0.05	4.02	3.87	3.91	3.81
HD76r3_a	7.34	6.82	7.40	7.42	0.05	3.99	3.74	3.80	3.68
HD76r8_a	7.41	7.16	3.50	3.52	0.03	4.09	3.97	3.99	3.92
HD76r10_a	7.16	7.01	2.20	2.15	0.03	3.91	3.87	3.89	3.82
HD76r11_a	7.04	6.90	2.00	1.27	0.03	3.80	3.77	3.79	3.75
HD76r14_a	7.06	6.88	2.60	2.21	0.03	3.85	3.79	3.81	3.76
HD78r1_a	7.31	7.10	2.90	1.54	0.10	3.99	3.94	3.96	3.92
HD78r2_a	6.80	6.63	2.60	3.14	0.08	3.64	3.54	3.59	3.48
HD78r5a	7.31	7.12	2.60	1.59	0.03	3.98	3.94	3.96	3.92
HD78r5b	7.09	6.90	2.80	2.27	0.08	3.89	3.80	3.83	3.78
HD78r5x4	7.17	7.00	2.40	2.63	0.05	3.93	3.88	3.91	3.83
HD78r6_a	7.33	7.07	3.50	3.50	0.05	4.05	3.93	3.98	3.87
HD78r7_a	7.05	6.97	1.20	1.49	0.03	3.86	3.81	3.83	3.80
4G11-2-5	7.16	6.95	2.90	2.49	0.03	3.90	3.83	3.85	3.80
4G-12-2	7.20	7.08	1.60	1.78	0.05	3.97	3.91	3.94	3.89
4G-12-3-8B	7.37	7.09	3.80	3.74	0.05	4.04	3.90	3.96	3.87
4G-13-1-9Ab	7.18	7.04	1.90	1.60	0.00	3.91	3.87	3.90	3.84
Reunion, Cirque de Salazie									
SaG2	7.61	7.12	6.70	2.78	0.02	4.09	3.99	4.02	3.97
SaG3	7.55	7.39	2.20	1.73	0.05	4.21	4.14	4.17	4.13
SaG4	7.87	7.76	1.30	2.38	0.04	4.53	4.44	4.47	4.39
SaG6	7.99	7.75	3.10	0.82	0.00	4.51	4.48	4.48	4.47
SaG6b	7.86	7.67	2.60	0.59	0.00	4.42	4.39	4.40	4.39
SaG7	7.67	7.16	6.80	3.33	0.05	4.15	4.05	4.10	4.01
SaG8	7.56	7.33	3.10	2.13	0.07	4.18	4.08	4.13	4.06
SaG9	7.53	7.39	2.00	2.22	0.02	4.23	4.13	4.27	4.11
SaG10	7.09	7.83	2.00	1.74	0.11	4.57	4.50	4.52	4.49
SaG11	7.71	7.59	1.60	1.53	0.05	4.36	4.30	4.33	4.39
St Thibéry lava flows									
005									
016	6.02	5.76	4.60	4.62	0.15	3.46	3.34	3.39	3.28
029	6.89	6.44	6.80	8.36	0.17	3.76	3.48	3.58	3.40
074	7.38	7.07	4.30	2.80	0.05	4.04	3.92	3.99	3.91
Mid Atlantic ridge, ODP Leg 209									
114	6.89	6.59	4.40	6.66	0.14	3.75	3.55	3.60	3.45
121	7.24	7.09	2.10	2.71	0.03	3.99	3.92	3.97	3.86
137	7.44	7.12	4.40	3.73	0.05	4.10	4.00	4.07	3.94
Oklahama									
89ANOK	7.24	6.49	11.00	13.84	0.06	3.91	3.36	3.51	3.26

Table 6. Seismic properties (velocity and anisotropy) calculated as plagioclase 100% using gridded data for gabbros studied here. Vp: P-wave; AVp: P-wave anisotropy; AVs: S-wave anisotropy, respectively.

sample#	Vp Max (km/s)	Vp Min (km/s)	AVp (%)	AVs Max (%)	AVs Min (%)	Vs1 max (km/s)	Vs1 min (km/s)	Vs2 max (km/s)	Vs2 min (km/s)
Oman ophiolite									
86OA20A	7.06	6.44	9.20	16.68	0.06	4.03	3.43	3.72	3.24
86OA20B	6.93	6.57	5.40	7.57	0.09	3.77	3.49	3.53	3.44
92OB139	6.94	6.50	6.50	7.04	0.11	3.71	3.48	3.59	3.41
06OA31b	7.00	6.41	8.70	13.85	0.33	3.81	3.44	3.66	3.31
07OA20a	6.74	6.63	1.70	2.91	0.08	3.59	3.52	3.58	3.48
07OA20c1	6.75	6.63	1.90	1.49	0.03	3.58	3.53	3.55	3.52
07OA20d	6.84	6.59	3.80	2.73	0.03	3.61	3.51	3.55	3.50
07OA20e	6.85	6.60	3.70	3.18	0.09	3.61	3.51	3.56	3.49
07-2OA13	6.83	6.54	4.30	4.98	0.06	3.66	3.52	3.57	3.48
ODP Hole 735B									
735B-22D	6.92	6.34	8.80	10.67	0.26	3.81	3.47	3.54	3.38
735B-22F	6.96	6.41	8.20	13.50	0.23	3.83	3.46	3.61	3.32
735B-32B	6.93	6.47	6.90	8.17	0.23	3.75	3.47	3.58	3.41
735B-BI-50	6.85	6.41	6.70	7.95	0.06	3.73	3.49	3.62	3.38
735B-79B	6.97	6.52	6.70	9.69	0.20	3.77	3.46	3.57	3.41
133-3-0-7A	6.80	6.48	4.90	5.07	0.06	3.64	3.51	3.54	3.45
142-5-6-8b	6.89	6.43	7.00	6.95	0.03	3.70	3.48	3.54	3.44
154-5-42-44B	6.83	6.54	4.30	5.48	0.11	3.67	3.51	3.55	3.44
735B-BI-6	6.90	6.51	5.90	4.95	0.14	3.67	3.51	3.56	3.46
735B-BI-7	6.79	6.55	3.70	4.48	0.06	3.63	3.50	3.60	3.46
735B-BI-15	6.83	6.50	4.90	5.19	0.06	3.66	3.50	3.56	3.47
735B-BI-19	6.83	6.55	4.20	6.46	6.14	3.69	3.49	3.61	3.43
735B-BI-25	6.78	6.55	3.50	2.96	0.08	3.60	3.52	3.56	3.49
735B-BI-26	6.80	6.56	3.60	3.79	0.14	3.63	3.51	3.57	3.48
735B-BI-33	6.95	6.48	7.00	12.69	0.16	3.84	3.44	3.65	3.29
735B-BI-34	6.91	6.51	5.90	7.31	0.06	3.70	3.49	3.59	3.41
735B-BI-38	6.78	6.60	2.70	2.83	0.03	3.59	3.53	3.56	3.49
735B-BI-49	6.85	6.42	6.50	5.90	0.14	3.68	3.49	3.58	3.43
735B-BI-51	6.76	6.60	2.50	3.26	0.03	3.62	3.52	3.55	3.50
735B-BI-52	6.94	6.50	5.00	8.47	0.22	3.69	3.48	3.61	3.39
735B-BI-52a	6.79	6.58	3.10	5.30	0.03	3.65	3.51	3.58	3.44
735B-BI-52b	6.88	6.53	5.30	7.95	0.14	3.72	3.49	3.62	3.37
735B-BI-52c	6.82	6.49	5.00	5.81	0.06	3.65	3.52	3.60	3.42
735B-BI-55	6.83	6.47	5.40	4.19	0.20	3.64	3.52	3.53	3.46
735B-BI-57	6.95	6.46	7.20	8.07	0.11	3.72	3.49	3.57	3.39
735B-BI-58	6.87	6.47	6.00	5.65	0.31	3.64	3.54	3.57	3.41
735B-BI-64a2	6.89	6.51	5.70	6.06	0.08	3.68	3.49	3.58	3.45
735B-BI-64b	6.85	6.51	5.10	4.62	0.06	3.66	3.51	3.57	3.44
735B-BI-70	6.82	6.55	4.00	6.30	0.06	3.67	3.50	3.62	3.44
735B-BI-82a	6.85	6.44	6.10	5.05	0.11	3.64	3.49	3.54	3.45
735B-BI-82b	6.91	6.48	6.30	6.63	0.03	3.69	3.48	3.60	3.42
735B-BI-83a	6.89	6.53	5.40	6.66	0.25	3.74	3.49	3.55	3.42
735B-BI-83b	6.90	6.38	7.90	5.98	0.14	3.69	3.49	3.53	3.43
735B-BI-92	6.80	6.60	3.00	4.99	0.08	3.66	3.50	3.55	3.46
ODP Hole 1256D									
1256D_78_a	6.75	6.60	2.20	3.25	0.06	3.60	3.52	3.58	3.47
1256D_91_c	6.89	6.49	6.10	6.40	0.00	3.69	3.49	3.60	3.44
1256D_103_a	6.78	6.58	3.00	4.09	0.03	3.66	3.52	3.60	3.42
1256D_108_a	6.85	6.51	5.10	5.96	0.23	3.64	3.50	3.58	3.43
1256D_109_b	6.79	6.58	3.10	3.37	0.03	3.61	3.53	3.56	3.46
1256D_112_a	6.86	6.54	4.70	3.58	0.06	3.63	3.52	3.56	3.47
1256D_112_b	6.86	6.51	5.30	5.97	0.09	3.66	3.48	3.57	3.44
1256D_115	6.77	6.60	2.60	2.66	0.00	3.59	3.53	3.56	3.48

Table 6. *(continued)*

sample#	Vp Max (km/s)	Vp Min (km/s)	AVp (%)	AVs Max (%)	AVs Min (%)	Vs1 max (km/s)	Vs1 min (km/s)	Vs2 max (km/s)	Vs2 min (km/s)
1256D_116_a	6.70	6.66	0.70	1.19	0.03	3.57	3.53	3.56	3.52
1256D_116_b	6.75	6.62	2.00	2.71	0.00	3.60	3.53	3.56	3.50
1256D_117_a	6.71	6.64	1.00	1.10	0.03	3.57	3.53	3.55	3.52
1256D_117_b	6.71	6.66	0.80	1.44	0.03	3.57	3.53	3.56	3.52
Hess Deep									
HD69r6_a	6.76	6.61	2.10	3.75	0.06	3.62	3.53	3.60	3.45
HD69r10_a	7.09	6.49	8.80	12.24	0.23	3.89	3.41	3.52	3.33
HD69r16_a	6.79	6.57	3.20	2.91	0.03	3.60	3.51	3.56	3.49
HD70r2_a	7.10	6.51	8.70	15.75	0.26	3.91	3.42	3.61	3.31
HD70r14_a	6.91	6.54	5.60	4.29	0.20	3.62	3.49	3.58	3.46
HD70r15_a	6.97	6.52	6.70	5.36	0.20	3.68	3.50	3.56	3.45
HD70r17_a	7.03	6.53	7.40	11.81	0.23	3.84	3.42	3.56	3.37
HD70r18_a	6.91	6.45	6.80	9.23	0.06	3.72	3.47	3.58	3.39
HD73r2_a	6.94	6.54	5.80	4.63	0.11	3.64	3.49	3.56	3.47
HD73r4_a	6.92	6.45	7.00	10.63	0.06	3.80	3.49	3.58	3.31
HD73r5_a	6.88	6.57	4.60	3.07	0.06	3.61	3.51	3.55	3.49
HD73r9_a	7.04	6.53	7.50	12.35	0.26	3.87	3.41	3.57	3.33
HD73r13_a	6.92	6.54	5.60	4.16	0.06	3.64	3.49	3.58	3.45
HD73r15_a	6.91	6.49	6.30	4.73	0.06	3.65	3.51	3.56	3.45
HD73r16_a	6.97	6.55	6.20	4.65	0.00	3.65	3.50	3.53	3.48
HD73r18_a	6.99	6.47	7.70	6.01	0.11	3.69	3.50	3.55	3.45
HD73r20_a	6.96	6.49	7.00	6.71	0.17	3.70	3.47	3.59	3.38
HD75r5_a	6.91	6.51	6.00	4.31	0.11	3.63	3.50	3.57	3.46
HD75r8_a	6.83	6.55	4.20	2.45	0.06	3.60	3.52	3.56	3.49
HD75r11_a	6.93	6.42	7.60	12.76	0.09	3.87	3.42	3.67	3.31
HD76r1_a	7.02	6.44	8.60	7.63	0.14	3.70	3.47	3.57	3.42
HD76r3_a	7.12	6.41	10.60	10.49	0.20	3.81	3.47	3.53	3.39
HD76r8_a	7.04	6.50	8.10	7.18	0.09	3.71	3.48	3.56	3.43
HD76r10_a	6.86	6.55	4.70	5.12	0.11	3.65	3.52	3.55	3.46
HD76r11_a	7.00	6.46	8.00	12.15	0.09	3.86	3.45	3.52	3.36
HD76r14_a	6.89	6.48	6.10	4.41	0.11	3.64	3.50	3.56	3.47
HD78r1_a	6.89	6.57	4.80	4.56	0.08	3.62	3.52	3.57	3.44
HD78r2_a	6.90	6.48	6.40	9.85	0.20	3.83	3.51	3.58	3.36
HD78r5a	6.88	6.55	4.80	3.68	0.20	3.61	3.52	3.58	3.46
HD78r5b	6.89	6.46	6.40	6.81	0.17	3.71	3.49	3.57	3.42
HD78r5x4	6.84	6.54	4.60	4.77	0.17	3.63	3.50	3.57	3.46
HD78r6_a	7.04	6.42	9.30	11.58	0.14	3.81	3.42	3.59	3.36
HD78r7_a	6.75	6.64	1.70	2.20	0.03	3.59	3.52	3.56	3.51
4G11-2-5	6.89	6.50	5.80	8.20	0.08	3.77	3.47	3.57	3.40
4G-12-2	6.98	6.54	6.20	6.11	0.17	3.68	3.50	3.56	3.43
4G-12-3-8B	7.01	6.53	7.20	8.50	0.03	3.72	3.46	3.57	3.40
4G-13-1-9Ab	6.82	6.60	3.30	4.23	0.00	3.64	3.52	3.58	3.45
Reunion, Cirque de Salazie									
SaG1									
SaG2	6.96	6.54	6.20	4.47	0.03	3.64	3.50	3.56	3.47
SaG3	6.87	6.60	4.10	3.41	0.03	3.62	3.52	3.55	3.48
SaG4	6.92	6.51	6.10	4.28	0.11	3.64	3.51	3.58	3.46
SaG6	6.84	6.59	3.80	3.72	0.03	3.61	3.52	3.58	3.48
SaG6b	6.82	6.58	3.60	3.75	0.00	3.61	3.52	3.57	3.48
SaG7	6.96	6.58	5.60	4.82	0.00	3.66	3.50	3.53	3.47
SaG8	6.97	6.47	7.50	6.18	0.20	3.70	3.51	3.54	3.46
SaG9	6.95	6.48	7.00	6.00	0.34	3.69	3.51	3.54	3.47
SaG10	6.84	6.54	4.40	4.29	0.11	3.63	3.53	3.57	3.46
SaG11	6.76	6.62	2.10	2.40	0.06	3.60	3.52	3.57	3.49

Table 7. Seismic properties (velocity and anisotropy) calculated based on modal composition of each samples using gridded data for gabbros studied here. Vp: P-wave; AVp: P-wave anisotropy; AVs: S-wave anisotropy, respectively.

sample#	Vp Max (km/s)	Vp Min (km/s)	AVp (%)	AVs Max (%)	AVs Min (%)	Vs1 max (km/s)	Vs1 min (km/s)	Vs2 max (km/s)	Vs2 min (km/s)
Oman ophiolite									
86OA20A	7.00	6.47	7.80	8.12	0.03	3.72	3.44	3.48	3.42
86OA20B	6.93	6.57	5.40	7.57	0.09	3.77	3.49	3.53	3.44
92OB139	7.52	7.30	3.00	3.37	0.02	4.21	4.11	4.17	4.05
06OA31b	7.33	6.96	5.20	7.44	0.18	4.07	3.84	3.99	3.75
07OA20a	6.75	6.68	1.10	1.78	0.06	3.63	3.59	3.61	3.56
07OA20c1	7.08	6.99	1.30	1.36	0.03	3.86	3.83	3.85	3.81
07OA20d	7.14	6.90	3.30	2.19	0.03	3.84	3.77	3.79	3.75
07OA20e	7.11	6.86	3.50	2.47	0.03	3.81	3.73	3.77	3.71
07-2OA13	7.65	7.42	3.10	2.31	0.02	4.29	4.24	4.27	4.19
07_2_OA_10B	6.99	6.50	7.40	6.05	0.03	3.70	3.49	3.54	3.47
07_2_OA_18b	7.14	6.56	8.50	9.35	0.12	3.81	3.45	3.50	3.40
07_2_OA_18c	6.98	6.57	6.10	5.11	0.03	3.67	3.49	3.53	3.48
07_2_OA_30b	6.94	6.49	6.70	7.32	0.11	3.74	3.51	3.52	3.46
07_2_OA_30h	7.10	6.65	6.60	5.79	0.03	3.77	3.57	3.59	3.55
07_2_OA_37	7.11	6.70	5.90	6.11	0.08	3.83	3.61	3.62	3.59
07_2_OA_37b	6.99	6.48	7.50	6.68	0.06	3.72	3.49	3.54	3.46
07_2_OA_41g	7.16	6.89	3.90	4.32	0.05	3.91	3.74	3.77	3.72
07_2_OA_42c	7.02	6.74	4.10	2.65	0.08	3.72	3.63	3.65	3.61
07_2_OA_45c3	7.18	6.41	11.30	11.76	0.11	3.92	3.46	3.54	3.44
07_2_OA_45c4	7.26	6.75	7.30	6.35	0.08	3.90	3.66	3.70	3.63
07_2_OA_66	7.20	6.56	9.40	8.91	0.11	3.83	3.51	3.56	3.48
07_OA_8g_2S	6.88	6.58	4.40	2.56	0.14	3.60	3.53	3.54	3.51
ODP Hole 735B									
735B-22D	6.92	6.34	8.80	10.67	0.26	3.81	3.47	3.54	3.38
735B-22F	6.96	6.41	8.20	13.50	0.23	3.83	3.46	3.61	3.32
735B-32B	7.27	6.97	4.20	5.10	0.05	4.03	3.84	3.90	3.81
735B-BI-50	7.35	7.18	2.30	3.34	0.02	4.11	4.01	4.08	3.93
735B-79B	7.24	6.92	4.60	6.07	0.16	4.03	3.83	3.90	3.76
116R4									
133R3									
133-3-0-7A	7.09	7.25	2.30	3.23	0.03	3.91	4.00	3.86	3.94
142R5									
142-5-6-8b	7.07	7.49	5.70	4.39	0.05	3.95	4.09	3.91	4.02
154-5-42-44B	7.19	7.42	3.20	2.95	0.07	4.10	3.99	4.05	3.98
735B-BI-6	7.28	7.12	2.30	2.34	0.08	4.02	3.93	3.97	3.91
735B-BI-7	7.18	7.34	2.10	1.50	0.03	4.04	3.99	4.02	3.97
735B-BI-15	1.09	6.95	2.00	2.61	0.05	3.86	3.77	3.82	3.74
735B-BI-19	7.38	7.23	2.10	2.55	0.05	4.11	4.02	4.06	3.97
735B-BI-25	7.75	7.57	2.40	1.82	0.02	4.34	4.29	4.32	4.26
735B-BI-26	7.42	7.31	1.50	1.86	0.02	4.12	4.05	4.09	4.03
735B-BI-33	7.58	7.23	4.70	6.23	0.12	4.29	4.06	4.18	3.99
735B-BI-34	7.20	6.84	5.10	3.98	0.00	3.88	3.76	3.80	3.71
735B-BI-38	7.11	6.98	1.80	1.78	0.00	3.86	3.82	3.84	3.79
735B-BI-49	7.23	7.04	2.70	2.97	0.10	4.00	3.90	3.96	3.85
735B-BI-51	7.34	7.06	4.00	3.69	0.05	4.06	3.94	4.00	3.88
735B-BI-52	7.53	7.21	4.30	4.52	0.05	4.17	4.03	4.11	3.97
735B-BI-52a	7.34	7.24	1.50	2.65	0.05	4.10	4.01	4.05	3.98
735B-BI-52b	7.24	6.98	3.60	4.81	0.05	4.00	3.84	3.93	3.76
735B-BI-52c	7.22	7.51	3.90	3.41	0.05	4.03	4.15	4.01	4.09
735B-BI-55	7.26	7.13	1.90	2.09	0.05	4.02	3.95	3.97	3.93
735B-BI-57	7.39	7.19	2.70	4.36	0.15	4.13	3.99	4.07	3.95
735B-BI-58	7.22	6.77	6.40	5.12	0.05	3.89	3.77	3.83	3.69
735B-BI-64a									
735B-BI-64a2	7.36	7.12	2.40	2.95	0.05	4.07	3.97	4.02	3.93

Table 7. *(continued)*

sample#	Vp Max (km/s)	Vp Min (km/s)	AVp (%)	AVs Max (%)	AVs Min (%)	Vs1 max (km/s)	Vs1 min (km/s)	Vs2 max (km/s)	Vs2 min (km/s)
735B-BI-64b	7.39	7.23	2.30	1.91	0.05	4.09	4.01	4.07	3.99
735B-BI-70	7.34	7.11	3.20	3.97	0.05	4.06	3.93	4.01	3.90
735B-BI-82a	7.26	7.09	2.40	2.14	0.08	4.01	3.95	3.98	3.92
735B-BI-82b	7.30	6.99	4.30	4.13	0.08	3.98	3.85	3.92	3.81
735B-BI-83a	7.28	6.86	6.00	5.10	0.03	3.97	3.80	3.84	3.72
735B-BI-83b	7.20	6.93	3.80	3.17	0.08	3.95	3.83	3.86	3.81
735B-BI-92	7.61	7.14	6.40	7.85	0.07	4.28	4.05	4.15	3.95
ODP Hole 1256D									
1256D_78_a	6.92	6.77	2.10	2.66	0.03	3.74	3.67	3.73	3.63
1256D_91_c	7.46	7.14	4.40	3.94	0.05	4.04	3.92	3.97	3.88
1256D_103_a	7.24	7.11	1.80	2.80	0.05	4.03	3.93	3.98	3.87
1256D_108_a	7.57	7.42	2.00	2.40	0.05	4.27	4.20	4.23	4.15
1256D_109_b	7.17	7.05	1.80	1.98	0.03	3.94	3.89	3.92	3.85
1256D_112_a	7.15	6.94	3.00	2.20	0.10	3.90	3.83	3.86	3.81
1256D_112_b	7.26	7.03	3.20	3.18	0.03	3.99	3.89	3.95	3.86
1256D_115	7.14	7.02	1.80	1.73	0.03	3.90	3.86	3.89	3.83
1256D_116_a	7.16	7.09	0.90	1.22	0.00	3.94	3.91	3.93	3.90
1256D_116_b	7.15	7.03	1.70	1.57	0.03	3.92	3.87	3.90	3.85
1256D_117_a	7.20	7.15	0.70	0.83	0.03	3.97	3.95	3.96	3.93
1256D_117_b	7.09	7.04	0.70	1.11	0.03	3.88	3.84	3.87	3.84
Hess Deep									
HD69r6_a	6.98	6.84	2.10	3.08	0.05	3.78	3.70	3.77	3.64
HD69r10_a	7.63	7.11	7.10	8.14	0.13	4.25	3.94	4.01	3.86
HD69r16_a	7.12	7.01	1.60	1.71	0.00	3.89	3.84	3.87	3.83
HD70r2_a	7.66	7.19	6.40	9.81	0.15	4.42	3.97	4.16	3.92
HD70r14_a	7.45	7.29	2.10	1.97	0.12	4.12	4.05	4.08	4.02
HD70r15_a	7.31	6.97	4.80	3.31	0.05	3.96	3.87	3.91	3.83
HD70r17_a	7.11	6.71	5.70	9.53	0.20	3.91	3.56	3.65	3.52
HD70r18_a	7.43	7.15	3.90	3.84	0.02	4.12	3.99	4.09	3.95
HD70r20_a									
HD73r2_a	7.19	6.83	5.10	4.25	0.11	3.85	3.73	3.77	3.68
HD73r4_a	7.39	7.05	4.80	7.58	0.08	4.16	3.88	3.96	3.81
HD73r5_a	7.22	6.94	3.90	3.61	0.03	3.92	3.83	3.86	3.78
HD73r9_a	7.36	7.01	4.80	7.22	0.21	4.07	3.81	3.90	3.77
HD73r13_a	7.43	7.08	4.80	2.49	0.03	4.04	3.93	4.01	3.92
HD73r15_a	7.40	7.05	4.70	2.77	0.05	4.07	3.99	4.03	3.96
HD73r16_a	7.10	6.76	5.00	3.94	0.05	3.78	3.64	3.67	3.63
HD73r18_a	6.03	5.60	7.40	4.69	0.09	3.47	3.33	3.44	3.29
HD73r20_a	7.10	6.74	5.30	5.18	0.19	3.84	3.63	3.74	3.57
HD75r5_a	7.20	6.98	3.10	3.45	0.03	3.92	3.83	3.89	3.79
HD75r8_a	7.36	7.12	3.40	2.75	0.02	4.06	4.00	4.05	3.94
HD75r11_a	7.38	6.97	5.80	8.77	0.08	4.18	3.86	4.03	3.78
HD76r1_a	7.37	6.96	5.70	5.29	0.08	4.03	3.87	3.91	3.79
HD76r3_a	7.37	6.80	8.00	7.66	0.11	4.01	3.76	3.80	3.68
HD76r8_a	7.41	7.13	3.90	4.08	0.10	4.11	3.97	4.00	3.91
HD76r10_a	7.18	6.98	2.80	3.05	0.05	3.93	3.86	3.90	3.81
HD76r11_a	7.26	6.79	6.70	8.63	0.16	4.01	3.71	3.74	3.63
HD76r14_a	7.09	6.87	3.20	2.71	0.03	3.85	3.79	3.82	3.74
HD78r1_a	7.37	7.08	4.00	2.30	0.05	4.01	3.93	3.98	3.91
HD78r2_a	6.93	6.51	6.20	9.48	0.14	3.85	3.54	3.60	3.39
HD78r5a	7.32	7.08	3.30	1.88	0.10	3.98	3.92	3.95	3.89
HD78r5b	7.19	6.87	4.50	4.45	0.08	3.94	3.80	3.86	3.74
HD78r5x4	7.26	7.01	3.50	2.69	0.00	3.96	3.88	3.94	3.85
HD78r6_a	7.52	7.03	6.70	8.68	0.23	4.16	3.89	4.00	3.80
HD78r7_a	7.05	6.98	1.00	1.70	0.03	3.86	3.81	3.84	3.79
4G11-2-5	7.23	6.90	4.70	5.63	0.03	3.79	4.00	3.73	3.86
4G-12-2	7.26	7.06	2.80	3.51	0.10	4.01	3.92	3.94	3.85
4G-12-3-8B	7.39	7.06	4.50	4.91	0.08	4.06	3.90	3.97	3.85
4G-13-1-9Ab	7.19	6.99	2.90	2.83	0.03	3.95	3.87	3.90	3.80

Table 7. *(continued)*

sample#	Vp Max (km/s)	Vp Min (km/s)	AVp (%)	AVs Max (%)	AVs Min (%)	Vs1 max (km/s)	Vs1 min (km/s)	Vs2 max (km/s)	Vs2 min (km/s)
Reunion, Cirque de Salazie									
SaG1									
SaG2	7.66	7.09	7.70	3.61	0.10	4.09	4.01	4.03	3.94
SaG3	7.66	7.35	4.10	2.61	0.02	4.23	4.13	4.19	4.12
SaG4	7.97	7.71	3.30	3.07	0.07	4.58	4.44	4.48	4.38
SaG6	7.91	7.71	2.60	1.19	0.00	4.49	4.44	4.47	4.44
SaG6b	7.85	7.64	2.70	1.09	0.02	4.43	4.38	4.41	4.38
SaG7	7.72	7.20	6.90	3.82	0.07	4.19	4.03	4.07	4.02
SaG8	7.68	7.36	4.20	2.91	0.05	4.26	4.12	4.17	4.09
SaG9	7.61	7.38	3.10	2.93	0.02	4.26	4.13	4.18	4.08
SaG10	7.99	7.84	2.00	2.63	0.00	4.59	4.49	4.54	4.47
SaG11	7.79	7.61	2.40	2.08	0.05	4.38	4.32	4.35	4.29

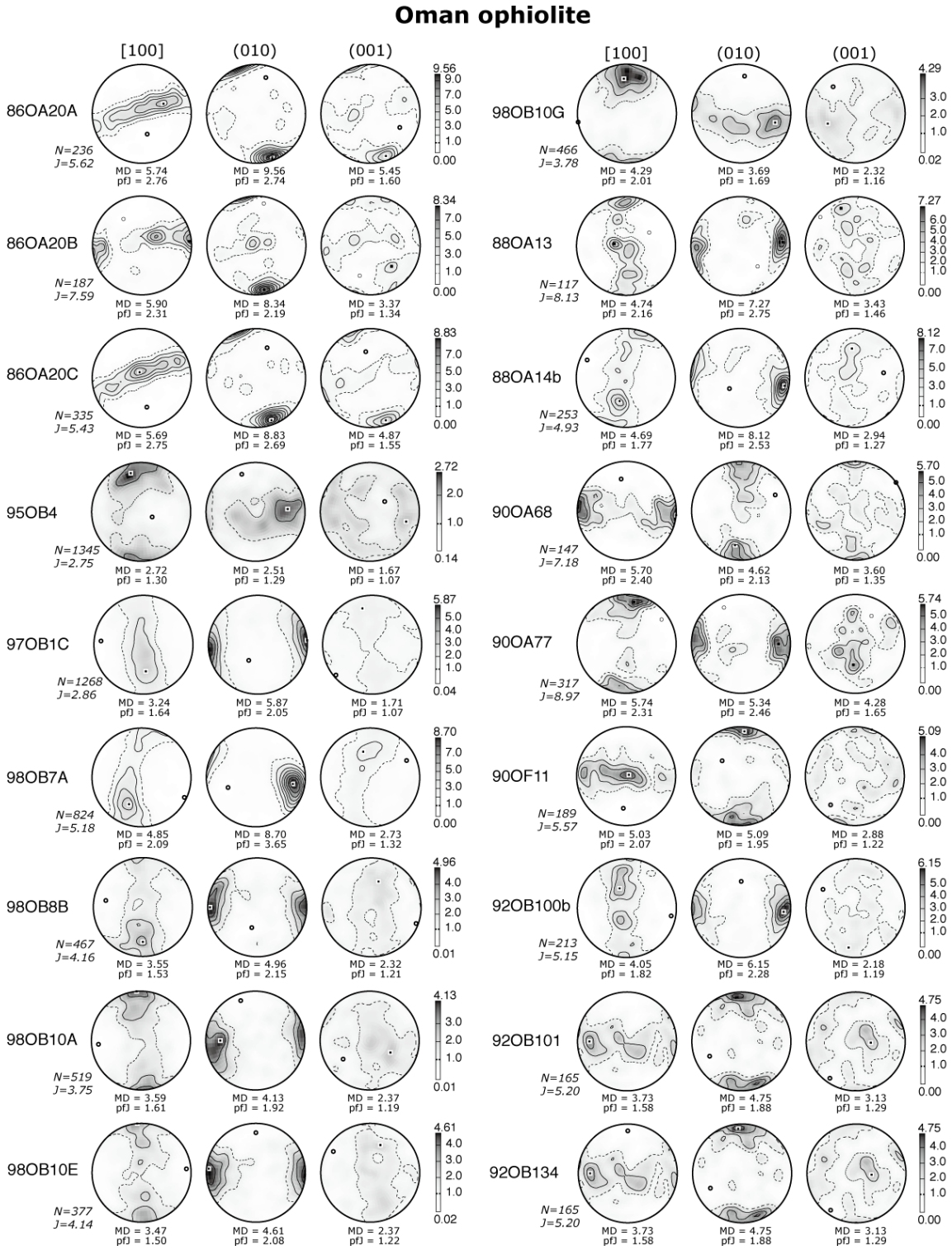

Supplementary figure 1. Plagioclase CPOs of Oman ophiolite gabbro samples. Lower hemisphere, equal-area stereographic projections, contours at one multiple of uniform distribution. N is number of measured grains. *J* and *pfJ* are indexes of fabric intensity, and MD is the maximum density.

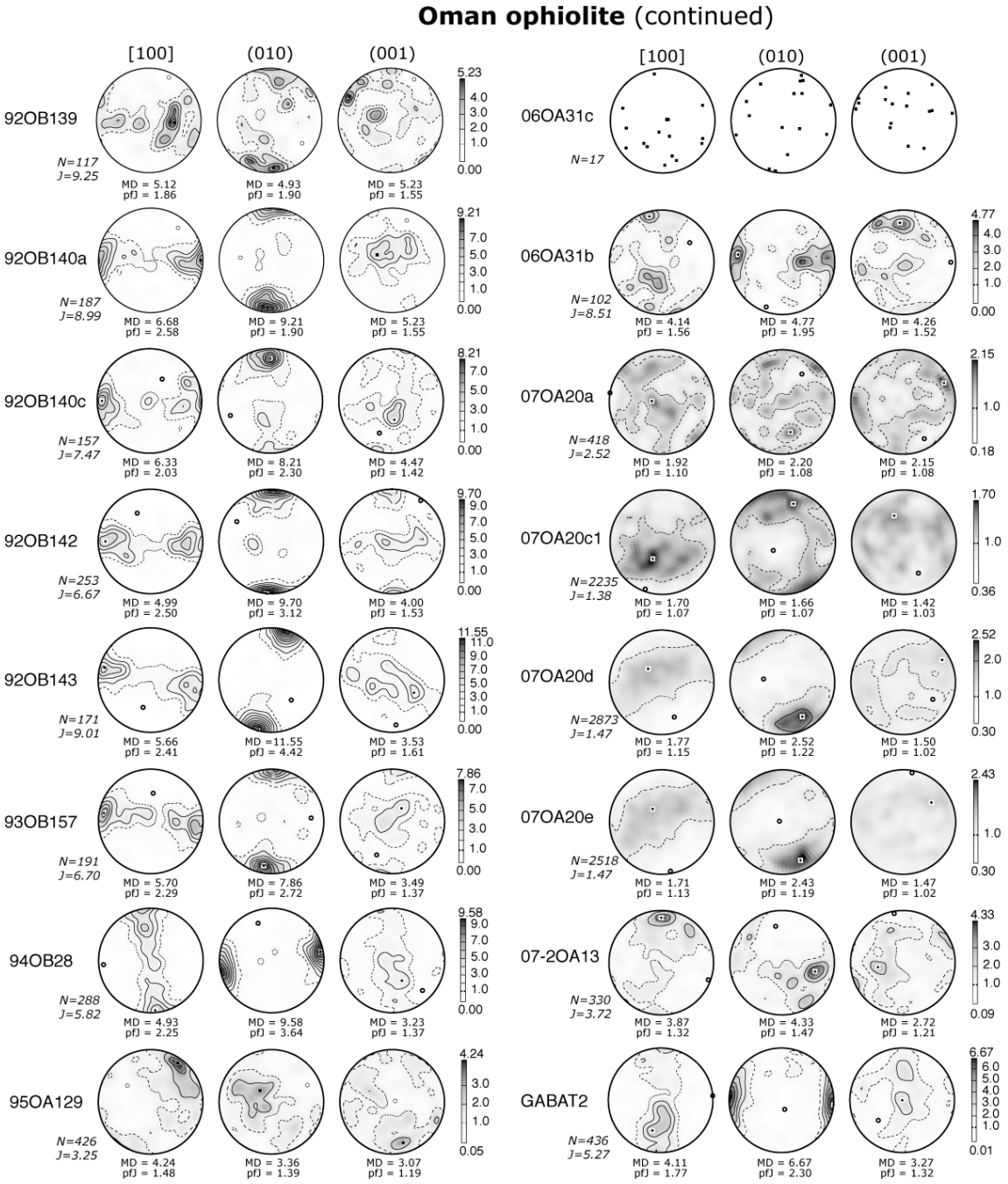

Supplementary figure 1. *(Continued)*

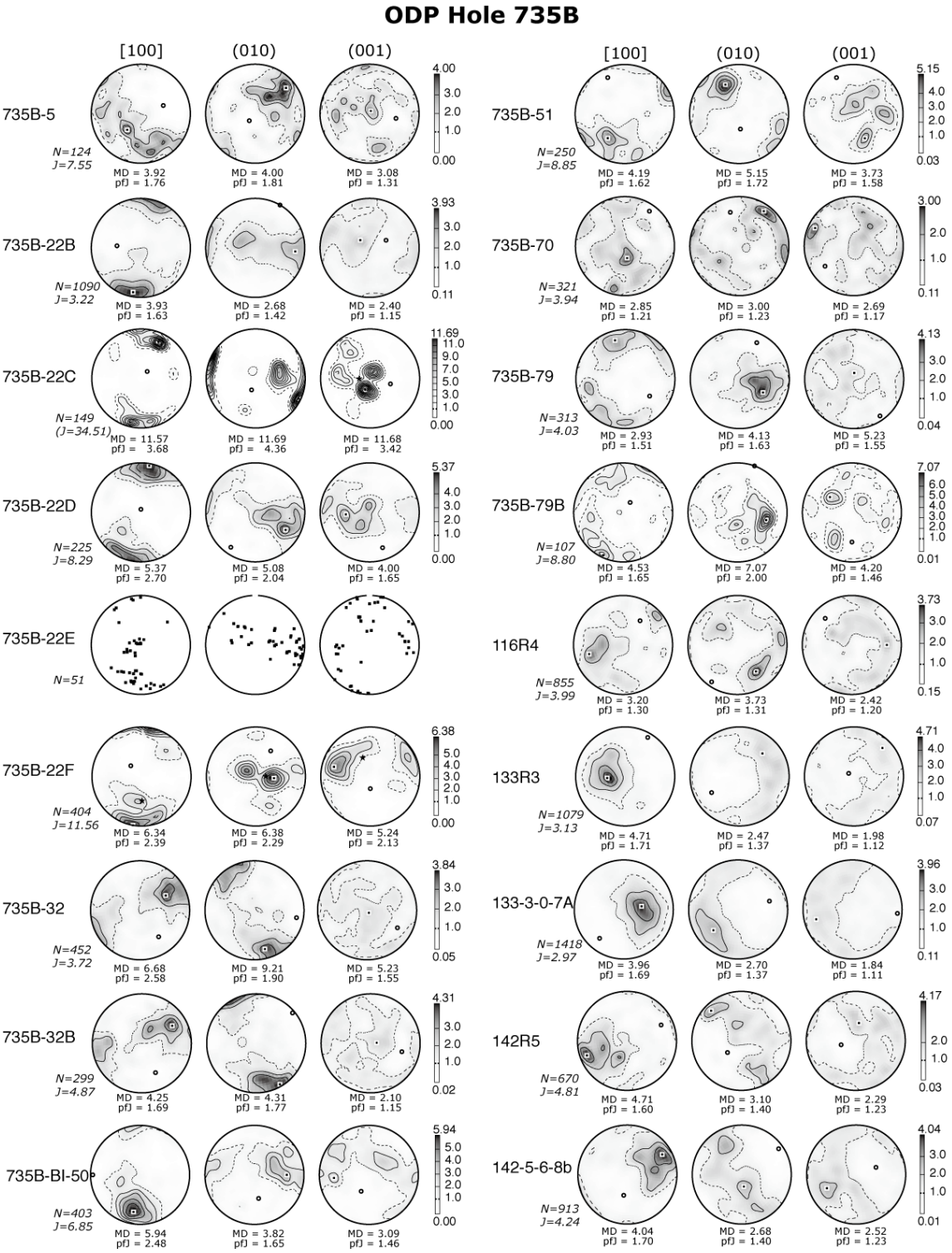

Supplementary figure 2. Plagioclase CPOs of gabbros from the Southwest Indian ridge, ODP Hole 735B. Lower hemisphere, equal-area stereographic projections, contours at one multiple of uniform distribution. N is number of measured grains. *J* and *pfJ* are indexes of fabric intensity, and MD is the maximum density.

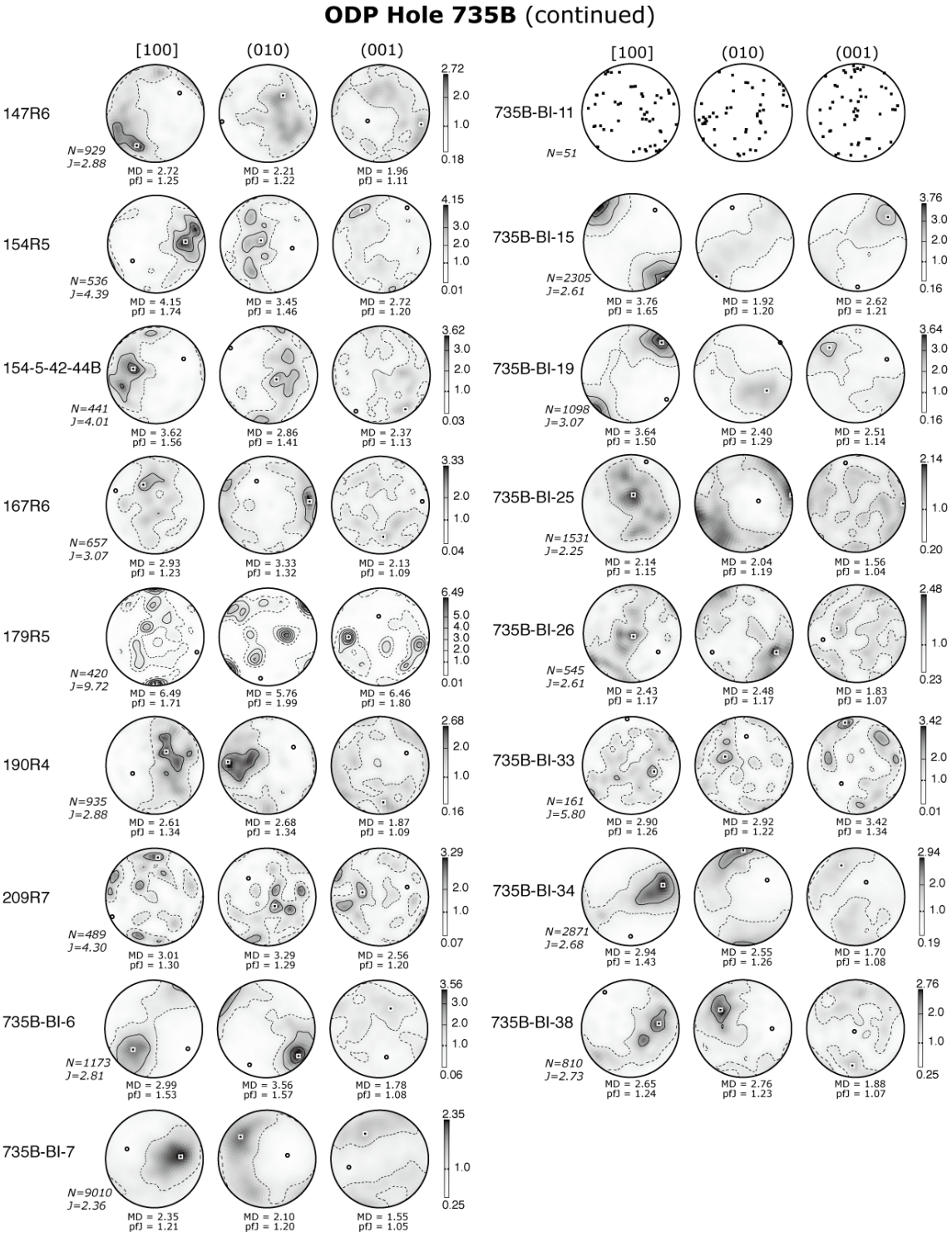

Supplementary figure 2. *(Continued)*

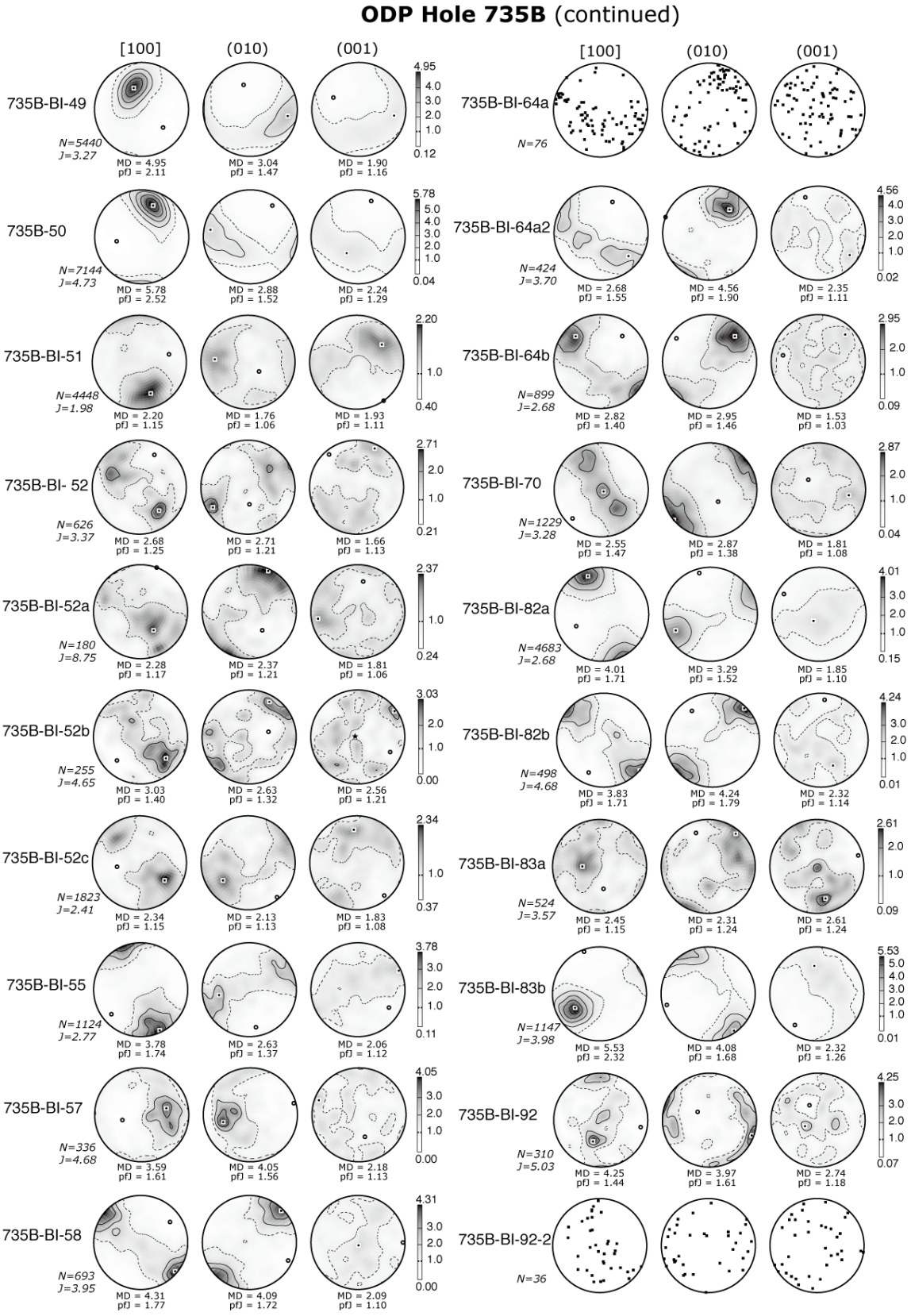

Supplementary figure 2. *(Continued)*

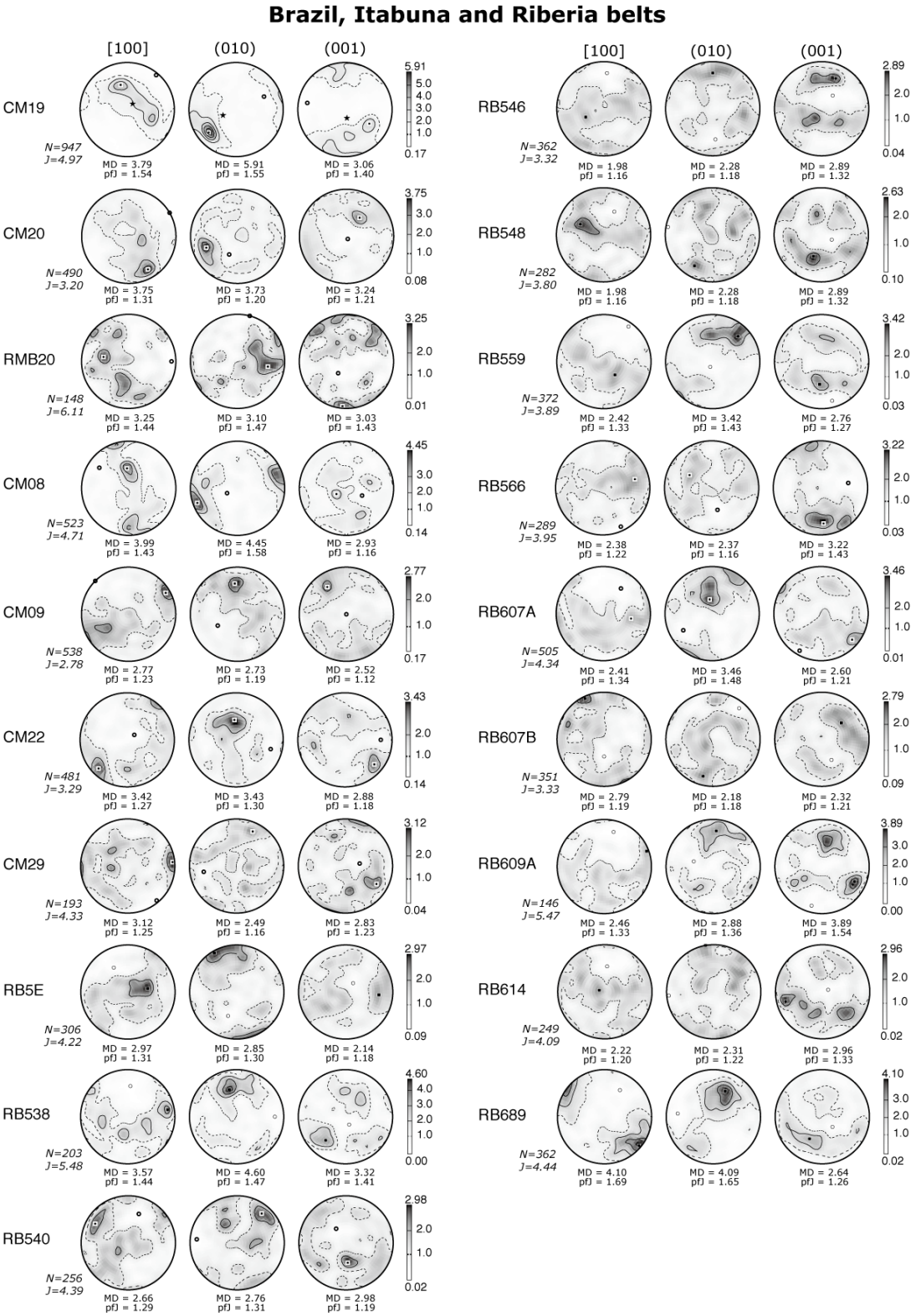

Supplementary figure 3. Plagioclase CPOs of gabbros, charnockites, and granulites from Brazil. Lower hemisphere, equal-area stereographic projections, contours at one multiple of uniform distribution. N is number of measured grains. *J* and *pfJ* are indexes of fabric intensity, and MD is the maximum density.

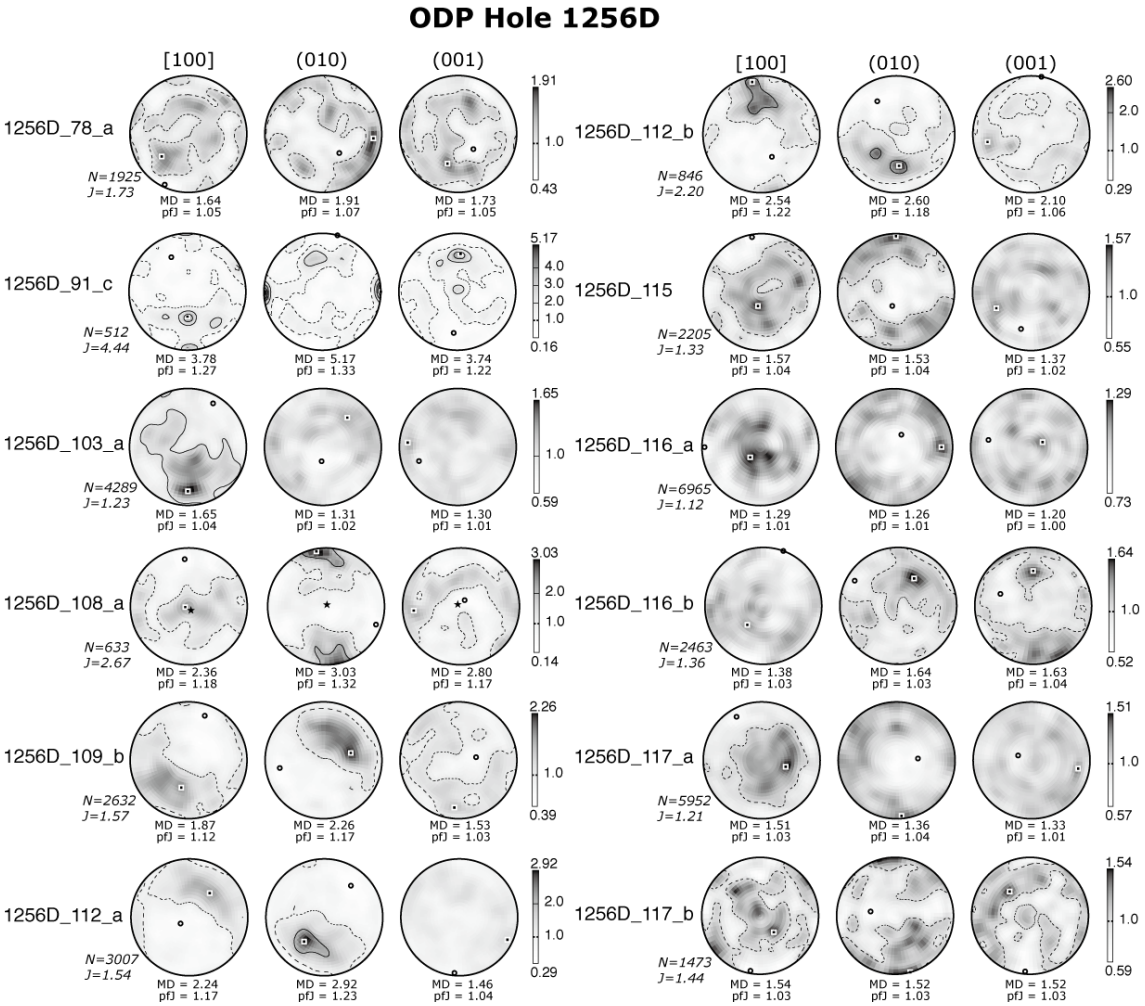

Supplementary figure 4. Plagioclase CPOs of gabbros from ODP Hole 1256D in the eastern Pacific. Lower hemisphere, equal-area stereographic projections, contours at one multiple of uniform distribution. N is number of measured grains. *J* and *pfJ* are indexes of fabric intensity, and MD is the maximum density.

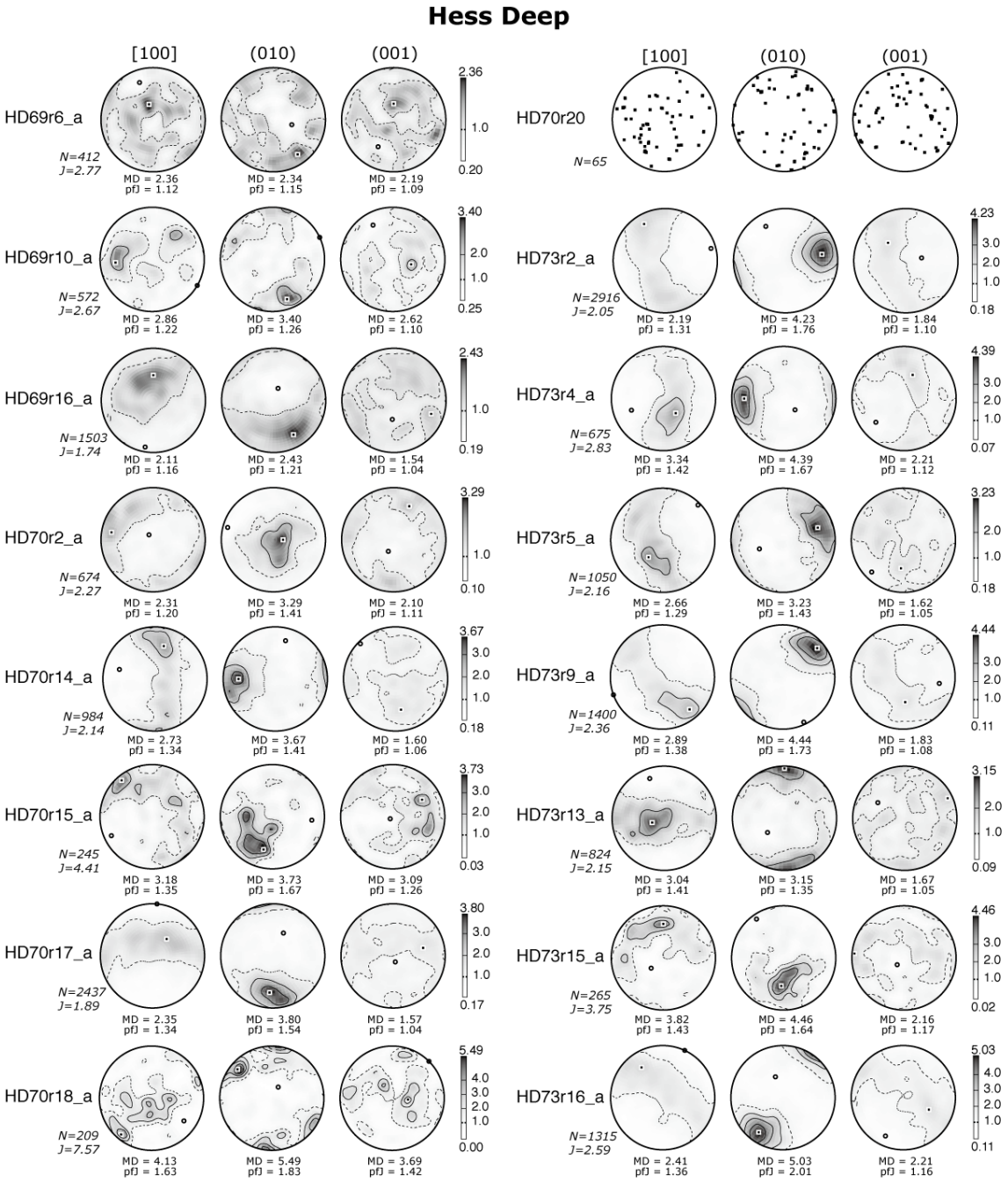

Supplementary figure 5. Plagioclase CPOs of gabbros from Hess Deep, in the Eastern Pacific. Lower hemisphere, equal-area stereographic projections, contours at one multiple of uniform distribution. N is number of measured grains. *J* and *pfJ* are indexes of fabric intensity, and MD is the maximum density.

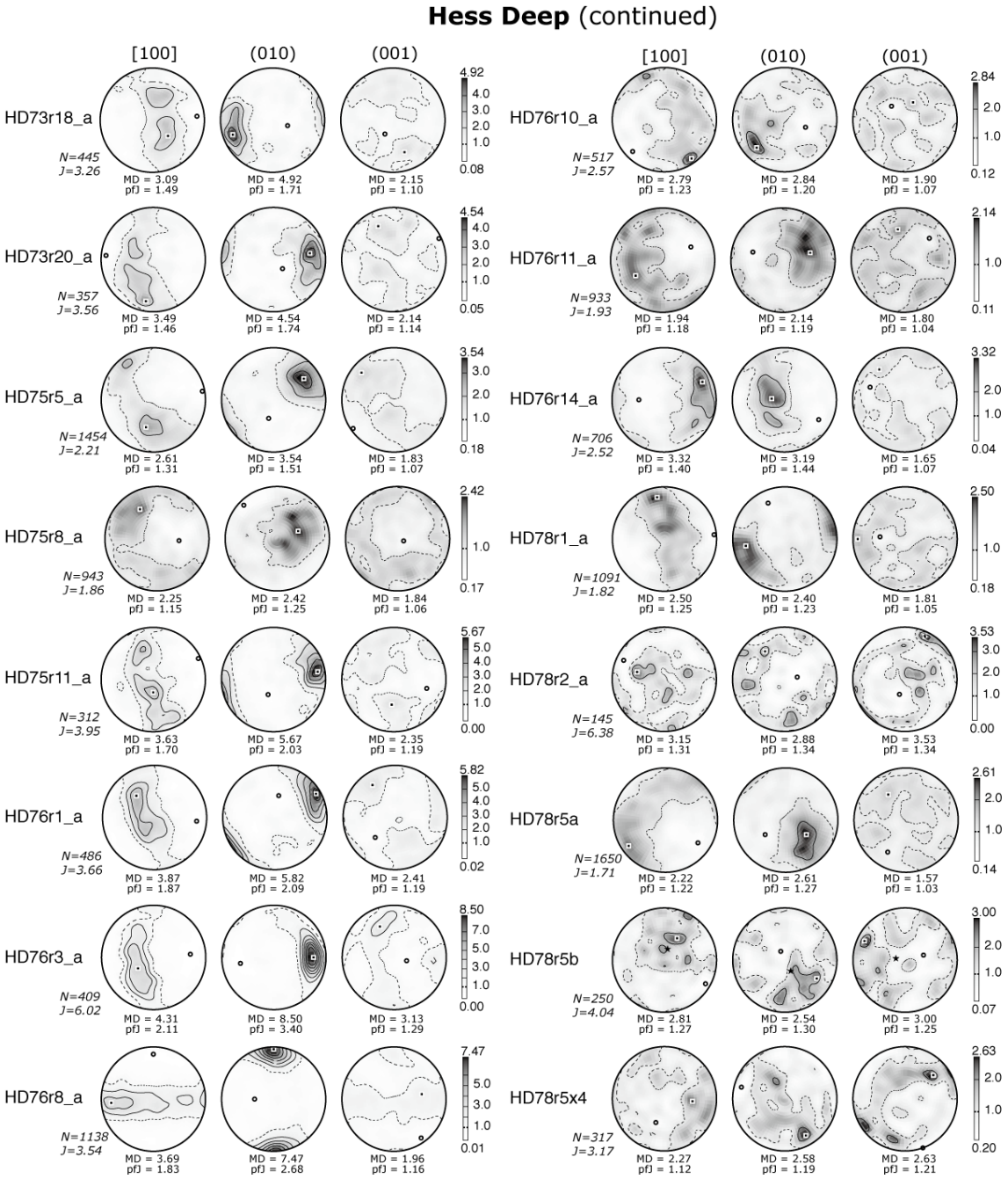

Supplementary figure 5. *(Continued)*

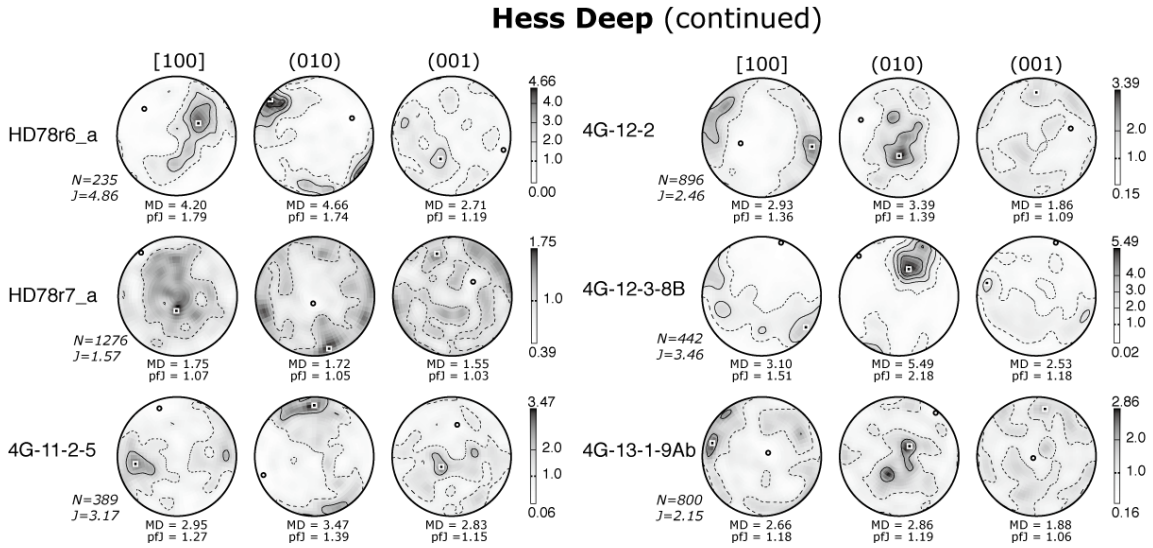

Supplementary figure 5. *(Continued)*

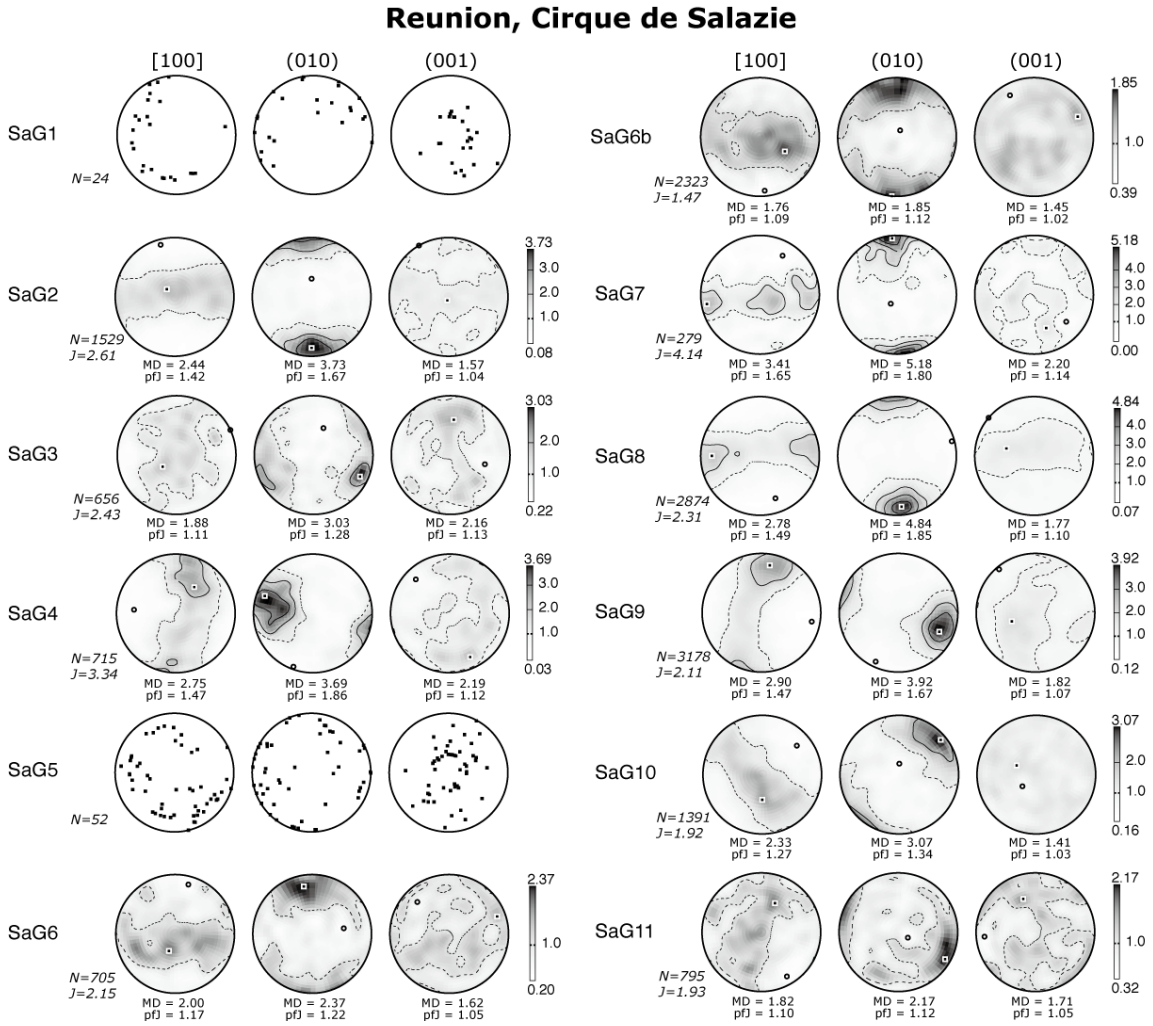

Supplementary figure 6. Plagioclase CPOs of gabbros from La Réunion (Cirque de Salazie, Piton des Neiges). Lower hemisphere, equal-area stereographic projections, contours at one multiple of uniform distribution. N is number of measured grains. *J* and *pfJ* are indexes of fabric intensity, and MD is the maximum density.

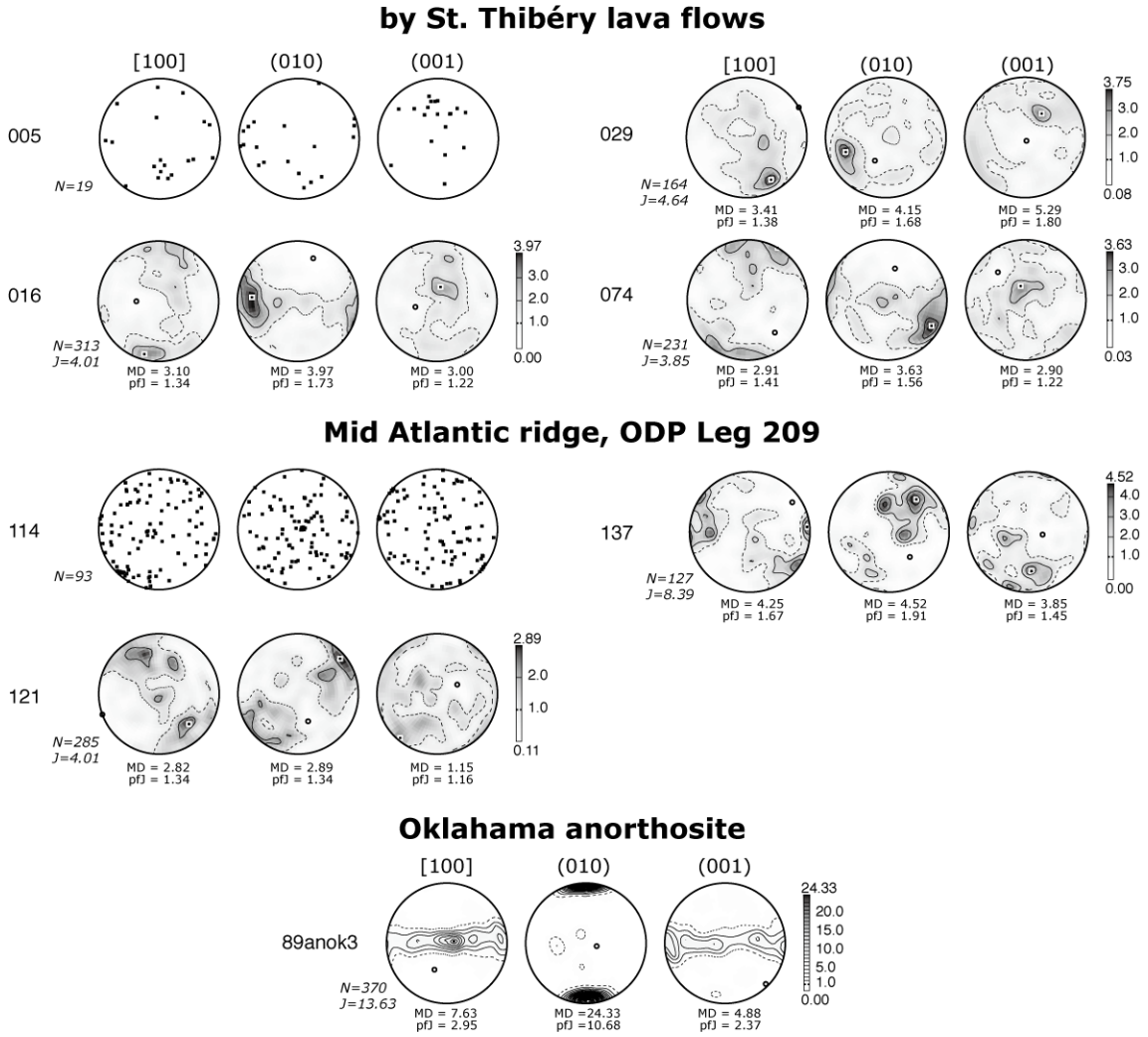

Supplementary figure 7. Plagioclase CPOs of basalts from St-Thibery, gabbros from the Mid-Atlantic ridge (ODP Leg 209), and foliated anorthosite from Oklahama. Lower hemisphere, equal-area stereographic projections, contours at one multiple of uniform distribution. N is number of measured grains. *J* and *pfJ* are indexes of fabric intensity, and MD is the maximum density.

References

Abe, N., Arai, S. and Saeki, Y., 1992, Hydration processes in the arc mantle; petrology of the Megata peridotite xenoliths, the Northeast Japan arc. *Journal of Mineralogy, Petrology and Economic Geology*, **87**, 305–317. (in Japanese with an English abstract)

Abe, N. and Arai, S., 1993, Petrographical characteristics of ultramafic xenoliths from the Megata volcano, the Northeast Japan arc. *Sci. Rep. Kanazawa Univ.*, **38**, 1–24.

Abe, N., Arai, S. and Ninomiya, A., 1995, Peridotite xenoliths and essential ejecta from the Ninomegata crater, the Northeastern Japan arc. *J. Mineral. Petrol. Econ. Geol.*, **90**, 41–49 (in Japanese with English abstract).

Abe, N., 1997, Petrology of mantle xenoliths from the arcs: Implications for the petrochemical evolution of the wedge mantle. Doctoral Thesis, Kanazawa University, Kanazawa, Japan.

Abe, N., Arai, S. and Yurimoto, H., 1998, Geochemical characteristics of the uppermost mantle beneath the Japan island arcs; implications for the upper mantle evolution. *Phys. Earth Planet. Int.*, **107**, 233–248.

Abe, N., Tamaki, M. and Arai, S., 1999, Geochemistry of the ultramafic xenoliths from Oki-Dogo island: Implications for the wedge mantle evolution. *Ofioliti*, **24**, 47.

Abe, N., Takami, M. and Arai, S., 2003, Petrological feature of spinel lherzolite xenoliths from Oki-Dogo Island: An implication for variety of the upper mantle peridotite beneath southwestern Japan. *Island Arc*, **12**, 219–232.

Abramson, E. H., Brown, J. M., Slutsky, L. J. and Zang, J. J., 1997, The elastic constants of San Carlos olivine to 17 GPa, *J. Geophys. Res.*, **102**, 12253– 12263.

Afonso, J. C., Ranalli, G., Fernandez, M., Griffin, W. L., O'Reilly, S. Y. and Faul, U., 2010, On the Vp/Vs-Mg# correlation in mantle peridotites: Implication for the identification of thermal and compositional anomalies in the upper mantle. *Earth Planet. Sci. Lett.*, **289**, 606-618.

Aki, K. and Lee, W. H. L., 1976, Determination of three dimensional velocity anomalies under a seismic array using first P arrival times from local earthqukakes, 1, A homogeneous initial model. *J. Geophys. Res.*, **81**, 4381-4399.

Aleksandrov, K. S. and Ryzhova, T. V., 1961, The elastic properties of rock forming minerals, pyroxenes and amphiboles. *Bull. Acad. Sci. USSR Geophys. Ser.*, 871-875.

Aleksandrov, K. S., Alchikov, U. V., Belikov, B. P., Zaslavskii, B. I. and Krupnyi, A. I. 1974, Velocities of elastic waves in minerals at atmospheric pressure and increasing precision of elastic constants by means of EVM (in Russian). *Izvestiya of the Academy of the Sciences of the USSR*, Geologic Series, **10**, 15–24.

Amelinckx, S. and Dekeyser, W., 1959, The structure and properties of grain boundaries. *Solid State Physics*, **8**, 325-499.

Anthony, E. Y., Hoffer, J. M., Wagner, W. K. and Chen, W., 1992, Compositional diversity in late Cenozoic mafic lavas in the Rio Grande rift and Basin and Range province, southern New Mexico. *Geol. Soc. America Bull.*, **104**, 973-979.

Anthony, E. Y. and Poths, J., 1992, 3He surface exposure dating and its implications for magma evolution in the Potrillo volcanic field, Rio Grande Rift, New Mexico, USA. *Geochim Cosmochim Acta*, **56**, 4105-4108.

Anthony, E. Y., 2005. Source regions of granites and their links to tectonic environment: Examples from the western United States. *Lithos* (Ilmari Haapala Retirement Special Volume), **80**, 61-74.

Arai, S., 1994, Characterization of spinel peridotites by olivine-spinel compositional relationships: Review and interpretation. *Chemical Geology*, **113**, 191–204.

Arai, S., Abe, N. and Hirai, H., 1998, Petrological characteristics of the sub-arc mantle: An overview on petrology of xenoliths from the Japan arcs. *Trends in Mineralogy (Indeia)*, **2**, 39–55.

Arai, S., Hirai, H., and Uto, K., 2000, Mantle peridotite xenoliths from the Southwest Japan arcs: A model for the sub-arc upper mantle structure and composition of the Western Pacific rim. *Journal of Mineralogical and Petrological Sciences*, **95**, 9–23.

Arai, S., Abe, N., Hirai, H. and Shimizu, Y., 2001, Geological, petrographical and petrological characteristics of ultramafic-mafic xenoliths in Kurose and Takashima, northern Kyushu, southwestern Japan. *Sci. Rep. Kanazawa Univ.,* **46**, 9–38.

Barreiro, J. G., Lonardelli, I., Wenk, H. R. Dresen, G., Rybacki, E., Ren, Y. and Tomé, C. N., 2007, Preferred orientation of anorthite deformed experimentally in Newtonian creep. *Earth Planet. Sci. Lett.,* **264**, 188-207.

Barruol, G. and Mainprice, D., 1993. 3-D seismic velocities calculated from lattice-preferred orientation and reflectivity of a lower crustal section: example of the Val Sesia section (Ivrea zone, Northern Italy). *Geophysical Journal International*, **115**, 1169-1188.

Bascou, J., Camps, P. and Dautria, J. M., 2005, Magnetic versus crystallographic fabrics in a basaltic lava flow. *J. volcano. Geotherm. Res.*, **145**, 119-135.

Bascou, J., Deipech, G., Vauchez, A., Moine, B. N., Cottin, J. Y. and Barruol, G., 2008, An integrated study of microstructural, geochemical, and seismic properties of the lithospheric mantle above the Kerguelen plume (Indian Ocean). *Geochem. Geophys. Geosyst.*, **9**, Q04036, doi:10.1029/2007GC001879.

Bell, D. R., Rossman, G. R., Maldener, A., Endisch, D. and Rauch, F., 2003, Hydroxide in olivine: A quantitative determination of the absolute amount and calibration of the IR spectrum. *J. Geophys. Res.*, **108**, doi: 10.1029/2001JB000679.

Ben Ismaïl, W. and Mainprice, D., 1998, An olivine fabric database: An overview of upper mantle fabrics and seismic anisotropy. *Tectonophysics*, **296**, 145– 157.

Bolfan-Casanova, N., Keppler, H. and Rubie, D. C., 2000, Water partitioning between nominally anhydrous minerals in the MgO-SiO_2-H_2O system up to 24GPa: implications for the distribution of water in the Earth's mantle. *Earth Planet. Sci. Lett.,* **182**(3-4), 209-221.

Bowman, J. R. and Ando, M., 1987, Shear-wave splitting in the upper-mantle wedge above the Tonga subduction zone. *Geophys. J. R. Astron. Soc.,* **88**, 25–41.

Brearly, M., Scarfe, C. M., Fujii, T., 1984. The petrology of ultramafic xenoliths from Summit Lake, near Prince George, British Columbia. *Contrib. Mineral. Petrol.,* **88**, 53-63.

Brey, G. P. and Köhler, T., 1990. Geothermobarometry in four-phase lherzolites II. New thermobarometers, and practical assessment of existing thermobarometers. *J. Petrology*, **31**, 1535-1378.

Buck, W. R., 2006, The role of magma in the development of the Afro–Arabian rift system. *Geological Society of London, Special Publications*, **259**, 43–54.

Bunge, H. J., 1982, *Texture Analysis in Materials Sciences*. Buttleworth, London.

Burg, J. –P., Bodinier, J. –L., Gerya, T., Bedini, R. –M., Boudier, F., Dautria, J. –M., Prikhodko, V., Efimox, A., Pupier, E. and Balanex, J. –L., 2009. Translithospheric mantle diapirism: Geological evidence and numerical modeling of the Kondyor zoned ultramafic complex (Russian Far-East). *J. Petrology*, **50**(2), 289-321.

Bussod, G. Y. A. and Irving, A. J., 1981, Thermal and rheologic history of the upper

mantle beneath the Southern Rio Grande Rift: evidence from Kilbourne Hole xenoliths, Conference on the Processes of Planetary Rifting. *Lunar and Planetary Institute*, pp. 145-148.

Bystricky, M., Kunze, K., Burlini, L. and Burg, J.-P., 2000, High shear strain of olivine aggregates: rheological and seismic consequences. *Science*, **290**, 1564–1567.

Ceuleneer, G., Nicolas, A. and Boudier, F., 1988, Mantle flow patterns at an oceanic spreading centre: The Oman peridotites record, *Tectonophysics*, **151**, 1-26.

Chai, M., Brown, J. M., Slutsky, L. J. and Zang, J., 1997, The elastic constants of an aluminous orthopyroxene to 12.5 GPa. *J. Geophys. Res.*, **102**, 14779-14785.

Clark, S. R., Stegman, D. and Müller, R. D., 2008, Episodicity in back-arc tectonic regimes, *Phys. Earth Planet. Int.,* Special Volume on Computational Geology and Geodynamics, edited by B. J. P. Kaus, T. V. Gerya and D.W. Schmid, 171, 265-279.

Crampin, S., 1984, Effective anisotropic elastic constants for wave propagation through cracked solids. *Geophys. J. Royal Astro. Soc.,* **76**, 135-145.

Collins, M. D. and Brown, J. M., 1998, Elasticity of an upper mantle clinopyroxene. *Phys. Chem. Miner.*, **26**, 7 – 13.

Crosson, R. S. and Lin J. W., 1971, Voigt and Reuss prediction of anisotropic elasticity of dunite. *J. Geophys. Res,*. **76** , 570-578.

Demouchy, S., 2004, Water in the Earth's interior: Thermodynamics and kinetics of hydrogen incorporation in olivine and wadsleyite. Universität Bayreuth.

Demouchy, S., Mainprice, D., Tommasi, A., Couvy, H., Barou, F., Frost, D. J. and Cordier, P., 2011, Forsterite to wadsleyite phase transformation under shear stress and consequences for the Earth's mantle transition zone, *Earth Planet. Sci. Lett.,*

184, 91-104.

Dick, H. J. B. and Bullen, T., 1984, Chromian spinel as a petrogenetic indicator in abyssal and alpine-type peridotites and spatially associated lavas. *Contrib. Mineral. Petrol.*, **86**, 54–76.

Dick, H. J. B., Natland, J. H., Miller, D. J., et al., 1999, *Proc. ODP, Init. Repts.,* 176.

Dick, H. J. B., Natland, J. H., Alt, J. C., Bach, W., Bideau, D., Gee, J. S., Haggas, S., Hertogen, J. G. H., Hirth, G., Holm, P. M., Ildefonse, B., Iturrino, G. J., John, B. E., Kelley, D. S., Kikawa, E., Kingdon, A., Le Roux, P. J., Maeda, J., Meyer, P. S., Miller, D. J., Naslund, H. R., Niu, Y., Robinson, P. T., Snow, J., Stephen, R. A., Trimby, P. W., Worm, H. -U. and Yoshinobu, A., 2000, A long in situ section of the lower ocean crust: results of ODP Leg 176 drilling at the Southwest Indian Ridge. *Earth Planet. Sci. Lett.,* **179**, 31-51.

Dijkstra, A. H., Drury, M. R. and Vissers, R. L. M., 2002, On the role of melt-rock reaction in mantle shear zone formation in the Othris Peridotite Massif (Greece). *J. Struct. Geol.*, **24**, 1431–1450.

Doukhan, J. -C., Doukhan, N., Naze, L. and Van Duysen, J. -C., 1986, Défauts de réseau et plasticité cristalline dans les pyroxenes: Une revue. *Bulletin de Minéralogie*, **109**, 377-374.

Drouin, M., Ildefonse, B. and Godard, M., 2009, A microstructural imprint of melt impregnation in slow spreading lithosphere: Olivine-rich troctolites from the Atlantis Massif, Mid-Atlantic Ridfe, 30ºN, IODP Hole U1309D. *Geochem. Geophys. Geosyst.*, **11**, Q06003, doi:10.1029/2009GC002995.

Dvorkin, J., Nur, A., Mavko, G. and Ben-Avraham, Z., 1993, Narrow subducting slabs and the origin of backarc basins. *Tectonophysics*, **227**, 63-79.

Egydio-Silva, M., Vauchez, A., Bascou, J. and Hippertt, L., 2002, Hightemperature deformation in the Neoproterozoic transpressional Ribeira belt, southeast Brazil. *Tectonophysics*, **352**, 203–224.

Faccenna, C., Davy, P., Brun, J. P., Funiciello, R., Giardini, D., Mattei, M. and Nalpas, T., 1996, The dynamic of backarc basins: An experimental approach to the opening of the Tyrrhenian Sea. *Geophys. J. Int.*, **126**, 781–795.

Falus, G., Tommasi, A., Ingrin, J. and Szabo, C., 2008, Deformation and seismic anisotropy of the lithospheric mantle in the southeastern Carpathians inferred from the study of mantle xenoliths. *Earth Planet. Sci. Lett.,* **272**, 50-64.

Fouch, M. J. and S. Rondenay, 2006, Seismic anisotropy beneath stable continental interiors. *Phys. Earth Planet. Int.*, **158**, 292-320.

Frank, F. C. and Read, W. T. J., 1950, Multiplication processes for slow moving dislocations. *Physical Review*, **79**, 722-723.

Fujiwara, M., and Arai, D., 1982, Ultramafic xenoliths in Aratoyama alkali basalt, Okayama Prefecture, as upper mantle materials beneath a typical island arc. *Journal of Mineralogy, Petrology and Economic Geology*, **3**, 219–227. (in Japanese with an English abstract)

Gao, S., Davis, P. M., Liu, H., Slack, P. D., Rigor, A. W., Zorin, Y. A., Mordvinova, V. V., Kozhevnikov, V. M. and Logatchev, N. A., 1997, SKS splitting beneath continental rift zones. *J. Geophys. Res.*, **102**, B10, 22781-22797.

Gao, W., Grand, S. P., Baldridge, W. S., Wilson, D., West, M., Ni, J. F. and Aster, R., 2004, Upper mantle convection beneath the central Rio Grande rift imaged by P and S wave tomography. *J. Geophys. Res.*, **109**(B03305), doi:10.1029/2003JB002743.

Gao, S. S., Liu, K. H., Stern, R. J., Keller, G. R., Hogan, J. P., Pulliam, J. and Anthony,

E. Y., 2008, Characteristics of mantle fabrics beneath the south-central United states: Constraints from shear-wave splitting measurements. *Geosphere*, **4**(2), 411-417.

Gao, S. S. and Liu, K. H., 2009, Significant seismic anisotropy beneath the southern Lhasa Terrane, Tibetan Plateau. *Geochem. Geophys. Geosyst.*, **10**(Q02008), doi:10.1029/2008GC002227.

Gao, S. S., Liu, K. H. and Abdelsalam, M. G., 2010, Seismic anisotropy beneath the Afar Depression and adjacent areas: Implications for mantle flow. *J. Geophys. Res.*, **115**(B12330), doi:10.1029/2009JB007141.

Gillis, K., Mével, C., Allan, J., et al., 1993. *Proc. ODP, Init. Repts.,* 147: College Station, TX (Ocean Drilling Program).

Goto, K., 1986, Lamprophyre dikes and mafic-ultramafic xenoliths at Shingu, the outer zone of southwestern Japan. Master's thesis, University of Tsukuba, Japan.

Goto, K. and Arai, S., 1987, Petrology of peridotite xenoliths in lamprophyre from Shingu, Southwestern Japan: Implications for origin of Fe-rich mantle peridotite. *Mineralogy and Petrology*, **37**, 137–155.

Goto, A. and Yokoyama, K., 1988, Lherzolite inclusions in olivine nephelinite tuff from Salt Lake Crater, Hawaii. *Lithos*, **21**, 67–80.

Grant, K., Ingrin, J., Lorand, J. and Dumas, P., 2007, Water partitioning between mantle minerals from peridotite xenoliths. *Contrib. Mineral. Petrol.,* **154**(1), 15-34.

Griffin, W. L., O'Reilly, S. Y., Afonso, J. C. and Begg, G., 2008, The composition and evolution of lithosphericmantle: a re-evaluation and its tectonic implications. *J. Petrol.*, doi:10.1093/petrology/egn033.

Griffin, W. R., Foland, K. A., Stern, R. J. and Leybourne, M. L., 2010, Geochronology

of Bimodal Alkaline Volcanism in the Balcones Igneous Province, Texas: Implications for Cretaceous Intraplate Magmatism in the Northern Gulf of Mexico Magmatic Zone. *Journal of Geology*, **118**, 1-23.

Grimmer, H., 1979, The distribution of disorientation angles if all relative orientations of neighbouring grains are equally probable. *Scripta Metallurgica*, **13**(2), 161-164.

Gripp, A. E. and Gordon, R. G., 2002, Young tracks of hotspots and current plate velocities. *Geophys. J. Int.*, **150**, 321 – 361.

Günther, D. and Heinrich, C. A., 1999, Enhanced sensitivity in LAICP-MS using helium-argon mixtures as aerosol carrier. *Journal of Analytical Atomic Spectrometry*, **14**, 1369-1374.

Hamblock, J. M., Andronicos, C. L., Miller, K. C., Barnes, C. G., Ren, M. -H., Averill, M. G. and Anthony, E. Y., 2007, A composite geologic and seismic profile beneath the southern Rio Grande rift, New Mexico, based on xenoliths mineralogy, temperature, and pressure. *Tectonophys*, **442**, 14-48.

Harigane, Y., Michibayashi, K. and Ohara, Y., 2008, Shearing within lower crust during progressive retrogression: Structural analysis of gabbroic rocks from the Godzilla Mullion, an oceanic core complex in the Parece Vela bacarc basin. *Tectonophysics*, **457**, 183-196.

Hey, R. N., Deffeyes, K. S., Johnson, G. L. and Lowrie, A., 1972, The Galapagos triple junction and plate motionsin the East Pacific, *Nature*, **237**, 20-22.

Hielscher, R. and Schaeben, H., 2008. A novel pole figure inversion method: specification of the MTEX algorithm. *Journal of Applied Crystallography*, **41**, 1024–1037.

Hill, R., 1952, The elastic behaviour of a crystalline aggregate. *Proc. Phys. Soc. London Ser. A,* **65**, 349-354.

Hirth, G. and Kohlstedt, D. L., 1995, Experimental constraints on the dynamics of the partially molten upper mantle: deformation in the dislocation creep regime. *J. Geophys. Res.*, **100**, 15441–15449.

Holtzman, B. K., Kohlstedt, D. L., Zimmerman, M. E., Heidelbach, F., Hiraga, T. and Hustoft, J., 2003, Melt segregation and strain partitioning: Implications for seismic anisotropy and mantle flow. *Science*, **301**, 1227–1230, doi:10.1126/science.1087132.

Ildefonse, B., Mainprice, D., Gusmao de Burgos, C. M., 2002, Crystallographic preferred orientations and seismic properties of gabbroic rocks. *AGU 2002 Fall Meeting*, abstract.

Irving, A. J., 1980, Petrology and geochemistry of composite ultramafic xenoliths in alkalic basalts and implications for magmatic processes within the mantle. *Am. J. Sci.*, **280-A**, 389–426.

Ishise, M., and Oda, H., 2005, Three-dimensional structure of P-wave anisotropy beneath the Tohoku district, northeast Japan. *J. Geophys. Res.*, **110**(B07304), doi:10.1029/2004JB003599.

Iwamori, H., 1989, Compositional zonation of Cenozoic basalts in the Central Chugoku district, Southwestern Japan: Evidence for mantle upwelling. *Bulletin of the Volcanological Society of Japan*, **34**(2), 105–123.

Ji, S. and Mainprice, D., 1988. Natural deformation fabrics of plagioclase : implication for slip systems and seismic anisotropy. *Tectonophysics*, **147**, 145-163.

Jung, H. and Karato, S., 2001, Water-induced fabric transitions in olivine. *Science* **293**, 24–27.

Jolivet, L., Tamaki, K. and Fournier, M., 1994, Japan Sea, opening history and mechanism: A synthesis. *J. Geophys. Res.*, **99**(B11), 22,237–22,259.

Kaminski, É., Ribe, N. M., 2001, A kinematic model for recrystallization and texture development in olivine polycrystals. *Earth Planet. Sci. Lett.*, **189**, 253–267.

Kaneoka, I., Matsuda, J., Xashu, D., Takahashi, E. and Aoki, K., 1978, Ar and Sr isotopes of mantle-derived rocks from the Japanese islands. *Bulletin of Volcanology*, **41**, 424–433.

Karato S. -I., 1998, Seismic anisotropy in the deep mantle, boundary layers and the geometry of mantle convection. *Pure and Applied Geophysics*, **151**, 565-587.

Karato, S. –I., 2008, *Deformation of Earth Materials*. Cambridge University Press.

Katayama, I., Jung, H. and Karato, S. -I., 2004, New type of olivine fabric from deformation experiments at modest water content and low stress. *Geology*, **32** (12), 1045–1048.

Kelemen, P. B. and Dick, H. J. B., 1995, Focused melt flow and localized deformation in the upper mantle: juxtaposition of replacive dunite and ductile shear zones in the Josephine peridotite, SW Oregon. *J. Geophys. Res*, **100**, 423–438.

Kelemen, P. B., Kikawa, E., Miller, D. J., et al., 2004, *Proc. ODP, Init. Repts.,* 209.

Keller, G. R., Kruger, J. M., Smith, K. J. and Voight, W. M., 1989, The Ouachita system: A geophysical overview, in *The Appalachian–Ouachita Orogen in the United States (The Geology of North America F2)*, Edited by R. D. Hatcher Jr., W. A. Thomas, G. W. Viele, pp. 689-694, Geol. Soc. Am.

Kendall, J. -M., Stuart, G. W., Ebinger, C. J., Bastow, I. D. and Keir, D., 2005, Magma-assisted rifting in Ethiopia. *Nature*, **433**, 146-148.

Kendall, J. -M., Pilidou, S., Keir, D., Bastow, I. D., Stuart, G. W. and Ayele, A., 2006, Mantle upwellings, melt migration and the rifting of Africa: insights from seismic anisotropy. *Geological Society of London, Special Publications,* **259**, 55–72.

Kimura, J., Stern, R. J. and Yoshida, T., 2005, Reinitiation of subduction and

magmatic responses in SW Japan during Neogene time. *GSA Bulletin*, **117**(7/8), 989–986.

Koepke, J., France, L., Mueller, T., Faure, F., Goetze, N., Dziony, W., Ildefonse, B., 2011. Gabbros from IODP Site 1256, equatorial Pacific: Insight into axial magma chamber processes at fast spreading ocean ridges. *Geochem. Geophys. Geosyst.*, **12**(Q09014), doi: 10.1029/2011gc003655.

Kruhl, J.H., 1987. Preferred lattice orientations of plagioclase from amphibolite and greenschist facies rocks near the Insubric Line (Western Alps). *Tectonophysics*, **135**, 233-242.

Kono, Y., Ishikawa, M., Harigane, Y., Michibayashi, K. and Arima, M., 2009, P- and S-wave velocities of the lowermost crustal rocks from the Kohistan arc: Implications for seismic Moho discontinuity attributed to abundant garnet. *Tectonophysics*, **467**, 44-54.

Kuno, H., 1967, Mafic and ultramafic nodules from Itinome-gata, Japan. In: Wyllie, P.J. (Ed.), Ultramafic and Related Rocks. John Wiley & Sons, New York, pp. 337–346.

Lee, C. -T. A., 2003, Compositional variation of density and seismic velocities in natural peridotites at STP conditions: implications for seismic imaging of compositional heterogeneites in the upper mantle. *J. Geophys. Res.*, **108**. doi:10.1029/2003JB002413.

Le Roux, V., Bodinier, J. -L., Tommasi, A., Alard, O., Dautria, J. -M., Vauchez, A. and Riches, A. J. V., 2007, The Lherz spinel lherzolite: refertilized rather than pristine mantle. *Earth Planet. Sci. Lett.*, **259**, 599–612.

Le Roux, V., Tommasi, A. and Vauchez, A., 2008, Feedback between melt percolation and deformation in an exhumed lithosphere-asthenosphere boundary. *Earth Planet.*

Sci. Lett., **274**, 401-413.

Libowitzky, E. and Rossman, G. R., 1997, An IR absorption calibration for water in minerals. *Am. Mineral.*, **82**, 1111–1115.

Linckens, J., M. Herwegh, O. Müntener, and I. Mercolli (2011), Evolution of a polymineralic mantle shear zone and the role of second phases in the localization of deformation, J. Geophys. Res., 116, B06210, doi:10.1029/2010JB008119.

Liu, K. H., Gao, S. S., Gao, Y. and Wu, J., 2008, Shear wave splitting and mantle flow associated with the deflected Pacific slab beneath northeast Asia. *J. Geophys. Res.*, **113**(B01305), doi:10.1029/2007JB005178.

Liu, K. H., 2009, NA-SWS-1.1: A uniform database of teleseismic shear wave splitting measurements for North America. *Geochem. Geophys. Geosyst.*, **10**, Q05011, doi:10.1029/2009GC002440.

MacLeod, C. J. and Yaouancq, G., 2000, A fossil melt lens in the Oman ophiolite: implications for magma chamber processes at fast spreading ridges. *Earth Planet. Sci. Lett,* **176**, 357–373.

MacLeod, C. J., Lissenberg, J. C. L., Howard, K. A., Ildefonse, B. and Morris, A., 2011, Fast Spreading Mid Ocean Ridge Magma Chamber Processes: New Constraints from Hess Deep. *AGU 2011 Fall Meeting*, abstract, V21B-2499.

Mackwell, S. J., 1991, High-temperature rheology of enstatite: implications for creep in the mantle. *Geophys. Res. Lett.,* **18**(11), 2027-2030.

Mainprice, D. and Silver, P. G., 1993, Interpretation of SKS-waves using samples from the subcontinental lithosphere. *Phys. Earth Planet. Int.*, **78**, 257-280.

Mainprice, D. and Humbert, M., 1994, Methods of calculating petrophysical properties from lattice preferred orientation data. *Surv. Geophys.,* **15**, 575-592.

Mainprice, D., 1997, Modelling anisotropic seismic properties of partially molten

rocks found at mid-ocean ridges. *Tectonophys*, **279**, 161-179.

Mainprice, D., Barruol, G. and Ben Ismaïl, W., 2000, The anisotropy of the Earth's mantle: From single crystal to polycrystal. *in Mineral Physics and Seismic Tomography: From Atomic to Global*, Geophys. Monogr. Ser., vol. 117, edited by S. Karato et al., pp. 237–264, AGU, Washington, D. C.

Mainprice, D., 2007, Seismic anisotropy of the deep Earth from a mineral and rock physics perspective, In: Schubert, G. (ed.), *Treatise on Geophysics*, vol. 2. Elsevier, Oxford, pp. 437–492.

Mainprice, D., Barruol, G. and Ben Ismaïl, W., 2000, The anisotropy of the Earth's mantle: From single crystal to polycrystal. *in Mineral Physics and Seismic Tomography: From Atomic to Global*, Geophys. Monogr. Ser., vol. 117, edited by S. Karato et al., pp. 237–264, AGU, Washington, D. C.

Martinez, F., Okino, K., Ohara, Y., Reysenbach, A., and Goffredi, S., 2007, Back-Arc Basins. *Oceanography*, **20**(1), 116-127.

Martinod, J., Hatzfeld, D., Brun, J. -P., Davy, P., Gautier, P., 2000, Continental collision, gravity spreading, and kinematics of Aegean and Anatolia. *Tectonics*, **19**, 290–299.

Matsukage, K. N., Nishihara, Y. and Karato, S. I., 2005, Seismological signature of chemical differentiation of Earth's upper mantle. *J. Geophys. Res.*, **110**(B12305), doi:10.1029/2004JB003504.

Mehl, L., Hacker, B. R., Hirth, G. and Kelemen, P. B., 2003, Arc-parallel flow within the mantle wedge: Evidence from the accreted Talkeetna arc, south central Alaska. *J. Geophys. Res.*, **108**(B8, 2375), doi:10.1029/2002JB002233.

Mehl, L., and Hirth, G., 2008. Plagioclase preferred orientation in layered mylonites: Evaluation of flow laws for the lower crust. Journal of Geophysical Research-Solid

Earth, 113, B05202, doi:10.1029/2007JB005075.

Michael, A. H., 1988, Effects of three-dimensional velocity structure on the seismic of the seismicity of the 1984 Morgan Hill, California, aftershock sequence. *Bull. Seismol. Soc. Am.*, **78**, 1199-1221.

Michibayashi, K. and Mainprice, D., 2004, The role of pre-existing mechanical anisotropy on shear zone development within oceanic mantle lithosphere: and example from the Oman ophiolites. *J. Petrol*, **45**(2), 405-414, doi: 10.1093/petrology/egg099.

Michibayashi, K., Ina, T. and Kanagawa, K., 2006, The effect of dynamic recrystallization on olivine fabric and seismic anisotropy: insight from a ductile shear zone, Oman ophiolite. *Earth Planet. Sci. Lett.*, **244**, 695–708.

Michibayashi, K., Oohara, T., Satsukawa, T., Ishimaru, S., Arai, S. and Okrugin, V. M., 2009, Rock seismic anisotropy of the low velocity zone beneath the volcanic front in the mantle wedge. *Geophys. Res. Lett.,* ***36***(L12305), doi:10.1029/2009GL038527.

Mickus, K., Stern, R. J., Keller, G. R. and Anthony, E. Y., 2009, Potential field evidence for a volcanic rifted margin along the Texas Gulf Coast. *Geology,* **37**, 387-390.

Miyashiro, A., 1973, Metamorphism and Metamorphic Belts. George Allen & Unwin, London.

Montardi, Y. and Mainprice, D., 1987, A TEM study of the natural plastic deformation of calcic plagioclase. *Bull. Mineral.*, **110**, 1-14.

Morales, L. F. G., Boudier, F. and Nicolas, A., 2011, Microstructures and crystallographic preferred orientation of anorthosites from Oman ophiolite and dynamics of melt lenses. *TECTONICS*, **30**(TC2011), doi:10.1029/2010TC002697.

Nagao, K., and Takahashi, E., 1993, Noble gases in the mantle wedge lower crust: An inference from the isotopic analyses of xenoliths from Oki-Dogo and Ichinomegata, Japan. *Geochemical Journal,* **27**, 229–240.

Nakajima, J., Matsuzawa, T., Hasegawa, A. and Zhao, D., 2001, Threedimensional structure of Vp, Vs, and Vp/Vs beneath the northeastern Japan arc: implications for arc magmatism and fluids. *J. Geophys. Res*, **106**, 21843–21857.

Nakajima, J. and Hasegawa, A., 2004. Shear-wave polarization anisotropy and subduction-induced flow in the mantle wedge of northeastern Japan. *Earth Planet. Sci. Lett.*, **225**, 365-377.

Nakajima, J., Takei, Y. and Hasegawa, A., 2005, Quantitative analysis of the inclined low-velocity zone in the mantle wedge of northeastern Japan: A systematic change of melt-filled pore shapes with depth and its implications for melt migration. *Earth Planet. Sci. Lett.*, **234**, 59-70.

Naze, L., Doukhan, N., Doukhan, J. C. and Latrous, K., 1987, TEM study of lattice defects in naturally and experimentally deformed orthopyroxenes. *Bull. Mineral.*, **110**, 497–512.

Nicolas, A., Boudier, F. and Boullier, A. M., 1973, Mechanisms of flow in naturally and experimentally deformed peridotites. *Am. J. Sci.*, **273**, 853–876.

Nicolas, A. and Christensen, N. I., 1987, Formation of anisotropy in upper mantle peridotites: A review, in Composition, Structure and Dynamics of the Lithosphere-Asthenosphere System. Geodyn. Ser., vol. 16, edited by K. Fuchs and C. Froidevaux, pp. 111 – 123, AGU, Washington, D. C.

Nicolas, A., Boudier, F., Ildefonse, B. and Ball, B., 2000, Accretion of Oman and United Arab Emirates ophiolite: Discussion of a new structural map. *Mar. Geophys. Res.*, **21**, 147–179, doi:10.1023/A:1026769727917.

Nicolas, A., and Boudier, F., 2008, Large shear zones with no relative displacement. *Terra Nova*, **20**(3), 200-205.

Nimis, P. and Taylor, W. R., 2000, Single clinopyroxene thermobarometry for garnet peridotes. Part I. Calibration and testing of a Cr-rich-Cpx barometer and an enstatite-in Cpx thermometer. *Contrib. Mineral. Petrol.,* **139**, 541–554.

Nixon, P. H., 1987. Mantle Xenoliths. John Wiley & Sons, New York.

Olsen, T. S. and Kohlstedt, D. L., 1984, Analysis of Dislocations in Some Naturally Deformed Plagioclase Feldspars. *Phys. Chem. Mineral.*, **11**, 153-160.

Otofuji, Y. and Matsuda, T., 1984, Timing of rotational motion of Southwest Japan inferred from paleomagnetism. *Earth Planet. Sci. Lett.*, **70**, 373–382.

Otofuji, Y., Matsuda, T. and Nohda, S., 1985. Paleomagnetic evidence from the Miocene counter-clockwise rotation of Northeast Japan—rifting process of the Japan Sea. *Earth Planet. Sci. Lett.*, **75**, 265–277.

Passchier, C. W. and Trouw, R. A. J., 2005, *Microtectonics*. Springer Berlin Heidenlberg, New York.

Paterson, M. S., 1982, The determination of hydroxyl by infrared absorption in quartz, silicate-glasses and similar materials. *Bulletin de Minéralogie,* **105**(1), 20-29.

Pearce, M. A., Wheeler, J. and Prior, D. J., 2011, Relative strength of mafic and felsic rocks during amphibolite facies metamorphism and deformation. *J. Struct. Geol.*, **33**, 662-675.

Pera, E., Mainprice, D. and Burlini, L., 2003, Anisotropic seismic properties of the upper mantle beneath the Torre Alfina area (northern Apennines, central Italy). *Tectonophys*, **370**, 11 –30.

Perkins, D. and Anthony, E. Y., 2011, The evolution of spinel lherzolite xenoliths and the nature of the mantle at Kilbourne Hole, New Mexico. *Contrib. Mineral. Petrol.*,

doi: 10.1007/s0410-011-0644-1.

Peslier, A. H., Francis, D. and Ludden, J., 2002, The lithospheric mantle beneath continental margins: melting and melt-rock reaction in Canadian Cordillera xenoliths. *J. Petrol.*, **43**, 2013-2047.

Peslier, A. and Luhr, J., 2006, Hydrogen loss from olivines in mantle xenoliths from Simcoe (USA) and Mexico: Mafic alkalic magma ascent rates and water budget of the sub-continental lithosphere. *Earth Planet. Sci. Lett.,* **242**(3-4), 302-319.

Pulliam, J., Suhardja, S., Stern, R. J., Anthony, E. Y., Gao, S., Keller, G. R. and Mickus, K., 2009, Broadband Seismic Study of the Texas Continent-Ocean Boundary: A Pilot Project. Geological Society of America, South-Central Section – 43rd Annual Meeting, Richardson, TX, 16-17 March 2009.

Ramsay, J. G. and Graham, R. H., 1970, Strain variation in shear belts. *Can. J. Earth Sci.*, **7**, 786–813.

Ramsay, J. G., 1980, Shear zone geometry: a review. *J. Struct. Geol.*, **2**(1/2), 83–99.

Raye, U., Stern, R. J., Anthony, E. Y., Ren, M., Kimura, J., Tani, K. and Qing, C., 2009, Characterization of mantle beneath Texas: Constraints from Knippa xenoliths, *GSA Abstracts,* **41**(2), 29.

Reuss, A., 1929, Berechnung der Fließgrenze von Mischkristallen auf Grund der Plastizitätsbedingung für Einkristalle. *Z. Angew. Math. Mech.* **9**, 49-58.

Robinson, P. T., Von Herzen, R., et al., 1989. *Proc. ODP, Init. Repts.* 118: College Station, TX (Ocean Drilling Program).

Rosenberg, C. L. and Handy, M. R., 2000, Syntectonic melt pathways during simple shearing of a partially molten rock analogue (Norcampher–Benzamide). *J. Geophys. Res.,* **105**, 3135–3149.

Rosenberg, C. L. and Handy, M. R., 2005, Experimental deformation of partially

melted granite revisited: implications for the continental crust. *J. Metamor. Geol.,* **23**, 19–28.

Sato, H., 1993, The relationship between late Cenozoic tectonic events and stress field and basin development in NE Japan. *J. Geophys. Res,.* **99**(B11), 22261–22274.

Sato, H., 1994, The relationship between late Cenozoic tectonic events and stress field and basin development in northeast Japan. *J. Geophys. Res.*, **99**, 22,261– 22,274.

Satsukawa, T. and Michibayashi, K., 2009, Determination of slip system in olivine based on crystallographic preferred orientation and subgrain-rotation axis: examples from Ichinomegata peridotite xenoliths, Oga peninsula, Akita prefecture. *J. Geol. Soc. Jpn.*, **115**, 288-291.

Satsukawa, T., Michibayashi, K., Raye, U., Anthony, E. Y., Pulliam, J. and Stern, R., 2010, Uppermost mantle anisotropy beneath the southern Laurentian margin: Evidence from Knippa peridotite xenoliths, Texas. *Geophys. Res. Lett.,* **37**(L20312), doi:10.1029/2010GL044538.

Satsukawa, T., Michibayashi, K., Anthony, E. Y., Stern, R. J., Gao, S. S. and Liu, K. H., 2011, Seismic anisotropy of the uppermost mantle beneath the Rio Grande rift: Evidence from Kilbourne Hole peridotite xenoliths, New Mexico. *Earth Planet. Sci. Lett.*, **311**(1-2), 172-181, doi:10.1016/j.epsl.2011.09.013.

Savage, M. K., 1999, Seismic anisotropy and mantle deformation: what have we learned from shear wave splitting? *Rev. Geophys*., **37**, 65-106.

Sen, G. and Leman, W. P., 1991, Iron-rich lherzolitic xenoliths from Oahu: Origin and implications for Hawaiian magma sources. *Earth Planet. Sci. Lett.*, **102**, 45–57.

Seront, B., Mainprice, D., Christensen, N. I., 1993, A determination of the three-dimensional seismic properties of anorthosite: comparison between values calculated from the petrofabric and direct laboratory measurements. *J. Geophys.*

Res., **98**, 2209–2221.

Siegesmund, S. and Kruhl, J.H., 1991. The effect of plagioclase textures on velocity anisotropy and shear wave splitting at deeper crustal levels. *Tectonophysics*, **191**, 147-154.

Silver, P. G. and Chan, W. W., 1991, Shear wave splitting and subcontinental mantle deformation. *J. Geophys. Res.*, **96**, 16429–16454

Silver, P. G., 1996, Seismic anisotropy beneath the continents: Probing the depths of geology. *Ann. Rev. Earth. Planet. Sci*, **24**, 385-432.

Skemer, P., Katayama, I., Jiang, Z. and Karato, S., 2006, The misorientation index: development of a new method of olivine lattice preferred orientations. *Tectonophysics,* **411**, 157–167.

Soustelle, V., Tommasi, A., Bodinier, J. I., Garrido, C. J. and Vauchez, A., 2009, Deformation and reactive melt transport in the mantle lithosphere above a large-scale partial melting domain: the Ronda peridotite massif, southern Spain. *J. Petrol.*, **50**(7), 1235–1266.

Soustelle, V., Tommasi, A., Demouchy, S. and Ionov, D. A., 2010, Deformation and Fluid-Rock Interaction in the Supra-subduction Mantle: Microstructures and Water Contents in Peridotite Xenoliths from the Avacha Volcano, Kamchatka. *J. Petrol.,* **51**(1&2), 363-394, doi:10.1093/petrology/egp085.

Soustelle, V. and Tommasi, A., 2010, Seismic properties of the supra-subduction mantle: Constraints from peridotite xenoliths from the Avacha volcano, southern Kamchatka. *Geophys. Res. Lett.*, **37**(L13307), doi:10.1029/2010GL043450.

Stein, M., Garfunkel, Z. and Jagoutz, E., 1993, Chronothermometry of peridotitic and pyroxenitic xenoliths: Implications for the thermal evolution of the Arabian lithosphere. *Geochim Cosmochim Acta,* **57**, 1325-1337.

Stünitz, H., Fitz Gerald, J. D., and Tullis, J., 2003, Dislocation generation, slip systems, and dynamic recrystallization in experimentally deformed plagioclase single crystals. *Tectonophysics*, **372**, 215-233.

Svahnberg, H. and Piazolo, S., 2010, The initiation of strain localisation in plagioclase-rich rocks: Insights from detailed microstructural analyses. *J. Struct. Geol.*, **32**, 1404-1416.

Takahashi, E., Shimazaki, T., Tsuzaki, Y. and Yoshida, H., 1993, Melting study of a peridotite KLB-1 to 6.5 GPa, and the origin of basaltic magmas. *Phil. Trans. R. Soc. Lond. A.,* **342**, 105-120.

Takahashi, E., 1975, Finding of spinel-lherzolites inclusions in Oki-Dogo Island, Japan. *J. Geol. Soc. Jpn.,* **81**, 81–83. (in Japanese)

Takahashi, E., 1978a, Petrologic model of the crust and upper mantle of the Japanese Island arcs. *Bulletin of Volcanology,* **41**, 529–547.

Takahashi, E., 1978b, Petrology of the upper mantle and lower crust of the Japanese Island arcs. Doctoral Thesis, University of Tokyo, Tokyo, Japan.

Takahashi, E., 1986, Genesis of calc-alkali andesite magma in a hydrous mantle–crust boundary: petrology of lherzolite xenoliths from the Ichinomegata crater, Oga Peninsula, Northeast Japan, Part II. *J. Volcanol. Geotherm. Res.,* **29**, 355–395.

Takamura, H., 1978, Finding of spinel–lherzolite xenolith in basaltic sheets from Shingu, Ehime Prefecture, Japan. *J. Geol. Soc. Jpn.,* **84**, 475–479 (in Japanese).

Takei, Y., 2002, Effect of pore geometry on VP/VS: From equilibrium geometry to crack. *J. Geophys. Res.,* **107**(B2), 2043, doi:10.1029/2001JB000522.

Takei, Y., 2005, Deformation-induced grain boundary wetting and its effects on the acoustic and rheological properties of partially molten rock analogue. *J. Geophys. Res.,* **110**, doi:10.1029/2005JB003801.

Tamaki, K., Suyehiro, K., Allam, J., Ingle, J. C. and Pisciottto, K. A., 1992, *Tectonic synthesis and implication of Japan Sea ODP Drilling*, IN: Tamaki, K., et al. (eds.), Proceedings of the Ocean Drilling Program, Scientific Results 127/128, Part 2. Ocean Drilling Program, College Station, pp. 1333–1348.

Tamaki, K., 1995, Opening tectonics of the Japan-Sea in Backarc Basins: Tectonics and Magmatism. Edited by B. Taylor 407-450, Plenum Press New York.

Tamaki, K. and Honza, E., 1991, Global tectonics and formation of marginal basins: role of the western Pacific. *Episodes*, **14**, 224–230.

Tanaka, T., Hoshino, M., 1987, Sm–Nd ages of Oki metamorphic rocks and their geological significance. *In* 94th Annual Meeting, Geological Society of Japan., Osaka, Japan, pp. 492.

Tasaka, M., Michibayashi, M. and Mainprice, D., 2008, B-type olivine fabrics developed in the fore-arc side of the mantle wedge along a subducting slab. *Earth Planet. Sci. Lett.*, **272**, 747-757.

Thomas, W. A., 2006, Tectonic inheritance at a continental margin, *GSA Today,* **16**, 4-11.

Thompson, R. N., Ottley, C. J., Smith, P. M, Pearson, D. G., Dickin, A. P., Morrison, M. A., Leat, P. T. and Gibson, S. A., 2005, Source of the quaternary alkalic basalts, pictrites and basanites of the Potrillo Volcanic Field, New Mexico, USA: Lithosphere or convecting mantle? *J. Petrol.,* **46**, 1603-1643.

Thoraval, C., Tommasi, A. and Doin, M. -P., 2006, Plume–lithosphere interactions beneath a fast-moving plate. *Geophys. Res. Lett.,* **33**(L01301), doi:01310.01029/02005GL024047.

Tommasi, A., Mainprice, D., Canova, G. and Chastel, Y., 2000, Viscoplastic self-consistent and equilibrium-based modeling of olivine lattice preferred

orientations: Implications for the upper mantle seismic anisotropy. *J. Geophys. Res.,* **105**(B5), 7893–7908.

Tommasi, A., Godard, M., Coromina, G., Dautria, J. M. and Barsczus, H., 2004, Seismic anisotropy and compositionally induced velocity anomalies in the lithosphere above mantle plumes: a petrological and microstructural study of mantle xenoliths from French Polynesia. *Earth Planet. Sci. Lett.,* **227**(3-4), 539-556.

Tommasi A. Vauchez A. Godard M. and Belley F., 2006, Deformation and melt transport in a highly depleted peridotite massif from the Canadian Cordillera: Implications to seismic anisotropy above subduction zones. *Earth Planet. Sci. Lett.,* **252**, 245–259.

Tommasi, A., Vauchez, A. and Ionov, D. A., 2008, Deformation, static recrystallization, and reactive melt transport in shallow subcontinental mantle xenoliths (Tok Cenozoic volcanic field, SE Siberia). *Earth Planet. Sci. Lett.,* **272**, 65-77.

Uchimizu, M., 1966, Geology and petrology of alkali rocks from Dogo, Oki Islands. *Journal of the Faculty of Science, University of Tokyo, Series II,* **16**, 85–159.

Ulich, S. and Mainprice, D., 2005, Does cation ordering in omphacite influence development of lattice-preferred orientation? *J. Struct. Geol.*, **27**, 419-431.

Uto, K., Takahashi, E., Nakamura, E. and Kaneoka, I., 1994, Geochronology of alkali volcanism in Oki-Dogo Island, Southwest Japan: Geochemical evolution of basalts related to the opening of the Japan Sea. *Geochemical Journal,* **28**, 431–449.

Uto, K., Hirai, H., Goto, K. and Arai, S., 1987, K–Ar ages of carbonate-and mantle nodule-bearing lamprophyre dikes from Shingu, central Shikoku, Southwest Japan. *Geochem. J.*, **21**, 283–290.

Uto, K., 1990, Neogene volcanism of Southwest Japan: its time and space on K–Ar dating. PhD thesis, University of Tokyo, Japan.

Van Achterbergh, E., Griffin, W. L. and Stiefenhofer, J., 2001, Metasomatism in mantle xenoliths from the Letlhakane kimberlites: estimation of element fluxes. *Contrib. Mineral. Petrol.,* **141**, 397–414.

Vauchez A. Tommasi A. Barruol G. and Maumus J., 2000, Upper mantle deformation and seismic anisotropy in continental rifts. *Phys. Chem. Earth, Part A Solid Earth Geod,.* **25** 111–117.

Vauchez, A. and Garrido, C. J., 2001, Seismic properties of an asthenospherized lithospheric mantle: constraints from lattice preferred orientation in peridotite from the Ronda massif. *Earth Planet. Sci. Lett.,* **192**, 235–249.

Vauchez, A. and Tommasi, A., 2003, Wrench faults down to the asthenosphere: Geological and geophysical evidence and thermo–mechanical effects, IN: Storti, F., Holdsworth, R.E., Salvini, F. (eds.), Intraplate Strike-Slip Deformation Belts. Geological Society of London Special Publications, London, pp. 15–24.

Vauchez, A., Dineura, F. and Rudnick, R., 2005, Microstructure, texture and seismic anisotropy of the lithospheric mantle above a mantle plume: Insights from the Labait volcano xenoliths (Tanzania). *Earth Planet. Sci. Lett.*, **232**, 295-314.

Voigt, W., 1928, *Lerrbuch der Kristallphysik*, Teubner-Verlag, Leipzig.

Vonlanthen, P., Kunze, K., Burlini, L. and Grobety, B., 2006, Seismic properties of the upper mantle beneath Lanzarote (Canary Islands): Model predictions based on texture measurements by EBSD. *Tectonophysics,* **428**, 65–85.

Vollmer (1990) Vollmer, F.W., 1990. An application of eigenvalue methods to structural domain analysis. Geological Society of America Bulletin 102, 786–791.

Wagner, L. S., Beck, S., Zandt, G. and Ducea, M. N., 2006, Depleted lithosphere, cold,

trapped asthenosphere, and frozen melt puddles above the flat slab in central Chile and Argentina. *Earth Planet. Sci. Lett.*, **245**, 289–301, doi:10.1016/j.epsl.2006.02.014.

Watanabe, T., Shirasugi, Y., Yano, H. and Michibayashi, K., 2011, Seismic velocity in antigorite-bearing serpentinite mylonites. *Geological Society, London, Special Publications 2011*, **360**, 97-112.

West, M., Ni, J., Baldridge, W. S., Wilson, D., Aster, R., Gao, W. and Grand, S., 2004, Crust and upper mantle shear wave structure of the southwest United States: Implications for rifting and support for high elevation. *J. Geophys. Res.,* **109**(B03309), doi:10.1029/2003JB002575.

Wilkinson, J. F. and Binns, R. A., 1977, Relatively iron-rich lherzolite xenoliths of the Cr-diopside Suite: A guide to the primary nature of anorogenic tholeiitic andesite magmas. *Contrib. Mineral. Petrol.,* **65**, 199–212.

Williams, W. J. W., 1999, Evolution of Quaternary intra plate mafic lavas from the Potrillo volcanic field, USA, and the San Quintin volcanic field, Mexico. Univ. Texas at El Paso. Unpub PhD dissertation, 186p.

Wilson, D. S., 1996, Fastest known spreading on the Miocene Cocos-Pacific plate boundary. *Geophys. Res. Lett.,* **23**, 3003–3006.

Wilson, D., Aster, R. and LA RISTRA Team, 2003, Imaging crust and upper mantle seismic structure in the southwestern United States using teleseismic receiver functions. *The Leading Edge*, **22**(3), 232-237.

Wilson, D. S., et al. (2006), Drilling to gabbro in intact ocean crust, *Science*, **312**, 1016 – 1020, doi:10.1126/science.1126090.

Wüstefeld, A., Bokelmann, G., Zarol, C., and Barruol, G., 2008, SplitLab: A shear-wave splitting environment in Matlab. *Computers & Geosciences*, **34**(5),

515-128.

Wilshire, H. G., Meyer, C. E., Nakata, J. K., Calk, L. C., Shervais, J. W., Nielson, J. E. and Schwartzman, E. C., 1988, Mafic and ultramafic xenoliths from volcanic rocks of the western United States. U.S. *Geological Survey Professional Paper*, **1443**, 179 pp.

Yamamoto, J., Kagi, H., Kawakami, Y., Hirano, N. and Nakamura, M., 2007, Paleo-Moho depth determined from the pressure of CO_2 fluid inclusions: Raman spectroscopic barometry of mantle- and crust-derived rocks. *Earth Planet. Sci. Lett.,* **253**, 369–377.

Young, H. P., and Lee, C.-T. A., 2009, Fluid-metasomatized mantle beneath the Ouachita belt of southern Laurentia: Fate of lithopsheric mantle in a continental orogenic belt. *Lithosphere,* **1**, 370-383.

Zhang, S. and Karato, S.-I., 1995, Lattice preferred orientation of olivine aggregates deformed in simple shear. *Nature,* **375**, 774–777.

Zhao, D., Horiuchi, S. and Hasegawa, A., 1990, 3-D seismic velocity structure of the crust and the uppermost mantle in the northeastern Japan Arc. *Tectonophysics*, **181**, 135–149.

Zhao, X. O., 1997, Microstructure et petrofabrique des minéraux à haute température: example du terrain du Morin, Province de Grenville, Québec. PhD Thesis, Université de Montréal, Canada.